ROYAUME DU MAROC
Université Mohammed V - RABAT -
جامعة محمد الخامس – الرباط –
Faculté des sciences
كلية العلوم
CENTRE D'ETUDES DOCTORALES - SCIENCES ET TECHNOLOGIES

N° d'ordre : 3341

THESE DE DOCTORAT

Présentée par :

AIT TAMERD Mohamed

Discipline : Sciences Physique
Spécialité : Sciences des Matériaux et modélisation des systèmes

Theoretical investigations and magnetoelectric prediction in some functional thin films.

Soutenue le : **26 Septembre 2020**

Devant le jury :

Abdelilah BENYOUSSEF	PES, membre résident de l'Académie Hassan II des Sciences et Techniques, Rabat.	Président
Abdallah EL KENZ	PES, Université Mohammed V de Rabat, Faculté des Sciences.	Directeur de Thèse
Mohammed LOULIDI	PES, Université Mohammed V de Rabat, Faculté des Sciences.	Rapporteur /Examinateur
Ahmed HOURMATALLAH	PES, Université Sidi Mohamed Ben Abdellah, Ecole Normale Supérieure de Fès.	Rapporteur /Examinateur
Noureddine BENAYAD	PES, Université Hassan II de Casablanca, Faculté des Sciences Aïn Chock.	Rapporteur /Examinateur
Mimoun El MARSSI	PES, Université de Picardie Jules Verne, Amiens, France.	Examinateur
Abdelilah LAHMAR	PH, Université de Picardie Jules Verne, Amiens, France.	Examinateur
Omar MOUNKACHI	PA, Université Mohammed V de Rabat, Faculté des Sciences.	Invité

Preamble

This PhD was carried out at "Laboratoire de Matière Condensée et Sciences Interdisciplinaires (LaMCScI)" at the Faculty of Sciences, Mohammed V University of Rabat.

This thesis was supported by MESRSFC (Ministère de L’Enseignement Supérieur, de la Recherche Scientifiqueet de la Formation des Cadres) in the Framework of the national program PPR15/2015.

Dedication

To My parents

To my wife

To my brothers and sisters

To all my professors

To all my friends

Acknowledgement

The present research work was carried out at "Laboratoire de Matière Condensée et Sciences Interdisciplinaires (LaMCScI)" Faculty of Science, Mohammed V University of Rabat, under the supervision of Prof Abdallah EL KENZ.

I would like to express my sincere appreciation to my supervisor Abdallah EL KENZ for providing the opportunity to work on this project and continues both in academic and scientific supports with great helps in my Ph.D. Also for his scientific qualities, encouraging, advising, great guidance.

I would like to express my thanks to all the members of my jury for agreeing to evaluate my thesis and providing helpful suggestions and constructive comments.

I would like to extend my thanks to Prof. Abdelilah BENYOUSSEF, the chairman of the jury, from the Faculty of Science in Rabat, for reviewing this thesis. Also for his availability and his sense of transmitting scientific knowledge that allowed me to carry out this work.

I would like also to offer my thanks to Prof. Mohammed LOULIDI, from the Faculty of Science Rabat, for reporting and reviewing this PhD thesis.

I would like to express my thanks to Prof. Ahmed HOURMATALLAH, from the Sidi Mohamed Ben Abdellah University of Fes, for reporting and reviewing this PhD thesis.

I would like also to offer my thanks to Prof. Noureddine BENAYAD, from Hassan II University Casablanca - Faculty of Sciences Ain Chock, for reporting and reviewing this PhD.

I present my sincere thanks to Prof. Mimoun EL MARSSI from Picardie Jules Verne University, Amiens, France, for the interesting discussions and contributions and reviewing this thesis. Also, for his invaluable assistance, overall supervision, and encouragement throughout my time at LPMC.

My sincere thanks also to Professor Abdelilah LAHMAR from Picardie Jules Verne University , Amiens, France, for his scientific ideas, his availability and for finding the time to read my manuscript and his suggestions on how to improve the quality of this thesis. I cannot thank you enough for your conversations, your efforts, and dedication to our combined work and the science presented in this thesis. I wish you and your family the best in future.

I would like also to express my thanks to Prof. Omar MOUNKACHI, from the Faculty of Science in Rabat, for reviewing this thesis.

I would like also to acknowledge Prof Mohammed HAMEDOUN, Omar MOUNKACHI, Brahim ABRIME, Hassan ElMOUSSAOUI, Zakariya MAHHOUTI, khadija ELMAALEM at MAScIR -morocco foundation for advanced science innovation and research- for their helps.

I would like to acknowledge Pr. Omar ELRHAZOUANI for his help. I would also like to thank all the members of the LaMCScI and also my colleagues, who supported me in all scientific and technical matters.

Lastly, I also would like to thank MESRSFC. This thesis was supported by MESRSFC (Ministère de L'Enseignement Supérieur, de la Recherche Scientifiqueet de la Formation des Cadres) in the Framework of the national program PPR15/2015.

Finally, I would like to thank my family for their encouragement and support.

Abstract:

Numerical modelling of functional materials is developing rapidly to provide an accurate interpretation of the experimental results, necessary to improve existing devices and to set up innovative systems. The goal of this thesis work is the theoretical investigations and magnetoelectric prediction in some functional thin films. The emphasis is placed on the study of the mechanisms governing extrinsic and intrinsic magnetoelectric coupling, using density functional theory (DFT) and Monte Carlo simulation in multiferroic compounds. Firstly, the electronic origin of the strong magnetoelectric coupling of the NiFe2O4/PZT heterostructure was analyzed by the density functional theory. In addition, the ferroelectric, magnetic and magnetoelectric properties of NiFe2O4/PZT , CoFe2O4/PZT, NiFe2O4/PZT/CoFe2O4 and NiFe2O4/PZT/NiFe2O4 heterostructures were investigated by Monte Carlo simulation. The maximum magnetoelectric voltage coefficient of 1405 mV/(cm.Oe) was predicted in NiFe2O4/PZT/NiFe2O4. The second part of this manuscript is dedicated to the simulation of the intrinsic magnetoelectric coupling in BiFeO3. A large magnetoelectric voltage coefficient of 104 mV/(cm.Oe) has been predicted in BiFeO3 thin films with 25% of the defects. Besides, the multiferroic properties of BiFeO3 doped with rare earth and Mn were analyzed by the DFT.

Keywords: magnetoelectric, DFT, Monte Carlo simulation, multiferroics, NiFe2O4/PZT , BiFeO3.

Résumé :

La modélisation numérique des matériaux fonctionnels se développe rapidement pour satisfaire le besoin d'améliorer les dispositifs existants et de mettre en place des systèmes innovants. Le but de ce travail de thèse est l'analyse théorique et la prédiction de l'effet magnétoélectrique dans certaines couches minces fonctionnelles. Dans le cadre de cette thèse, nous avons étudié les mécanismes gouvernant le couplage magnétoélectrique extrinsèque et intrinsèque en utilisant la théorie de la fonctionnelle de la densité (DFT) et la simulation de Monte Carlo dans les composés multiferroïques. L'origine électronique du fort couplage magnétoélectrique de l'hétérostructure NiFe2O4/PZT a été analysé par la théorie de la fonctionnelle de la densité. De plus, les propriétés ferroélectriques, magnétiques et magnétoélectriques des hétérostructures NiFe2O4/PZT, CoFe2O4/PZT, NiFe2O4/PZT/CoFe2O4 et NiFe2O4/PZT/NiFe2O4 ont été obtenu par la simulation Monte Carlo etle coefficient maximum de voltage magnétoélectrique est de 1405 mV/(cm.Oe) a été prédit dans NiFe2O4/PZT/NiFe2O4. La deuxième partie de ce manuscrit est consacrée à la modélisation et la simulation du couplage magnétoélectrique intrinsèque dans le $BiFeO_3$. Un coefficient important de voltage magnétoélectrique de 104 mV/(cm.Oe) a été prédit dans les couches minces de BiFeO3 avec 25% des défauts. En addition, les propriétés multiferroïques de $BiFeO_3$ dopé par terre rare et Mn sont été analysées par la DFT.

Mots-clés : magnétoélectrique, DFT, simulation Monte Carlo, multiferroïques, hétérostructure NiFe2O4/PZT, $BiFeO_3$.

Résumé détaillé :

Chapitres 1& 2 :

Les matériaux multiferroïques, caractérisés par la présence de deux ou plusieurs ordres ferroïques (ferromagnétique, ferroélectrique et ferroélastique) ont attiré une attention particulière en raison de leur potentiel application technologique[1]. Notamment, les matériaux magnétoélectriques, dans lesquels les ordres ferromagnétiques et ferroélectriques existent simultanément, présentent un potentiel élevé dans les domaines de l'ingénierie électronique, spintronique et électrique[2], [3]. En fait, les matériaux magnétoélectriques sont divisés en deux types (**Figure.1**). Le premier est constitué de matériaux homogènes dans lesquels l'effet magnétoélectrique est intrinsèque. La conversion d'énergie (l'effet magnétoélectrique) obtenue en pratique par ce type de matériau est faible. La seconde catégorie est constituée de matériaux composites ; la combinaison de matériaux piézoélectriques et magnétostrictifs produit un effet magnétoélectrique extrinsèque. La présence d'un champ magnétique crée une déformation magnétostrictive. Cette déformation est transmise au matériau piézoélectrique et provoque une polarisation électrique. Inversement, l'application d'un champ électrique génère une contrainte qui peut modifier l'état magnétique des matériaux magnétostrictifs. La conversion d'énergie résultant des deux couplages successifs est plus importante que l'effet intrinsèque. L'intérêt de l'utilisation des matériaux composites est de combiner les avantages de chaque composant [4], [5].

L'effet magnétoélectrique direct, qui est l'apparition d'une polarisation électrique (P) lorsqu'un champ magnétique (H) est appliqué, peut être exprimé par l'équation : $\Delta P = \alpha \Delta H$, où, E est le champ électrique externe et α est le coefficient magnétoélectrique. En revanche, l'effet magnétoélectrique inverse, c'est-à-dire la polarisation magnétique induite (M) par l'application d'un champ électrique externe (E), s'écrit sous la forme : $\Delta M = \alpha \Delta E$ [6].

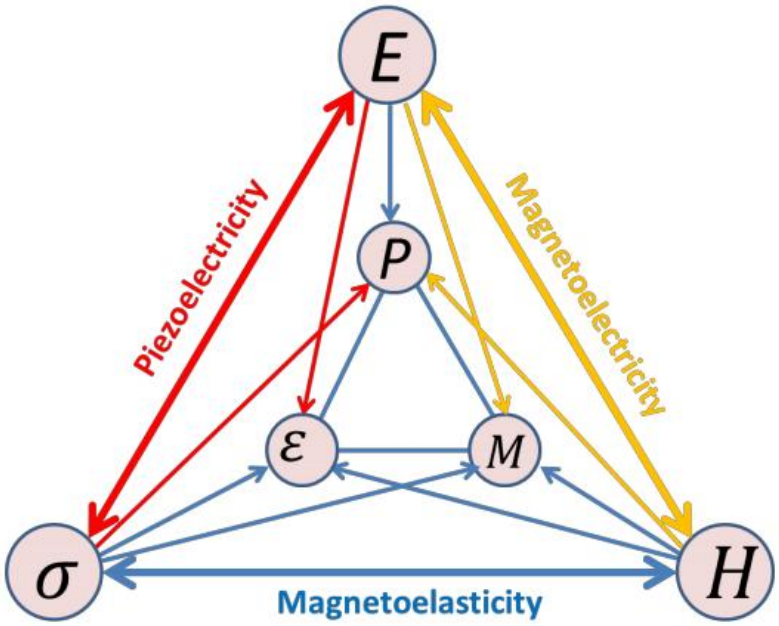

Figure.1: Diagramme des interactions intrinsèques et extrinsèques entre les propriétés ferroélectrique, élastique et ferromagnétique .

Malheureusement, l'effet magnétoélectrique intrinsèque dans les matériaux monophasés est très faible et ne se produit généralement qu'à basse température, ceci est dû au fait que l'effet magnétoélectrique est très faible dans les matériaux monophasés. La réalisation de composites magnétoélectriques, basée sur le couplage extrinsèque des matériaux ferroélectriques et magnétostrictive, permet d'obtenir un effet magnéto-électrique "géant", qui est plus intéressant pour les applications technologiques. La **figure.2** présente les différentes connectivités adaptées aux composites multiferroiques. Parmi ces matériaux multiferroïques, le BiFeO3 (BFO) est l'un des plus étudiés récemment en raison de l'existence simultanée à température ambiante de la ferroélectricité et de l'antiferromagnétisme avec une température de Curie très élevée T_C = 1103 K et un ordre antiferromagnétique de type G avec une température de Néel T_N = 643 K [7].

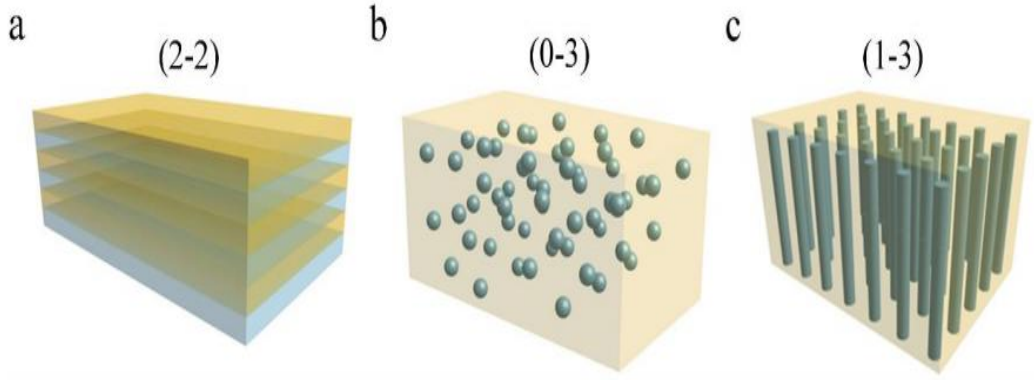

Figure.2 : les connectivités adaptées aux composites multiferroiques. **(a)** des couches minces ferroélectriques/ magnétiques, (2-2), **(b)** des nanoparticules dans une matrice (0-3) et **(c)** des nanopilliers dans une matrice (1 -3).

Ce travail de thèse porte sur la modélisation et la simulation des propriétés multiferroïques telles que le couplage magnéto-électrique, magnétique, électronique, ferroélectrique des nanocomposites de type (2-2) ($CoFe_2O_4/PbZr_{0.5}Ti_{0.5}O_3$ et $NiFe_2O_4/PbZr_{0.5}Ti_{0.5}O_3$), du BFO monophasé et du $BiFeO_3$ dopé au $MnGdO_3$, en utilisant la théorie de la fonctionnelle de la densité et la simulation Monte Carlo.

Chapitre 3 :

Nous avons utilisé la théorie de la fonctionnelle de densité avec GGA+U pour étudier les propriétés électroniques, magnétiques et magnétoélectriques de l'hétérostructure $NiFe_2O_4/PbZr_{0.5}Ti_{0.5}O_3$(001). Nous avons considéré deux différents types d'atomes interfaciaux NFO/ZTO et NFO/PbO (**Figure.3**).Le travail de séparation interfaciale est respectivement : 0,733 et 0,469 J/m^2, pour NFO/PbO et NFO/ZTO, dans la bicouche $NiFe_2O_4$/PZT. Ces résultats indiquent que le NFO/ZTO est énergétiquement plus favorable que le NFO/PbO à l'interface $NiFe_2O_4$/PZT.Il est intéressant de noter que le couplage

magnétoélectrique dans cette hétérostructure est strictement dépendant des propriétés électroniques des atomes de l'interface. L'origine électronique du fort couplage magnétoélectrique à l'interface NFO/ZTO est due à l'hybridation des orbitales des atomes de l'interface Ni, Fe, T, Zr, O (**Figure.4)**. Les couplages magnétoélectriques calculés à l'interface $NiFe_2O_4$/PZT pour NFO/ZTO et NFO/PbO sont respectivement : $\alpha_s = 3.15 \times 10^{-10}$ et 0.52×10^{-10} G.cm/V, qui sont du même ordre de grandeur que le coefficient magnétoélectrique calculé rapport dans la littérature. Les résultats théoriques présentés peuvent fournir des indications adéquates pour les dispositifs magnétoélectriques.

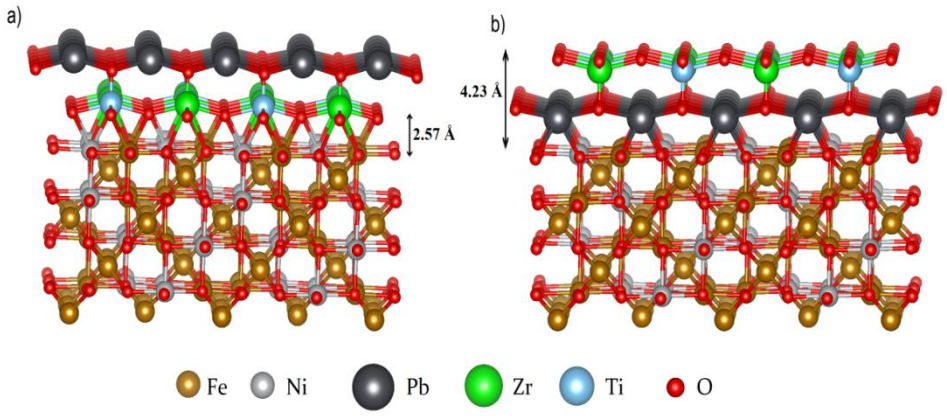

Figure.3 : **(a)** la structure de NFO/PZT (001) avec NFO/ZTO à l'interface, **(b)**la structure de NFO/PZT (001) avec NFO/PbO à l'interface.

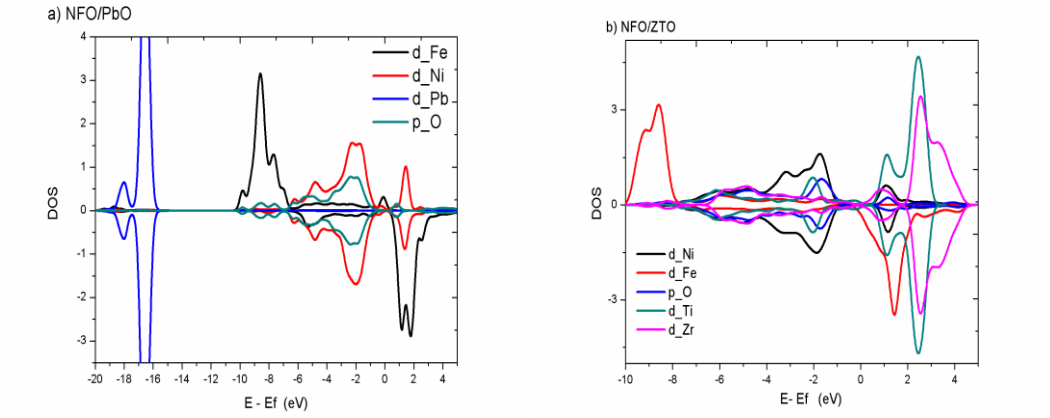

Figure.4 : Densité partielle d'états (PDOS) des atomes interfaciaux dans l'interface NiFe2O4/PZT, (a) interface NFO/PbO, (b) interface NFO/ZTO.

Chapitre 4 :

Dans ce chapitre, nous avons étudié les propriétés ferroélectriques et de stockage d'énergie du PZT par simulation Monte Carlo. Les constantes de couplage d'échange calculées correspondant aux températures de curie expérimentalessont :J_{1tt} = 6,915 meV, J_{2tt} =3,457

meV, J_{1zz} = 4,542 meV, J_{2zz} =2,271 meV, J_{1tz} = 5,947 meV et J_{2tz} =2,973 meV. Le diagramme de phase de PZT en fonction de la valeur de concentration de Ti 'x' dans le PZT a été prédit à travers la simulation Monte Carlo (**figure.5**). À température ambiante, la structure cristalline est tétragonale pour le PZT riche en Ti et rhomboédrique pour le PZT riche en Zr. Lorsque la température augmente, le centre de symétrie apparaît dans les deux structures, la structure se transforme alors en une phase cubique, et le PZT perd sa polarisation spontanée. Les diagrammes de phase calculés sont en bon accord avec les résultats expérimentaux rapportés par Noheda et al [6]. La **figure.6(a-b)** présente les cycles d'hystérésis des couches minces de PZT à 300K. Nous avons observé que les courbes de polarisation sont symétriques. De plus, la surface des cycles d'hystérésis devient plus étroite lorsque la concentration de Zr dans le PZT augmente. Pour x=0, les couches minces de $PbZrO_3$ étaient à l'état antiferroélectrique, qui caractérisé par la présence d'une double boucle d'hystérésis avec une polarisation rémanente nulle. En augmentant la valeur de x, une faible ferroélectricité est observée pour $PbZr_{0,9}Ti_{0,1}O_3$ et $PbZr_{0,8}Ti_{0,2}O_3$. Cependant, au-delà de x=0,3, on observe le cycle d'hystérésis de ferroélectrique, indiquant que le film de PZT était dans son état ferroélectrique Figure.6 **(a-b).** La**figure.7 (a-b)** montre la polarisation à saturation (Ps), la polarisation rémanente (Pr) et le champ coercitif (Ec) (déterminé à partir des cycles d'hystérésis) en fonction de la valeur x. Lorsque les valeurs x augmentent, le couplage d'échange entre les moments dipolaires aux sites Zr-Ti etTi-Ti augmente dans $PbZr_{1-x}Ti_xO_3$. Par conséquence, la surface des cycles d'hystérésis devient plus importante, ce qui augmente le champ coercitif Ec. Les valeurs calculées du champ coercitif sont Ec=45, 95, 140 et 275 kV/cm pour x=0,3, 0,5, 0,6 et 1, respectivement. Les valeurs obtenues sont en bon accord avec les résultats expérimentaux.

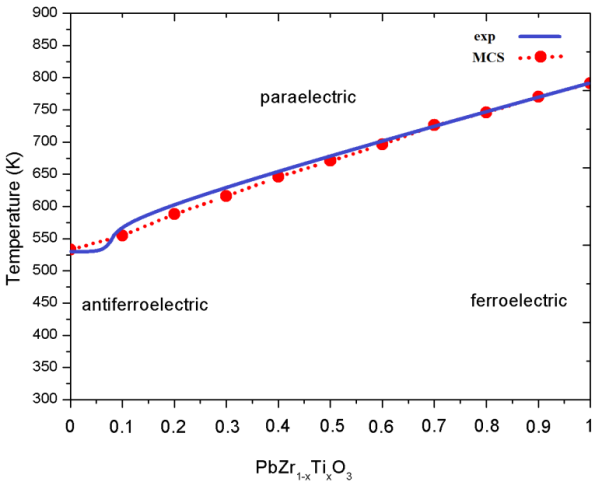

Figure 5 : Diagramme de phase PbZr1-xTixO3 simulé par Monte Carlo simulation, et le diagramme de phase expérimental de PbZr1-xTixO3 adapté de [32] (représenté en bleu).

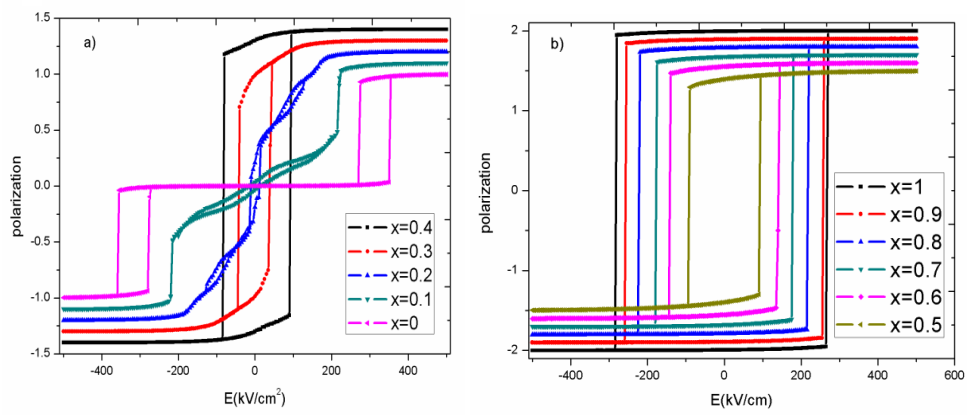

Figure.6 : Cycles d'hystérésis P-E des couches minces de PbZr1-xTixO3 (a) :x=0, 0,1, 0,2, 0,3, 0,4 et (b) : x=0,5, 0,6, 0,7, 0,8, 0,9, 1. à 300 K.

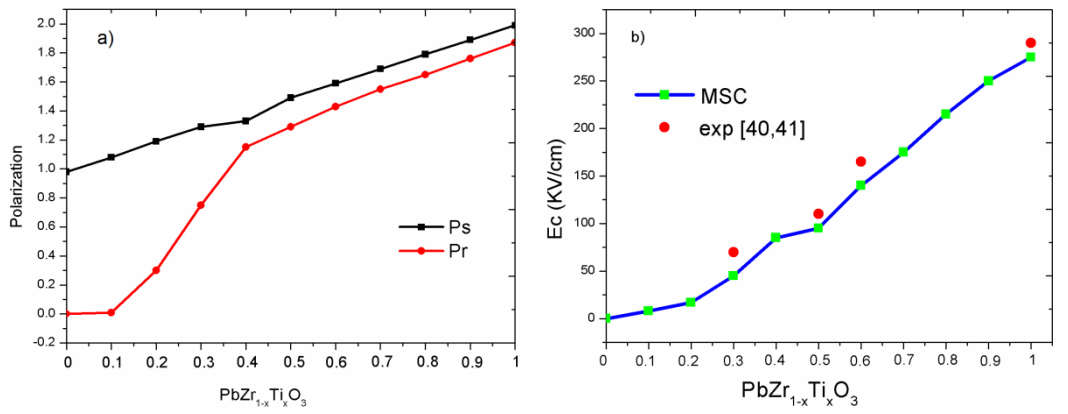

Figure.7 :(a) polarisation rémanente (Pr) et polarisation de saturation (Ps), **(b)** champ coercitif des couches minces de PbZr1-xTixO3 en fonction de la valeur x à 300(K) en comparaison avec certains résultats expérimentaux.

Chapitre 5 :

Nous avons étudié dans ce chapitre les propriétés ferroélectriques, magnétiques et magnétoélectriques des hétérostructures NiFe2O4/PZT (NFO/PZT), CoFe2O4/PZT (CFO/PZT), NiFe2O4/PZT/CoFe2O4 (NFO/PZT/CFO) et NiFe2O4/PZT/NiFe2O4 (NFO/PZT/NFO) en utilisant la simulation Monte Carlo (**figure.8**). Les cycles d'hystérésis, M-H et P-H, pour les interfaces NFO/PZT et CFO/PZT, calculés à 300K pour différentes valeurs de couplage magnéto-électrique interfacial $\mathbf{J}_{me}$, sont illustrés sur la **Figure.9**. Pour $\mathbf{J}_{me}$=0, uncycle d'hystérésis M-H typique a été obtenue pour les deux interfaces NFO/PZT et CFO/PZT. Dans ce cas, la polarisation électrique est restée constante et n'est pas influencée par le champ magnétique H. lorsque on augmente la valeur de $\mathbf{J}_{me}$, on observe une influence du champ magnétique sur la polarisation électrique. Ce comportement est dû au fait que les moments de spin et les dipôles électriques à l'interface interagissent via l'interaction du couplage magnéto-électrique interfacial $\mathbf{J}_{me}$. Dans cette section, nous choisissons les valeurs calculées de Jme correspondant au coefficient de voltage magnétoélectrique expérimental ($\mathbf{J}_{me}$=4.202 meV pour l'interface NFO/PZT et $\mathbf{J}_{me}$=0,625 meV pour l'interface CFO/PZT). Une grande surface de cycle d'hystérésis P-H a été observée dans NFO/PZT par rapport à

CFO/PZT, en raison de la valeur élevée de $\mathbf{J}_{me}$ à l'interface NFO/PZT. La **figure 6(c-d)** montre les boucles d'hystérésis M-H et P-H à 300K pour les hétérostructures. La **figure.10** présente le coefficient de voltage magnétoélectrique en fonction du champ magnétique appliqué (H) pour NFO/PZT, CFO/PZT, NFO/PZT/CFO et NFO/PZT/NFO à 300K. Les coefficients de voltage magnétoélectrique maximum prévus sont respectivement : 460, 50, 650 et 1405 mV/(cm.Oe) pour NFO/PZT, CFO/PZT, NFO/PZT/CFO et NFO/PZT/NFO.

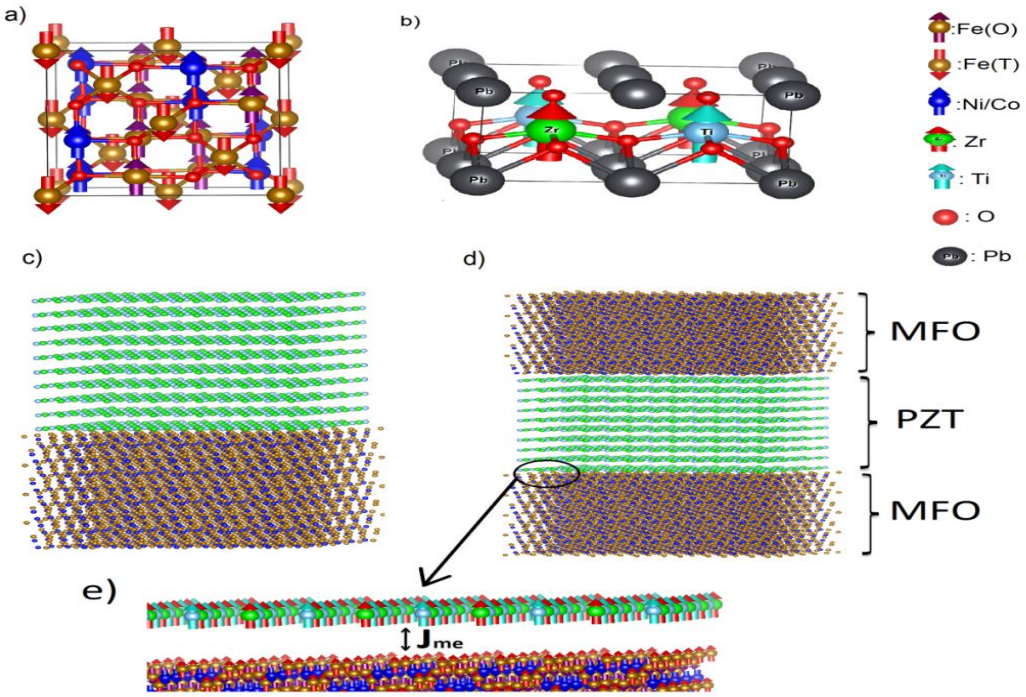

Figure.8: Représentation des structures: **(a)** MFO, **(b)** PZT, **(c)** l'heterostructure MFO/PZT, **(d)** l'heterostructure MFO/PZT/MFO, **(e)** interface MFO/PZT, (M = Ni et Co).

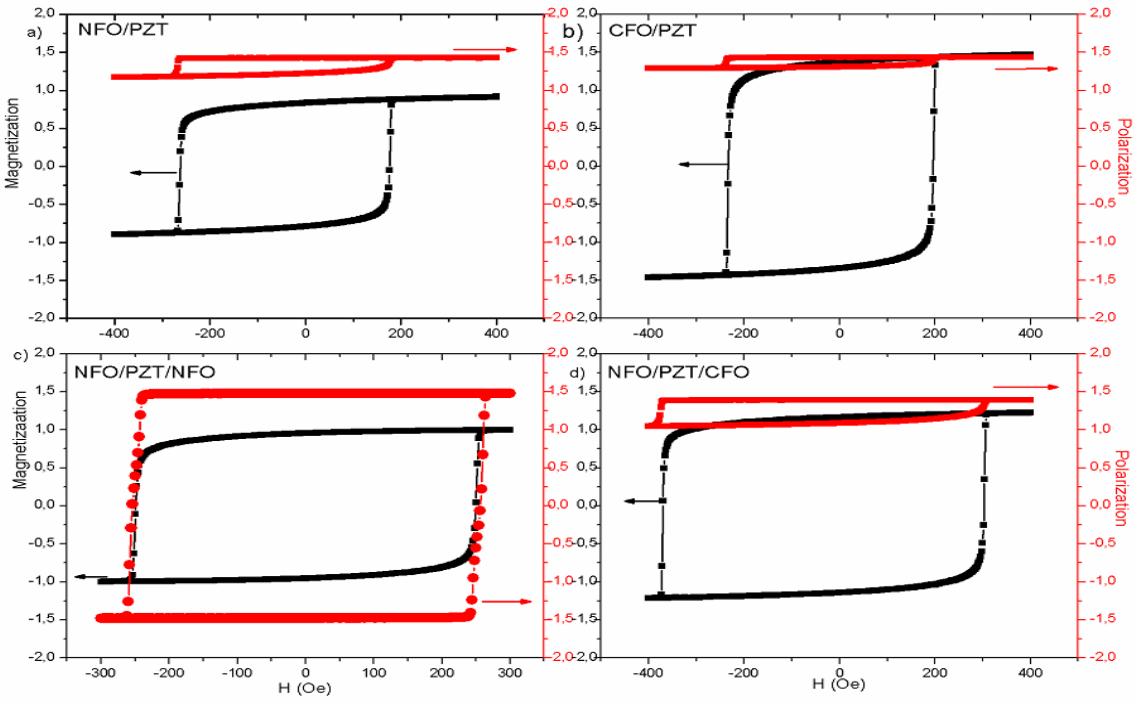

Figure.9 : Les cycles d'hystérésis M-H et P-H pour :(a) NFO/PZT, (b) CFO/PZT, (c) NFO/PZT/CFO et (d) NFO/PZT/NFO à 300K.

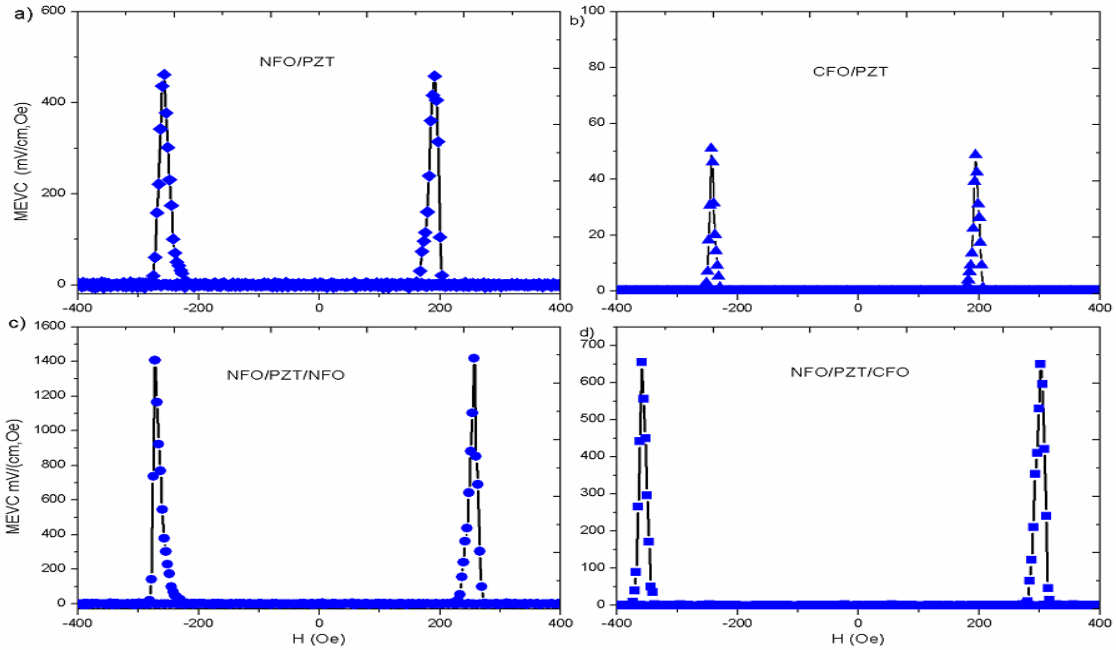

Figure.10 : coefficient de voltage magnétoélectrique en fonction du champ magnétique appliqué (H) pour: (a) NFO/PZT, (b) CFO/PZT, (c) NFO/PZT/NFO et (d) NFO/PZT/CFO à 300K.

Chapitre 6 :

Dans le chapitre 6, nous avons étudié par simulation Monte Carlo les propriétés ferroélectriques, magnétiques et magnétoélectriques de multiferroïque BiFeO3 (BFO) avec les défauts en couches minces (**figure.10**). Nous avons estimé les interactions de couplage d'échange dans les sous-réseaux magnétiques et ferroélectriques qui correspondent à la température critique expérimentale.

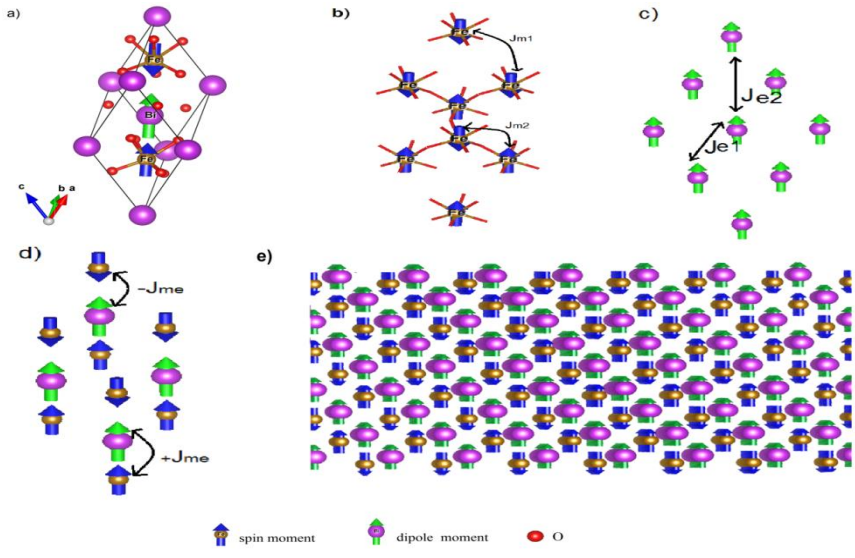

Figure.10 : (a) la structure rhomboédrique de BiFeO3, la représentation schématique des interactions magnétiques (b), les interactions électriques dipôle-dipôle (c) et l'interaction magnétoélectrique (d), BiFeO3 en couches mince (e).

Le coefficient de voltage magnétoélectrique en fonction de l'interaction de couplage magnétoélectrique $\mathbf{J}_{me}$ à température ambiante est représenté sur la **figure.11**. Lorsqu'en augmentant $\mathbf{J}_{me}$, la valeur du coefficient de voltage magnétoélectrique augmente légèrement jusqu'à $\mathbf{J}_{me}$ de 4.560 meV, suivi d'une augmentation rapidement de 15 à 200 mV/(cm.Oe). L'effet du défaut de dipôle électrique sur le coefficient de voltage magnétoélectrique à T= 300K et $\mathbf{J}_{me}$=4.202 meV dans les couches minces de BFO est montré dans la **figure.12**, Nous constatons que pour une concentration de défauts jusqu'à 25%, le coefficient de voltage magnétoélectrique augmente rapidement et atteint son maximum à 25%, puis diminue avec l'augmentation de la concentration de défauts. Le coefficient de voltage magnétoélectrique maximale est 104 mV/(cm.Oe) obtenu pour 25% de défauts dans les couches minces de BFO. Cette grande valeur du coefficient magnétoélectrique peut être attribuée à la réduction des interactions de couplage d'échange ($\mathbf{J}_{e1}$ et $\mathbf{J}_{e2}$) entre les dipôles électriques en raison des défauts des dipôles électriques.

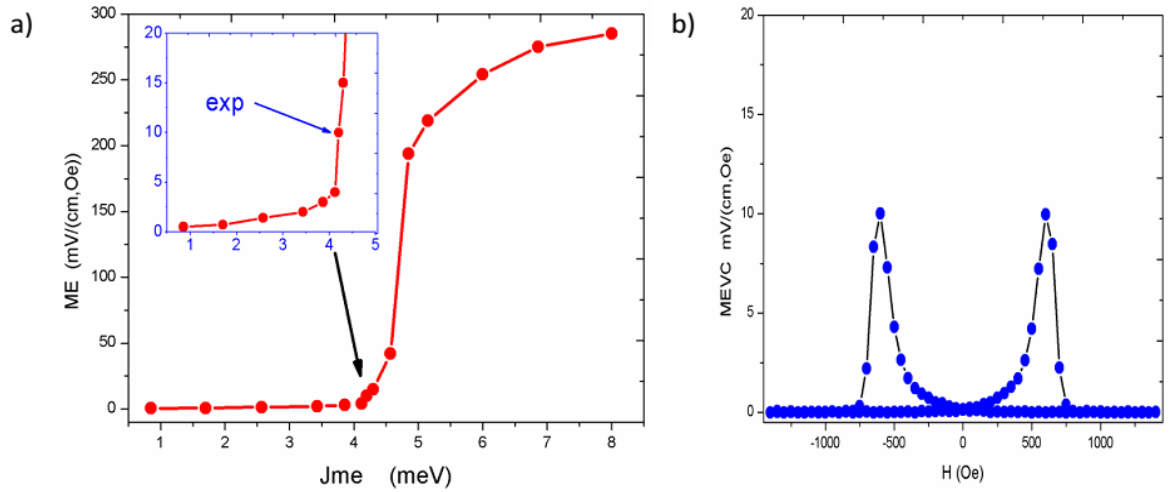

Figure.11 : (a) coefficient de voltage magnétoélectrique en fonction des valeurs de **Jme** et (b) coefficient de voltage magnétoélectrique en fonction du champ H appliqué pour le BFO.

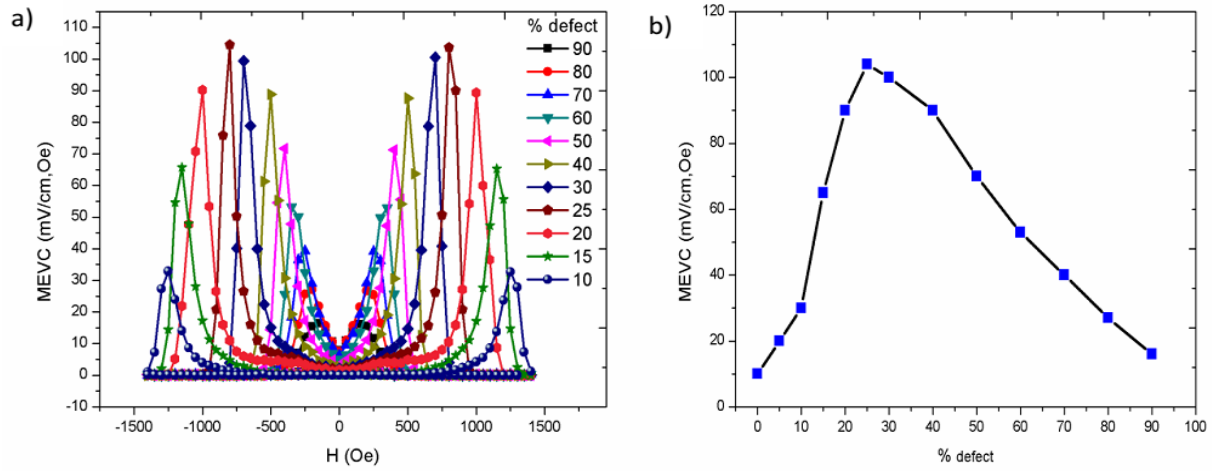

Figure.12 : **(a)** le coefficient de voltage magnétoélectrique (MEVC) en fonction du champ magnétique appliqué H pour différentes concentrations de défauts dans BFO à 300K et **(b)** effets des défauts sur le coefficient de voltage magnétoélectrique.

Chapitre 7 :

Nous avons étudié les propriétés structurelles et multiferroïques de la solution solide BiFeO3-REMnO3 (RE = Er, Eu, Gd, Ho, La, Tb) (**Figure.13)**en utilisant la théorie fonctionnelle de la densité. Une substitution simultanée de RE et Mn dans le $BiFeO_3$ de 12,5 % a été effectuée. La **figure.14a** illustre la densité totale des états de $BiFeO_3$-$REMnO_3$ (RE = Er, Eu, Gd, Ho, La, Tb). La densité totale d'état de BiFeO3-LaMnO3 est symétrique ce qui donne le minimum de moment magnétique de 1,5 μB pour le $BiFeO_3$-$LaMnO_3$. Tandis que, une densité totale asymétrique des états avec une caractéristique métallique est observée pour $BiFeO_3$-$REMnO_3$ avec RE = Er, Eu, Ho et Tb. Pour le BiFeO3-GdMnO3 nous avons constaté la présence d'une propriété semi-métallique et une augmentation du moment magnétique total de 4.3μ_B par rapport à BiFeO3-LaMnO3. La **figure.14b** montre les moments magnétiques totaux et partiels dans BiFeO3-REMnO3. Le moment magnétique total dans $BiFeO_3$-$REMnO_3$ pour RE= Er, Eu, Gd, Ho, La et Tb, est respectivement: 3,58, 4,69, 5,8, 4,27, 1,5 et 6,31 μ_B. Nous avons observé que le moment magnétique total dans BiFeO3-REMnO3 est gouverné par les moments magnétiques des éléments des terres rares. Les calculs de polarisation spontanée dans BiFeO3-REMnO3 sont respectivement : 56,06, 60,84, 47,80, 62,02, 49,73 et 34.97μC/cm2, pour RE= Er, Eu, Gd, Ho, La et Tb, en utilisant la méthode de phase Berry (**figure.15**).

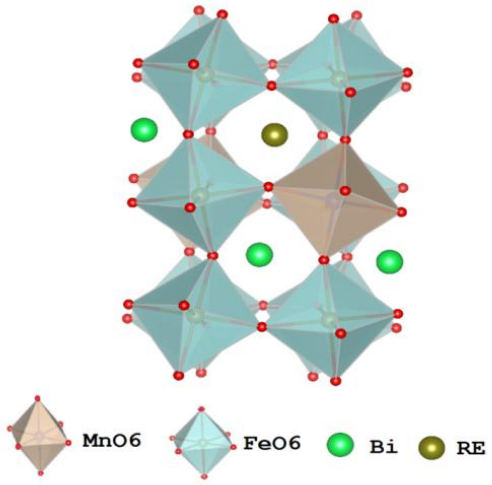

Figure.13 : structure de BiFeO3-REMnO3 (RE=Er, Eu, Gd, Ho, La, Tb)

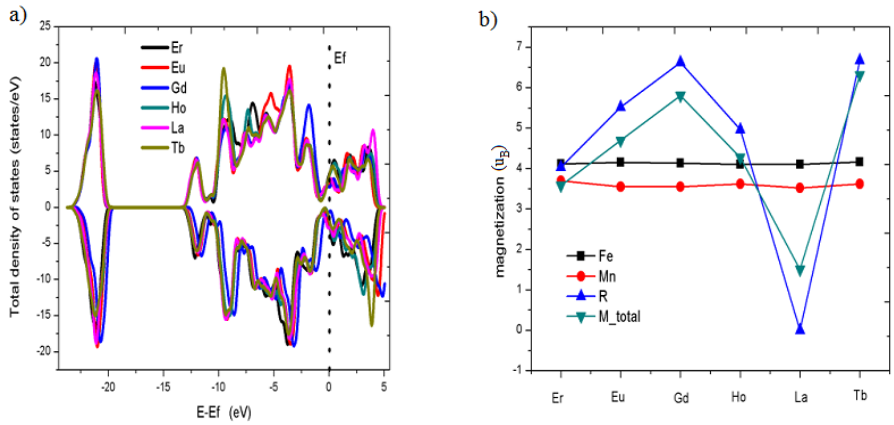

Figure.14 : **(a)** Densité électronique totale des états et **(b)**les moments magnétiques de BiFeO3-REMnO3 (RE = Er, Eu, Gd, Ho, La, Tb),

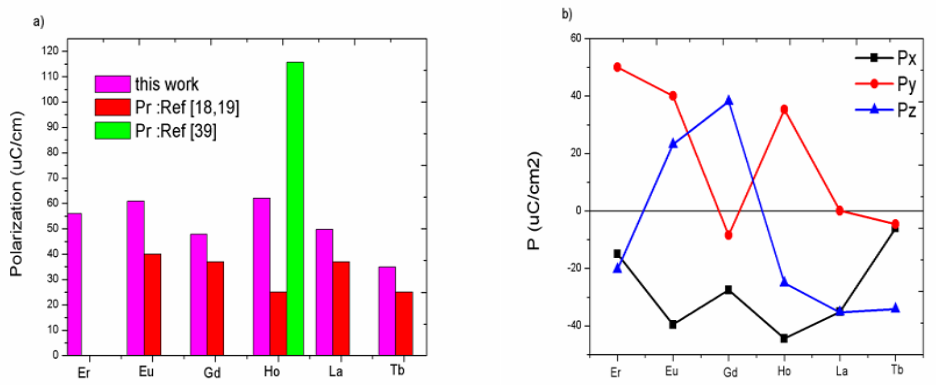

Figure.15 : **(a)** la polarisation spontanée totale avec les résultats expérimentaux et **(b)** sa projection sur l'axe (x, y, z) pour BiFeO3-REMnO3 (RE = Er, Eu, Gd, Ho, La, Tb).

Conclusion:

Ce travail de thèse visait la modélisation et la simulation des propriétés magnéto-électrique, magnétique, électronique et ferroélectrique des nanocomposites de type (2-2) ($CoFe_2O_4/PbZr_{0.5}Ti0.5O_3$ et $NiFe_2O_4/PbZr_{0.5}Ti_{0.5}O_3$), du BFO monophasé et du $BiFeO_3$ dopé par $MnGdO_3$, en utilisant la théorie fonctionnelle de la densité (DFT) et la simulation Monte Carlo.

Ces résultats indiquent que le NFO/ZTO est énergétiquement plus favorable que le NFO/PbO à l'interface de NiFe2O4/PZT. Ainsi que l'origine électronique du fort couplage magnétoélectrique à l'interface NFO/ZTO est due à l'hybridation des orbitales des atomes de l'interface Ni, Fe, T, Zr, O. Les couplages magnétoélectriques calculés à l'interface NiFe2O4/PZT pour NFO/ZTO et NFO/PbO sont respectivement : $\alpha_s = 3.15 \times 10^{-10}$ et 0.52×10^{-10} G.cm/V, qui sont du même ordre de grandeur que le coefficient magnétoélectrique calculé indiqué dans la littérature.

Un modèle de Monte Carlo a été développé pour étudier les propriétés ferroélectriques du PbZr1-xTixO3 (PZT). Le modèle proposé vise à calculer les couplages d'échange dans le $PbZr_{1-x}Ti_xO_3$. Ainsi, l'effet de la température sur les propriétés ferroélectriques des de PZT, telles que les cycles d'hystérésis, la polarisation et le champ coercitif ont été étudiés. De plus, le diagramme de phase en fonction des valeurs x du Ti dans PbZr1-xTixO3 a été déterminé. D'autre part, les propriétés ferroélectriques, magnétiques et magnétoélectriques des hétérostructures NiFe2O4/PZT (NFO/PZT), CoFe2O4/PZT (CFO/PZT), NiFe2O4/PZT/CoFe2O4 (NFO/PZT/CFO) et NiFe2O4/PZT/NiFe2O4 (NFO/PZT/NFO) ont été obtenus. L'effet de la température sur la polarisation magnétique, la polarisation électrique et leurs susceptibilités ont été examinés. Ainsi que l'interaction de couplage magnéto-électrique interfaciale calculée $\mathbf{J}_{me}$ dans les interfaces NFO/PZT et CFO/PZT. Le coefficient de voltage magnétoélectrique de 650 et 1405 mV/(cm.Oe) a été prédit dans NFO/PZT/CFO et NFO/PZT/NFO, respectivement.

La simulation des propriétés ferroélectriques, magnétiques et magnétoélectriques des couches minces du multiferroïque BiFeO3 (BFO) est obtenue dans le cadre de ces travaux. Les interactions de couplage d'échange dans les sous-réseaux magnétiques et ferroélectriques qui correspondent à la température critique expérimentale ont été estimées. De plus, les effets de l'interaction de couplage magnétoélectrique $\mathbf{J}_{me}$ sur les cycles d'hystérésis M-H et P-H et le coefficient de voltage magnétoélectrique ont été étudiés. Un coefficient important de voltage magnétoélectrique de 104 mV/(cm.Oe) a été prédit dans les couches minces de BFO avec 25% de défauts.

Les propriétés structurelles et multiferroïques de la solution solide BiFeO3-REMnO3 (RE = Er, Eu, Gd, Ho, La, Tb) ont été étudiées en utilisant la théorie fonctionnelle de la densité. Une substitution simultanée de RE et Mn dans le BiFeO3 de 12,5 % a été effectuée. Nous avons découvert que le moment magnétique total dans BiFeO3-REMnO3 est gouverné par les moments magnétiques des éléments des terres rares. Les moments magnétiquesestimés sont 3,58, 4,69, 5,8, 4,27, 1,5 et 6,31μB dans BiFeO3-REMnO3 pour RE= Er, Eu, Gd, Ho, La et Tb, respectivement. La polarisation spontanée dans BiFeO3-REMnO3 est respectivement : 56,06, 60,84, 47,80, 62,02, 49,73 et 34.97μC/cm2, pour RE= Er, Eu, Gd, Ho, La et Tb. Les résultats obtenus sont similaires aux résultats expérimentaux.

Table of Contents

List of Figures

List of Tables:

General introduction:

The multiferroic materials, characterized by possessing two or more ferroic orders (ferromagnetic, ferroelectric and ferroelastic) have attracted great attention due for their possible use as multifunctional materials[1], [11]. Magnetoelectric materials, in which the ferromagnetic and ferroelectric orders exist simultaneously, show a high potential in the fields of electronic, spintronic and electrical engineering[12], [13]. In fact, Magnetoelectric materials are divided into two types. The first consists of homogeneous materials in which the magnetoelectric effect is intrinsic. The energy conversion obtained in practice by this type of material is weak. The second category consists of composite materials. The combination of piezoelectric and magnetostrictive materials arises an extrinsic magnetoelectric effect. The presence of a magnetic field creates a magnetostrictive deformation. This deformation is transmitted to the piezoelectric material and an electrical polarization is induced. Conversely, the application of an electric field generates a stress that can modify the magnetic state of magnetostrictive materials[4], [5].The energy conversion resulting from the two successive couplings is more important than the intrinsic effect. The interest of using composite materials is to combine the advantages of each component.

Artificial multiferroicis a matrix where the ferroelectric and ferromagnetic phases are separated in the same material. This approach offers advantages for the choice of materials and their properties, and makes it possible to achieve higher coupling values. Oxides are particularly interesting for these applications because they exhibit many interface effects, also for their stability under normal atmospheric conditions[14].For applications based on ME materials, particularly, $\mathbf{Pb(Zr_xTi_{1-x})O_3}$ is one of the best materials, well referenced as ferroelectric and piezoelectric at room temperature. It should be noted that the $\mathbf{Pb(Zr_xTi_{1-x})O_3}$ **(PZT)** has received a more specific attention as its piezoelectric response relates to the existence of competition between rhombohedral and tetragonal phases leading to one of the highest piezoelectric response, around **-170 pm/V** and **374 pm/V** for the piezoelectric coefficient $\mathbf{d_{31}}$ and $\mathbf{d_{33}}$, respectively[15], [16]. It is important to provide insight into the performance and polarization switching of this material in order to widen the range of operating conditions of PZT based devices. Recall that this system can undergoes gradual phase transition with different behavior: classical ferroelectrics (FE), antiferroelectrics (AFE) and relaxor ferroelectrics (RFE). Especially, the AFE state attracts much attention for the potential application in high energy storage capacitors [17]

For the magnetostrictive material, the $\mathbf{CoFe_2O_4}$ has retained a particular attention as a suitable candidate for the magnetostrictive layer due to its high magnetostriction constant[18]. In addition, the $\mathbf{NiFe_2O_4}$ is ferrimagnetic at room temperature, and has high magnetoelectric coefficients[19]. The choice to use oxides of this nature is also economical and environmentally sustainable. The materials used in ferrite are available and are cheap in contrast to rare earths. However, $\mathbf{CoFe_2O_4/PZT}$ and $\mathbf{NiFe_2O_4/PZT}$ have shown to exhibit a high magnetoelectric coupling[19],but the mechanisms involved in the coupling are not well understood.

Currently, thenumber of intrinsic multiferroics (which **$BiFeO_3$** is the best known) is very small, even extending the definition of magnetoelectric materials to antiferromagnetic compounds, and their magnetoelectric coupling values are low. In the **$BiFeO_3$** compound, the observed magnetoelectric effect is of the second order due to the symmetry constraints related to the cycloidal structure[20]. Therefore, if we substitute bismuth by rare earth (**REMnO3** (**RE= rare earth**), the magnetic order becomes antiferromagnetic and a first order linear magnetoelectric effect can be observed [21].

In addition to the experimental measurement, the study of magneto-electric effect required mostly the development of a computational technique to obtain the magneto-electric couplings in a compound. In this objective, we have developed a methodology to calculate the magneto-electric coupling. This methodology is based on the estimation of the evolution of the magnetic polarization under the effect of an electric field. In this work, we propose the First-principle calculations and Monte Carlo Simulation methods to understand the mechanisms involved in magneto-electric effect. The available experimental data was an important point for our work, which is giving the point of comparison. Furthermore, the experimental results allow confirming and validatingthe used methods: First-principle calculations and Monte Carlo simulation.

This thesis is composed of seven chapters. In the first chapter, we recall some useful concepts for understanding the manuscript. We describe the essential characteristics of the ferroelectricity, magnetism and magnetoelectric properties, which exist in multiferroic compounds and we introduce the magnetoelectric voltage coefficient made up until now on various multiferroic compounds. In addition, we present the different types of multiferroics (intrinsic and artificial), different types of magneto-electrical couplings observed, as well as the most applications of these materials.

In the second chapter, we describe the methodology used to determine the magneto-electric coupling, as well as the electrical, magnetic and properties. We define the basic concepts of the density functional theory (**DFT**) [22], [23], as well as its different approximations, in particular, the **LDA** and **GGA** approximation. We indicate at the end of this chapter the basic concepts of Monte Carlo simulation and we describe the Metropolis algorithm that allows computing the configurations of the Ising model.

The third chapter represents the first part of our results in which we report a first-principles investigation of interfacial magnetoelectric coupling in the **$NiFe_2O_4$/PZT (001)** heterostructure. Two termination surfaces are considered, namely the **$(Zr_{0.5}Ti_{0.5})O_2$**-terminated **PZT** surface and the **PbO**-terminated **PZT** surface at the **$NiFe_2O_4$/PZT** interface. The magnetic, electronic, interfacial separation work and magnetoelectric coefficient were investigated.

The chapter fourth concerns the investigation of the ferroelectric and energy storage properties of $PbZr_{1-x}Ti_xO_3$ using Monte Carlo simulation. We propose a new model to

calculate the exchange coupling constants to approach the phase diagram, dielectric, ferroelectric and energy storage properties of $PbZr_{1-x}Ti_xO_3$ system.

In the chapter 5, we propose a Monte Carlo simulation for determining the ferroelectric, magnetic and magnetoelectric properties of **NFO/PZT, CFO/PZT, NFO/PZT/CFO** and **NFO/PZT/NFO** heterostructures. We focus on the direct magnetoelectric effect where the electric polarization **(P)** in the ferroelectric thin film **PZT** is modified by a magnetic field (**H**). Magnetoelectric voltage coefficient of **NFO/PZT, CFO/PZT,NFO/PZT/CFO** and **NFO/PZT/NFO** heterostructures was carried out using Monte Carlo simulation. The emphasis was on the effect of the temperature on the magnetization, electric polarization and their susceptibilities. The influence of interfacial magnetoelectric coupling interaction $\mathbf{J_{me}}$ on **P-H** hysteresis loops and magnetoelectric voltage coefficient was also discussed.

In chapter **6**, a Monte Carlo simulation investigation of ferroelectric, magnetic and magnetoelectric properties of multiferroic **$BiFeO_3$ (BFO)** thin films, has been carried out. Exchange coupling interactions in magnetic and ferroelectric sublattices that corresponds to the experimental critical temperature have been estimated. Temperature dependence of the internal energy, specific heat, magnetization, electric polarization and their susceptibilities in **BFO** thin films have been detailed. Moreover, the effect of magnetoelectric coupling interaction $\mathbf{J_{me}}$ on **M-H** and **P-H** hysteresis loops and magnetoelectric voltage coefficient were studied.

A complete and detailed study of structural and multiferroic properties of **$BiFeO_3$-$REMnO_3$(RE = Er, Eu, Gd, Ho, La, Tb**) have been investigated using the first-principle calculations within density functional theory in chapter **7**. The spontaneous polarization, magnetic and electronic properties of a simultaneous substitution of **Gd** and **Mn** in **$BiFeO_3$** of **12.5 %**were investigated. In addition, a pseudo Jahn−Teller distortion was predicted for **$BiFeO_3$-$GdMnO_3$**.

Finally, we conclude this manuscript by summarizing the main results obtained during this research work.

Chapter 1

Ferroelectrics, Magnetismand magnetoelectric coupling

The goal of this chapter is to introduce the basics essential for understanding the manuscript. It will be divide into four sections. Firstly, we recall the main properties of a ferroelectric compound. Then, the magnetic properties and the different magnetic order that could be exist within multiferroic materials, were detailed. We report the magnetoelectric effect with a list of the main multiferroic compounds already studied and those currently under investigations. Finally, we recall the most applications of the magneto-electric effect.

1.1. Fundamentals of Ferroelectrics:

In this part, we recall the useful notions on dielectrics, piezoelectrics, ferroelectrics and the Landau theory of ferroelectric phase transitions.

1.1.1.Dielectrics

A dielectric material is a compound that does not have a free internal charge. Therefore, the dielectric compound is an insulator. When an electric field is applied to a dielectric material, positive charges are displaced in the direction of the electric field and negative charges are shifted in the opposite direction simultaneously, thus generating a polarization ***P***.

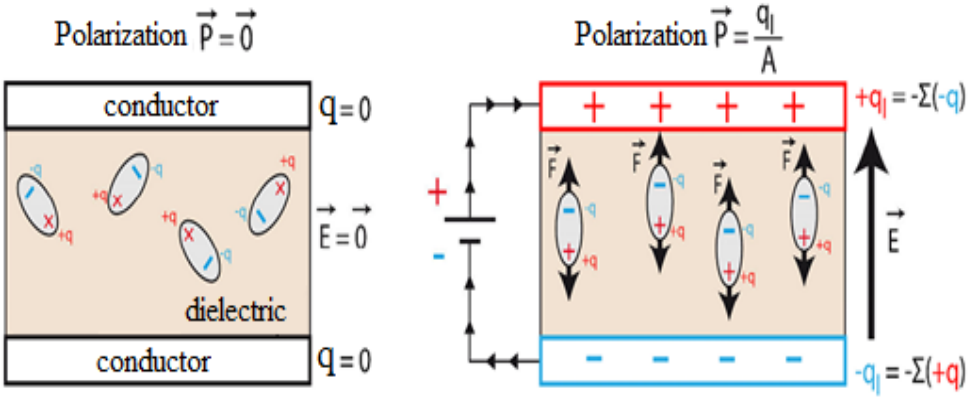

Figure.1.1: Schematic illustration of polarization of dielectric material.

In a dielectric material, the linear relation between the polarization ***P***and an applied electric field ***E*** is given by the expression:

$$\vec{\boldsymbol{P}} = \boldsymbol{\varepsilon_0 \chi_e \vec{E}} \tag{1.1}$$

where $\boldsymbol{\chi_e}$ is the electrical susceptibility of the dielectric material and $\boldsymbol{\varepsilon_0} = 8.854 \times 10^{-12}\ F/m$is the permittivity of the vacuum.

The permittivity or dielectric constant is also used to define the reaction of the material under an applied electric field $\boldsymbol{E}$. This permeability connects the induction $\boldsymbol{D}$ and **E**:

$$\vec{D} = \varepsilon_0 \vec{E} + \vec{P} = \varepsilon_0 \vec{E} + \varepsilon_0 \chi_e \vec{E} = \varepsilon_0 (1 + \chi_e) \vec{E} = \varepsilon_0 \varepsilon_r \vec{E} = \varepsilon \vec{E} \quad (1.2)$$

where ε_r is the relative dielectric constant and The permittivity εequals to $\varepsilon_0 \varepsilon_r$.

There are several mechanisms for the origin of the polarization phenomenon. These mechanisms divide into two categories: induced polarization and spontaneous polarization.

1.1.2. Piezoelectricity

a) Definition of piezoelectricity

Piezoelectricity is defined as a linear interaction between mechanical and electrical properties. Piezoelectricity is a property of certain materials (crystals, ceramics, polymers or composites) to be able to transform mechanical energy into electrical energy, or an electrical polarization induced by mechanical deformation. This polarization depends on the mechanical deformation. This effect is called the "direct piezoelectric effect". The inverse effect of piezoelectricity is: a mechanical deformation induced by an electric field. The **Figure.1.2** shows a schematic representation of these effects of piezoelectricity.

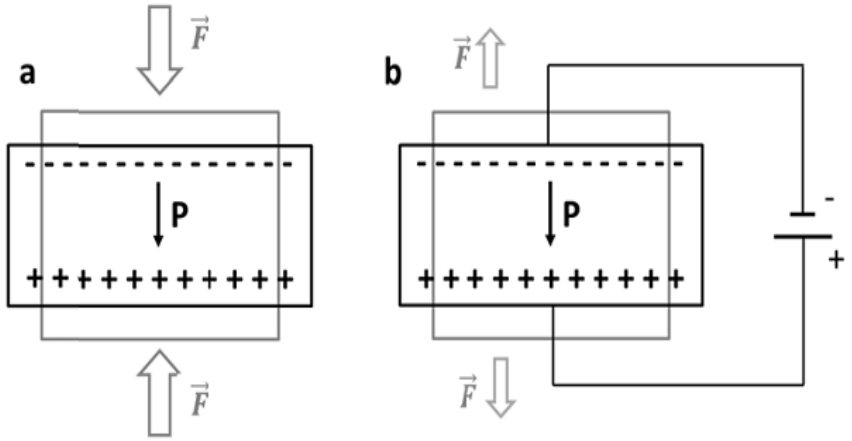

Figure.1.2: piezoelectric effect: **(a)** direct and **(b)** inverse

b) Classification of piezoelectric materials:

The structure of a piezoelectric material has not a center of symmetry (non-centrosymmetric). The existence of an electric polarization is therefore possible only for certain properties of symmetry of the crystalline structure of the material. Among the 32 crystallographic point groups, 20 are piezoelectric, 10 are polar without an external applied electric field. In these piezoelectric classes, they possess a spontaneous electric polarization. Their spontaneous polarization varies with temperature, so these crystals are pyroelectric. Finally, among the pyroelectric crystals, only some are ferroelectric. The organization of these classes is shown in **Figure.1.3.**

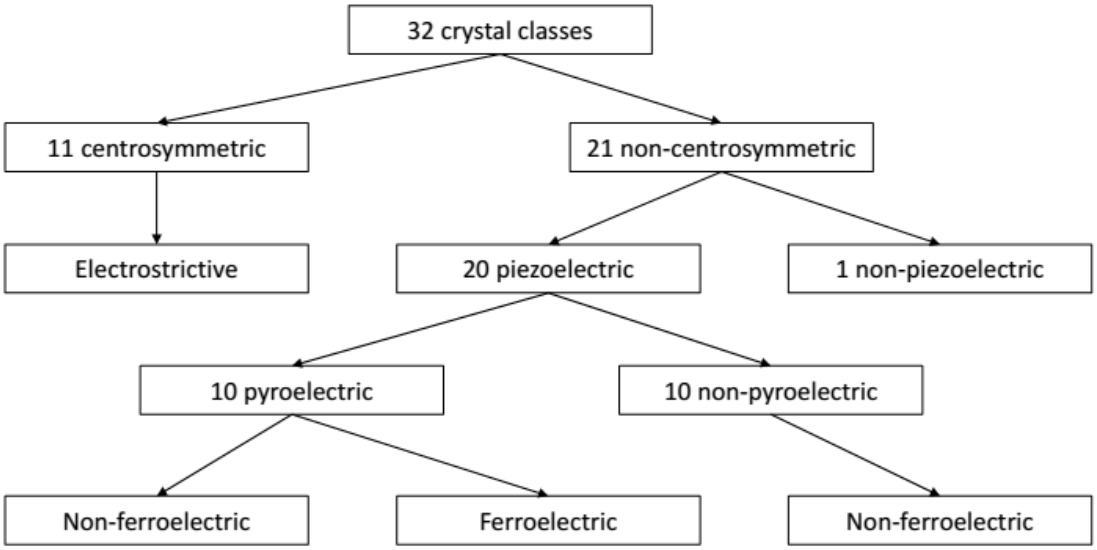

Figure.1.3 : Classification of piezoelectric and subgroups based on symmetry[24]

1.1.3. Ferroelectric Materials

a) Definition

Ferroelectricity forms a subgroup of pyroelectricity. A ferroelectric material is characterized by a structural transition temperature (T_c) between a high temperature phase exhibiting paraelectric (non-polar) behavior and a low temperature phase exhibiting spontaneous polarization due to spontaneous distortion of the crystal mesh(**Figure.1.4**)[25], [26].

This polarization can be reoriented or reversed (switching) according to equivalent crystallographic directions under the effect of the external electric field, resulting in a hysteretic behavior similar to that observed in ferromagnetic materials under the effect of a magnetic field. The hysteresis cycle $P = f(E)$ is thus considered as the signature of ferroelectricity.

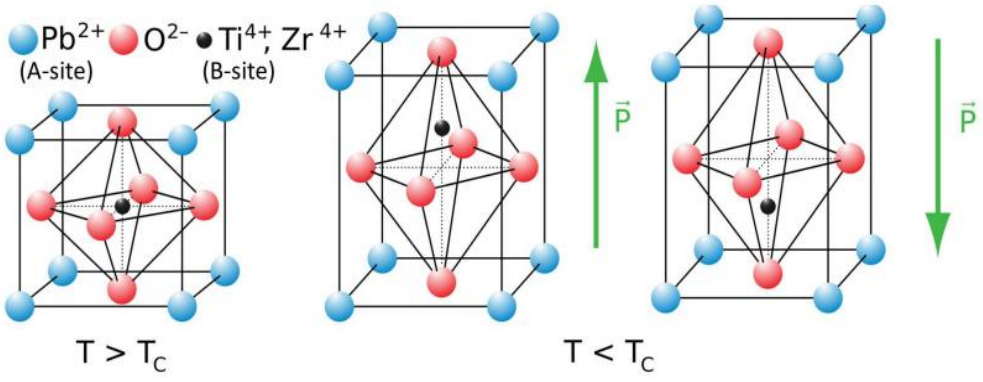

Figure.1.4 : Schematization of spontaneous polarization in PZT.

b) Ferroelectric domains

By analogy with ferromagnetic domains, a ferroelectric crystal is formed by homogeneous regions called "domains" which are separated by domain walls. Each domain has a direction of polarization vector that is different from that of its neighbor. The total

polarization in the crystal represents the geometric sum of the polarization vectors of different domains.

When a ferroelectric material is synthesized, it does not possess initially no remanent polarization. Indeed, all dipole moments are randomly oriented in all crystallographic directions, resulting in a zero moment. On the other hand, if an electric field is applied, a process of redirection of the polarization directions is initiated. This allows the material to keep part of its aligned moments, even in the absence of a field. As shown in **Figure.1.5**, the ferroelectric materials characterized by a hysteresis loop. By analogy with magnetic materials, $\boldsymbol{P_S}$ presents the saturation polarization when all dipole moments are aligned; $\boldsymbol{P_r}$ is the remanent polarization corresponding to the polarization when the applied electric field is zero; and $\boldsymbol{E_c}$ is the coercive field corresponds to the applied field for removing the polarization in the material.

The main characteristics of this cycle are:

- at zero electric field, the macroscopic polarization is zero
- when the applied field is low, there is a displacement of the domain walls because the volume of domains oriented along the easy axis increases, at the expense of domains that are unfavorably oriented.
- when the applied field is strong, the polarization of the domains turns in the direction of the field until saturation polarization is reached.
- when the applied field is cancelled, the loop intersects the ordinate axis in a point Pr corresponding to the remanent polarization.
- when the applied negative field is high enough, the loop intersects the x-axis at a point $\mathbf{E_c}$, corresponding to the coercive field.

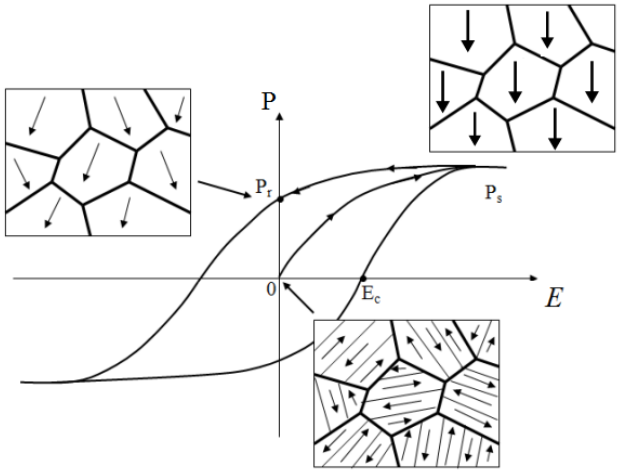

Figure.1.5: Schematic illustration of a typical ferroelectric hysteresis loop

1.1.4. Different types of polarization:

There are different types of polarization depending on the nature of the atoms and their arrangement in the crystal structure:

- **Electronic polarization:** All materials have this characteristic. It results from an oscillation of the charges relative to the nucleus under the influence of an electric field. These oscillations occur at very high frequencies from 10^{14} to 10^{16} Hz.

- **Ionic Polarization:** Only materials with ionic bonds can exhibit this characteristic, which is due to the movement of the cation in one direction and the anion in another, which results the formation of dipoles. The frequencies where this polarization occurs are of the order of 10^{12} to 10^{13} Hz.

- **Dipolar polarization:** Only compounds with spontaneous polarization have this type of polarization. It is described as the rotation of dipoles when an electric field is applied. It is observed in the radio wave range (10^{3} to 10^{11} Hz).

- **Polarization at interfaces:** It is due to the accumulation of charges at the interfaces of systems and is found at low frequencies (< 10^{2} Hz).

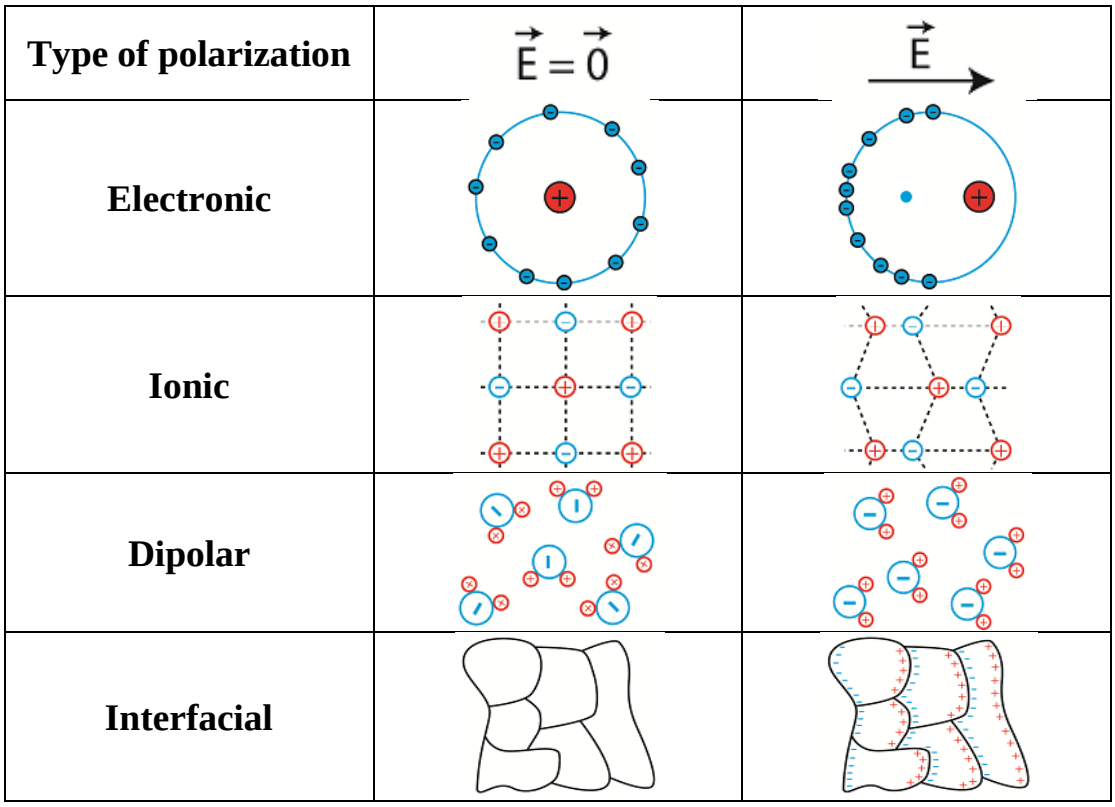

Figure.1.6 : mechanism of different types of polarization.

1.1.5. Phase transitions

a)Landau-Ginzburg-Devonshire Theory

Landau's thermodynamic theory is used to describe the equilibrium of a system that has a phase transition[27]. In Landau's hypothesis, free energy is an analytical function of the order parameter deduced from the symmetry properties of the high temperature phase. For a ferroelectric compound, the order parameter is the polarization $\boldsymbol{P}$. In the case where the paraelectric phase has a centre of symmetry (as is often the case in so-called displacive transition ferroelectrics) this series does not contain any odd terms. The development of free energy in this hypothesis is as follows:

$$\boldsymbol{F(P;\, T, E)} = -\boldsymbol{EP} + \boldsymbol{g_0} + \frac{1}{2}\boldsymbol{g_2 P^2} + \frac{1}{4}\boldsymbol{g_4 P^4} + \frac{1}{6}\boldsymbol{g^6 P^6} + \cdots \qquad (1.3)$$

where the coefficients $\boldsymbol{g_n}$ are temperature dependent, $\boldsymbol{T}$ is temperature in $\boldsymbol{K}$ and $\boldsymbol{E}$ is external electric field. Odd powers are not included due to the symmetry reason.

The calculation of the electrical polarization $\boldsymbol{P}$ in thermal equilibrium condition is given by the minimum of $\boldsymbol{F}$. At an applied electric field $\boldsymbol{E}$, the equilibrium polarization satisfies the condition :

$$\frac{\partial F}{\partial P} = -E + g_2 P + g_4 P^3 + g_6 P^5 + \cdots \quad (1.4)$$

The coefficient $\boldsymbol{g_2}$ depends on the temperature as follows:

$$g_2 = \gamma(T - T_0) \quad (1.5)$$

where $\boldsymbol{\gamma}$ is a positive constant, which equals to $\boldsymbol{1/\varepsilon_0 C_{CW}}$. $\boldsymbol{\varepsilon_0}$is permittivity of free space ($\boldsymbol{8.85419 \times 10^{-12}\ F/m}$) and$\boldsymbol{C_{CW}}$is Curie-Weiss constant.

Spontaneous polarization $\boldsymbol{P_0}$ is obtained by minimizing the free energy $\boldsymbol{F}$, such as $\frac{\partial F}{\partial P} = 0$, while the susceptibility $\boldsymbol{\chi}$is calculated from the relations :$\frac{1}{\chi} = \frac{\partial E}{\partial P} = \frac{\partial^2 F}{\partial^2 P}$

Being γ positive, we neglect the 5th order term in the expression (2.5) and we obtain the following results:

$$P_0 = \pm\sqrt{\frac{\gamma}{g_4}(T_0 - T)} \quad (1.6)$$

$$\chi = \begin{cases} [\gamma(T - T_0)]^{-1}, & if \quad T > T_0 \\ -2\gamma\,[(T - T_0)]^{-1}, & if \quad T < T_0 \end{cases} \quad (1.7)$$

- $g_4 > 0$ and $g_6 \approx 0$, corresponding to a second-order phase transition. Polarization varies continuously around the transition temperature (**figure.1.7.)**
- $g_4 < 0$ and $g_6 > 0$, resulting in a first-order phase transition. The polarization varies discontinuously in this case (**figure.1.7.**).

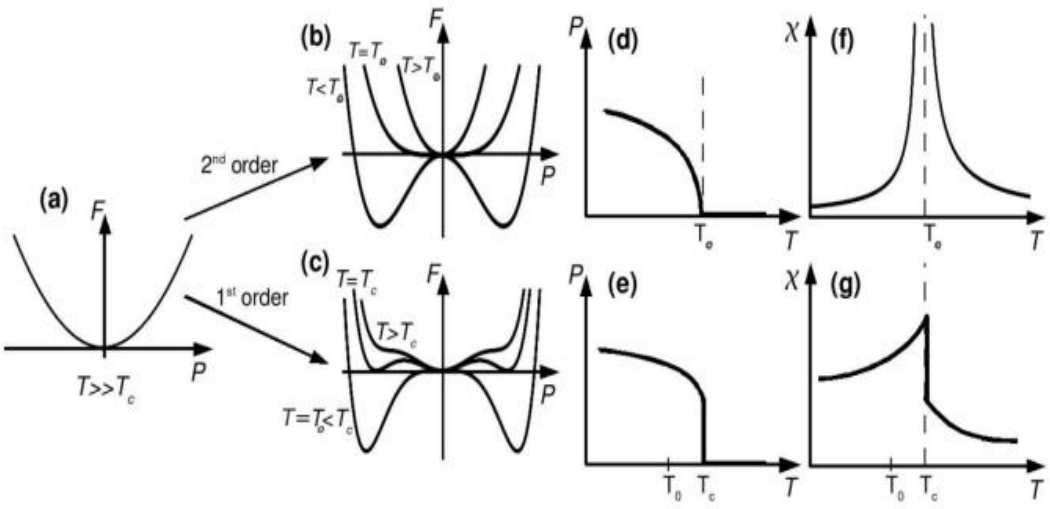

Figure.1.7: Free energy as a function of polarization for; the paraelectric phase (a), ferroelectric material in a second-order phase transition (b) and ferroelectric material in a first-order phase transition(c) at$\boldsymbol{T > T_0}$,$\boldsymbol{T = T_0}$and $\boldsymbol{T < T_0}$. (d) and (f) are respectively the spontaneous polarization **P** and the dielectric susceptibility **χ** as a function of temperature for a second-order phase transition. (e) and (g) are respectively the spontaneous polarization P and the susceptibility **χ** as a function of temperature for a first-order phase transition. Adapted from Refs [28], [29].

b)Structural aspects of phase transitions

Two types of ferroelectric transitions should be identified:

- **order-disorder transition:** dipole moments exist in the ferroelectric phase as well as in the paraelectric phase, but macroscopic polarization in the paraelectric phase is zero because the dipole moments are randomly oriented. The transition to an ordered phase reveals a non-zero polarization in the crystal. This transition is often of the second order, i.e. the polarization decreases continuously to zero at the temperature of transition. This type of transition is found in hydrogen-bonded compounds such as Rochelle salts NaKC4H4O6, 4H2O [30] (see **Figure 1.8**).

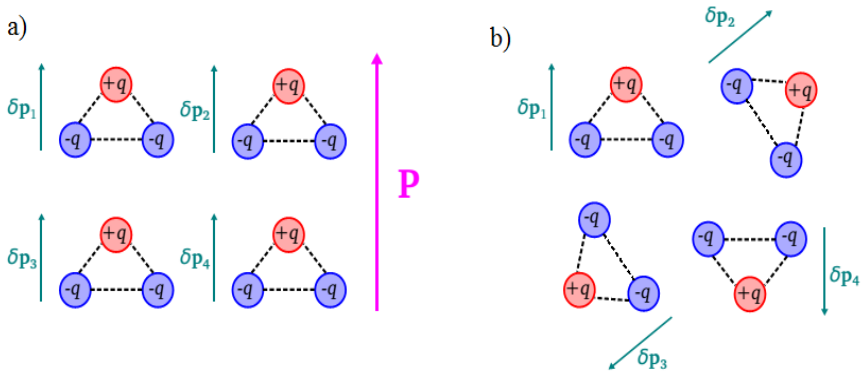

Figure 1.8: Alignment of dipoles in an order-disorder transition: (a) Ferroelectric phase (T < Tc) and (b) Paraelectric phase (T > Tc).

- **displacive transition:** dipole moments are not exist in the paraelectric phase (of high symmetry), but in the ferroelectric phase with lower symmetry, the dipole moments appear following the displacement of atoms in the cell. The first compound, in which this type of transition was discovered, is **$BaTiO_3$** oxide with a perovskite structure (see **Figure.1.9**).

  This type of transition exists in other perovskites and other structures such as pyrochlores. Such transition is often of the first order, it is manifested by a divergence of the dielectric constant and an abrupt decrease in the polarization as the transition approaches.

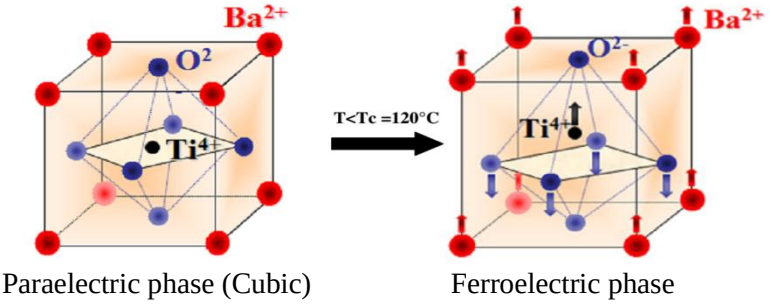

Figure.1.9: Displacif-type phase transition in the perovskite structure of **$BaTiO_3$**. The relative displacement of the T_i^{4+} and O^{2-} ions in opposite directions is at the origin of the appearance of spontaneous polarization.

1.2. Magnetic properties:

For atoms with an asymmetry in their electron shell such as an incomplete shell are effective to produce a magnetic moment, which is the case for some transition metal ions. Exchange interactions between neighboring elementary moments give rise to a molecular field called the Weiss field, which can reach up to $\mathbf{10^3}$ tesla. The magnetic order is therefore the result of competition between two energies: exchange energy and thermal agitation energy. The critical temperature below which the magnetic order is established is called Curie temperature ($\boldsymbol{T_C}$) in the ferromagnetic case and Néel temperature ($\boldsymbol{T_N}$) in the antiferromagnetic case. Above $\boldsymbol{T_C}$ (or $\boldsymbol{T_N}$), the disordered phase appears, called the paramagnetic phase.

1.2.1. Paramagnetic phase:

In magnetostatics, Magnetic moments are considered to be magnetic dipoles with fictitious magnetic charges (comparable to electrical charges) and currents from these charges. Thus, according to local Maxwell's equations, a relationship can be defined between the applied magnetic field $\boldsymbol{H}$, magnetization $\boldsymbol{M}$ and induction magnetic $\boldsymbol{B}$:

$$\boldsymbol{B} = \mu_0 (\boldsymbol{H} + \boldsymbol{M}) \tag{1.8}$$

Where μ_0 is the permittivity of the vacuum.

In reality, in the total magnetic field $\boldsymbol{H}$, a distinction must be made between the applied field $\boldsymbol{H_0}$ and the demagnetizing field $\boldsymbol{H_d}$:

$$\boldsymbol{H} = \boldsymbol{H_0} + \boldsymbol{H_d} \text{ where } \boldsymbol{H_d} = -\hat{N}\,\boldsymbol{M} \tag{1.9}$$

where $\hat{N}$ is the tensor of the demagnetizing field which depends on the shape of the sample.
Above the transition temperature and for weak fields, the magnetization (or total magnetic moment per unit volume) in the phase obeys Langevin's law, which is linear under the application of a weak magnetic field:

$$\boldsymbol{M} = \chi_M \boldsymbol{H} \tag{1.10}$$

where χ_M is paramagnetic susceptibility. In fact, susceptibility is divided into two contributions: a negative diamagnetic susceptibility present in all compounds (low and always of the same order of magnitude) and a positive paramagnetic susceptibility (higher)present only in certain compounds.

Magnetic permeability μ is also used to define the reaction of the material to an applied magnetic field. This permeability connects the induction $\boldsymbol{B}$ to the excitation $\boldsymbol{H}$:

$$\boldsymbol{B} = \mu_0 (\mathbf{1} + \chi_M) \boldsymbol{H} = \mu_0 \mu_r \boldsymbol{H} \tag{1.11}$$

$$\boldsymbol{B} = \mu \boldsymbol{H} \tag{1.12}$$

As the permeability increases, As the capacity of the material to concentrate the magnetic flux rises.

In the paramagnetic, low-field phase, it is the thermal agitation energy that outweighs the energy exchange. We can therefore observe a starting alignment of the moments under field effect and a population of Boltzmann-type energy levels under the effect of the temperature.

In this hypothesis, the paramagnetic susceptibility obeys a Curie law:

$$\chi_p = \frac{C}{T} \tag{1.13}$$

where C is the Curie constant.

In the presence of exchange interaction, the paramagnetic susceptibility is modified, becoming Curie-Weiss's law:

$$\chi_p = \frac{C}{(T - \theta_p)} \tag{1.14}$$

where θ_p is the paramagnetic Curie temperature.

In a simple model of exchange with the first neighboring ions, θ_p is equal to $+T_C$in the case of a ferromagnetic interaction and to $-T_N$ in the case of a antiferromagnetic. Note that at high field strength($> 1T$), we can account for the variation in magnetization according to the applied field, using an expression of magnetisation involving the Brillouin function (in H/kT).

1.2.2. Exchange Interaction and Anisotropy

In a magnetically ordered compound, the exchange interaction between neighboring ions that tends to align the magnetic moments between them. As a first approximation and in the case of an isotropic interaction, the exchange interaction between two spins S_i andS_j, of quantum origin, can be described by the Hamiltonian of Heisenberg:

$$H = -2J_{ij}S_iS_j \tag{I.15}$$

Where J_{ij} is the exchange coupling between the S_i and S_j spins. If J_{ij} is positive, the interaction will be ferromagnetic, if J_{ij} is negative, the interaction will be antiferromagnetic.

However, more often the interaction will be anisotropic. There are two types anisotropy: **crystalline anisotropy** linked to a deformation of the symmetry of the lattice crystalline and **magnetic anisotropy** linked to different exchange couplings according to the directions in space. The two main origins of magnetic anisotropy are the dipole (spin) coupling and spin-orbit coupling. It is therefore the contribution of these two anisotropies, which leads to a preferential orientation of the magnetic moments; it is why, it is called magnetocrystalline anisotropy. The direction of anisotropy in which the magnetization will saturate quickly is called "easy axis".

1.2.3. Ferromagnetism

In a ferromagnetic compound, the exchange integral is positive (θ_p is positive), which leads to a parallel coupling of the magnetic moments (**Figure.1.10**). This results in an alignment of the magnetic moments at the microscopic scale and the appearance of microscopic spontaneous magnetization without an applied magnetic field.

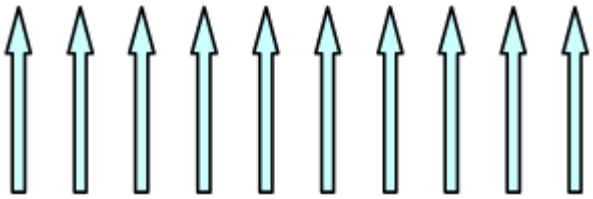

Figure.1.10: Parallel coupling of magnetic moments in a ferromagnetic domain. There is spontaneous microscopic magnetization without an applied magnetic field.

However, on a macroscopic scale, the application of a magnetic field is necessary to saturate completely the sample. This is due to the presence of ferromagnetic domains, in which the locally saturated magnetization is not directed in the same direction as the way for all areas. **Landau** and **Lifshitz** [31] have shown that this domain structure is the most favorable energy configuration when exchange energy is in competition with magnetocrystalline anisotropy energy.

A Bloch wall is the transition layer separating two magnetic domains in which the transition from one direction of magnetization to the other occurs gradually. This domain structure is also observed in the compounds antiferromagnetic, ferrimagnetic and ferroelectric.

The representation of the magnetization of a ferromagnetic material as a function of the applied magnetic field produces a hysteresis cycle (**Figure.1.11**).

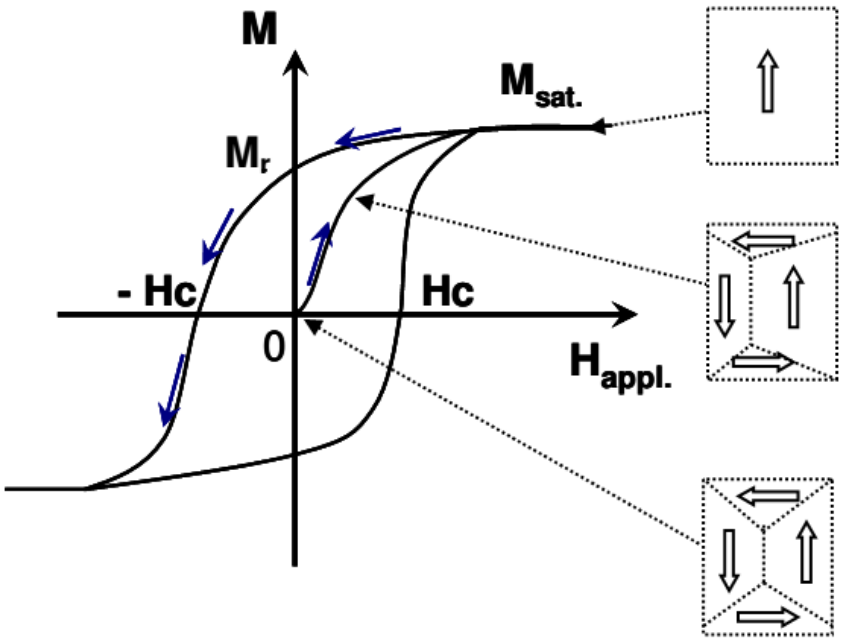

Figure.1.11: Ferromagnetic hysteresis cycle showing the evolution of magnetization as a function of the applied magnetic field.

1.2.4. Antiferromagnetism:

In an antiferromagnetic compound, the exchange integral is negative ($\boldsymbol{\theta_p}$ is negative), leading to an antiparallel coupling of the magnetic moments of two sublattices (**Figure1.12**). The alternating direction of the sublattice moments results in a zero resulting moment and there is no spontaneous magnetization in the absence of an applied field.

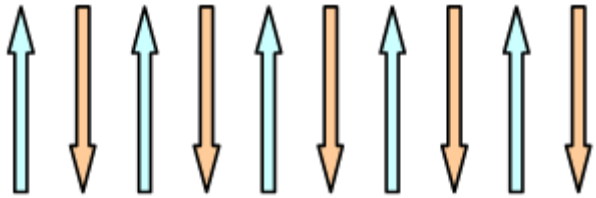

Figure1.12: Anti-parallel coupling of the magnetic moments of two sub-arrays in an antiferromagnetic domain. Microscopic magnetization is zero without an applied magnetic field.

1.2.5. Superexchange mechanism

It is the super-exchange mechanism [32], [33] that is responsible for the antiferromagnetism in oxides. To promote this mechanism, it is necessary to optimize the overlap between the orbitals $\mathbf{e_g}$ $\mathbf{(t_{2g})}$ of the metal ion $\boldsymbol{M}$ of electronic configuration $\boldsymbol{d^n}$ in an octahedral environment and the orbitals **2p** of large spatial extension of oxygen (**Figure1.13**). For maximum overlap, two parameters must therefore be considered:
- short **M-O** distance.
- **M-O-M** angle close to $\mathbf{180}$°.

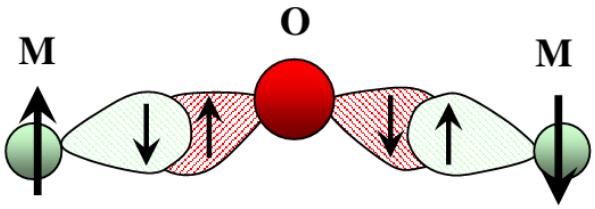

Figure.1.13: Overlap of the orbitals $\mathbf{e_g}$ of the metal ion **M** with the orbitals **2p** of the oxygen at the origin of the superexchange.

These two types of overlapping allow the transfer of electrons between the **2p** oxygen orbitals and the metallic d orbitals, leading to an antiferromagnetic coupling: this is the Goodenough superexchange.

1.2.6. Paramagnetic and antiferromagnetic susceptibilities

By plotting the inverse of the paramagnetic susceptibility as a function of temperature for an antiferromagnetic compound (**Figure.1.14**), two characteristic temperatures appear: (i) the Neel temperature $\boldsymbol{T_N}$ that separates the disordered phase from the ordered phase; (ii) the paramagnetic Curie temperature $\boldsymbol{\theta p}$. The main characteristics of this curve are:
- when $\boldsymbol{T}$ increases from $\mathbf{0}\ \boldsymbol{K}$, we progressively decouple the moments of the two sublattices in antiferromagnetic interaction, resulting in the appearance of increasing magnetization ($\boldsymbol{\chi^{-1}}$ is decreasing)
- when $\boldsymbol{T = T_N}$the decoupling of the spins is complete, we move into the paramagnetic phase.
- when $\boldsymbol{T}$ increases above$\boldsymbol{T_N}$, susceptibility follows a Curie-Weiss law.

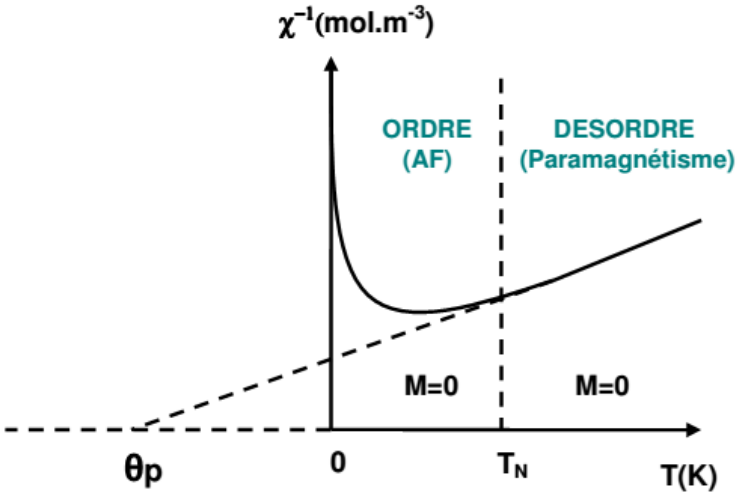

Figure.1.14: Inverse of paramagnetic susceptibility as a function of temperature in an antiferromagnetic compound.

Below T_N, in the antiferromagnetic phase, the magnetization curve as a function of the magnetic field follows a linear variation:

$$M = \chi_{AF} H \quad (1.16)$$

where χ_{AF} is called antiferromagnetic susceptibility. The response of the material under the action of the applied magnetic field leads to a slight folding of the two sublattices in antiparallel interaction and to the appearance of a weak ferromagnetic moment. At zero field strength, the ferromagnetic resultant is zero. When the field is applied, the folding enhanced. the applied magnetic field increases as the ferromagnetic moment is greater.

1.2.7. Magnetic structures in perovskites

In the case of perovskite structures, it is possible to classify magnetic structures into four classes according to the stacking of planes, in which the magnetic moments are parallel (**Figure.1.15**).

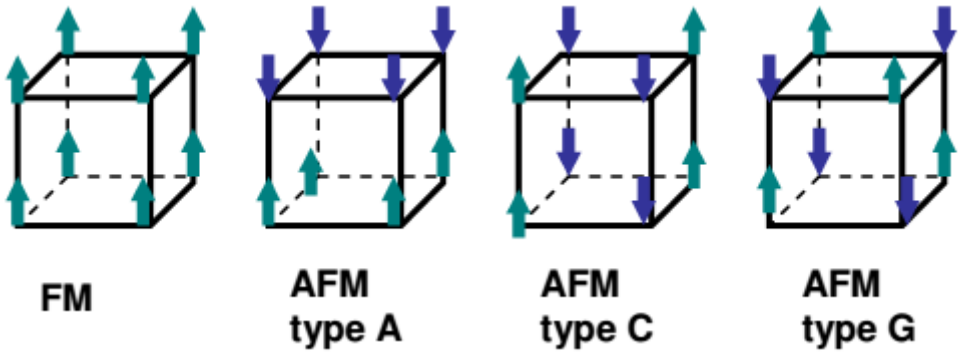

Figure.1.15: The different types of magnetic structures in perovskites.

1.2.8. Ferrimagnetism

A ferrimagnetic compound has two magnetic sub-lattices of different nature in antiferromagnetic interaction with each other leading to the occurrence of an uncompensated moment (**Figure1.16**).

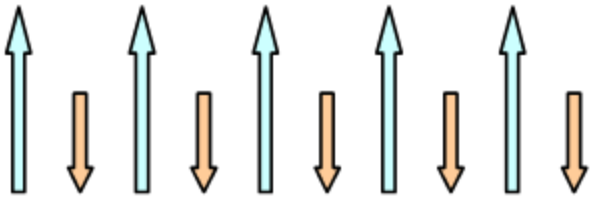

Figure.1.16: Anti-parallel coupling of the magnetic moments of two sublattices of different nature in a ferrimagnetic domain leading to the appearance of spontaneous magnetization.

For example, in cubic ferrites (which gave the name ferrimagnetism), it exists a sublattice of $\boldsymbol{Fe^{3+}}$ in antiparallel interaction with a sublattice of $\boldsymbol{Fe^{2+}}$. The ferrimagnetic compounds are mostly $\boldsymbol{ABO_4}$ spinel structures with sublattice $\boldsymbol{A}$ (the tetrahedral sites) interacting with a sublattice $\boldsymbol{B}$ (the octahedral sites). In such systems, the three exchange integrals $\boldsymbol{J_{AA}, J_{BB},}$ and $\boldsymbol{J_{AB}}$ are negative, thus, favour antiparallel interaction in all three cases, but the $\boldsymbol{J_{AB}}$ interaction being the The strongest is a parallel alignment of moments in sites $\boldsymbol{A}$ and $\boldsymbol{B}$ and an anti-parallel alignment of the two sites with each other. The behavior of a ferrimagnetic as a function of the applied magnetic field is similar to that of an antiferromagnetic compound with a weaker ferromagnetic component. However, the magnetization and coercivity field values in a ferrimagnetic are much higher.

1.3. Magnetoelectric effect

1.3.1. Multiferroics:

Multiferroic materials, which are materials with multiple order parameters (either ferroelectric, (anti-)ferromagnetic or ferro-elastic etc.) (**Figure1.17**) have attracted the interest of many researchers so far. The coexistence of ferroelectricity and ferromagnetism in the same material, resulting in the appearance of the magnetoelectric effect, is one of the most desirable properties currently being researched. The extensive use of magnetic and ferroelectric materials in various and varied applications logically supposes the combination of ferromagnetism and ferroelectricity in the same material.

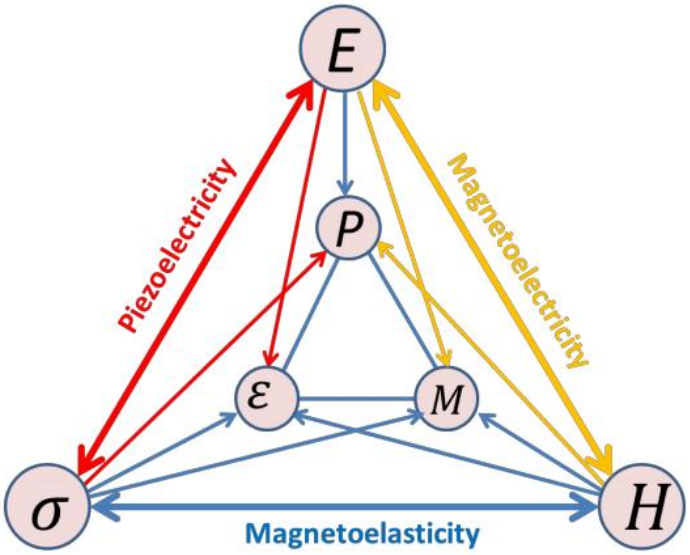

Figure1.17: Magnetoelectric effect described with the interaction between piezoelectric and ferromagnetic properties

1.3.2. brief history of Magnetoelectricity

since 1894, the magnetoelectricity is discovered by Pierre Curie's researchers, which observed that it is possible for an asymmetrical molecule to polarize electrically under the influence of a magnetic field [34]. Less than a century later, in 1960, Dzyaloshinskii predicts the existence of magneto-electricity in the antiferromagnetic Cr_2O_3 based on the work of Landau and Lifshitz in the same year [31], [35]. Magnetoelectricity in this material was confirmed experimentally by Astrov which measured a magnetization induced by an alternating electric field [36]. moreover , Rado and Folen affect the effect inverse, i.e. an electric polarization induced by a magnetic field [37]. Ten years more later, Van Suchetelenele - a researcher at Philips - proposes the conception which allows to produce the ME effect by using an intermediate coupling between the ferroelectric and ferromagnetic phase [38].

1.3.3. Definition of the magnetoelectric effect

The magnetoelectric effect is characterized by the magnetoelectric coefficient. An applied magnetic field H on magnetoelectric compounds of thickness e produces an electric polarization inside the sample and therefore an electric potential $\mathbf{V_{ME}}$(see**Figure.1.18**). There are two type of magnetoelectric effect:

- **Direct effect**: modification of the electrical state induced by a magnetic field
- **Inverse effect**: modification of the magnetic state induced by an electric field.

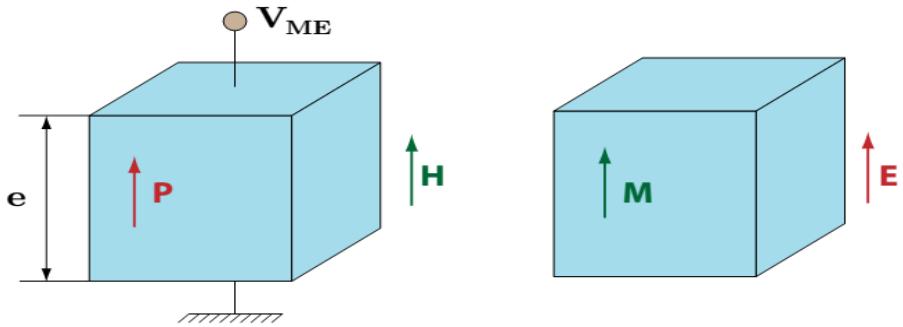

P: Electric polarization **E** : Electric field **M**: Magnetization **H** : magnetic field

Figure.1.18: Direct and inverse magnetoelectric effect

a) Intrinsic magnetoelectric effect

Figure.1.19 illustrates the intrinsic magnetoelectric effect. In a single-phase material, the intrinsic coupling between the electrical state and the magnetic state is defined as the magneto-electric effect.

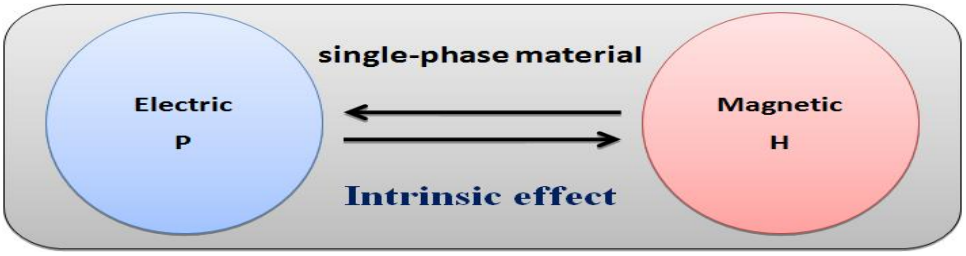

Figure.1.19:Intrinsic magnetoelectric effect.

b) Extrinsic magnetoelectric effect

Extrinsic magnetoelectric effect had appeared before the experimental discovery of the intrinsic effect[39], [40]. The combination of piezoelectric and magnetostrictive materials makes it possible to obtain a large extrinsic magnetoelectric coefficient than that of single-phase materials[41]. This magnetoelectric effect is illustrated in **Figure.1.20**: the application of a magnetic field generates a mechanical deformation on the magnetostrictive phases. This deformation is transmitted to the piezoelectric layers in which an electric polarization appears. The magneto-electric coefficient is therefore a property from the product of the coupling coefficients of piezoelectric and magnetostrictive materials[42]. In **Figure.1.20**, the constraints are noted T.

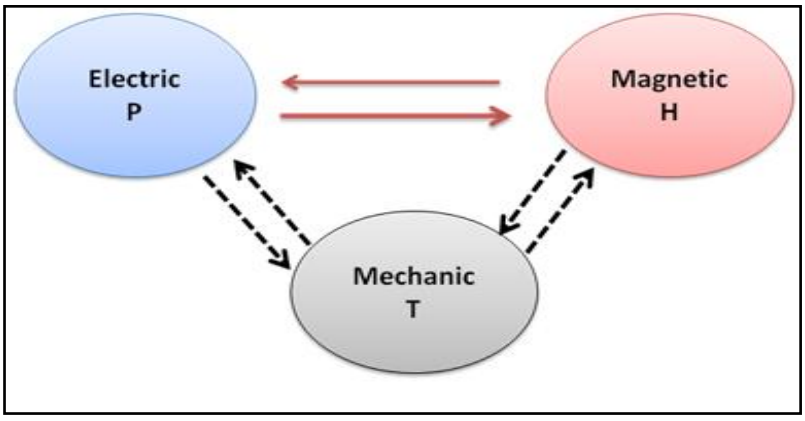

Figure.1.20: Extrinsic magnetoelectric effect

Van Suchetelen et al.[38] were the first to observe the extrinsic magnetoelectric effect in composite materials. The sample considered is a piezoelectric material containing magnetostrictive inclusions (**Figure.1.21**). Despite efforts to combine piezoelectric and magnetostrictive materials with high magnetoelectric coupling coefficient, the magnetoelectric coefficient remains low at ambient temperature (0.13 V.cm -1.Oe -1). **Figure.1.21** also shows another possible configuration in the form of multilayer.

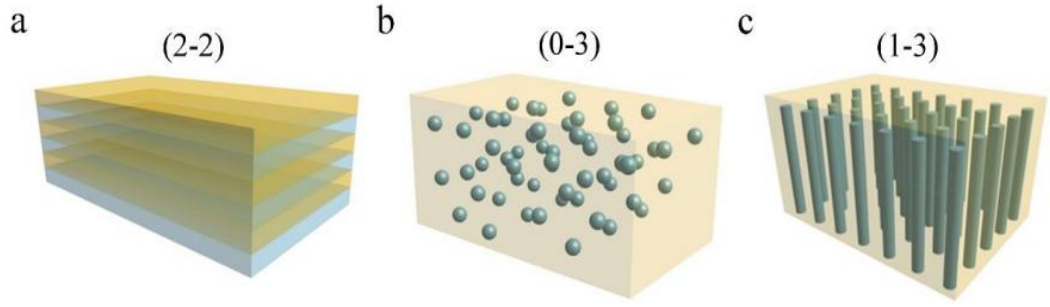

Figure.1.21: Schematic of the three types of multiferroic composites. (a) multilayers, which is (2-2) connectivity system, (b) particulate composites with (0-3) connectivity system, and (c) fibrous composite with 1-3 connectivity.

In order to improve the ME coefficient, different combinations of piezoelectric and magnetostrictive materials have been considered with different methods. The first multilayers

PZT/Terfenol-D allowed to reach a coefficient ME of 0.1 V/(cm.Oe) in static mode. The PZT/NiFe204 multilayers have an ME coefficient of up to 1.5 V/(cm.Oe)[19].The coefficient ME of multilayers depends on different parameters:

-The coupling coefficients of each constituent,
- The geometry of the layers and their number,
- The method of sticking.

1.3.4. Artificial Magnetoelectric Nanostructured Composites:

Since 1978, Newnham proposed different connectivity schemes for piezoelectric composites that account for the coupling between two phases[43]. In the case of magnetoelectric materials, the three interested connectivities are: 0-3, 2-2 and 1-3 types. These connectivities are shown in **Figure.1.22.**

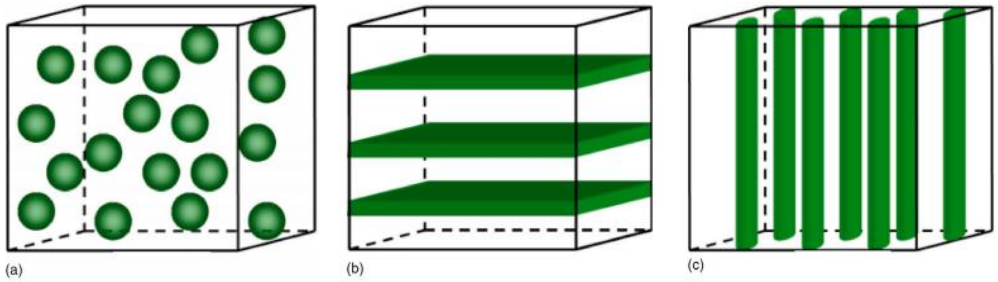

Figure.1.22: Schematic illustration of three bulk composites with the three common connectivity schemes: (a) 0–3 particulate composite, (b) 2–2 laminate composite, and (c) 1–3 vertically aligned composite.

a) Particulate composites (type 0-3)

Particulate composites are also referred, as a type 0-3. They consist on a connectivity used primarily with magnetic (electrical insulator) and piezoelectric (where green particles represent the magnetic phase in a white piezoelectric matrix). They require a homogeneous mixture with relatively insulating magnetic particles to properly polarize the piezoelectric material [44]. This therefore limits the magnetic phase to ferrites and excludes metal alloys. Particulate composites have exhibited a lower magnetoelectric effects than laminate composites [41]. This is notably due to the difficulty of obtaining a mixture of the two perfectly homogeneous phases.

The experimental results of magnetoelectric coupling coefficient in the particulate multiferroic system are presented in **Table.1.1**. It shows the magnetoelectric coefficient ranging from 16 to 3070 mV/(cm.Oe). Wan et al. analyzed the $CoFe_2O_4$ nanoparticles embedded in the $PbZr_{0.52}Ti_{0.48}O_3$ matrix as shown in **Figure.1.23**. The maximum saturation and remanent polarizations are 28 $\mu C/cm^2$ and 11.0 $\mu C/cm^2$, respectively, with a maximum value of magnetoelectric coefficient of 317 mV/(cm.Oe) was achieved [45].

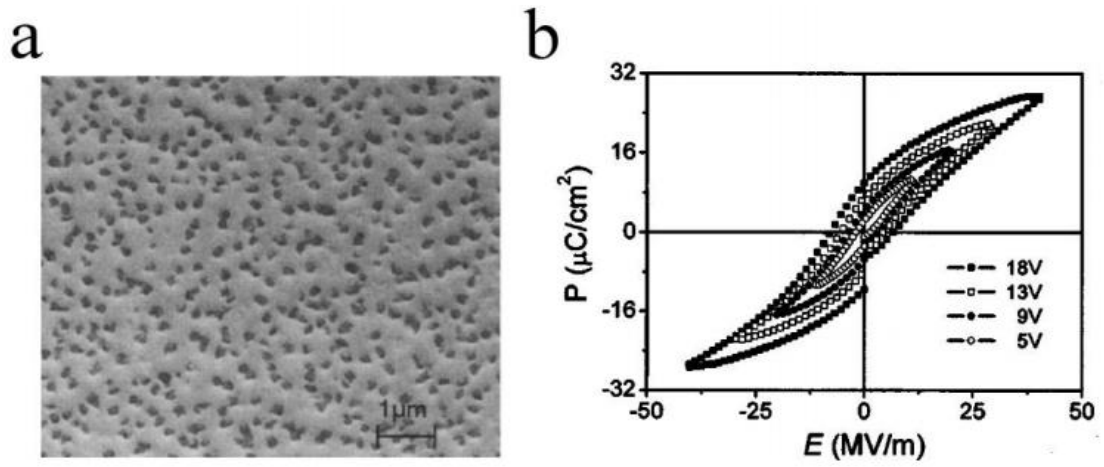

Figure.1.23 : (a) $CoFe_2O_4$-PZT thin film, and their P-E hysteresis loops (b)[45]

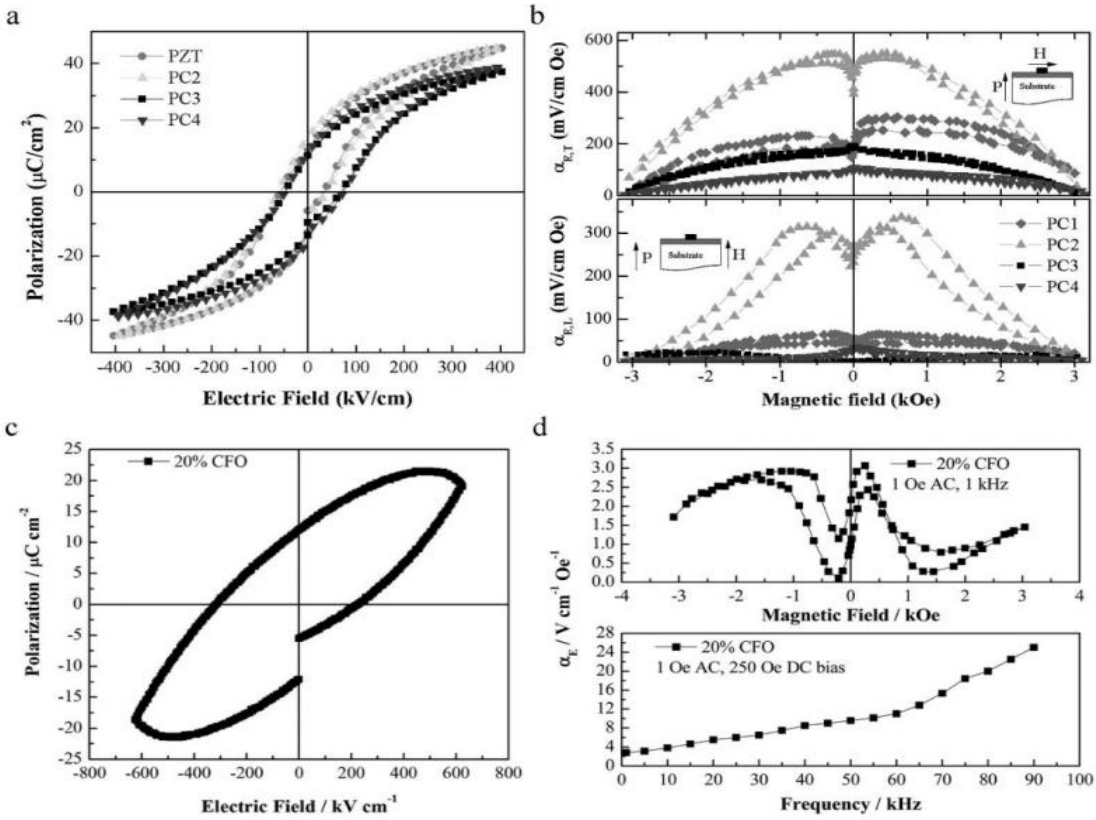

Figure.1.24: (a) P-E hysteresis loops of $CoFe_2O_4$-PZT and (b) The transverse (top) and longitudinal magnetoelectric coefficients in $CoFe_2O_4$-PZT [46]. P-E hysteresis behavior of PZT-CFO and (d) Transverse magnetoelectric coefficient[47].

Table.1.1:*magnetoelectric coefficients in some particulate composites (type 0-3).*

Component phases	H_{dc} (kOe)	F_{ac} (Hz)	α_{me} (mV/cm.Oe)	
$0.9PbZr_{0.52}Ti_{0.48}O_3$-$0.1NiFe_{1.9}Mn_{0.1}O_4$ (bulk)	0.1	1000	140	[48]
$PbZr_{0.52}Ti_{0.48}O_3$ (matrix)-$CoFe_2O_4$ (nanoparticles)	0.25	1000	3070	[47]
$PbZr_{0.52}Ti_{0.48}O_3$-$CoFe_2O_4$	0.45	1000	549	[46]

$BiFeO_3$–$CoFe_2O_4$	2.9	-	338	[33]
$0.69PbZr_{0.52}Ti_{0.48}O_3$-$0.31CoFe_2O_4$	2	1000	220	[45]
NCZF/0.8PZT-0.2PZN	2.6	1000	150	[49]
0.4 $CoFe_2O_4$ - 0.6 $BaTiO_3$	20	60 000	62	[50]
0.2 $CoFe_2O_4$ - 0.8 $BaTiO_3$	5	160 000	3.175	[51]
0.2 $CoFe_2O_4$ - 0.8 PZT	2	80 000	38	[52]
0.5 $CoFe_2O_4$ - 0.5 PMN-PT	16	100	18	[16]
0.5 $CoFe_2O_4$ - 0.5 $BaTiO_3$	-	-	225	[53]
0.4 $NiFe_{1.98}O_4$ - 0.6 $BaTiO_3$	10	100	315	[54]
0.2 $NiFe_2O_4$ - 0.8 PZT	10	1000	244	[55]
0.4 $Ni_{0.8}Zn_{0.2}Fe_2O_4$ - 0.6 PZT	1	300 000	16250	[56]
$0.5Ni_{0.83}Co_{0.15}Cu_{0.02}Fe_{1.9}O_{4-\delta}$– 0.5 $Na_{0.5}Bi_{0.5}TiO_3$	10	-	829	[57]
$CoFe_2O_4$–$BiFeO_3$	1	50 000	285	[58]
Terfenol-D/-PVDF	-	-	1430	[59]
$CoFe_2O_4$- $BaTiO_3$	1.5	-	200	[60]
$CuFe_2O_4$- $BaTiO_3$	-	-	425	[61], [62]

b) Vertically Aligned (1-3) type nanocomposites:

(1-3)-type nanocomposites is a connectivity used especially in nanocomposite fibers, where a fiber-like phase is surrounded by the second phase of matrix. Multiferroic nanocomposites with (1-3) type structure have attracted much interest due to the large vertical interfacial area between ferromagnetic and ferroelectric constituents, reduced substrate imposed clamping effect [41], [63].The magnetoelectric coupling in vertically aligned (1-3) type nanocomposites is strongly affected by the strain and the volume fraction of ferromagnetic pillars [64]. The magnetoelectric coefficient of (1-3) type $BaTiO_3$-$CoFe_2O_4$nanocomposite can be reached up to 2 V/(cm. Oe) by using the volume fraction of $CoFe_2O_4$ pillars ~60%.

Up to now, several thin film nanocomposites of (1-3) type are based on spinel and perovskite structures, such as $BaTiO_3$-$CoFe_2O_4$[65], $BiFeO_3$-$CoFe_2O_4$[66], PbTiO3-CoFe2O4[67], $Bi_5Ti_3FeO_{15}$-$CoFe_2O_4$[68], $PbMg_{1-x}Nb_xO_3$-$PbTiO_3$-$CoFe_2O_4$[69], $BiFeO_3$-$NiFe_2O_4$[70], and $BiFeO_3$-$Co_xNi_{1-x}Fe_2O_4$[71], have been shown a magnetoelectric effect. Recently, Amrillah et al. investigated the magnetoelectric coupling the (1 -3) type $BiFeO_3$-$CoFe_2O_4$ nanocomposite, the ferroelectric $BiFeO_3$ nanopillars embedded in the ferrimagnetic $CoFe_2O_4$ matrix [72]. In this work, a magnetoelectric coupling of 74 mV/(cm.Oe) was obtained, which is larger than the magnetoelectric coefficient reported earlier on flexible substrates. The recent results obtained on magnetoelectric coupling in the (1 -3) type nanocomposites are summarized in **Table.1.2.**

Wan et al. have successfully achieved to control phase connectivity in CoFe2O4–PZT (1-3) type using the PLD technique [73], **Figure.1.25** displays ferroelectric hysteresis loops and magnetization hysteresis loops (1-x)$PbZr_{0.52}Ti_{0.48}O_3$-x$CoFe_2O_4$composite thin films for x=0.25,0.5 and 0.75. It is established that all composite thin films with various x have clear

ferroelectric and ferromagnetic characteristics. The saturation magnetization and Hc coercivity of the composite films increase with increasing x. It is noted that the coercivity of a 1-3 type composite is Hc ~ 90 Oe. For x = 0.25, the composite thin film exhibits a very high initial α_E value of ~390 mV/ cm.Oe near H_{Bias} = 0 as shown in **figure.1.25c.**

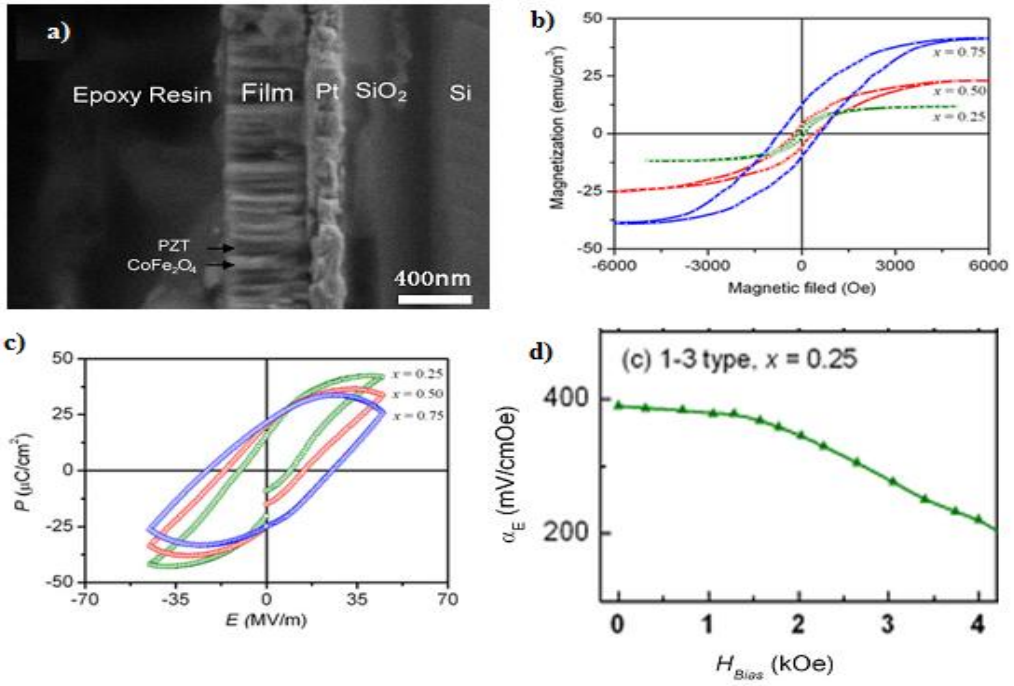

Figure.1.25: (a) SEM image of CoFe2O4–PZT (1-3) type, **(b)** M-H hysteresis loop, **(c)** Ferroelectric P-E hysteresis loop and **(d)** magnetoelectric effect in CoFe2O4–PZT (1-3).

Table.1.2:*magnetoelectric coefficients in vertically Aligned (1-3) type nanocomposites***.**

Component phases	H_{dc} (Oe)	f_{ac} (Hz)	α_{me} (mV/cm.Oe)	Ref
BiFeO3(pillars)- CoFe2O4 (matrix)	2000	-	11000	[72]
25%CoFe2O4:PZT/Pt/Ti/SiO_2/Si	0	10000	390	[73]
BiFeO3 (matrix)/ CoFe2O4 (pillars)	6000	1000	60	[74]
PZT- Terfenol-D/Epoxy	1500	100	500	[75]
BiFeO3 (pillars)- CoFe2O4 (matrix) on mica	-	-	74	[72]
35% CoFe2O4: BiFeO3/SrRuO3/SrTiO3(001)	100	-	20	[76]
35% CoFe2O4: BiFeO3/ SrRuO3/ SrTiO3 (001)	100	-	16	[77]

c) Laminate composites(2-2) Type :

Epitaxial grown of ferromagnetic and ferroelectric laminated composite thin films produced a magnetoelectric coupling at the interface ferromagnetic/ferroelectric. (2-2) type laminate magnetoelectric composites show a high magnetoelectric coupling.The leakage problem due to high concentration of the ferrite phase with low resistivity in the particulate

composite ceramics can be eliminated in the laminate 2–2 composite ceramics. Generally, laminate composite ceramics are fabricated, at high temperature, by cofiring ferrite and piezoelectric ceramic layers. ME behavior in laminate composites has been reported for various material couples. Some examples are gathered in **Table.1.3** [55], [78], [79]. Materials with a high piezoelectric and high piezomagnetic coefficient allow obtaining a large magnetoelectric effect. This is why the researchers have used magnetostrictive materials $NiFe_2O_4$, $CoFe_2O_4$ and Terfenol-D, while the piezoelectric phases used are PZT and PMN-PT. For example, Ryu et al. reported a magneto-electric coefficient of 7.38 V/A in Terfenol-D/PZT/Terfenol-D[80] and 12.88 V/A in trilayer Terfenol-D/PMN-PT/Terfenol-D , Moreover, Srinivasan et al.reported a coefficient Magnetoelectric of 1.88 V/A for a multilayer composed of nickel ferrite and PZT[19]. On the other hand, for Zn-substituted cobalt ferrite coupled with PZT, the reported magneto-electric coefficient is small (about 0.312 V/A) [81].

In addition, a transverse magnetoelectric coupling coeficient of 30 V/(cm. Oe) and 7 V/(cm. Oe) were achieved in $Pb(Mg,Nb)O_3$-$PbTiO_3$ laminated with Metglas (FeBSiC) [82]. Moreover, $Ir_{0.3}Mn_{0.7}$/FeCoSiB/AlN and FeCoSiB/AlN thin films showed a magnetoelectric coefficients value of 430 mV/(cm. Oe) and 3.1 mV/(cm. Oe), respectively, [83], [84]. It is worth mentioning that the mechanism behind the magnetoelectric coupling inmultiferroic thin films is the epitaxial strain. A tensile and compressive strain can be obtained by using substrate with specific lattice constant. The strain can be used to couple ferroelectric and ferromagnetic domains through strain-stress mediated interfacial magnetoelectric coupling[85], [86] .

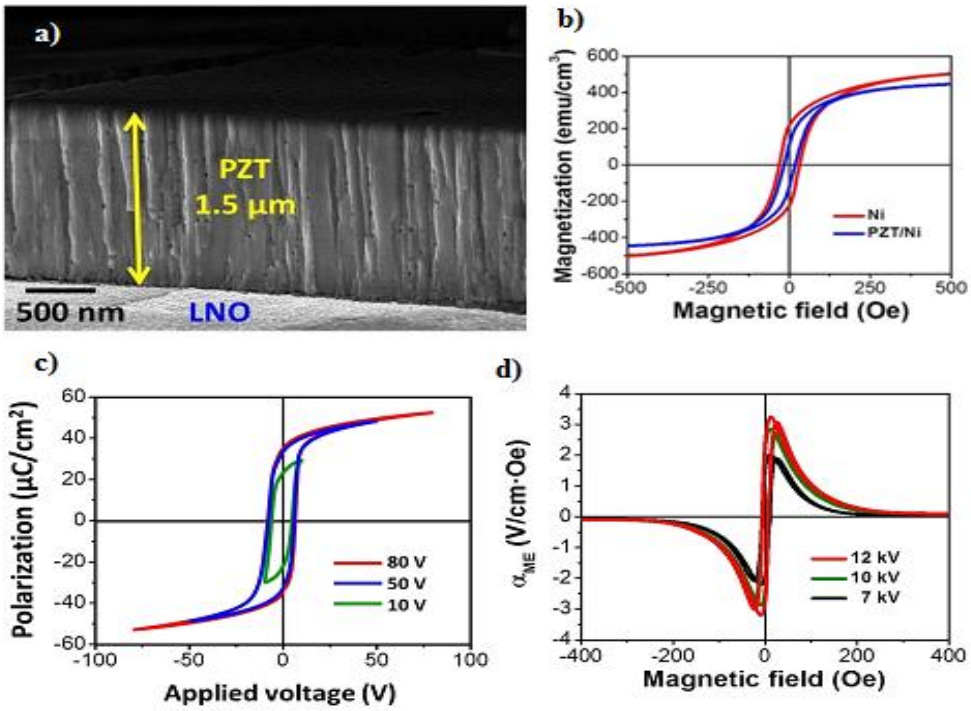

Figure.1.26 : **(a)** Cross-sectional images of the PZT film on LNO/HfO2/Ni, **(b)** ferroelectric hysteresis loops, **(c)** magnetization hysteresis loops and **(d)** magnetoelectric effect of the PZT/Ni[87].

As an example of bilayer anocomposite, PZT film on LNO/HfO2/Ni was investigated by Palneedi et al [87]. A magnetoelectric coefficient of the PZT/Ni nanocomposite of 3200 mV/(cm.Oe), under a dc magnetic field, has been carried out. **Figure.1.26(a,c)** shows the ferroelectric and ferromagnetic hysteresis loops of the PZT/Ni films. Therefore, this type of multiferroic nanocomposites is promising for several applications such as field sensors, actuators, transducers, filters, phase shifters, and gyrators.

Table.1.3*:magnetoelectric coefficients in some laminate composites with (2-2) Type.*

Component phases	H_{dc} (kOe)	f_{ac} (Hz)	α_{me} (mV/cm.Oe)	
Metglas/PMN-PT (fiber)/Metglas (bulk)	8	1000	52000	[88]
$(BaTiO_3–BiFeO_3)\times15$	0	1000	55000	[89]
$Pb(Zr,Ti)O_3$/Metglas	22	1000	7000	[90]
$Pb(Zr_{0.52}Ti_{0.48})O_3/LaNiO_3/HfO_2$/Ni	10	1000	3200	[87]
$Pb(Zr_{0.52}Ti_{0.48})O_3$/Pt/Ni	86	1000	772	[91]
$La_{0.7}Sr_{0.3}MnO_3$/PZT	35	100	60	[18]
PZT/$NiFe_2O_4$ (bilayer)	1	-	460	[56]
PZT/$NiFe_2O_4$ (multilayer)	1	-	1500	[56]
PZT-CFO	-	-	55	[56], [92]
PZT/$La_{0.7}Sr_{0.3}MnO_3$	-	100	160	[18]
PZT/$La_{0.7}Ca_{0.3}MnO_3$	-	100	60	[18]
PZT/ Terfenol-D discs	4	4000	4680	[80]
Terfenol-D/PZT	-	-	7380	[80]
$Co_{0.6}Zn_{0.4}Fe_2O_4$/PZT	-	100	280	[81]
$NiCoZnFe_2O_4$/PZT (disk)	037	-	550(mV/A)	[78]
$NiCoZnFe_2O_4$/PZT (tore)	0.37	-	2000(mV/A)	[78]
$NiCuZnFe_2O_4$/PZT	0.5	-	195(mV/A)	[55]
$MnZnFe_2O_4$/PZT (tore)	-	-	3250(mV/A)	[78]
Metglas/PVDF	0.38	20	21460	[93]
Galfenol/PZT	-	1-100	8750	[79]

1.3.5. The choice of materials:
a) BiFeO3

In single-phase multiferroic materials, the coexistence of the ferroelectric and ferromagnetic orders. BiFeO3 is one of the most studied multiferroic materials since 2003. It is one of the only magnetoelectric multiferroics compound at room temperature. BFO was synthesized for the first time in massive form in 1957 by Royen and Swars [94]. Currently BFO is synthesized in different forms: bulk, thin layers, nano-columns and nano-cubes, etc.

At room temperature, BFO has a rhombohedral crystal structure with R3c as space group [95], [96]. As illustrates in **Figure.1.27a,** the iron atom is located in the center of the octahedra and it is surrounded by 6 atoms of oxygen. The magnetic order of BFO is **G**-type [95] which means that the ferromagnetic planes are perpendicular to [111] and are arranged in an antiferromagnetic order along this axis. Its Neel temperature is around 640K. Ramesh et al.

asserted in 2003 that epitaxial stress increases ferroelectric properties and changes the magnetic order from antiferromagnetic to weakly ferromagnetic [97].

BFO is the only monolithic material that exhibits magnetoelectric coupling at room temperature. This bismuth ferrite belongs to the perovskite family and has a very high electrical polarization of 90µC.cm^{-2}. (particularly strong polarization in thin films [97]). Nowadays, the BFO is considered as a promising multiferroic compound for spintronic application. Recall that the magnetoelectric effect is still weak for this family of multiferroics as shown in **Figure.1.27b**

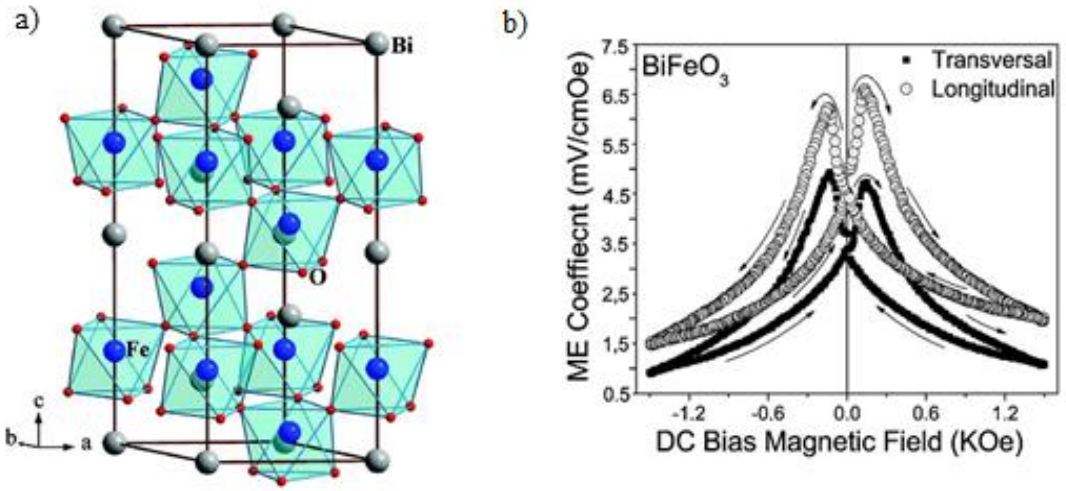

Figure.1.27: Crystal structure of BiFeO3 in the ferroelectric *R*3*c* structure (a), The magnetolectric coefficient versus dc bias magnetic field (b) [98].

b)The ferrimagnetic ferrite CoFe2O4 and NiFe2O4:

Iron or cobalt have good magnetic properties as individual metals, but they have the disadvantage of oxidizing in the air. Despite the modest magnetizations, this problem does not exist for $CoFe_2O_4$ and $NiFe_2O_4$. These compounds have some considerable properties.

Noting that the ferrite $CoFe_2O_4$ and $NiFe_2O_4$ adopt a spinel structure of the form AB_2O_4, in a face-centred cubic structure of the oxygen anions O^{2-}, with Fe^{3+} and Co^{2+}/Ni^{2+} occupying a number of tetrahedral A and octahedral B sites. $CoFe_2O_4$ and $NiFe_2O_4$crystallize in the inverted spinel structure in contrast to another MnFe2O4 ferrite that adopts a normal spinel structure.The difference lies in the distribution of cations within the different sites (**Figure.1.28**). The distribution of cations in the tetrahedral A and octahedral B sites can be characterized by the parameter inversion of the spinel structure XFe2O4 (X is a metal atom), in the formula $[Fe_yX_{1-y}]A[Fe_{2-y}X_y]BO_4$, where $0 < \mathbf{y} < 1$. The case of direct spinel is obtained on considering y=0 and that of the inverse spinel by taking y=1.

The reported magnetoelectric coupling of 104 mV/(cm.Oe) in the (2-2) $BaTiO_3/CoFe_2O_4$ nanocomposite is larger than the one reported for the $BaTiO_3/NiFe_2O_4$ bilayer [99], [100], which was explained by the larger magnetostriction of $CoFe_2O_4$ than that of $NiFe_2O_4$[101]. In **Table.1.4,** we present room-temperature magnetostriction of some magnetic ferrite compounds. Notice that the ferroelectric constituent should be chosen carefully.

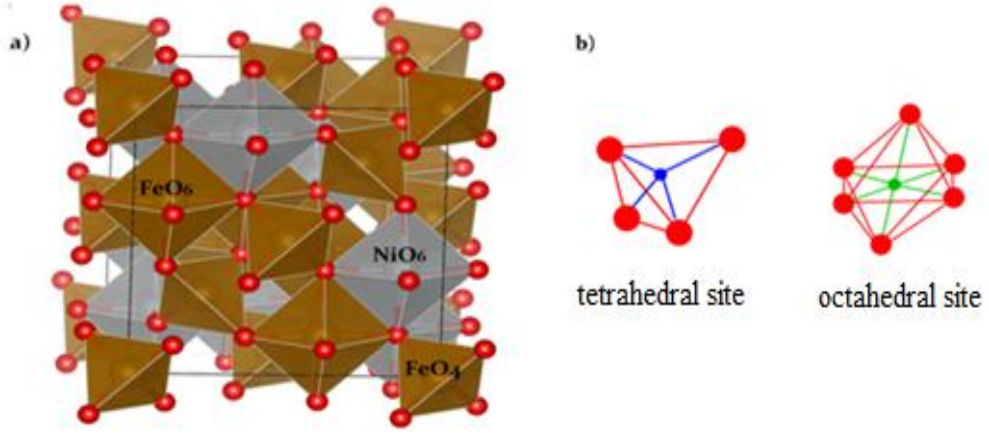

Figure.1.28: Structure representation of: **(a)** spinel NiFe2O4, **(b)** tetrahedral site (A site) and octahedral site (B site)

Table.1.4*: magnetic and electromechanical properties of same magnetic ferrites* [102].

Compound	T_c (K)	P $\times 10^3$ kg/m^3	ε 1 kHz	λ_{100} $\times 10^{-6}$	λ_{111} $\times 10^{-6}$	λ_s $\times 10^{-6}$
Fe3O4	858	5.23	-	-20	80	40
Co0.8Fe2.2O4	-	-	-	-590	120	-210
CoFe2O4	793	4.82	-	-	-	-110
Co0.9Fe2.1O4	-	-	-	-	-	-250
NiFe2O4	858	5.38	21	-46	-22	-26

T_c : Curie temperature, ρ : density , ε : permittivity, λ : magnetostriction coefficient.

c) Lead Zirconate Titanate (PZT)

Lead Zirconate Titanate (PZT) of the general formula $PbZr_{1-x}Ti_xO_3$ (PZT) is a solid solutions formed from the soluble binary mixture of lead titanate $PbTiO_3$ and lead zirconate $PbZrO_3$ (see **Figure.1.29**). $PbTiO_3$ is cubic paraelectrically at high temperature and transits at 490 °C to a quadratic phase ferroelectric, whereas $PbZrO_3$ is antiferroelectric at room temperature (symmetrical orthorhombic) and changes at 230 °C to a paraelectric cubic phase. The crystallographic structure of PZT is strictly dependent on the $PbTiO_3$ mole fraction 'x' and temperature.

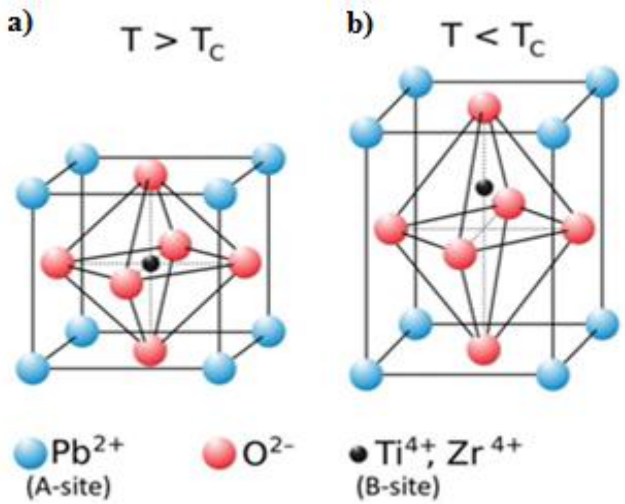

Figure.1.29: Perovskite structure of PZT : (a) $T > T_C$ and (b) $T < T_C$

At high temperature The **PZT** phase is cubic for all compositions. Below Tc, the diagram is marked by the existence of a morphotropic phase boundary (**MPB**) dividing the ferroelectric region into two parts: a titanium-rich region of quadratic symmetry (P4mm) and a zirconium-rich region of rhombohedral symmetry, which is divided into **R3c** and **R3m** symmetry at low-temperature and high-temperature, respectively. The morphotropic phase boundary (MPB) is located near **x=0.48** where the dielectric and piezoelectric properties are maximum [103]–[105] . **Figure.1.30** shows the phase diagram of the $PbZrO_3$- $PbTiO_3$ system proposed by Woodward et al.[106]**.**

The PZT has very interesting dielectric, piezoelectric, pyroelectric and ferroelectric properties. In addition to PZT, there are others piezoelectric materials with the perovskite structure type such as lead-magnesium niobate-titanate PMN-PT (Pb(Mg1/3Nb2/3)O3 - PbTiO3), lead-zinc niobate-titanate PZN-PT (Pb(Zn1/3Nb2/3)O3-PbTiO3), barium titanate BTO (BaTiO3), barium strontium titanate BSTO ($Ba_xSr_{1-x}TiO_3$).

A strong magnetoelectric coupling of 772 mV/cm. Oe was achieved in PZT-Ni nanocomposite [91], which is possibly due to the large piezoelectric coefficient of PZT. Also a large magnetoelectric coupling of 300 mV/cm.Oe was obtained in BaSrTiO3/LaSrMnO3 [107]. Room temperature permittivity and piezoelectric coefficient of some bulk ferroelectric materials are summarized in **Table.1.5**.

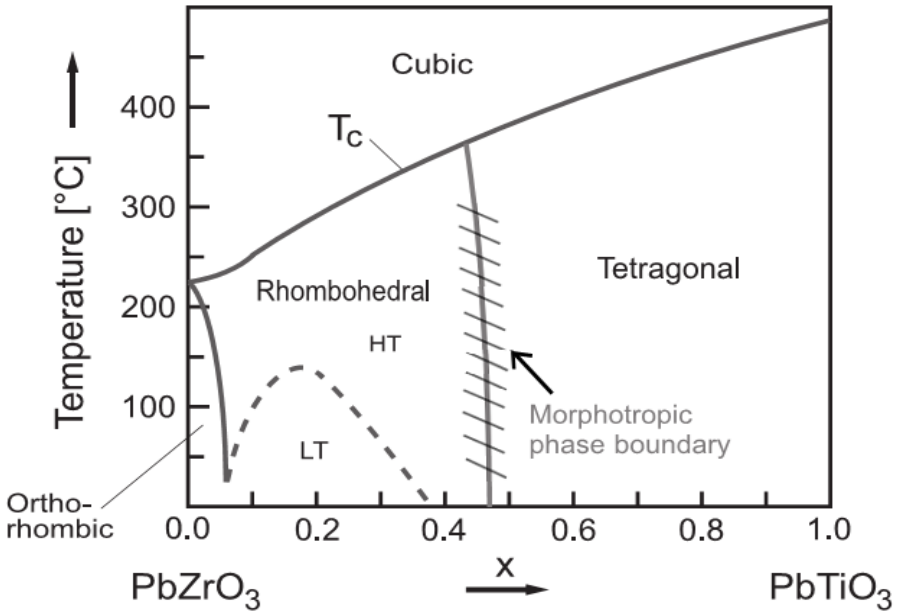

Figure.1.30: Phase diagram of PZT. Strokes denote the MPB.(adapted from Waser et al.[108])

Table.1.5:*dielectric and electromechanical properties of same oxide ferroelectric*[109]

compound	T_c **(K)**	ε *1kHz*	$P_r \times 10^{-2}$ C/m^2	$P_s \times 10^{-2}$ C/m^2	$E_c \times 10^{-2}$ V/m	d_{15} *pC/N*	d_{31} *pC/N*	d_{33} *pC/N*
$BaTiO_3$	**396**	**1350**	**25**	**25**	**3**	**270**	**-79**	**190**
$PbTiO_3$	**743**	**230**	**12**	**75**	**-**	**53**	**-20**	**51**
PZT	**601**	**800**	**-**	**36**	**13.6**	**494**	**-93.5**	**223**
$Ba_{70}Sr_{30}TiO_3$	**298**	**20000**	**-**	**8**	**11**	**-**	**-**	**-**

1.4. Applications of magnetoelectricity

Magneto-electric composites make it possible, in particular, to convert magnetic energy into electrical energy, which makes them very good candidates for electrical engineering applications[40], [41], [110]. In this section, we present the different available applications for magneto-electric composites.

1.4.1. Magnetic field sensors:

The first applications of magnetoelectric composites was a sensor of magnetic field. Immediate is to use them as an alternating field sensor, which corresponds to the excitation field of the sensor. In the literature, a large number of papers reports this type of application for sensors capable of measuring magnetic fields between $1\ pT < H_{AC} < 1\ mT$ depending on the operating frequency [111], [112]. Thedetection curve of the magnetoelectric sensor developed by Dong et al. is reproduced in**Figure.1.31.** The laminate magnetoelectric composite needs to be magnetically polarized at a certain DC field. Further, the magnetoelectric composite can be used as a static magnetic field sensor. This has also developed by Dong et al., yielding a composite capable of detecting DC fields of the order of 0.1 (mOe)[113] Also Fang et al.,[114]Burdin et al., [115] Reis et al., [116] and Chu et al. [117] have been worked ed on magnetic field sensors (AC)and DC).

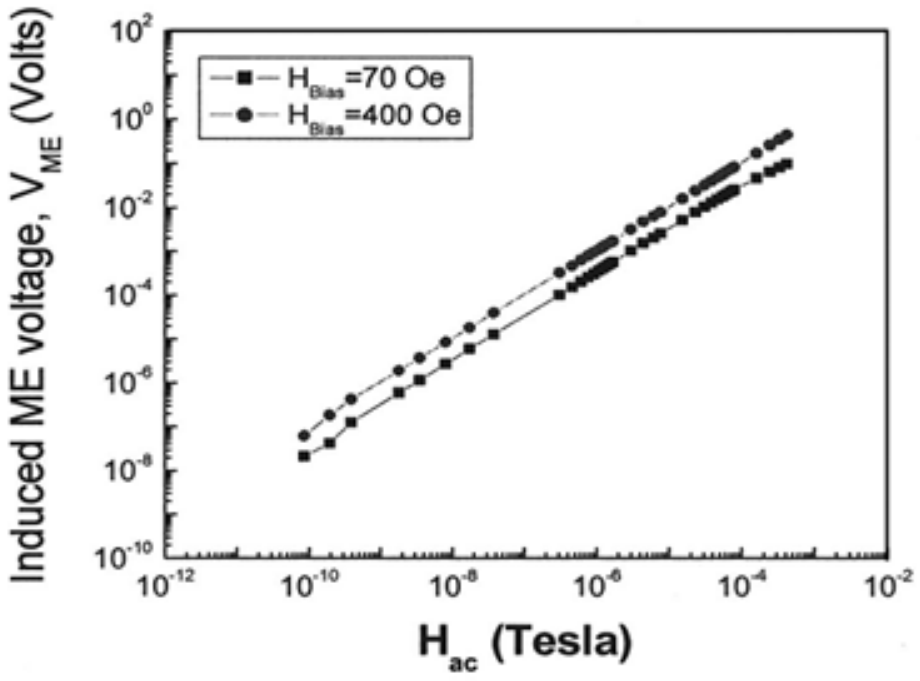

Figure.1.31: Induced magnetoelectric voltage as a function of magnetic fiel from $10^{-11}<H_{ac}<10^{-3}$ T

1.4.2. Current sensors:

The second application of the magnetoelectric composites is the AC and DC current sensor. It exists in the literature two main architectures for AC current sensors. The first one, proposed by Dong, consists of a ring-shaped ME composite (see**Figure.1.32a**)[118].This structure has the advantage of being very sensitive to the magnetic field because the magnetic field is zero, which makes it a very sensitive sensor for a wide range frequency. This was particularly highlighted in the case of a sensor composed of Terfenol-D and PZN-PT, where the measured current could reach 10^{-7} A, which is represented **Figure.1.32b.**

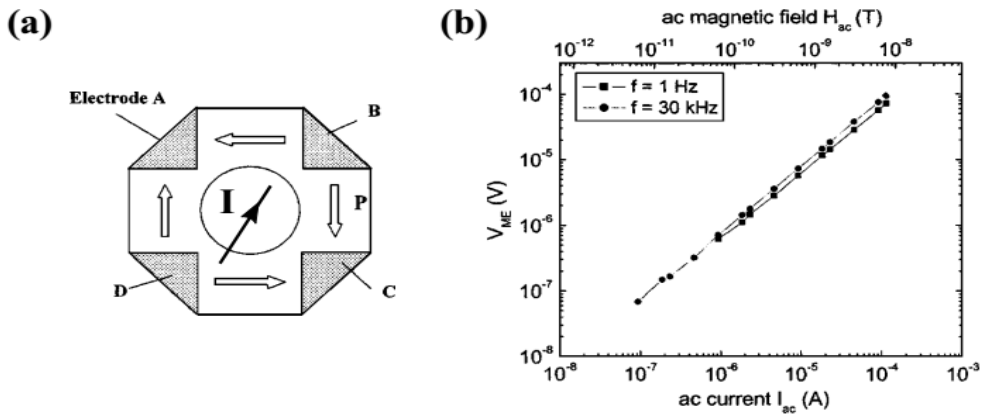

Figure.1.32 : (a) Ring-type Current Sensor and (b) ME Response (Terfenol-D / PZN-PT) obtained for 10^{-12} < Hac <10^{-8} Tesla which equivalents current of 10-8 <Iac <10-4 A for a frequency of 1 Hz and 30 kHz [118].

Later, Zhang et al. proposed a ring-type sensor, but using a rectangular ME (Terfenol-D/PZT) composite placed in the interstice of FeCuNbSiB alloy in high permeability (μr ~

100000) (see **Figure.1.33a**) [119]. This structure makes it possible, in particular, to omit the magnets necessary to polarize the magnetostrictive material and to achieve good linearity for high currents (I>100 A) (see **Figure.1.33b**). On the other hand, one of the disadvantages of this structure is the probable perturbation of the current measured by effect Inductive Faraday that induced flux concentrator with a high permeability.

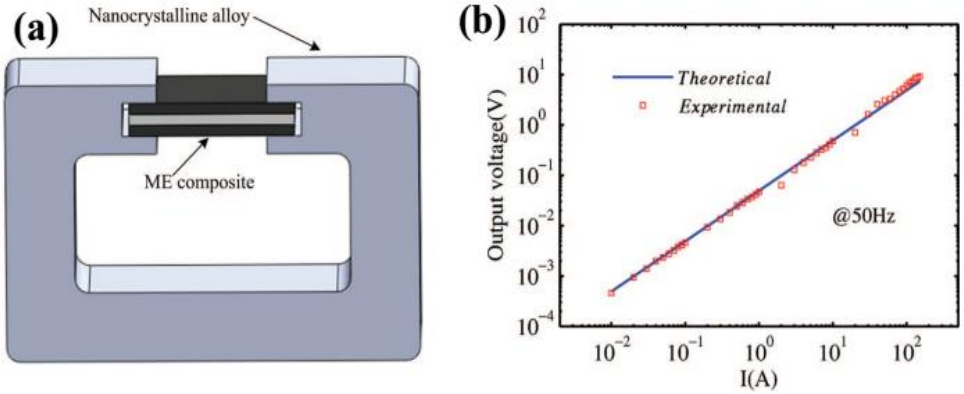

Figure.1.33 :(a) Ring type current sensor using a flux concentrator and (b) ME response (Terfenol-D / PZT) obtained for currents of 10^{-2}<Iac <10^{2}A at 50 Hz [119]

The second sensor architecture uses a monolithic laminar ME composite, the Current is induced by a coil wound around the composite. In this case, the current measured is directly connected to the sensor via the coil. Yu et al. have reported this sensor type for a Terfenol-D/PZT composite [120] as shown in **Figure.1.34**a. This type of sensor has the advantage of being very sensitive (1V/A) (see **Figure.1.34b**) but the disadvantage to be limited in amplitude of the current measured.

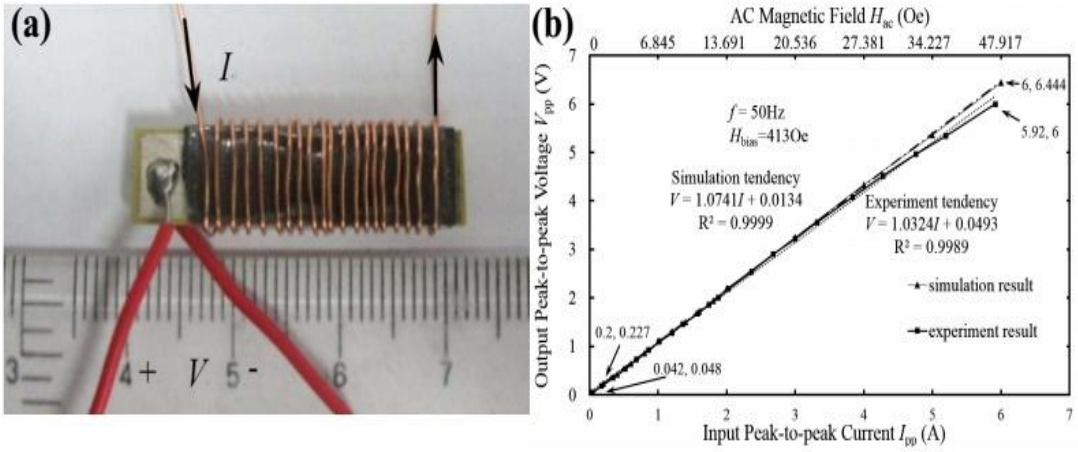

Figure.1.34: (a) Laminate-type current sensor and (b) ME response (Terfenol-D/PZT) obtained for currents of 10^{-2}<Iac <10A at 50 Hz , reported by Yu [120])

In addition, DC current sensors have been studied. The principle is the sameonly for magnetic field sensors. the DC current is measured from the linear part of the ME curve

Figure.1.35, [121]. These sensors can therefore be excited at their resonance frequency, which allows in particular improving their sensitivity. Bichurin et al.[121] have been reported a current sensor up to 5 A and having a high sensitivity of 0.53 V/A.

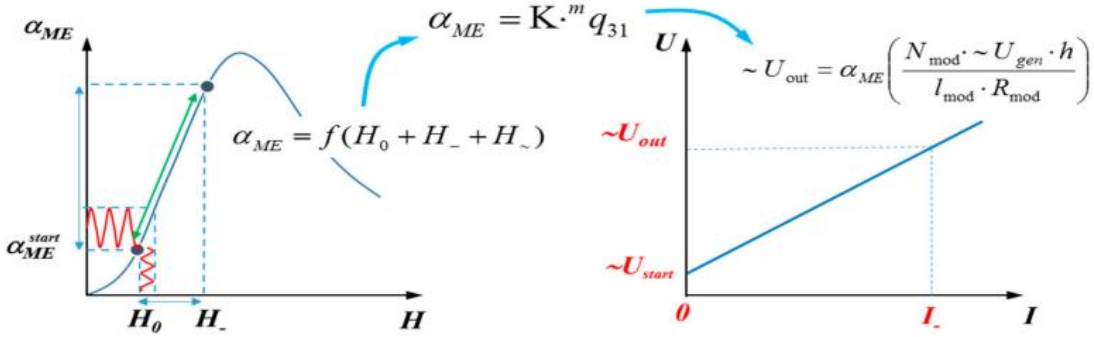

Figure.1.34: Principle of the magneto-electric DC current sensor (Bichurin [121])

1.4.3. Position sensors

Another type of sensor has recently been developed. Indeed, Wu et al. have proposed a position sensor based on the magnetoelectric effect (see **Figure.1.36**) [122] . The magnets have been positioned on the rotating body. Thus, depending on the position of these magnets with respect to the magnetoelectrics, the ME sensor informs about the angle of rotation (see **Figure.1.36b**). This also allows to go up to the speed of rotation.

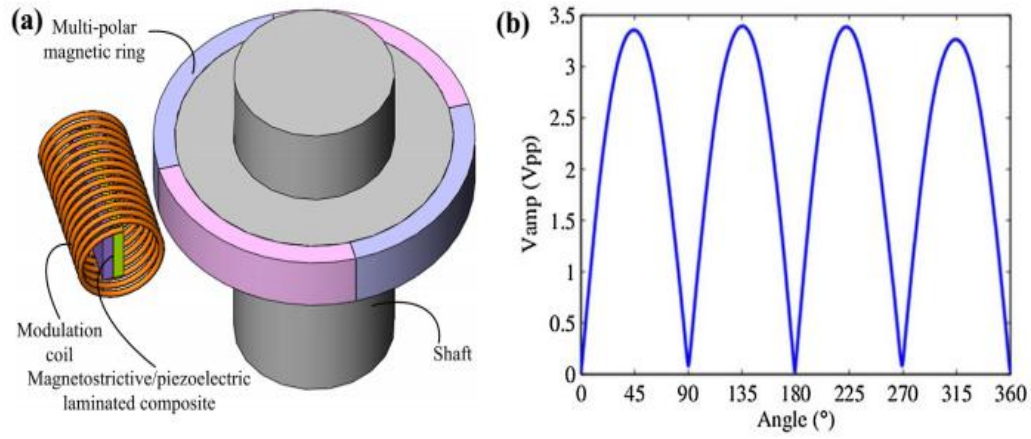

Figure.1.36: (a) magnetoelectric Position Sensor and (b) ME Position-Based Voltage (from Wu[122])

1.4.4. Energy recovery and transmission:

Energy recovery is one of the most popular applications in the field of electrical engineering. Magnetoelectric composites are good candidates for these applications because they convert magnetic or mechanical energy into electrical energy. Indeed, Qiu et al. proposed to integrate the **Terfenol-D/PZT** ME composite into a "wireless sensor network", and combined vibration energy recovery to power the sensor network. Lafont et al. have proposed to recover the magnetic energy induced by rotating magnets (see **Figure.1.37**) [123]. Although the recovered voltages can reach a few volts, these structures suffer for the moment from the

low power recovered at the terminals of the piezoelectric material (about 200 μJ), which limits their applications.

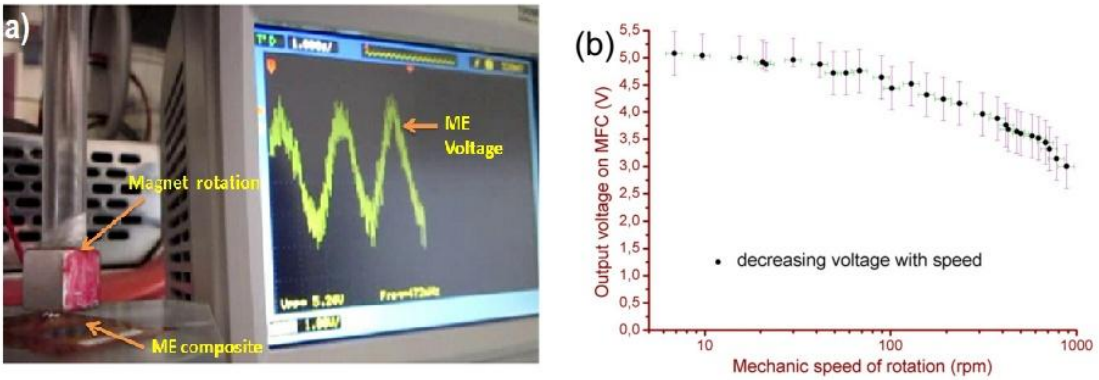

Figure.1.37: (a) Electric output of device with a permanent magnet rotating and (b) Voltage amplitude as a function of speed of rotation of the magnet. (reported by Lafont [123])

Another application in electrical engineering is the transmission of electromagnetic energy without wires. Today, wireless transmission is usually with two coils. However, this system remains very inefficient at low frequency. In 2004, Dong et al. have highlighted the advantage of ME composites compared to a single coil for an induced voltage at low frequency (see **Figure.1.38a**). In 2009, Bian et al. emphasized the improvement of the power recovered when the composite ME is excited at its electro-mechanical resonance frequency [124], and a power density close to 1 mW/cm3 was obtained (**Figure.1.38b).**

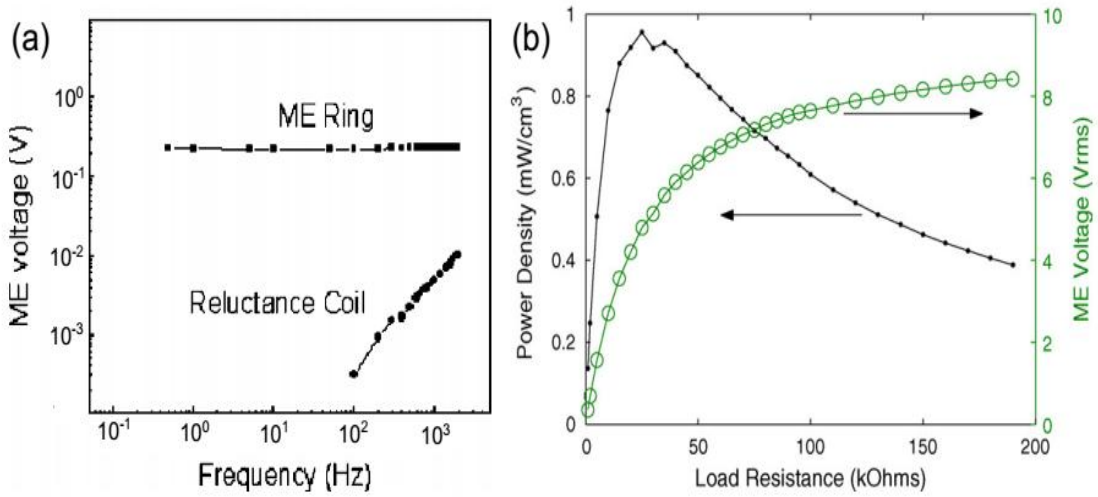

Figure.1.38: (a) ME-induced Tensions in a Terfenol-D/PZT Composite (Dong [7]) and (b) generated ME Power as a Function of load resistance in FeNi/PZT Composite at resonance frequency (Bian [124]).

1.4.5. Transformers and gyrators

Applications using electro-mechanical composite resonances are also studied because the voltages involved in these conditions are higher. Which lows to use this electro-mechanical composite in converter type applications in particular via transformer [125] or

gyrator [126] (see**Figure.1.39**). These applications make particular use of ferrites because they are conductors.

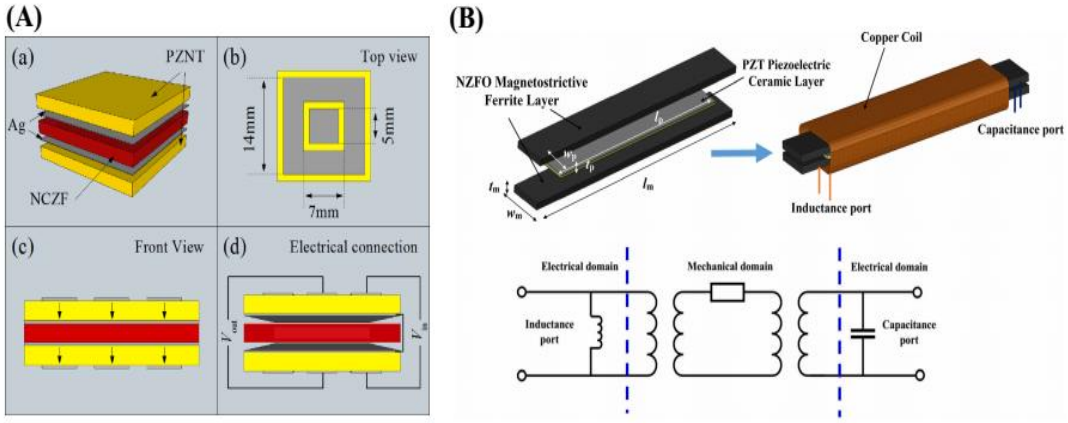

Figure.1.39: (A) Magnetoelectric Transformer (Zhou [125]) and (B) Magnetoelectric Gyrator (Leung [126]).

I.4.6. Variable inductance

The inverse magnetoelectric effect makes it possible to modify the magnetic properties of a composite when an electric voltage is applied to its terminals. This is a search path to develop variable inductances that use this reverse effect [127]. The factor for characterizing the inductance change for a given electric field is $\gamma = (L_H - L_E) / L_E$ where L_E and L_H are the inductances with electric field and without electric field respectively. As the anisotropy of the material is weak (and therefore its permeability is high), the coefficient γ is high (see **Figure.1.40a**)[128]. This coefficient has been able to reach more than 1150% at 1 kHz for an electric field of 8 kV / cm in the case of ME ring composed of Metglas and PMN-PZT (see **Figure.1.40b**)[128].

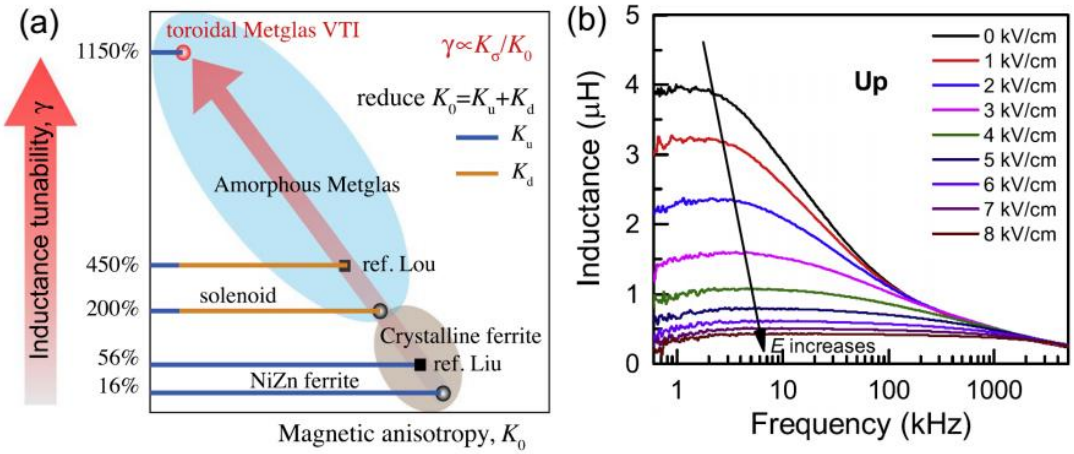

Figure.1.40: (a) Coefficient of "tunability" of inductance versus magnetic anisotropy and (b) Inductance as a function of frequency and electric field applied to a torus of Metglas / PMN-PT (from Yan [128])

1.4.7. Microwave technology

At the electromechanical resonance, a phase difference appears between the excitation field and the induced voltage ME. This phase shift allows ME composites to position themselves as potential phase shifter / oscillator, [129] or filter [130] (see **Figure.1.41**).

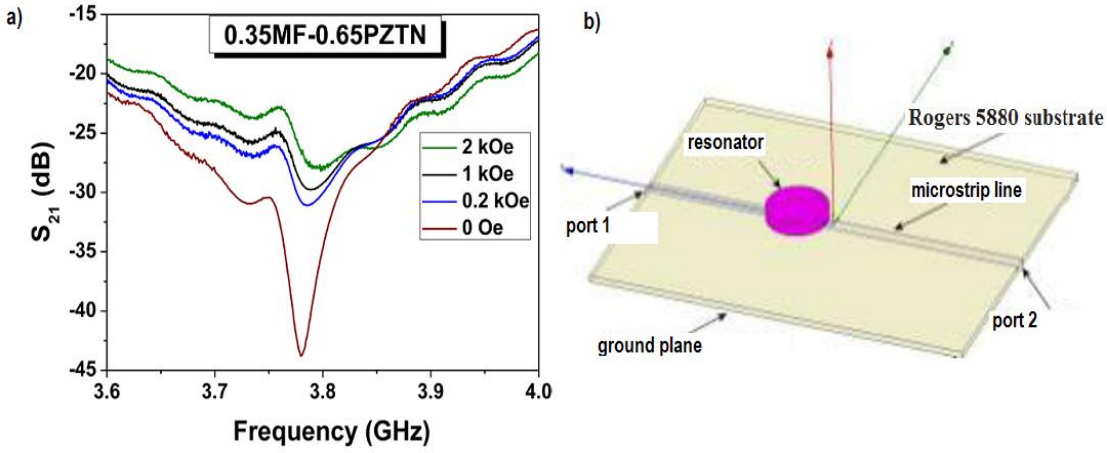

Figure.1.41: (a) Experimental setup for the stopband microwave filter with magnetoelectric resonator.(b) Measured transmission coefficient for the magnetically tunable microwave bandstop filter at different magnetic fields [130].

1.4.8. data processing

The magnetic random access memory (***MRAM***), the paradigm of spintronics, is based on the discovery of the giant magneto-resistance (***GMR***) by ***Fert*** and ***Grünberg*** (***Nobel prize 2007***[131]) but suffers from a fundamental drawback: the magnetic switching of bits produces by far too large Joule heat as to remain compatible with future miniaturized electronic devices. A spontaneous question comes into mind: why not use pure voltage switching for this elementary job? Being aware of the ***ME*** effect in chromia since more than 50 years [36] a functional device should be feasible after all. A prototype had already been proposed by **Zvezdin** [132], who designed a hypothetical ***ME*** data write head (**Figure.1.42**). It avoids Joule heating by using an interesting simple manner which is applied to future MRAMs by implementing voltage writing and magnetic reading of the computer hard disk.

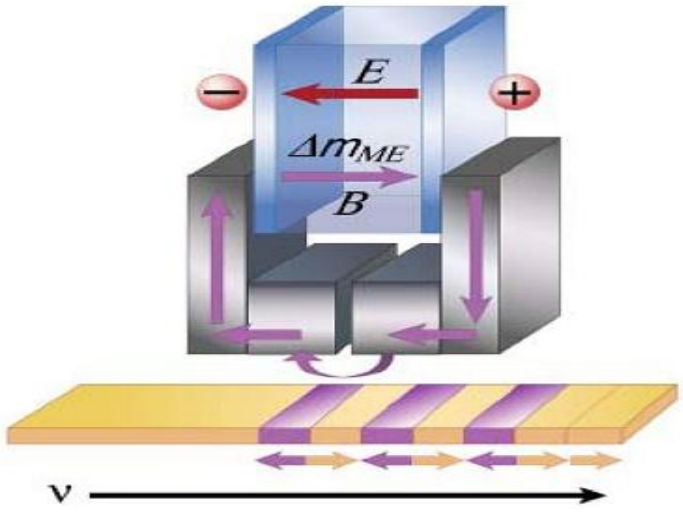

Figure.1.42:Capacitor-like write head with insulating ME filling controlled by electric field *E* and guiding the emerging magnetic flux density *B* to a hard disk via yoke and air gap.

Conclusion

Piezoelectric and ferroelectric materials are dielectric materials, which can polarized and deformed by electrostriction under an electric field. Further, the piezoelectric property gives the material the ability to polarize under mechanical stress and also to deform under an electric field. Furthermore, ferroelectric materials are polar piezoelectric materials and their polarization can be oriented by an electric field or an external mechanical stress.

Nowadays, the BFO is considered as a single-phase multiferroic being considered for spintronic devices. Remember that the magnetoelectric effect is still weak for this family of multiferroics. The realization of magnetoelectric composites, based on the extrinsic coupling of the ferroelectric and magnetostrictive phases, has allowed obtaining a "giant" magnetoelectric effect, which is promising for various industrial applications.

Chapter 2 :

Computational Methods:

2.1.Density Functional Theory (DFT)

2.1.1. Introduction

Density functional theory (**DFT**) is one of the most commonly used quantum methods in the fields of solid-state physics and quantum chemistry for the determination of physical and quantum quantities of a system, especially systems containing a large number of electrons, such as its electronic structure, ionization energy, etc. It is a so-called first-principle method. Indeed, it is based on the foundations of quantum mechanics and involves only a limited number of input data. For a given multi-body system, it allows the Schrödinger equation to be solved without the introduction of experimentally adjusted parameters.
Besides, Ab initio methods based on **DFT** allow reliable and quantitative material modeling and the processing of large systems. They therefore allow comparison with experimental results.

In this section, we will explain the basis of **DFT** and discuss the different levels of approximations necessary to solve the Schrödinger equation. In the following, the approximations used for the calculation of energy and exchange-correlation potential will be presented.

In contrast to the Hartree-Fock method [133] where the system energy is a function of the wave function $\boldsymbol{\Psi}$, the **DFT** expresses the energy as a function of the electron density $\boldsymbol{\rho}$. This method allows a simplification of the solution of the Schrödinger equation. Here, the **N** electrons (**3N** spatial coordinates) are replaced by the total electron density, which depends on only **3** spatial variables. The principle of the **DFT** consists in reformulating a quantum N-body problem into a single-body problem (spin function) with the electron density as a variable.

2.1.2.The quantum many-body problem

a) The Schrödinger equation

Understanding the structural, electronic, optical and magnetic properties of materials consists of studying the system of electrons and the highly interacting nuclei that make it up. Unfortunately, solving the Schrödinger equation (2.1) for such a system is extremely difficult, as Dirac reported [134].

$$\hat{\mathbf{H}}\boldsymbol{\Psi} = \mathbf{E}\boldsymbol{\Psi} \qquad (2.1)$$

Where $\hat{\mathbf{H}}$is the Hamiltonian operator, ψ is the wave function, which depends on the position of each electron and each nucleus in the system. and E is the total energy of the system.

The related Hamiltonian $\hat{\mathbf{H}}$ for a system with many interacting particles (**N** nucleus + **NZ** electrons), is given by the sum of the operator of the total kinetic energy $\hat{\boldsymbol{T}}_{\boldsymbol{T}}$ and the sum

of the operator of Coulomb interactions ($\widehat{V}_T$). For such a system of interacting electrons and nucleus, the total Hamiltonian $\widehat{\mathbf{H}}$ decomposes as:

$$\widehat{\mathbf{H}} = \widehat{\mathbf{T}}_\mathbf{n} + \widehat{\mathbf{T}}_\mathbf{e} + \widehat{\mathbf{V}}_\mathbf{nn} + \widehat{\mathbf{V}}_\mathbf{ne} + \widehat{\mathbf{V}}_\mathbf{ee} \qquad (2.2)$$

Where,

$\widehat{\mathbf{T}}_\mathbf{n} = -\frac{\hbar^2}{2}\sum_\mathbf{i}\frac{\nabla^2_{\mathbf{Ri}}}{\mathbf{M_N}}$ the kinetic energies of nucleus.

$\widehat{\mathbf{T}}_\mathbf{e} = -\frac{\hbar^2}{2}\sum_\mathbf{i}\frac{\nabla^2_{\mathbf{ri}}}{\mathbf{m_e}}$ the kinetic energies of electrons.

$\widehat{\mathbf{V}}_\mathbf{nn} = -\frac{1}{4\pi\varepsilon_0}\sum_{i,j}\frac{e^2 Z_i}{|R_i - r_j|}$ the potential energy of nucleus-nucleus interaction.

$\widehat{\mathbf{V}}_\mathbf{ne} = \frac{1}{8\pi\varepsilon_0}\sum_{i\neq j}\frac{e^2 Z_i Z_j}{|R_i - R|}$ the potential energy of electron-nucleus interaction.

$\widehat{\mathbf{V}}_\mathbf{ee} = \frac{1}{8\pi\varepsilon_0}\sum_{i\neq j}\frac{e^2}{|r_i - r_j|}$ the potential energy of electron-electron interaction.

The total Hamiltonian (2.2) can be rewritten as :

$$\hat{\mathrm{H}}_T = -\frac{\hbar^2}{2}\sum_\mathbf{i}\frac{\nabla^2_{\mathbf{Ri}}}{\mathbf{M_N}} - \frac{\hbar^2}{2}\sum_\mathbf{i}\frac{\nabla^2_{\mathbf{ri}}}{\mathbf{m_e}} - \frac{1}{4\pi\varepsilon_0}\sum_{i,j}\frac{e^2 Z_i}{|R_i - r_j|} + \frac{1}{8\pi\varepsilon_0}\sum_{i\neq j}\frac{e^2 Z_i Z_j}{|R_i - R|} + \frac{1}{8\pi\varepsilon_0}\sum_{i\neq j}\frac{e^2}{|r_i - r_j|} \qquad (2.3)$$

where $\mathbf{M_N}$ is the mass of a nucleus with coordinates $\mathbf{R_i}$, and $\mathbf{m_e}$ is the mass of an electron with coordinates $\mathbf{r_i}$.

The eigenvalues of equation (2.1) can only be calculated accurately in the case of hydrogen systems. Analytical resolution of the total Hamiltonian for a multi-particle system still impossible due to the interactions in the system: **N** nucleus and **NZ** electrons are interacting and moving in an electromagnetic field, creating a multi-body problem.

For example, the Schrödinger equation on a $\mathbf{10 \times 10 \times 10}$ grid for each spatial coordinate represents $\mathbf{10^{3N}}$ independent variables. In the case of a system containing **10** particles, and accounting for the spin ($\mathbf{2^N}$ times more variables), the evaluation of the ground state would require almost $\mathbf{10^{30}}$ operations, which would be performed at most within **15000** years. A set of approximations is therefore needed to solve numerically the quantum many-body problem. To overcome this problem, there are many approximations such as Born-Oppenheimer approximation; Hartree, Hartree-Fock and **DFT** have been developed to solve the Schrödinger equation.

b) Born-Oppenheimer approximation

The first accepted approximation which introduced by Born-Oppenheimer in 1927 [135] consists in decoupling the electrons and the nuclei degrees of freedom. Considering the nuclei as being fixed with respect to the electrons because the mass of electron is less than the nuclei mass and the nuclei move much slower than the electrons. We rewrite equation (2.2) as follows:

$$\widehat{\mathbf{H}}_\mathbf{T} = \widehat{V}_e + \widehat{\mathbf{T}}_\mathbf{ee} + \widehat{\mathbf{V}}_\mathbf{ne} \qquad (2.4)$$

Where $\widehat{\mathbf{V}}_{\mathbf{ne}} = \widehat{\mathbf{V}}_{\mathbf{ext}}$: operator of Coulomb potential energy of electrons in the potential of nuclei.

The electronic Schrödinger equation to be solved writes:

$$\hat{H}_T = -\frac{\hbar^2}{2}\sum_i \frac{\nabla_{ri}^2}{m_e} - \frac{1}{4\pi\varepsilon_0}\sum_{i,j}\frac{e^2 Z_i}{|R_i - r_j|} + \frac{1}{8\pi\varepsilon_0}\sum_{i\neq j}\frac{e^2}{|r_i - r_j|} \quad (2.5)$$

In order to solve this many-body problem of electrons, that involves such a large number of particles and the difficult electron-electron interaction, further approximations must be applied.

c) Hartree Approximation:

The Hartree Approximation Based on the independence between electrons (each electron is independent of the other). Each electron can move in a mean field generated by nuclei and other electrons. The total wave function $\boldsymbol{\psi}$ is the product of the single electron wave functions$\boldsymbol{\psi_i}$[136] **:**

$$\boldsymbol{\Psi}(\mathbf{r_1}, \mathbf{r_2} \ldots\ldots\ldots \mathbf{r_n}) = \boldsymbol{\psi_1}(\mathbf{r_1})\boldsymbol{\psi_2}(\mathbf{r_2}) \ldots\ldots\ldots \boldsymbol{\psi_N}(\mathbf{r_N}) \quad (2.6)$$

Schrödinger equation corresponds to each wave function $\boldsymbol{\psi_i}$is:

$$-\frac{\hbar^2}{2m}\boldsymbol{\Delta\psi_i}(\vec{r}) + \boldsymbol{V_{eff}\psi_i}(\vec{r}) = \boldsymbol{\varepsilon_i\psi_i}(\vec{r}) \quad (2.7)$$

The equation (2.7) is called the Hartree equations, $\boldsymbol{\varepsilon_i}$ represents the electronic level corresponding to $\boldsymbol{\psi_i}(\vec{r})$.

$-\frac{\hbar^2}{2m}\Delta$: kinetic energy of electron.

V_{eff} : Effective potential that the electron undergoes under the influence of the nucleus as well as that of other electrons.

The potential of electron-nucleus interaction defined by:

$$V_N(\vec{r}) = -Ze^2\sum\frac{1}{\left|\vec{r} - \vec{R}\right|} \quad (2.8)$$

For electron-electron interaction, we assume that the electron is moving in a potential $V_H(\vec{r})$ such that:

$$V_H(\vec{r}) = -e\int\frac{d^3\vec{r}'}{\left|\vec{r} - \vec{r}'\right|}\rho(\vec{r}') \quad (2.9)$$

This potential describes the interaction of an electron undergoes the interaction of other electrons which represented by a density $\rho(\vec{r})$.

Thus, The applied effective potential on an electron becomes:

$$V_{eff}(\vec{r}) = V_H(\vec{r}) + V_N(\vec{r}) \tag{2.10}$$

The new electronic density can be calculated using the eigenfunctions of the solution:

$$\rho(\vec{r}) = \sum_{i}^{occu} \psi_i^*(\vec{r})\psi_i(\vec{r}) \tag{2.11}$$

Introducing the Poisson's equation that relates Hartree's potential to electron density:

$$V_H(\vec{r}) = -4\pi\rho(\vec{r}) \tag{2.12}$$

Hartree introduced a self-Consistent Field method (SCF) as a qualitative method to solve the equation of Schrödinger (Equation 2.1). The wave function, electron density and potential are interdependent. This process is also used in other approaches.

Hartree's approximation overestimates the Coulomb repulsion because the correlations are not included in the calculation. Moreover, the electrons being considered without spin, therefore the solutions are not antisymmetric and do not verify the principle of Pauli.

d) Hartree-Fock approximation

The Hartree-Fock approximation (1930) is the extension of the Hartree approximation[137], including the permutation symmetry of the wave functions leading to the exchange interaction. The exchange is due to Pauli's exclusion principle, which is derived from the Heisenberg principle, which states that any wave function for a given system must be antisymmetric with respect to the exchange of two particles. Fock has therefore proposed to express the wave function of an n-electron system, using a linear combination of the wave functions of the independent electrons, in the general form of a Slater determinant [136]**,**The principle of Pauli-Heisenberg is thus satisfied since the wave functions of the two electrons occupying the same spin-orbit state cannot exist. The wave function of the quantum electronics is given by:

$$\boldsymbol{\Psi}(\vec{\mathbf{r}}_1, \ldots \vec{\mathbf{r}}_a, \ldots \vec{\mathbf{r}}_b, \ldots \vec{\mathbf{r}}_n) = -\boldsymbol{\Psi}(\vec{\mathbf{r}}_1, \ldots \vec{\mathbf{r}}_a, \ldots \vec{\mathbf{r}}_b, \ldots \vec{\mathbf{r}}_n) \tag{2.13}$$

Ψrepresents the wave function of a system of n electrons.

$$-\frac{\hbar^2}{2m}\Delta\psi_i(\vec{r}) + V_{eff}\psi_i(\vec{r}) - \sum_j \left\{\frac{d^3\vec{r}'}{|\vec{r}-\vec{r}'|}\psi_i^*(\vec{r}')\psi_i(\vec{r}')\right\} = \varepsilon_i\psi_i(\vec{r}) \tag{2.14}$$

The hypothesis of antisymmetry of wave function ψ is included in an exchange term between the electron located in r and the electron located in r'. Therefore, the difference between the Hartree method and the Hartree-Fock method lies in this exchange term. In the Hartree-Fock method, each orbital is undergoes to an average electrostatic field, and the exchange operator expresses the change in energy because two electrons of the same spin cannot occupy the same position.

The difference between the exact non-relativistic energy and the Hartree-Fock energy is the correlation energy. Its estimation is one of the major issues in Ab initio calculations. The correlation energy that appears in complex systems, especially crystals, can be taken into account using Khon-Sham's approach in the framework of the Density Functional Theory.

2.1.3. Density Functional Theory (DFT)

The main idea of DFT is to describe a system of interacting electrons through their density and not through the wave function of each electron. In DFT, the states of the n electrons in the system are determined by applying the variational principle to a functional, i.e. a function of another function, the first being the total energy and the second the electron density $\boldsymbol{\rho}(\vec{\boldsymbol{r}})$.

Historically, it was Thomas [138] and Fermi [139] who expressed energy in terms of density (1928). But the DFT theory was formally established in 1964 by two theorems that were stated and demonstrated by Hohenberg and Kohn[22]. The principle of these two theorems is well explained in more recent books on DFT such as Eschrig's [140] and Parr and Yang's[141].

a) Theorems of Hohenberg-Kohn (1964)

The two theorems Hohenberg and Kohn [22]are applicable for any interacting particle system operating in an external potential. We present their statements in the following:

First Theorem:

Statement: "For any system of interacting particles in an external potential $\boldsymbol{V_{ext}}(\vec{\boldsymbol{r}})$, the potential $\boldsymbol{V_{ext}}(\vec{\boldsymbol{r}})$ is determined uniquely, except for a constant, by the ground state density $\boldsymbol{\rho_0}\ (\vec{\boldsymbol{r}})$."

Second Theorem:

Statement: "A universal function for the energy $\boldsymbol{E}(\boldsymbol{\rho})$ in terms of the density $\boldsymbol{\rho}(\vec{\boldsymbol{r}})$ can be defined, and valid for any external potential $\boldsymbol{V_{ext}}(\vec{\boldsymbol{r}})$. The exact ground state energy of the system is the global minimum of this functional, and the density that minimizes the functional is the exact ground state density $\boldsymbol{\rho_0}(\vec{\boldsymbol{r}})$."

The approach of Hohenberg and Kohn have demonstrated that for such a system the ground state wave function is a unique function of the electron density, $\boldsymbol{E} = \boldsymbol{E}[\boldsymbol{\rho}(\vec{\boldsymbol{r}})]$ so any observable $\widehat{\boldsymbol{O}}$ depends on the density function [142]. The total energy of the system is written as follows:

$$\mathbf{E}(\boldsymbol{\rho}) = \mathbf{F_{HK}}(\boldsymbol{\rho}) + \mathbf{V_{ext}}(\boldsymbol{\rho}) \qquad (2.15)$$

With $\boldsymbol{F_{HK}}(\boldsymbol{\rho}) = \boldsymbol{T}(\boldsymbol{\rho}) + \boldsymbol{V_{ee}}(\boldsymbol{\rho})$ and $\boldsymbol{V_{ext}} = \int \widehat{\boldsymbol{V}}_{\boldsymbol{ext}}(\boldsymbol{r})\boldsymbol{\rho}(\boldsymbol{r})\boldsymbol{dr}$ (2.16)

Where, $\boldsymbol{F_{HK}}(\boldsymbol{\rho})$ is the universal function of Hohenberg and Kohn, $\boldsymbol{V_{ext}}$ is the external potential, $\boldsymbol{T}(\boldsymbol{\rho})$ inter-electronic repulsions and $\boldsymbol{V_{ee}}(\boldsymbol{\rho})$is the external potential due to the nuclei.

The term $\mathbf{E}(\boldsymbol{\rho})$ is minimal when the density $\boldsymbol{\rho}(\boldsymbol{r})$corresponds to the electron density of the ground state.

The Hohenberg-Kohn theorems ascertain that the Hamiltonian of a system of N interacting electrons in an external potential can be derived from the ground state density, and that the ground state energy can be found by minimizing the energy functional $\mathbf{E}(\boldsymbol{\rho})$, instead of determining the many-electron wave function from the electronic Schrödinger equation. However, they do not provide an explicit formulation of $\boldsymbol{F_{HK}(\rho)}$.

b) **The Kohn and Sham equations (1965)**:

In 1965, Kohn and Sham [143] formulated an approximation scheme to use Hohenberg Kohn's theorem by integrating the effects of exchange and correlation. They proposed to replace the many-body electron problem by an alternative fictitious independent-particles problem. The concept is to map the system of interacting particles into a set of fictitious particles moving in an effective potential, with the same ground-state electronic density.

In the framework of a fictitious system of non-interacting electrons with replacing the repulsion by an effective potential and using the wave function to determine the density and equation (**2.15**) can be rewritten in the following form [144]:

$$\boldsymbol{E(\rho) = T_{KS}(\rho) + V_{ext}(\rho) + V_H(\rho) + E_{XC}(\rho)} \qquad (2.17)$$

Where, $\boldsymbol{T_{KS}(\rho)}$ is the kinetic energy of non-interacting electrons, $\boldsymbol{V_H(\rho)}$ is Coulombian electron-electron interaction energy and $\boldsymbol{E_{XC}(\rho)}$: Exchange correlation energy
The kinetic energy of non-interacting electrons $\boldsymbol{T_{KS}(\rho)}$ is given by:

$$\boldsymbol{T_{KS}(\rho) = \sum_{i=1}^{N} \left\langle \Psi_i \left| -\frac{\nabla^2}{2} \right| \Psi_i \right\rangle} \qquad (2.18)$$

Using the atomic units of Hartree ($\boldsymbol{m_e = \hbar = e = 1}$)

with$\boldsymbol{\rho(r) = \sum_{i=1}^{N} |\Psi_i(r)|^2}$

For a given set of atomic positions, the ground-state is determined via the minimization of $\boldsymbol{E(\rho)}$ with respect to $\boldsymbol{\Psi_i}$ taking second theorem of **H.K** and introducing the Lagrange parameters $\boldsymbol{\in_i}$, Kohn-Sham equations are given by:

$$\boldsymbol{\left[-\frac{\nabla^2}{2} + V_{eff}(r)\right] \Psi_i(r) = \in_i \Psi_i(r)} \qquad (2.19)$$

Where,$\boldsymbol{V_{eff}(r) = V_{ext}(r) + V_H(r) + V_{XC}(r)}and\boldsymbol{V_H(r) = \int \frac{\rho(r')}{|r-r'|} dr}$: is the Hartree potential. The Exchange-correlation potential $\boldsymbol{V_{XC}(r) = \frac{\partial E_{XC}}{\partial \rho(r)}}$ depends on the electron density, which itself is calculated from the wave functions of the independent electrons, the wave functions depends on the potential calculated from the density, ...
This approach leads to a self-consistent field: starting from an arbitrary value, the density, potential and function values are calculated through the convergence of the calculation cycles.
The properties of a system can be calculated using the Khon-Sham approach. This has become possible through the independent electron model. However, the function of the exchange-correlation energy $\boldsymbol{E_{xc}[\rho(\vec{r})]}$is still unknown and cannot be expressed exactly. It is

therefore necessary to derive approximations such as the local density approximation ***(LDA)*** and the generalized gradient approximation ***(GGA)*** to evaluate this term.

c) Local Density Approximation (LDA)

In first, Khon and Sham (1965) proposed Local Density Approximation (LDA),they assumed that the exchange-correlation potential is a function of the local electron density. The system is considered to behave locally as a homogeneous gas of electron density $\boldsymbol{\rho}(\vec{\boldsymbol{r}})$ (see Figure 2.3).Their approximation called local density approximation, known as **LDA**, which is particularly appropriate for systems with relatively slow spatial density variation $\boldsymbol{\rho}(\vec{\boldsymbol{r}})$. Thus, the exchange-correlation energy functional is the simple integral of a function of density at any point in space:

$$\boldsymbol{E_{XC}^{LDA}}[\boldsymbol{\rho}(\vec{\boldsymbol{r}})] = \int \boldsymbol{\rho}(\vec{\boldsymbol{r}})\boldsymbol{\epsilon_{XC}^{LDA}}[\boldsymbol{\rho}(\vec{\boldsymbol{r}})]\, \boldsymbol{d\vec{r}} \tag{2.20}$$

Where, $\boldsymbol{\epsilon_{XC}^{LDA}}[\boldsymbol{\rho}(\vec{\boldsymbol{r}})]$ is the exchange-correlation energy.

The exchange-correlation potential $\boldsymbol{V_{XC}^{LDA}}(\overrightarrow{\boldsymbol{r}})$ can be expressed by the following equation:

$$\boldsymbol{V_{XC}^{LDA}}(\overrightarrow{\boldsymbol{r}}) = \frac{\boldsymbol{\partial}(\boldsymbol{\rho}(\overrightarrow{\boldsymbol{r}})\boldsymbol{\epsilon_{XC}^{LDA}}[\boldsymbol{\rho}(\vec{\boldsymbol{r}})])}{\boldsymbol{\partial\rho}(\vec{\boldsymbol{r}})} \tag{2.21}$$

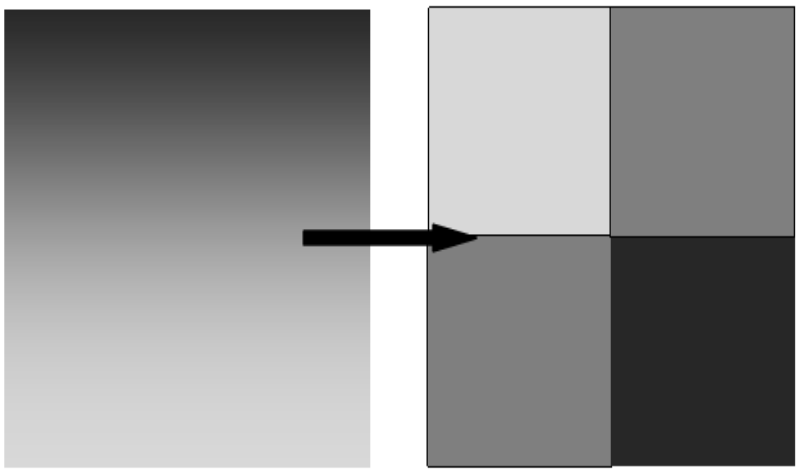

Figure.2.1: Schéma représentatif de l'approximation LDA en 2D.[145]

A local approximation such as the **LDA** gives good results especially in the case of covalent systems and simple metals in which the electron density varies slowly. The fundamental properties predicted by the **LDA**, including the total energy of the system under study, are in good agreement with the experimental results [146].

The **LDA** has been extended to handle polarized spin systems; it is Local Spin polarized Density Approximation, (**LSDA**) [147], [148]:

$$\boldsymbol{E_{XC}^{LDA}}[\boldsymbol{\rho}_{\uparrow}(\vec{\boldsymbol{r}}), \boldsymbol{\rho}_{\downarrow}(\vec{\boldsymbol{r}})] = \int [\boldsymbol{\rho}_{\uparrow}(\vec{\boldsymbol{r}}), \boldsymbol{\rho}_{\downarrow}(\vec{\boldsymbol{r}})]\, \boldsymbol{\epsilon_{XC}^{LDA}}[\boldsymbol{\rho}_{\uparrow}(\vec{\boldsymbol{r}}), \boldsymbol{\rho}_{\downarrow}(\vec{\boldsymbol{r}})]\, \boldsymbol{d\vec{r}} \tag{2.22}$$

Typical disadvantages of **LDA/LSDA** are the underestimation of lattice parameters, gap energy and spin orbital moments. Therefore, other terms must be added into the exchange-correlation expression. This is the purpose of the **GGA** method presented in the following section.

d) Generalized Gradient Approximation (GGA):

The electronic density of a real system is obviously not homogeneous. To generate more precise exchange-correlation functions, the Generalized Gradient Approximation (**GGA**) consists in considering the electronic density $\boldsymbol{E_{xc}}[(\boldsymbol{\rho}(\vec{\boldsymbol{r}})]$ and its gradient $\boldsymbol{[\nabla\rho(\vec{r})]}$ (its first derivative at a given point). Using the density gradient as an additional variable, the **GGA** can provide improved results. In general, the exchange-correlation function is defined in the **GGA** as:

$$\boldsymbol{E_{XC}^{GGA}[\rho(\vec{r})] \approx \int \rho(\vec{r})\epsilon_{XC}^{GGA}[\rho(\vec{r}), |\nabla\rho(\vec{r})|]d\vec{r}} \quad (2.23)$$

Where, $\boldsymbol{\epsilon_{XC}^{GGA}[\rho(\vec{r}), |\nabla\rho(\vec{r})|}$ is exchange-correlation energy of an electron in a system with non-uniform electronic density.

$\boldsymbol{GGA}$ functionals are also expressed in the general form for a spin-polarized system by the following equation :

$$\boldsymbol{E_{XC}^{GGA}[\rho_{\uparrow}(\vec{r}), \rho_{\downarrow}(\vec{r})] = \int [\rho_{\uparrow}(\vec{r}), \rho_{\downarrow}(\vec{r})]\, \epsilon_{XC}^{GGA}[\rho_{\uparrow}(\vec{r}), \rho_{\downarrow}(\vec{r}), \vec{\nabla}\rho_{\uparrow}(\vec{r}), \vec{\nabla}\rho_{\downarrow}(\vec{r})]\, d\vec{r}} \quad (2.24)$$

Although the $\boldsymbol{GGA}$ approximation and its different versions have widely demonstrated their efficiency (molecular bonds, magnetism in metals, cohesion, electronic surface properties of metals and semiconductors, etc.), it does not always give satisfactory results. They fail to determine the widths of the band gaps. The gap is underestimated by up to **50%** compared to experimental data [149]–[151]. This is due to the fact that $\boldsymbol{DFT}$ does not treat excited states. In other words, the $\boldsymbol{LDA/GGA}$ functionals do not take into account the discontinuity of the exchange-correlation potential: Generally, for an orbital-independent potential (i.e. the same potential for all orbitals), the band gap energy calculated from of the eigenvalues is different from the real gap energy. Thus, many approximations and methods have been developed such as $\boldsymbol{GGA+U, LDA+U}$, Green's function and screened Coulomb interaction ($\boldsymbol{GW}$), Full-Potential Linearized Augmented Plane Wave + Local Orbitals and ($\boldsymbol{FP-L/APW+lo}$), Augmented Plane Wave ($\boldsymbol{APW}$).

e) ABINIT code

The ABINIT code [152], [153] decomposes the periodic parts of the Kohn and Sham wave functions on a plane wave basis. This specificity involves the use of a cutoff energy that allows to take into account a certain number of plane waves per K points of the first Brillouin zone. It is also necessary to mesh the first Brillouin zone with a grid of K points, which is done using Monkhorst-Pack type grids[154]. In order to determine the best possible parameters, these two points have been studied: the evolution of the energy as a function of the K-point grid and the cut-off energy. We have therefore used these parameters for the calculations.

f) Quantum Espresso code

The calculations performed in this thesis are based on the Density Functional Theory (DFT), implemented in the Quantum Espresso code [155]. The PBE functional [156], [157] in the GGA approximation is used to process the exchange and correlation potential. The wave functions are developed on a plane wave basis using ultrasoft pseudopotentials established by Vanderbilt [158]. The occupancy of the electronic levels is treated with the Marzari-Vanderbilt method [159] with the smearing width $\sigma = 0,001$ Ry. The optimization of the structure is performed by including all atoms, with the condition that all residual forces are less than 0.003 eV/Å and that the change in the total energy between two consecutive steps is less than 0.001 eV.

2.2. Monte Carlo Simulation:

2.2.1. Introduction:

The Monte Carlo method gives approximate solutions to various problems in several domains by generating statistical draws. The method is useful for obtaining numerical solutions to problems that are too complicated to solve analytically. It was invented by Nicholas Metropolis in 1947, and first published in an article by Stanislaw Ulam in 1949 [160]. The name Monte Carlo refers to the city of Monaco famous for its casinos and slot machines which are games of chance with random behavior [161].

The Monte Carlo method is based on the idea of random sampling and the application of statistics to calculate the desired quantity [162]. The method tends to be used when it is impossible to calculate an exact result with a deterministic algorithm. The first Monte Carlo algorithm dates back to the middle of the 19th century. Nowadays, Monte Carlo techniques are used in many fields: biology, statistics, material sciences, finance, chemistry and physics, etc.

Several models have been developed to study magnetic behavior and properties in complex ordered and disordered systems. These modeling tools may exceed experimental capability and the mathematical limit. These tools can be used to predict new materials that are difficult to test experimentally, and to calculate their basic physical and chemical properties under extreme conditions that are difficult to achieve experimentally. The Monte Carlo method allows to calculate the properties in some cases easily and quickly, to test the theories compared to the experimental observations and to suggest experiments to validate the theories.

In this section, we present the Monte Carlo method. We have described the Ising model and the theoretical basis of the used methods and approximations. The Metropolis algorithm is also presented.

2.2.2. Concepts of Monte Carlo Simulation:

a) Estimation:

The estimation of any observable quantity ($\boldsymbol{Q}$), such as magnetization or internal energy, is typically calculated by averaging the quantity in phase space over all spin states of the system, which is generally canonical:

$$< \boldsymbol{Q} >= \frac{\sum_{\mathbf{a}} \mathbf{Q_a} \mathbf{e}^{-\boldsymbol{\beta} \mathbf{E_a}}}{\sum_{\mathbf{a}} \mathbf{e}^{-\boldsymbol{\beta} \mathbf{E_a}}} \tag{2.25}$$

where $\boldsymbol{\beta}$ is the inverse of temperature and $\boldsymbol{E}$ is the internal energy that usually includes the interactions that govern the behavior of the system.

In large systems, the best method is averaging over a sub-group of states. Monte Carlo techniques work by randomly choosing a subset of states $\{\boldsymbol{a_1} \dots \boldsymbol{a_M}\}$ from a probability distribution $\boldsymbol{p_a}$ that we specify. The best estimate of the quantity $\boldsymbol{Q}$ will then be given by :

$$\boldsymbol{Q_M} = \frac{\sum_{i=1}^{M} Q_{a_i} P_{a_i}^{-1} e^{-\beta E_{a_i}}}{\sum_{j=1}^{M} P_{a_j}^{-1} e^{-\beta E_{a_j}}} \tag{2.26 }$$

$\boldsymbol{Q_M}$is called the estimate of $\boldsymbol{Q}$. If the number $\boldsymbol{M}$ of sample states increases, $\boldsymbol{Q_M}$ becomes more accurate estimate of $< Q >$, and when $\boldsymbol{M} \to \infty$, we have $\boldsymbol{Q_M} = < Q >$. The simplest choice is to choose all states with equal probability, the $\boldsymbol{Q_M}$ is as follows:

$$\boldsymbol{Q_M} = \frac{\sum_{i=1}^{M} Q_{a_i} e^{-\beta E_{a_i}}}{\sum_{j=1}^{M} e^{-\beta E_{a_j}}} \tag{2.27}$$

b) Importance Sampling:

The average values of the quantities recovered by the Monte Carlo simulation are calculated on the basis of the system states. The system does not necessarily assume all possible states during measurements. Real systems behave as a kind of Monte Carlo simulation during their evolution to define their properties. The sample states are not equiprobable, but are distributed according to the Boltzmann distribution. This distribution is mainly used to improve the estimation of the average value. Therefore, the concept of a large sample is to create an appropriate Markov chain in which the configurations are chosen according to their weight, according to Boltzmann's probability [163].

Typically, the Monte Carlo simulation uses the Markov chain to generate a random configurations system. The transition to a configuration denoted ($\boldsymbol{b}$) depends only on the previous configuration denoted ($\boldsymbol{a}$) , but not on the whole configuration set in state space. This means that the transition is following the probability $\boldsymbol{W}(a \to b)$, in a Markov chain .

A Markov chain is constructed by a succession of states that satisfy the Boltzmann probability. This process of succession construction, also known as the Markov process, leading to the Boltzmann distribution, is called equilibrium. Ergodicity and detailed balance are additional ideas that are needed to carry out the Markov process.

c) Markov Process

The sensitive part of running a Monte Carlo simulation is to generate an appropriate random state according to Boltzmann's probability distribution. The states are selected randomly, thus they can be accepted or rejected according to a probability$\boldsymbol{e^{-\beta E_a}}$.

A Markov process is a mechanism that, for a given system in a single state $\boldsymbol{a}$, generates a new state$\boldsymbol{b}$of the system. This mechanism is randomly; it does not generate the same new state each time when it receives the initial state $\boldsymbol{a}$. The probability of generating the given state $\boldsymbol{b}$ from state $\boldsymbol{a}$ is called the transition probability $\boldsymbol{P}(\boldsymbol{a} \rightarrow \boldsymbol{b})$ from $\boldsymbol{a}$ to $\boldsymbol{b}$, and for a true Markov procedure, all transition probabilities must satisfy two conditions:

- it must not vary over time.
- it should depend only on the properties of the current states $\boldsymbol{a}$ and $\boldsymbol{b}$, and not on other system states.

A Markov process has been used in Monte Carlo simulation to generate a chain of Markov states. Starting with a state **a**, we use the process to generate a new state **b**, then we feed this state into the process to generate another **c**, …

We consider $\boldsymbol{P}\ (\boldsymbol{a}\ , \boldsymbol{k})$ the probability of the system in a configuration $\boldsymbol{a}$ at iteration **k**. The evolution of this probability is given by the equation:

$$\boldsymbol{P}\ (\boldsymbol{a}\ , \boldsymbol{k}\ +\ \mathbf{1})\ = \sum_{\boldsymbol{b}} \boldsymbol{W}\ (\boldsymbol{b}\ \rightarrow\ \boldsymbol{a}) \boldsymbol{P}\ (\boldsymbol{b}, \boldsymbol{k})\ -\ \boldsymbol{P}\ (\boldsymbol{a}, \boldsymbol{k}) \tag{2.28}$$

Where, $W\ (\boldsymbol{b} \rightarrow\ \boldsymbol{a}$ is the transition probability from state $\boldsymbol{b}$ to $\boldsymbol{a}$.

The Markov process is specially chosen because, when it runs from any state in the system and for enough times, it will eventually produce a succession of states that appear with probabilities given by the Boltzmann distribution. To do this, we put two other conditions on Markov process: the ergodicity conditions and the detailed balance.

d) Ergodicity

The condition for ergodicity is that the system can, from a given state, pass during the Markov process through any initial state for a new state [164]**.** The condition of ergodicity is not satisfied if all the transition probabilities of a given state are zero.

This is necessary to generate states with their Boltzmann probabilities. Each state $\boldsymbol{a}$appears with a non-zero probability $\boldsymbol{P_a}$ in the Boltzmann distribution. Transition rates, which are conditional probabilities, must be positive and normative:

$$\forall(\boldsymbol{\nu_i}, \boldsymbol{a}), \exists\ \boldsymbol{n}, \{\boldsymbol{\nu_{i+1}}, \boldsymbol{\nu_{i+2}} \ldots \boldsymbol{\nu_{i+n}}\}\ /$$

$$\boldsymbol{W}(\boldsymbol{\nu_i} \rightarrow \boldsymbol{\nu_{i+1}}) \boldsymbol{W}\ (\boldsymbol{\nu_{i+1}} \rightarrow\ \boldsymbol{\nu_{i+2}}) \ldots \boldsymbol{W}\ (\boldsymbol{\nu_{i+n}} \rightarrow\ \boldsymbol{a})\ > \mathbf{0} \tag{2.29}$$

Where, $\boldsymbol{p(v) = e^{-\beta E_{(v)}}}$

e) Detailed balance

The detailed balance condition ensures that the Boltzmann probability distribution generated an equilibrium state to the system under consideration [165]. If the system is in equilibrium, the transition rate from one state to the same state are equal:

$$\boldsymbol{\sum_a p(a) W\,(a \to b) = \sum_{\{b\}} p(b) W\,(a \to b)} \tag{2.30}$$

With, $\boldsymbol{\sum_a W\,(a \to b) = 1}$, we can obtain :

$$\mathbf{p(a) = \sum_b p(b) W\,(b \to a)} \tag{2.31}$$

For any set of transition probabilities, that satisfies equation 2.7 the partition will be the equilibrium distribution implied by the dynamics of Markov processes. This equation does not provide a guaranteed distribution of the state of the system. To overcome this difficulty, the required detail balance given by:

$$\mathbf{p(a) W\,(a \to b) = p(b) W\,(b \to a)} \tag{2.32}$$

This condition eliminates the cycle limit. When the time approaches infinity, the probabilities converge exponentially towards the eigenvector corresponding to the largest eigenvalue. The real systems satisfy the detail balance requirement.

In order for the Boltzmann distribution to be balanced, an additional condition is given by:

$$\boldsymbol{\frac{W(b \to a)}{W(a \to b)} = e^{-\beta(E_b - E_a)}} \tag{2.33}$$

The main objective is to create a program that builds the Markov chain based on transition probabilities. The program must run long enough time to ensure that $\boldsymbol{P_a(t)}$ tends to the Boltzmann $\boldsymbol{P_a}$ distribution at equilibrium.

f) Acceptance probability

Standard methods do not apply to new problems. New algorithms are developed for specific needs and several Markov processes can be proposed. A given algorithm does not necessarily define the exact set of transition probabilities. Therefore, the probability acceptance allows you to find the right transition probabilities of any Markov process [166]. In this case, condition $\boldsymbol{W(a \to a) \neq 0}$ is allowed and always responds to the detail balance.

Thus, the transition probability can be given by:

$$\boldsymbol{W(a \to b) = g\,(a \to b)\, A(a \to b)} \tag{2.34}$$

where $\boldsymbol{g(a \to b)}$ is the probability of selection. It is the probability of obtaining a new state b from the old state a by the algorithm. $\boldsymbol{A(a \to b)}$ is the acceptance probability, it is the probability of accepting the transition from the old state **a** to the new state **b**. The value of the

probability of acceptance is random between **0** and **1**. If $\boldsymbol{A(a \to b) = 0}$, then $\boldsymbol{W\ (a \to a) = 1}$ for any transition.

$$\frac{\boldsymbol{W(a \to b)}}{\boldsymbol{W(b \to a)}} = \frac{\boldsymbol{g\ (a \to b)\ A(a \to b)}}{\boldsymbol{g\ (b \to a)\ A(b \to a)}} \tag{2.35}$$

In order to avoid the slowness of the algorithm, we generally admit acceptance close to **1**. The best algorithm is therefore the one that adds the selection probability $\boldsymbol{g(a \to b)}$ and takes$\boldsymbol{A(a \to b)\ \simeq 1}$.

2.2.3. Ising model:

The study of magnetic properties is based on the reduction of the studied systems in simple models consisting of discrete variables. The magnetic moments of atoms can only take two directions, spin up (↑) spin down (↓). Therefore, the most appropriate models that can describe the magnetic properties under consideration are those based on discrete spins such as the Ising model [167].

This model, named by the physicist Ernst Ising [168]. The difference between the Ising model and the Heisenberg model, is that the first describes the spins as dipoles that can only have two possible directions, up or down, while the second allows the spin vectors to spot all directions. The Ising model has been used efficiently to study the phase transitions of the two-dimensional square lattice, which is the simplest model to show the magnetic transition.

The magnetization in the case of a compound is written as**:** $\boldsymbol{m} = < S >$

For a two-dimensional spin lattice, Ising's Hamiltonian is given by :

$$\boldsymbol{H} = -\sum_{<i,j>} \boldsymbol{J_{ij} S_i S_j} - \boldsymbol{H_{ext}} \sum_i \boldsymbol{S_i} \tag{2. 36}$$

The Hamiltonian consists of two sums. The first concerns the interactions between adjacent spins denoted $< i, j >$**,** which means that sites $\boldsymbol{i}$ and $\boldsymbol{j}$ are the nearest neighbors . The second sum refers to the energy resulting from a magnetic field external. The Hamiltonian function contains only signs ***(-)*** on its terms. This convention has allowed the classification of the Ising model according to the sign of the exchange coupling.

- $\boldsymbol{J_{ij}} > 0$, the interaction between the spins $\boldsymbol{S_i}$ and $\boldsymbol{S_j}$ is of the ferromagnetic type.

- $\boldsymbol{J_{ij}} < 0$, the interaction between the $\boldsymbol{S_i}$ and $\boldsymbol{S_j}$ spins is of the antiferromagnetic type.

- $\boldsymbol{J_{ij}} = 0$, there is no interaction between the $\boldsymbol{S_i}$ and $\boldsymbol{S_j}$ spins.

As a result, the Ising model is ferromagnetic when all spins are oriented in same direction. In contrast, the model is antiferromagnetic if the majority of the nearest neighboring spins are in an antiparallel configuration.

In the absence of an external magnetic field and assuming that all the nearest neighbors $< ij >$ have the same exchange coupling strength, the Ising model can be simplified:

$$\boldsymbol{H} = -\boldsymbol{J}\sum_{<i,j>}\boldsymbol{S_i S_j} \quad (2.37)$$

This model indicates that the spins are ordered and the magnetization value is not equal to zero at low temperature. Whereas at high temperature, the spins are disordered and the magnetization disappears. During the phase transition, we can identify either the Curie temperature ($\boldsymbol{T_C}$) for the ferromagnetic system or the Néel temperature ($\boldsymbol{T_N}$) if the antiferromagnetic system. Therefore, this model is the most appropriate basic model to study all disorder transitions in magnetic compounds.

2.2.4. Metropolis Algorithm

The Metropolis algorithm is known for its ability to be applied in practically all cases. However, this algorithm is closely related to the choice of acceptance$\boldsymbol{A(a \to b)}$. It should be noted that two types of dynamics of Monte Carlo simulations exist. In the first one, only one spin has an attempt to flip at each Monte Carlo step. However, in the second one all spins in the system show an attempt to flip at each Monte Carlo step. Nevertheless, the second dynamic is still limited due to the large size of the system and the computing time, which could be long in this case. The dynamic adopted, in the case of the application of this algorithm on the Ising model, consists in making a single reversal attempt at each Monte Carlo step [169]. In this case, all the selection probabilities are equal.

The selection probabilities are given by:

$$\boldsymbol{g\,(a \to b) = \frac{1}{N}} \quad (2.38)$$

Where N is the number of spins in the system.

The detailed balance equation can be written as follows:

$$\frac{\boldsymbol{W(a \to b)}}{\boldsymbol{W(b \to a)}} = \frac{\boldsymbol{g\,(a \to b)\,A(a \to b)}}{\boldsymbol{g\,(b \to a)\,A(b \to a)}} = \frac{\boldsymbol{A(a \to b)}}{\boldsymbol{A(b \to a)}} = \boldsymbol{e^{-\beta(E_b - E_a)}} \quad (2.39)$$

$$\boldsymbol{A(a \to b) = A_0 e^{\frac{-1}{2}\beta(E_b - E_a)}} \quad (2.40)$$

$\boldsymbol{A_0}$ determined randomly. The algorithm is more efficient for large values ofacceptance $\boldsymbol{A(a \to b)}$.

The Metropolis algorithm with a single flip dynamics is defined by the following acceptance:

$$\boldsymbol{A(a \to b)} = \begin{cases} \boldsymbol{e^{-\beta(E_b - E_a)}} & \boldsymbol{for E_b - E_a > 0} \\ \boldsymbol{1} & \boldsymbol{otherwise} \end{cases} \quad (2.41)$$

Therefore, the transition probability $\boldsymbol{W(a \to b)}$ assumes the same form as acceptance. With this choice of transition probabilities the system tends towards a stable state in which the configuration probability is given by $\boldsymbol{e^{-\beta E_a}}$, when the Markov state chain approaches infinity.

At each Mote Carlo step, a spin-flip is always accepted if it causes a loss of energy. On the other hand, when the flip is performed, therefore, the system assumes a new configuration that has a higher energy level, the update still has to be accepted with a certain probability[170]. According to a random number ($\boldsymbol{r}$)uniformly distributed: $\mathbf{0} < \boldsymbol{r} < \mathbf{1}$, and if $\boldsymbol{W} \leq \boldsymbol{r}$, the new configuration is accepted, otherwise the flip attempt is rejected. The system retains its old configuration and a new flip attempt is made for the next flip.

For the Ising model, the new state **b** is generated from the old state **a**. Some practical details should be respected during the practical implementation of the Metropolis algorithm:

1) Select an initial configuration, for example:
   - all spins aligned,
   - or randomly distributed spins
2) Select a random spin.
3) Flipping of this spin.
4) We calculate the difference in energy ΔE of interaction of the spins between the new configuration with a flipped spin and the initial configuration.
5) If $\boldsymbol{\Delta E} \leq \mathbf{0}$ i.e. the spin flip decreases the energy, then we accept the new configuration.
6) If $\boldsymbol{\Delta E} > 0$:
We draw a random number $\boldsymbol{r}$, following a uniform law on the segment **[0,1[**.

- If $\boldsymbol{r} < \boldsymbol{e}^{(\frac{-\Delta \boldsymbol{E}}{\boldsymbol{k_B T}})}$, we accept the configuration with flipped spin as the new configuration.
- If not, we reject the flip and the configuration at the next step is identical to the previous configuration.

7) The following quantities are calculated: magnetization, susceptibility, internal energy, specific heat, ...
8) We repeat.

The calculation steps with Metropolis algorithm are presented in **Figure.2.2**:

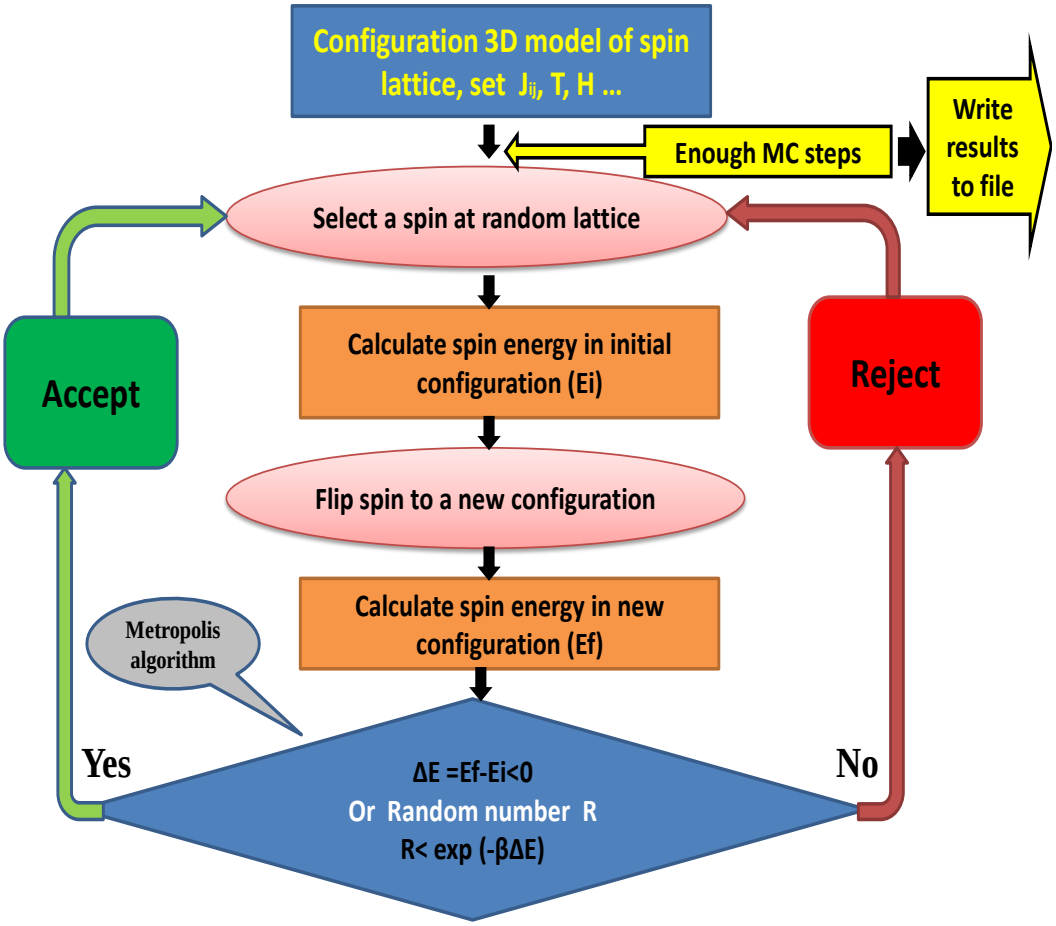

Figure.2.2: diagram of a Monte Carlo simulation with Metropolis algorithm

2.3 Conclusion

In this chapter, we have presented the basic concepts of the ***DFT*** theory, namely the Hohenberg and Khon theorems, the Khon Sham approach, as well as the ***LDA*** and ***GGA*** approximations and their different versions, which they can be used for the determination of the exchange-correlation energy. Since it includes local electron density, gradient and second-order gradient, the ***PBE-GGA*** version is frequently used to address the structural properties of oxides. For this reason, we plan to use it in our calculations of structural, electronic, magnetic and electrical properties. In fact, solving Schrödinger's equation is equivalent to solving the n Khon Sham equations corresponding to n independent electrons at an effective potential using the self-consistent field (***SCF***) method.

Furthermore, we have presented the essential on the concept and the steps of the Monte Carlo method, the Ising model and the Metropolis algorithms. The Monte Carlo method, which will be used in the following chapters, is an efficient computational method for the understanding of complex physical phenomena such as those found in the case of magnetic, ferroelectric and multiferroic materials.

Chapter 3

Magnetoelectric coupling at the $NiFe_2O_4$/PZT (001) interface: A density functional theory investigation.

3.1 Introduction:

Multiferroic heterostructures with ferroelectric and ferro-ferri-magnetic properties have attracted considerable interest due to their potential applications [1], [171]. These materials allow the possibility to control magnetic polarization via an electric field or vice versa through the magnetoelectric coupling. Such property could yield novel technological devices, such as sensors, magnetoelectric random access memories and capacitor[2], [3]. It should be noted that the magnetic-electric coupling of single-phase multiferroics materials was observed often at low temperature[172], [173]. However, a strong ME coupling at room temperature can be obtained in multiferroic heterostructures exhibiting both high ferroelectric and ferromagnetic Curie temperature transition. Noting that such coupling is induced through interfacial strain between magnetostrictive and piezoelectric layers[4], [14].

In recent years, many theoretical studied on interfacial magnetoelectricity have been carried out using first-principles. As an example, G. Zhong et al. [174] investigated $Fe_3Ga/BaTiO_3/Fe_3Ga$ heterostructure. In addition, M. K. Niranjan et al.[175], [176] obtained a magnetoelectric coefficients of $\alpha = 2.1 \times 10^{-10}$ G.cm/V and $\alpha = 2.3 \times 10^{-10}$ G.cm/V for Fe_3O_4/ $BaTiO_3$ (001) and $SrRuO_3/BaTiO_3$ (001) interfaces, respectively. Also, J. Lee et al.[177] predicted a magnetoelectric coupling of $\alpha = 4 \times 10^{-10}$ G.cm/V in $Fe/PbTiO_3/Fe$ superlattices. Moreover, $M/BaTiO_3$ (M = Ni, Fe) superlattices [178], $Co/BaTiO_3/Co$[179], $La_{0.66}Sr_{0.33}MnO_3$ /$PbZr_{0.2}Ti_{0.8}O_3$ heterostructure[180], $M/BiFeO_3$ (M = Co,Fe) superlattice [181] and Co/PZT (001) interface [182] was investigated by first-principles theory. Interestingly, it is found that magnetoelectric coupling in these systems is strictly dependent on the structural and electronic properties, surface termination, and interfacial exchange coupling. Experimentally, many researchers are successively realized an interfacial magnetoelectric coupling based on heterostructre system. G. Srinivasan et al. [19] achieved a high value magnetoelectric voltage coefficient of 460 mV/cm.Oe and 1500 mV/cm.Oe in bilayer and multilayer of $NiFe_2O_4$/PZT. For K. Bi et al. [183], they obtained a magnetoelectric voltage coefficient of 0.40 V/cm.Oe in Ni/Pb(Zr,Ti)O_3/Ni trilayers. Tahmasebi et al. [184] reported that the $SrRuO_3/Pb(Zr_{0.95}Ti_{0.05})O_3/CoFe_2O_4$ heteroepitaxial thin film exhibits a magnetoelectric coefficient of 287 mV/cm.Oe. Moreover, Cherifi et al. [185] observed that the electric field can produce a giant magnetization variation in FeRh/BaTiO3 with an antiferromagnetic- to-the ferromagnetic phase transition in FeRh.

In the presented chapter, we report a first-principles investigation of interfacial magnetoelectric coupling in the $NiFe_2O_4$/PZT (001) heterostructure. Two termination surfaces are considered, namely the $(Zr_{0.5}Ti_{0.5})O_2$-terminated PZT surfaces and the PbO-terminated PZT surfaces at the $NiFe_2O_4$/PZT interface. The magnetic, electronic, interfacial separation work and magnetoelectric coefficient were investigated.

3.2 Computational details and interface model:

Calculations in this chapter have been done using the Quantum-ESPRESSO package [155], which is based on the density functional theory(DFT) [22], [23] in the plane wave pseudo-potential formalism. Our calculations are performed using the Hubbard corrected GGA+U exchange-correlation functional [186], [187]. We include an effective Hubbard parameter U_{eff}=U-J of 4.5 eV, which is sufficient to describe related bulk properties and is a better description of localized Fe(3d) and Ni(3d) orbitals [188]. While for Ti(3d), the U_{eff} is fixed to8 eV[189], [190]. A kinetic energy cutoff of 40 Ry was employed with 8×8×8 and 8×8×4 Monkhorst-Pack k-point mesh, for ferrimagnetic $NiFe_2O_4$ and tetragonal PZT supercells, respectively. The $NiFe_2O_4$/PZT heterostructure was modeled using an 8×8×1 k-point mesh. Marzari-Vanderbilt cold smearing technique with the convergence threshold of forces on ions was set to be 10^{-5} Ry/Bohr are selected.

Recall that the ferromagnetic $NiFe_2O_4$ crystallizes in the inverse cubic spinel structure (space group Fd3m) at room temperature with chemical formula $[Fe(\downarrow)]_A[Ni(\uparrow)Fe(\uparrow)]_BO_4$ and lattice parameters of a = 8.337 Å [188]as shown in **Figure.3.1a**. The tetrahedron A sites are occupied by Fe^{3+} cations and octahedron B sites are occupied by an equal number of randomly distributed Ni^{2+} and Fe^{3+}cations. The ferrimagnetic ordering arises due to the strong antiferromagnetic coupling between Fe^{3+} cations on A and B sites. The Fe cations in B sites are coupled ferromagnetically [191]. Concerning the PZT, the structure is tetragonal with the lattice parameters of a = 4.030 Å and c = 4.145 Å[6] (see **Figure.3.1b**). The $NiFe_2O_4$/PZT heterostructre is simulated by constructing four unit cells of PZT (001) on top of one unit cell of $NiFe_2O_4$ (001), as shown in **Figure.3.2**. We use periodic boundary conditions along X- and Y-axes and open boundaries along Z-axis with a vacuum layer of over 10 Å [192]. We have considered both the (Zr0.5Ti0.5)O2 and PbO terminations of the PZT layer, as shown in Figure.2(a,b) . These are the (Zr0.5Ti0.5)O2-terminated interface with Zr, Ti and O atoms on top of NFO layer (labeled NFO/ZTO) and PbO-terminated interface with Pb and O on top of NFO layer. Thus, the interface atoms at NFO/ZTO interface are Ni, Fe, O, Zr, Ti and those of NFO/PbO interface are Ni, Fe, O, Pb.

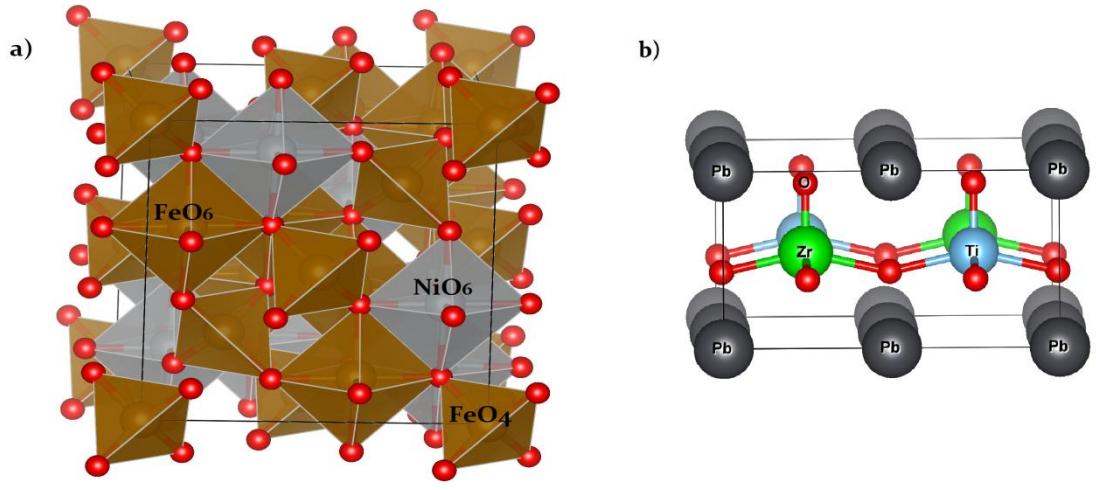

Figure.3.1: structure of: bulk **NiFe2O4 (a)** and tetragonal supercells of bulk **PZT (b)**.

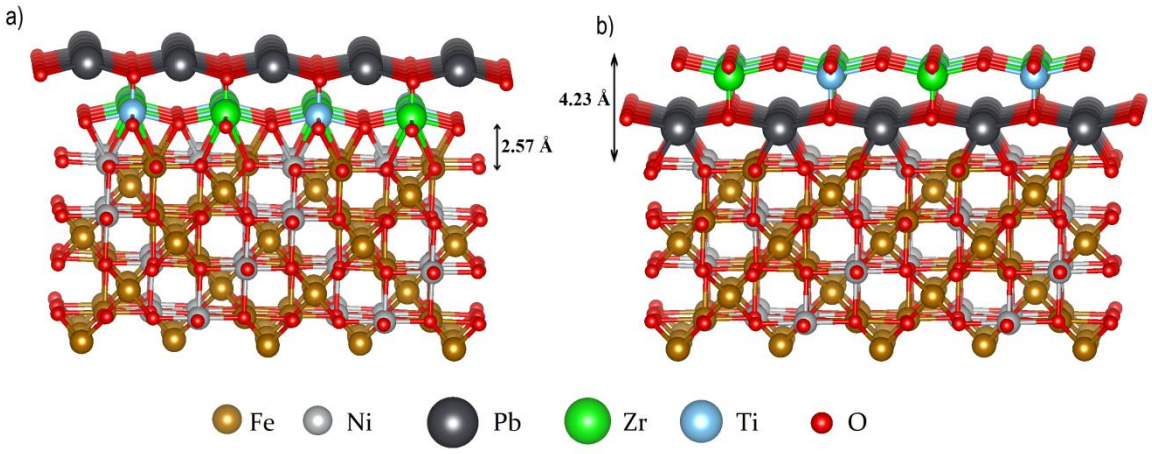

Figure.3.2: The atomic structure of NFO/PZT (001): (a) structure with NFO/ZTO interface, (b) structure with NFO/PbO interface

3.3 Results and discussion:

3.3.1 Structural, magnetic and electronic properties:

The optimized structures of tetragonal supercells $PbZr_{0.5}Ti_{0.5}O_3$ and $NiFe_2O_4$,in bulk form, are shown in **Figure.3.1(a,b)**. For the $NiFe_2O_4$, our calculations predicted a cubic structure with a lattice parameters of a =8.236 Å. This value is in line with the experimental one (a_{exp} = 8.337Å) reported in reference [188]. While the computed lattice parameters of the bulk PZT are: a = 4.017 Å and c = 4.251Å in the case of the tetragonal symmetry. The obtained values are closer to the experimental ones reported for PZT films (a = 4.030 Å and c = 4.145 Å) [6]. In the other hand, the heterostructure of $NiFe_2O_4$/PZT are built by stacking PZT on the top of NFO. Two different interface terminations of PZT are considered, $(Zr_{0.5}Ti_{0.5})O_2$- termineted and PbO-terminated PZT surfaces at $NiFe_2O_4$/PZT interface, denoted as NFO/ZTO and NFO/PbO stacking, respectively (see **Figure.3.2(a,b))**. The mismatch between $NiFe_2O_4$ and PZT is found to be around 2.18 %, which is reasonably low. The computed lattice parameters for NFO/ZTO and NFO/PbO interface are a =8.084 and 8.162 Å, respectively.

The magnetic moment of the ferrimagnetic $NiFe_2O_4$(bulk) was found to be -3.98/4.01μ_B per Fe(B)/Fe(A) atoms and 1.55 μB per Ni atoms. This value is found to be changed at the NFO/PZT and NFO/PbO interfaces, as listed in the **table.1**. Our theoretical magnetic moment values is in good agreement with the experimental magnetic moment of 4.73μ_B/Fe [193] and in accordance with some other first principle studies[194], [195]. It is worth mentioning that the induced magnetic moments on the interface O, Zr and Ti atoms at the NFO/ZTO interface are: 0.064, 0.05 and 0.21 μ_B, respectively. These values are larger than those calculated in NFO/PbO. The Zr, Ti, and O atoms are in the nearest layers for NFO/ZTO. While for NFO/PbO, the Zr, Ti and O atoms are the next nearest layers. The calculated bond lengths between NFO and ZTO layers are 2.57 (Å) and 4.23 (Å) for NFO/ZTO and NFO/PbO interfaces, respectively. In fact, the large bond lengths between NFO and ZTO layers in NFO/PbO interface leads to the reduction of the induced magnetic moments on O, Zr and Ti atoms in NFO/PbO interface (see **table.3.1**). Notice that the

spontaneous polarization of bulk PZT was found to be 68.5 μC/cm^2. This value agree well with the polarization of PZT obtained in previous experimental and theoretical studies [196], [197].

Table.3.1: magnetic moments in (μ_B)for the bulk NiFe2O4 and NiFe2O4/PZT interface.

		Ni	Fe(A)	Fe(B)	O	Ti	Zr
Bulk	this work	1.55	-3.98	4.01	-	-	-
	Exp[192]	2.2	-4.86	4.73	-	-	-
	Ref [193]	1.54	-3.99	4.09	-	-	-
	Ref [194]	1.71	-4.13	4.22	-	-	-
NFO/ZTO	this work	1.08	-3.52	3.73	0.064	0.21	0.05
NFO/PbO	this work	1.12	-3.55	3.78	0.03	0.009	0.0001
$Fe_3Ga/BaTiO_3/Fe_3Ga$	Ref [174]	-	2.59	-	0.042	-0.25	-
Co/PZT	Ref [182]	-	-	-	-	-0.292	-0.14
$Fe_3O_4/BaTiO_3$	Ref [175]	-	-3.53	3.70	-0.11	0.35	-

The calculated total and partial electronic density of states (TDOS and PDOS), for $NiFe_2O_4$ and PZT, are shown in **Figure.3.3 (a,b).** For PZT, it is found that the density of states of the Ti, Zr and O are strongly hybridized between 0 and -5 eV, also a weak overlapping of Pb-6s and O-2p states between -2 eV and 0 eV was observed. The hybridization between the Ti and Zr with O leads to the short-range repulsions and enhance the stability of the ferroelectric phase of PZT, which means that the ferroelectricity is manly originated from the interaction between the Ti, Zr and O ions [197]. The predicted band gap for PZT is 2.87 eV, which is in good agreement with the experimental optical gap (3.4 eV), measured in PZT films[198]. A band gap of 3.3 eV and 1.4 eV were obtained for spin-up and spin-down states in the $NiFe_2O_4$ using GGA+U calculations, indicating that $NiFe_2O_4$ is insulating. Moreover, the PDOS of $NiFe_2O_4$ indicates that the 3d states of cations (Fe and Ni) hybridize strongly with the O-2p states for both spin up and down states in the top of the valence band. In addition, Ni-3d states shows a sharp peak at -6 eV below the fermi level, between -8 to -6 eV is dominated by spin up of Fe3-d states with an addmixture of O-2p. The conduction band is occupied by the hybridation of spin down of Fe-3d and O-2p states between 1 to 3 eV, while the top of the conduction band is principally among the contribution of the hybridizations of the spin up of Ni-3d and O-2p states.

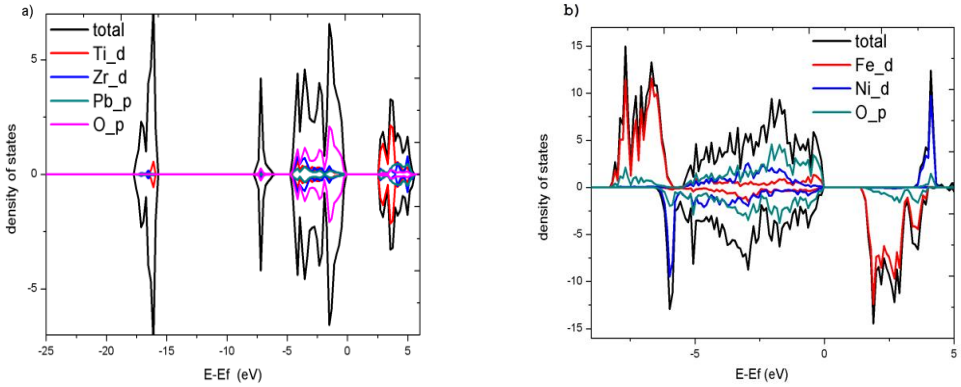

Figure.3.3: Total and partial density of states of PZT **(a)**and $NiFe_2O_4$**(b).**

The PDOS of the interface atoms for NFO/ZTO and NFO/PbO interfaces are illustrated in **Figure.3.4 (a,b).** In the case of NFO/ZTO interface, the conduction band

minimum is principally among the contribution of the strong hybridizations of Fe-3d (spin down), Ni-3d, Zr-3d and O-2p states between 0 to 5 eV above the Fermi level. Moreover, the valence band maximum is composed of the O-2p, Ni-3d and Zr-3d states with small admixture of Fe-3d and Ti-3d states between -5 to 0 eV. We note that these hybridizations are not presented in NFO/PbO interface because its interfacial atoms Pb and O show weaker hybridizations. Both of NFO/ZTO and NFO/PbO interfaces, spin up of Fe-3d are located at -9 eV, which is hybridized with the O-2p state. In addition, the main Pb-3d valence band is found at around
-16.5 eV.

From the obtained results, we can see that both spin up and spin down states of Fe-3d, Ni-3d, Zr-3d and O-2p shift toward the Fermi level in comparison to the bulk behavior. As a result, the NFO/PZT interface becomes conducting. Thus, indicating that the conductivity of $NiFe_2O_4$/PZT interface influenced by the interfacial atoms. In addition, the partial DOS of the interface Fe, Ni, Ti, Zr and O atoms in the NFO/PbO and NFO/ZTO interfaces, show a remarkable differences with their corresponding states of the bulk (see **Figure.3.4a and Figure.3.4b)**, indicating the strong overlapping between states of interfacial atoms (see **Figure.3.5(a,b).** As a result, formation of exchange-split bonding and antibonding states between 3d-3d and 3d-p orbitals, leading to an induced magnetic moments on the interfacial O, Zr and Ti atoms at the interfacial NFO/ZTO. The induced magnetic moment on the O, Zr and Ti atoms are 0.064, 0.05 and 0.21 μ_B, respectively (see **table.3.1**). This is consistent with the previous calculations reported by C.G. Duan et al [85] in Fe/$BaTiO_3$, using the first-principles and other theoretical results.

a) NFO/PbO

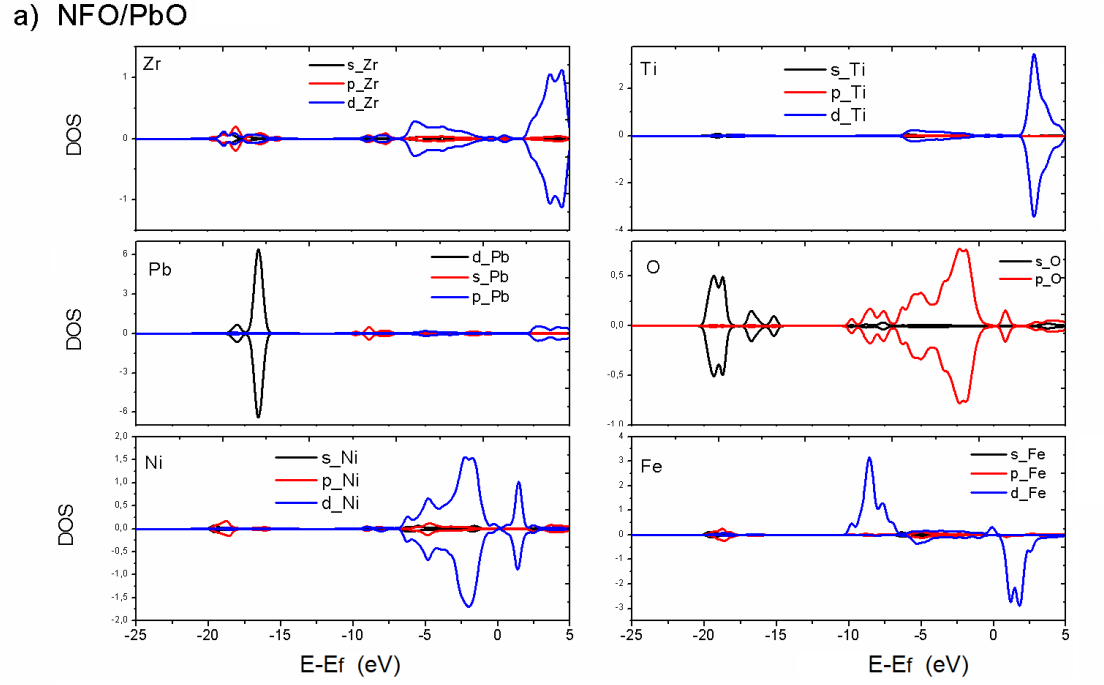

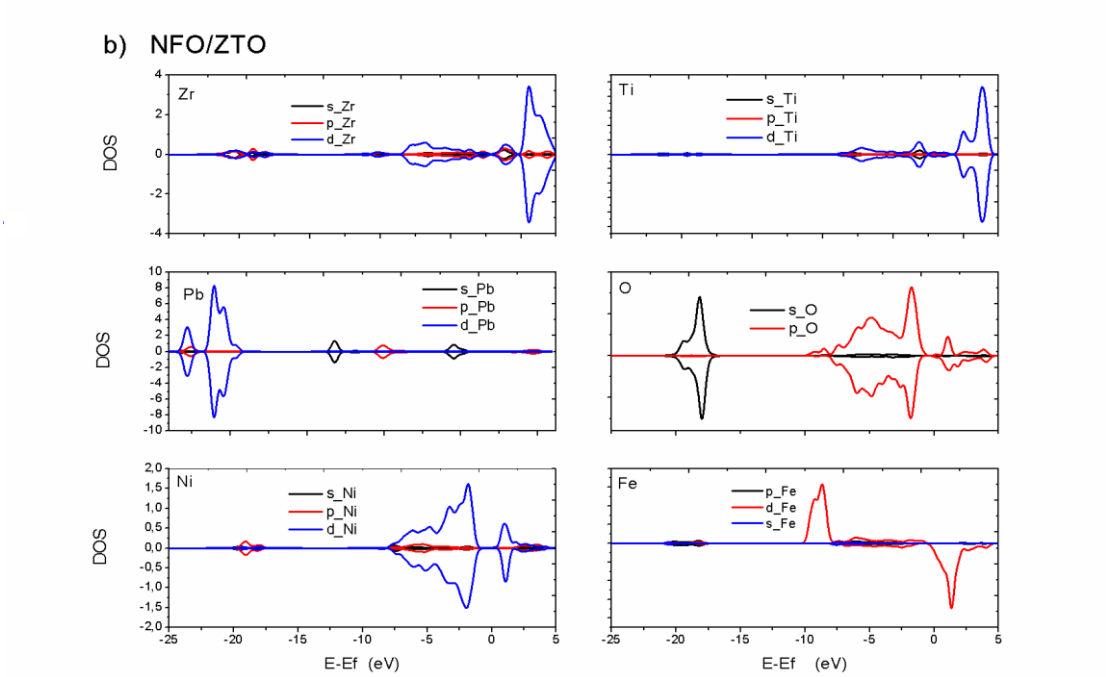

Figure.3.4: Partial density of states (PDOS) of the interface atoms in $NiFe_2O_4$/PZT interface, **(a)** PbO-terminated PZT(001), **(b)** $(Zr_{0.5}Ti_{0.5})O_2$-terminated PZT(001). The Fermi level is set to zero energy.

3.3.2 Cohesive energy:

In order to understand the mechanism of the high magnetoelectricity of $NiFe_2O_4$/PZT reported in [19], we calculated the work of separation that quantifies the energetics of adhesion between $NiFe_2O_4$ and PZT [199]. We have considered both of PbO and $(Zr_{0.5}Ti_{0.5})O_2$terminations of the PZT layer. The interfacial separation work is defined as [85]:

$$Wsep = (E_{NiFe2O4} + E_{PZT} - E_{NiFe2O4/PZT})/A \quad (1)$$

Where $E_{NiFe2O4/PZT}$ is the total energy of the heterostructure, $E_{NiFe2O4}$ and E_{PZT} are the energies of the same structure containing relaxed single slab of either $NiFe_2O_4$ and PZT, and A is the surface area of the interface.

The calculated interfacial separation work in the NFO/PbO and NFO/ZTO interfaces are 0.733 and 0.469 J/m^2, respectively (see **table.3.2**). We show that the separation work of NFO/ZTO interface is greater than its value found in NFO/PbO interface, indicating that the NFO/ZTO interface is energetically more favorable than NFO/PbO interface. Hence, the formation of the heterostructures are exothermic from the thermodynamic point of view. We note that in a previous study of Fe/BaTiO3 heterostructure, it is found that the TiO2-terminated surface of BaTiO3 is more energetically favorable over BaO-terminated surface at the Fe/BaTiO3 interface[85]. The calculated values are closer to the work of separation (0.8 J/m2) reported by I. I. Oleinik et al.[199] in $Co/SrTiO_3/Co$ structure with SrO on top of Cobalt.

Table.3.2: Cohesive energies in J/m^2 $(Zr_{0.5}Ti_{0.5})O_2$-termineted and PbO-termineted PZT surfaces at $NiFe_2O_4$/PZT interface.

Interface	Cohesive energies in J/m^2
$NiFe_2O_4$-$(Zr_{0.5}Ti_{0.5})O_2$	0.733
$NiFe_2O_4$-PbO	0.469

3.3.3 Magnetoelectric effects :

For both interface terminations, the magnetic moments of the atoms at the interface NFO/PZT undergo a change by reversing the polarization of PZT. We quantify the magnetoelectric effect using the definition of interface magnetoelectric coefficient [175]:

$$\alpha_s = \frac{\mu_0 \Delta M}{E_c} \tag{3.2}$$

where Ec is the coercive field of the ferroelectrics and μ_0 is the vacuum permittivity. For not too large electric fields, the relationship between the electric field and the induced magnetization is linear [200]. we consider that the polarization of PZT can be switched at the coercive field of Ec=100kV/cm [201] which resulting in the change of magnetic moment at the $NiFe_2O_4$/PZT interface. The change of magnetic moment ΔM for the NFO/PbO and NFO/ZTO interfaces are 0.15 and 0.9 μ_B, respectively. Our calculations predict that the interface magnetoelectric coefficient for both of NFO/ZTO and NFO/PbO interfaces are $\alpha_s = 3{,}15 \times 10^{-10}$ and 0.52×10^{-10} G.cm/V respectively. These values are of the same order in magnitude with the calculated magnetoelectric coefficient (6.7×10^{-10} G.cm/V) in Ni/$PbTiO_3$ heterointerface [202], and with 2.3×10^{-10} G.cm/V in Ni/$BaTiO_3$ system [178].

As demonstrated in M/BaTiO3 (M = Ni, Fe) system [178], the electronic origin of the magnetoelectric effect in Ni/BaTiO3 interface is due to the hybridization of orbitals of interface atoms. Therefore, the magnetoelectric coupling arises from the interface in NFO/PZT heterostructure and it induces by the interface bonding. In addition, the stronger bonding in the NFO/ZTO interfacial layers will inevitably increase the cohesive energy between the NFO and PZT layers, which is already evident from the results of work of separation (shown in Table 2). Obviously, the magnetoelectric coupling for the NFO/ZTO and NFO/PbO interfaces demonstrate that the magnetoelectric coupling depends strongly on the bonding mechanisms at the interface.

In order to understand the difference between the calculated magnetoelectric coefficient in NFO/ZTO and NFO/PbO interfaces, we display a partial density of states of interface atoms as shown in **Figure.3.5(a,b).** The valence band maximum of NFO/ZTO interface is composed by the hybridation of Fe-3d, Ni-3d,Zr-3d, Ti-3d and O-2p states. As a result, the formation of exchange-split bonding and antibonding states between 3d-3d and 3d-p orbitals, which is responsible and leads to an induced magnetic moments on the interfacial Ti, Zr and O atoms. Thus, the hybridation of Fe-3d, Ni-3d,Zr-3d, Ti-3d and O-2p orbitals increase the cohesive energy and magnetoelectric coefficient at NFO/ZTO. While, in NFO/PbO interface, we show that the main Pb-3d valence band is found at around -16.5 eV. This value is a deeper energy, indicating that the Pb-3d is not linked with the interfacial atoms. Probably, by an intermediate bonding via O, which leads to decrease of the cohesive energy and the change magnetic moment, as a result, magnetoelectric coefficient reduced. Thus, we conclude that the electronic origin of the large magnetoelectric coupling at NFO/ZTO interface is due to the hybridizations of orbitals of interface Ni, Fe, T, Zr, O atoms.

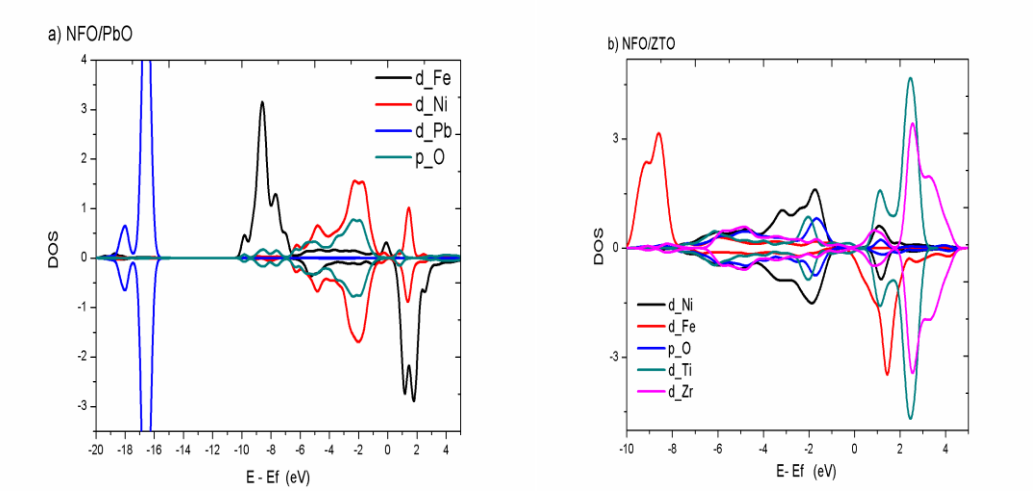

Figure.3.5 : Partial density of states (PDOS) of interfacial atoms in $NiFe_2O_4$/PZT interface, **(a)**NFO/PbO interface , **(b)** NFO/ZTO interface, the Fermi level is set to 0 eV.

3.4 Conclusion:

In summary, density-functional theory in framework of GGA+U was used to investigate the electronic, magnetic and magnetoelectric properties of $NiFe_2O_4/PbZr_{0.5}Ti_{0.5}O_3$ (001) heterostructure. Two different interfacial atoms NFO/ZTO and NFO/PbO are considered with the interfacial separation work of 0.733 and 0.469 J/m^2 for NFO/PbO and NFO/ZTO interfaces in NiFe2O4/PZT bilayer, respectively. These results indicating that the NFO/ZTO is energetically more favorable than NFO/PbO at the NiFe2O4/PZT interface. Interestingly, we found that magnetoelectric coupling in this heterostructure is strictly dependent on electronic properties and surface termination at the interface. The electronic origin of the large magnetoelectric coupling at NFO/ZTO interface is due to the hybridization of orbitals of interface Ni, Fe, T, Zr, O atoms. The calculated magnetoelectric coupling in $NiFe_2O_4$/PZT interface for NFO/ZTO and NFO/PbO are $\alpha_s = 3.15 \times 10^{-10}$ and 0.52×10^{-10} G.cm/V respectively, which are of the same order in magnitude with the calculated magnetoelectric coefficient reported in the literature. The presented theoretical results can provide proper guidance for magnetoelectric devices.

Chapter 4

Modelling of the ferroelectric and energy storage properties of $PbZr_{1-x}Ti_xO_3$ thin films using Monte Carlo simulation

4.1 Introduction:

Perovskite with formula $A(B'B'')O_3$ has been extensively studied and widely used in industry because of their excellent piezoelectric properties [203]. The most common perovskite in A(B'B")O3 family is the lead zirconate titanate $PbZr_{1-x}Ti_xO_3$ (PZT), due to its interesting properties compatible with various device applications, such as sensors, nonvolatile random access memories, electro-optic modulators, capacitors, detectors and micro-electro-mechanical systems[204]. It worth noting that PZT was, and still, a focal point of research due to its large remanant polarization, piezoelectric constant, high dielectric constant and low operation voltage [198]. It is important to provide insight into the performance and polarization switching of this material in order to widen the range of operating conditions of PZT based devices. Recall that this system can undergoes gradual phase transition with different behavior: classical ferroelectrics (FE), antiferroelectrics (AFE) and relaxor ferroelectrics (RFE). Especially, the AFE state attracts much attention for the potential application in high-energy storage capacitors [4], $PbZrO_3$-based antiferroelectric materials with high-saturated polarization and low remanent polarization leading to good energy storage properties [5]. For examples, TiO_2/PZT nanowire exhibits an energy storage density of 7 J/cm^3[6], Zhang et al. reported an energy storage density of 63.7 J/cm^3 in PZT/Al_2O_3/PZT heterojunction [7]. Further, X. Hao et al.[8] showed that Sr doped $PbZrO_3$ promoted the recoverable energy density to 14.5J/cm^3. Furthermore, the energy storage densities values of undoped and Eu-doped $PbZrO_3$ thin films are reported to be 14.5J/cm^3 and 18.8 J/cm^3, respectively [9].

In the other hand, many theoretical methods are used to investigate ferroelectric properties, such as, atomistic models methods [205], Ginzburg–Landau [206], constitute models [207], effective Hamiltonians fit to the first-principles [208], and Monte Carlo simulation [15]. Numerous research efforts have been employed to simulate ferroelectric

behavior using Monte Carlo simulation based on the DIFFOUR Hamiltonian [209], [210]. In this context, Y. Laosiritaworn et al. [211] investigated the effect of uniaxial stress on of the hysteresis behavior of ferroelectric films. Recently, Y. Benhouria et al. studied the dielectric properties of Ising ferrielectric nanowires with spin-3/2 core and spin-5/2 shell structure under an external longitudinal electric field by Monte Carlo simulation[212]. Further, S. Bin-Omran et al. applied the Wang-Landau Monte Carlo algorithm within an effective Hamiltonian approach to study the various properties of ferroelectric $BaTiO_3$[213].

The present study concerns the investigation of the ferroelectric properties of $PbZr_{1-x}Ti_xO_3$ using Monte Carlo simulation. We propose a new model to calculate the exchange coupling constants to approach the phase diagram, dielectric, ferroelectric and energy storage properties of $PbZr_{1-x}Ti_xO_3$ system.

4.2 Model and formalism:

Monte Carlo simulation within metropolis algorithm in the framework of Ising model has been used to study the ferroelectric properties of PZT [212]. PZT thin films with Zr-rich compositions crystallized under rhombohedral phase and changed to tetragonal phase for the Ti- rich compositions (see **Figure.4.1(a,b,c)**) [214]. The unit cells of PZT were assigned to an electrical dipoles in interaction between them, the results are carried out for a lattice contain N dipoles [215]. In the calculation, the cations Ti and Zr are randomly distributed in B-sites and dipole flips are accepted or rejected according to the Metropolis algorithm [216]. The size L of the system has been taken equal to 32, which is larger than the thermodynamic limit defined at 28 in such a system [217]. Periodic boundary conditions are applied in the x and y-directions and free boundary conditions are applied in the z-direction. typically running over 10^5 steps were used to reach the equilibrium in the system.

For PZT, the system is governed by the following Hamiltonian:

$$H = -\sum_{<ij>} J_{1tt} p_i p_j - \sum_{<ij>} J_{2tt} p_i p_j - \sum_{<ij>} J_{1zz} \sigma_i \sigma_j - \sum_{<ij>} J_{2zz} \sigma_i \sigma_j - \sum_{<ij>} J_{1tz} p_i \sigma_j - \sum_{<ij>} J_{2tz} p_i \sigma_j - 2\mu E \sum_i (\sigma_i + p_i) \quad (4.1)$$

In case of $PbTiO_3$, the Hamiltonian (1) becomes:

$$H_1 = -\sum_{<ij>} J_{1tt} p_i p_j - \sum_{<ij>} J_{2tt} p_i p_j - 2\mu E \sum_i p_i \quad (4.2)$$

For a pure $PbZrO_3$, we found from the Hamiltonian (1) the following expression:

$$H_2 = -\sum_{<ij>} J_{1zz} \sigma_i \sigma_j - \sum_{<ij>} J_{2zz} \sigma_i \sigma_j - 2\mu E \sum_i \sigma_i \quad (4.3)$$

Where, $p = \pm 2, \pm 1, 0$ and $\sigma = \pm 1, 0$ denote dipole moments of $PbTiO_3$ and $PbZrO_3$, respectively. J_{1tt} and J_{1zz} are the coupling constants between two first nearest neighbors dipoles p_i-p_j and σ_i–σ_j of $PbTiO_3$ and $PbZrO_3$, respectively. J_{2tt} and J_{2zz} are the coupling constants between two second nearest neighbors dipoles p_i-p_j and σ_i–σ_j for $PbTiO_3$ and $PbZrO_3$, respectively. J_{1tz} and J_{2tz} are the coupling constants between two first neighbors and two second nearest neighbors dipoles p_i-σ_j of $PbTiO_3$ and $PbZrO_3$, respectively (see **Figure.4.1 (d.f.h)).** The effective dipole moment is μ and E represents external electric field. The parameters; Polarizations (P), dielectric susceptibility (χ), Internal energy of the system (E) and Specific heat (C_v) computed from Monte carlo simulation [216] are given by:

- $P = \frac{1}{N}\sum_i^N p_i (4.4)$
- $\chi = \frac{N}{K_B T}(\langle p^2 \rangle - \langle p \rangle^2)$ (4.5)
- $E = \sum_i^N \varepsilon_i(p_i)$ (4.6)
- $C_v = \frac{N}{K_B T}(\langle \mathrm{E}^2 \rangle - \langle \mathrm{E} \rangle^2)$ (4.7)

Where $N = L^3$ represents the total number of dipole moments in lattice, K_B is the Boltzmann constant chosen to be equals 1 and ε_i is the internal energy per site.

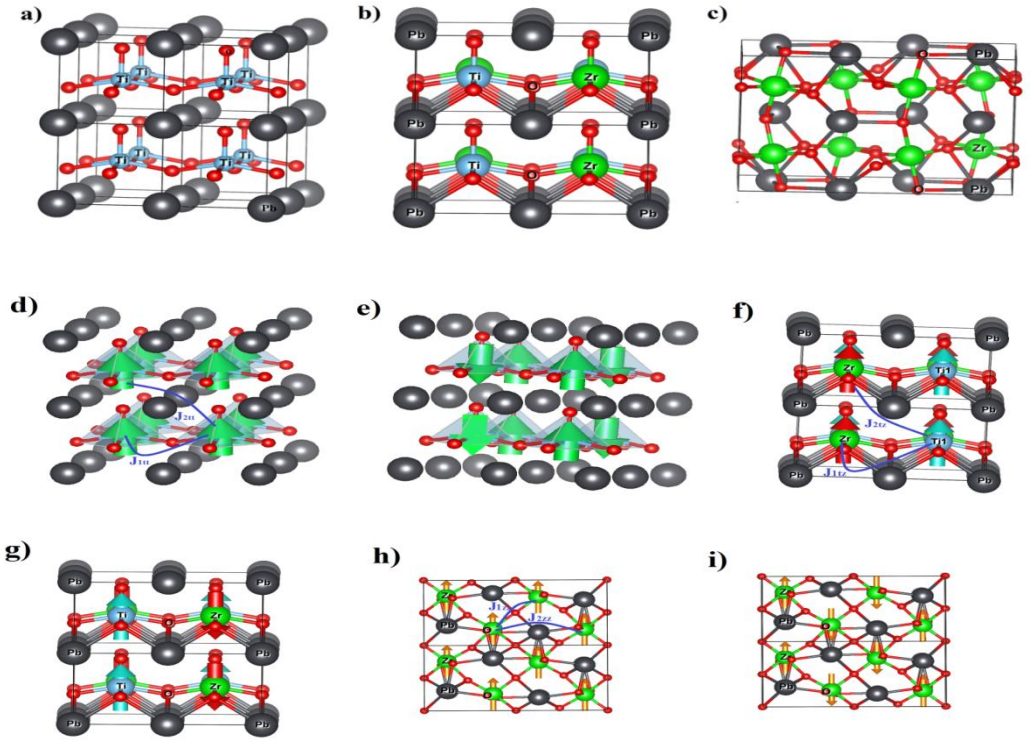

Figure.4.1 *: layered structure of (a) $PbTiO_3$, (b) PZT and (c) $PbZrO_3$, (d,f,h) ferroelectric and (e,g,i) antiferroelectric configurations for $PbTiO_3$, PZT and $PbZrO_3$ respectively.*

The Hamiltonians (1), (2) and (3) are applied on ferroelectric and antiferroelectric configurations to calculate the exchange coupling constants (J_{1tt}, J_{2tt}, J_{1zz}, J_{2zz}, J_{1tz} and J_{2tz}) in ferroelectric $PbZr_{1-x}Ti_xO_3$ (see **Figure.4.1(d-i)**).

The energy of the dipole-dipole interaction in ferroelectric structure calculated using the atomistic approach reported in [218], the expression of energy per site is given by:

$$E = 2\pi P^2 \tag{4.8}$$

An adjustable parameter α should be introduced ($J_{1tt}=\alpha J'_{1tt}$, $J_{2tt}=\alpha J'_{2tt}$, $J_{1zz}=\alpha J'_{1zz}$, $J_{2zz}=\alpha J'_{2zz}$, $J_{1tz}=\alpha J'_{1tz}$ and $J_{2tz}=\alpha J'_{2tz}$) to find the exchange coupling constants corresponding to the experimental Curie temperature T_c^{exp}.

4.3 Results and discussion :

4.3.1 Ferroelectric properties:

The values of the exchange coupling constants and the corresponding Tc for PZT, at different values of the parameter α, are presented in **Table.4.1**. At α=83, the simulated Curie temperature was close to experimental Curie temperature reported in [32-34], and the exchange coupling constants corresponding to the experimental Curie temperature were found equal to J_{1tt}= 6.915 (meV), J_{2tt} =3.457 (meV), J_{1zz} = 4.542 (meV), J_{2zz} =2.271 (meV), J_{1tz} = 5.947 (meV) and J_{2tz} =2.973 (meV). Yaxuan Cai et al [219] predicted by first-principles calculations the exchange coupling constants (J= 0.1 eV) in ferroelectric Trichloroacetamide. The finding value is bigger than that found in the present work, may be due to large energy barrier between the centric structure of paraelectric phase and the polar structure of ferroelectric phase.

Table.4.1: *values of exchange coupling constant and Tc calculated by Monte Carlo simulation for different values of parameter α.*

	Exchange coupling constants (meV)						Curie temperature (K)		
A	J_{1tt}	J_{2tt}	J_{1zz}	J_{2zz}	J_{1tz}	J_{2tz}	PbT_iO_3	PbZ_rO_3	$PbZr_{0.5}Ti_{0.5}O3$
0.75	6.248	3.121	4.701	2.050	5.370	2.684	**719**	**473**	**612**
0.83	**6.915**	**3.457**	**4.542**	**2.271**	**5.947**	**2.973**	**790=T_c^{exp}**	**533=T_c^{exp}**	**660=T_c^{exp}**
0.90	7.497	3.748	4.924	2.462	6.448	3.223	**872**	**569**	**714**
Ref [219]	**100 (meV)**								

Figure.4.2a shows the polarization as a function of the temperature of $PbZr_{1-x}Ti_xO_3$ (x=0, 0.5, 1) thin films. At low temperatures, The results show that the polarization starts

from a maximum and decreases and then vanishes when the temperature is bigger than the critical temperature (Tc), which indicates that the $PbZr_{1-x}Ti_xO_3$ (x=0, 0.5, 1) thin films undergo a phase transition from the ferro/antiferro-electric phase to the paraelectric phase [220]. This transition is showed in the dielectric susceptibility [213], which exhibits a peak at critical temperature (see **Figure.4.2b**). In addition, Critical temperature (Tc) presented a value close to 530 K, 690K and 790K for x=0, 0.5, and 1, respectively, which is in good agreement with the experimental reports[221], [222].

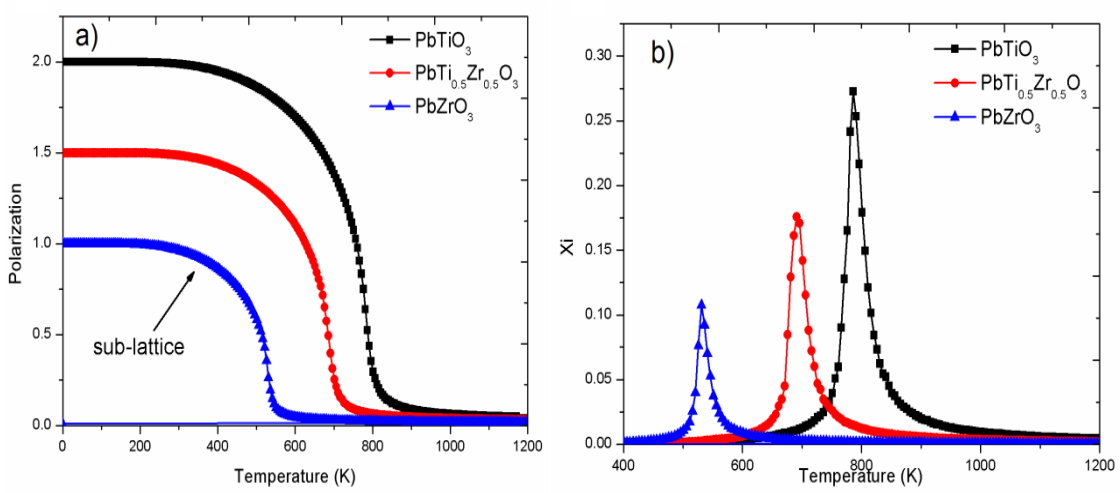

Figure.4.2. *Temperature dependence of:**(a)** the polarization, **(b)** dielectric susceptibility of $PbZr_{1-x}Ti_xO_3$ thin films for x=0, 0.5, 1.*

The phase diagram of critical temperature (Tc) as a function of the concentration value x % of T_i in PZT have been predicted using Monte Carlo Simulation (see **Figure.4.3**). At room temperature, the crystal structure is tetragonal on the Ti-rich and rhombohedral on the Zr-rich. When the temperature rises, a center of symmetry appears in both structures, the structure is transformed to a cubic phase, and it loses its spontaneous polarization. The calculated phase diagrams is in good agreement with experimental results reported by Noheda et al [6] and Jaffe et al [103].

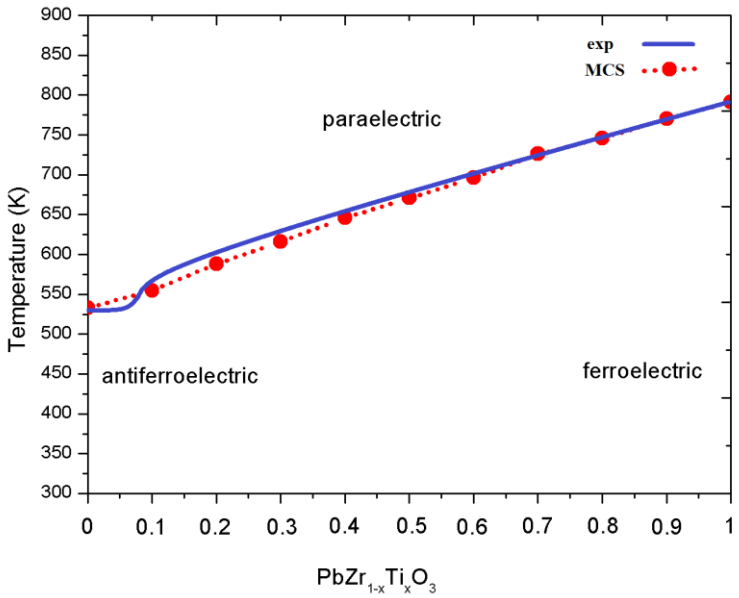

***Figure.4.3**: Calculated $PbZr_{1-x}Ti_xO_3$ phase diagram shown in red dots and experimental phase diagram of $PbZr_{1-x}Ti_xO_3$ thin films adapted from* [221] *(shown in blue).*

In ferroelectric materials, the most interesting property is the polarization switching. **Figure.4.4(a-b)** presents the hysteresis loops of $PbZr_{0.5}Ti_{0.5}O_3$, $PbZrO_3$ and$PbTiO_3$ thin films at 300K. For both positive and negative external electrical field values, we observed that the polarization curves are symmetric. In addition, the area of hysteresis loops becomes narrower as the content of Zr in PZT increases. For x=0, $PbZrO_3$ thin films was in the antiferroelectric state, evidenced by the presence of a double hysteresis loop with zero remanent polarization. While increasing x values, a weak ferroelectricity is observed for $PbZr_{0.9}Ti_{0.1}O_3$ and $PbZr_{0.8}Ti_{0.2}O_3$. However, beyond x=0.3, a typical ferroelectric hysteresis loops are observed, indicating that the PZT film was in its ferroelectric state. **Figure.4.5 (a-b)** shows the saturation polarization (P_s), the remanent polarization (P_r), and the coercive field(E_c) (determined from the simulated hysteresis loops) as a function of x value. We note that P_s and P_r polarizations exhibit an increase with increasing x values. In addition, when x values increase, the exchange coupling between dipole moments at Zr-Ti and Ti-Ti sites increase in $PbZr_{1-x}Ti_xO_3$. As a result, the area of hysteresis loops becomes large, thus the coercive field E_c augmented. The calculated values of coercive field are Ec=45, 95, 140 and 275 kV/cm for x=0.3, 0.5, 0.6 and 1, respectively. The obtained values are in good agreement with experimental results reported by Isaku Kanno et al [8] in (001) $PbZr_{1-x}Ti_xO_3$ epitaxial films grown on $SrTiO_3$ substrates using radio-frequency sputtering technique. Also, agree well with the results of Morita et al. [9] reported on highly epitaxial (001) $PbTiO_3$ films grown on a $SrRuO_3/SrTiO_3$ substrate by a hydrothermal process.

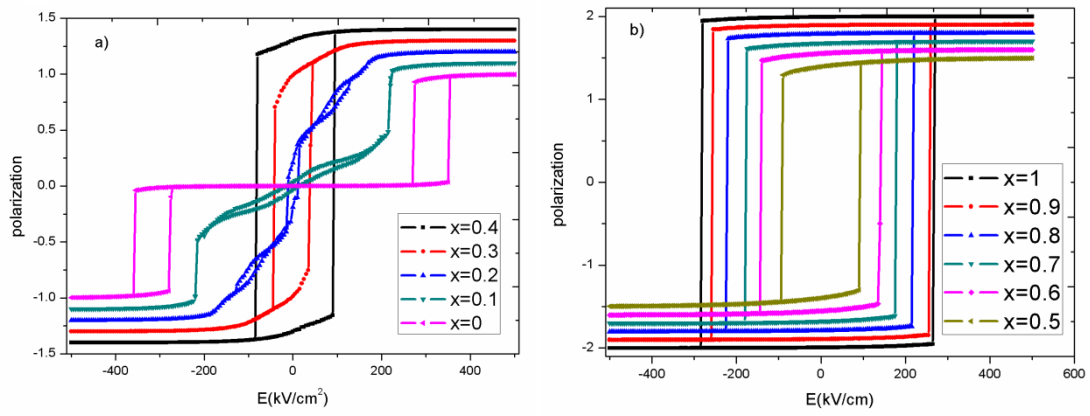

Figure.4.4. *P–E hysteresis loops of $PbZr_{1-x}Ti_xO_3$ thin films (a) :x=0, 0.1, 0.2, 0.3, 0.4 and (b) : x=0.5, 0.6, 0.7, 0.8, 0.9, 1. at 300 K.*

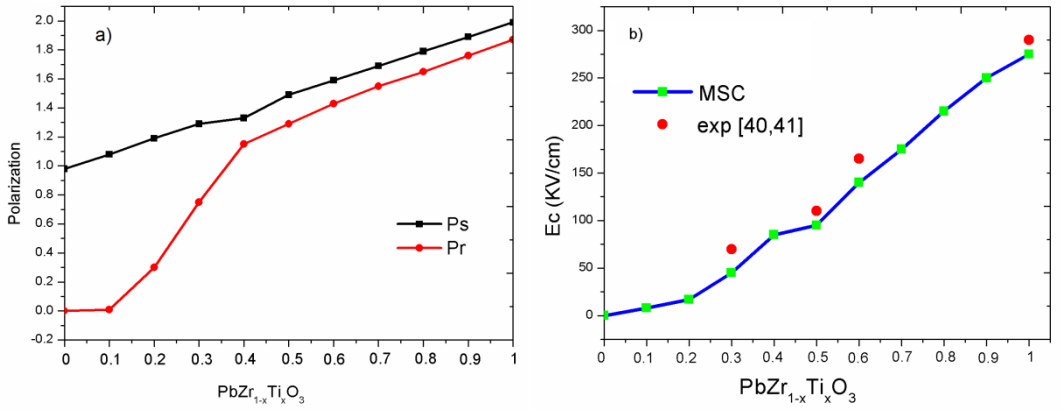

Figure.4.5 *:**(a)** remanent polarization (Pr) and saturation polarization (Ps), **(b)** coercive field of $PbZr_{1-x}Ti_xO3$ thin films as a function of x value at 300(K) in comparison with some experimental results taken from references* [8], [9], *represented by red dots in the figure.*

Figure.4.6 shows hysteresis loops of $PbZr_{0.5}Ti_{0.5}O_3$ thin films at different temperatures. As shown in the figure, the area of hysteresis loops becomes narrower as the temperature increases and then vanishes at critical temperature. The shape of calculated hysteresis loop presents a single central loop which look like a regular shape characteristic for ferroelectric materials [223]. **Figure.4.7a** plotted the temperature dependence of remanent polarization (Pr), which started from a maximum at low temperature and decreased when the temperature increased, and finally vanished at critical temperature Tc. The evolution of coercive field as a function of temperature is presented in **Figure.4.7b**. We can observe that the coercive field decreases with increasing the temperature. The calculated coercive field values are in strong agreement with the experimental reported by F. Xu et al [224] and Morita et al[9]. Notice that above the critical temperature, the remanent polarization and coercive field vanished becausethe $PbZr_{0.5}Ti_{0.5}O_3$ is in its paraelectric state.

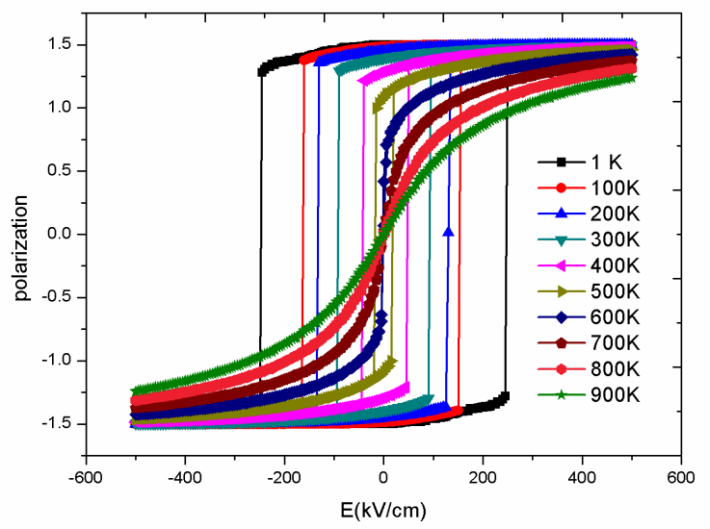

Figure.4.6 : Hysteresis loops of $PbZr_{0.5}Ti_{0.5}O_3$thin films at different temperatures.

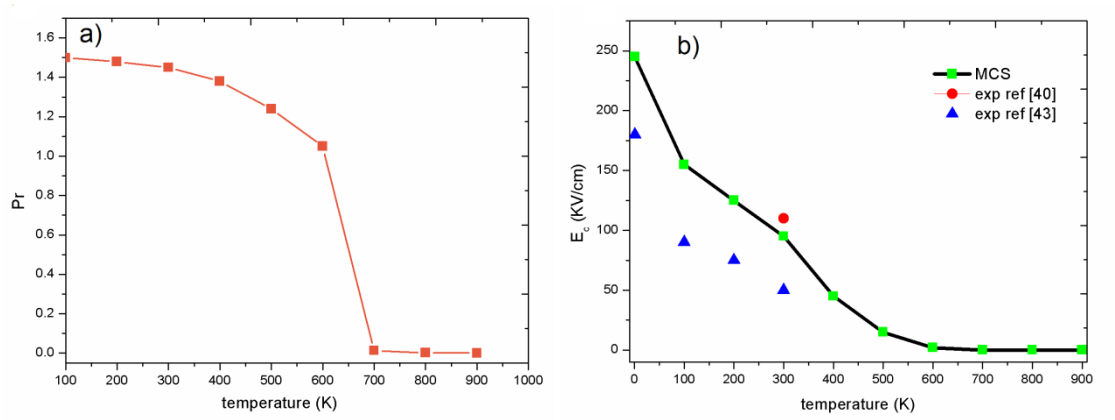

Figure.4.7: variation of the remanent polarization(a) and coercive field (b) of $PbZr_{0.5}Ti_{0.5}O_3$ thin films as a function of the temperature in comparison with the experimental results reported in [8], [225].

4.3.2 Energy storage properties:

Another important parameter in the ferroelectric/antiferroelectric materials is the recoverable energy storage density, which can be enhanced by increasing the maximum polarization (P_m) with a lower remanent polarization (P_r). Such behavior is in adequate with ferroelectric relaxor and antiferroelectric materials. The recoverable energy storage density (W_{reco}) is calculated from P-E loops with the following expression [226]:

$$W_{reco} = \int_{P_r}^{P_m} EdP \tag{4.9}$$

where E is the applied electric field, P_m is the maximum polarization, and P_r is the remanent polarization. Another interesting parameter is the energy density efficiency (η). It could be calculated also from the PE hysteresis using the following equation [226]:

$$\eta = \frac{W_{reco}}{W_{reco} + W_{loss}} \times 100 \qquad (4.10)$$

Where W_{reco} is the recoverable energy storage density and W_{loss} is the energy density loss (W_{loss} is integral of the area enclosed by the P–E loop and y-axis).

For the energy storage calculations, the maximum of polarization for x=0 ($PbZrO_3$) and x=1 ($PbTiO_3$) of 50 µC/cm^2 and 90 µC/cm^2 are selected to have the same order of magnitude as the experimental results**. Figure.4.8a** shows the ΔP as a function of x value in PZT thin films (ΔP = Pm−Pr, ΔP is the difference between the maximum polarization (Pm) and the remanent polarization (Pr)). For $PbZrO_3$ (x=0), ΔP has the relatively high values of 49 µC/cm^2. By increasing the x value, the ΔP rises and reaches a maximum of 53.6 µC/cm^2 at x=0.1 and then declinesto9 µC/cm^{2}at x=0.4. **Figure.4.8b** presents the recoverable energy density as a function of x values in the PZT system at 300K, which decreases rapidly with increasing x value. Above x=0.3, recoverable energy density becomes weaker. Also, at x=0.3, typical ferroelectric P–E hysteresis loops were observed, indicating that the PZT film is in ferroelectric states (see **Figure.4.4(a-b)).** The maximum of the recoverable energy density is 13.93 J/cm^3 in $PbZrO_3$ (x=0) which is closer to the experimental results (14.5J/cm^3) reported in[227]. The calculated energy density efficiency as a function of x value in PZT thin films at 300K is plotted in **Figure.4.8c**.We note that the energy density efficiency rises with increasing x value and reaches its maximum value of 94% at x=0.1 with W_{reco}=9.74 J/cm^3, then it decreases rapidly. Above x=0.3, the energy density efficiency is less than 10%, because the PZT thin films are dominated by the ferroelectric phases which leads to increase the W_{loss}. Thus, the energy density efficiency decreases.

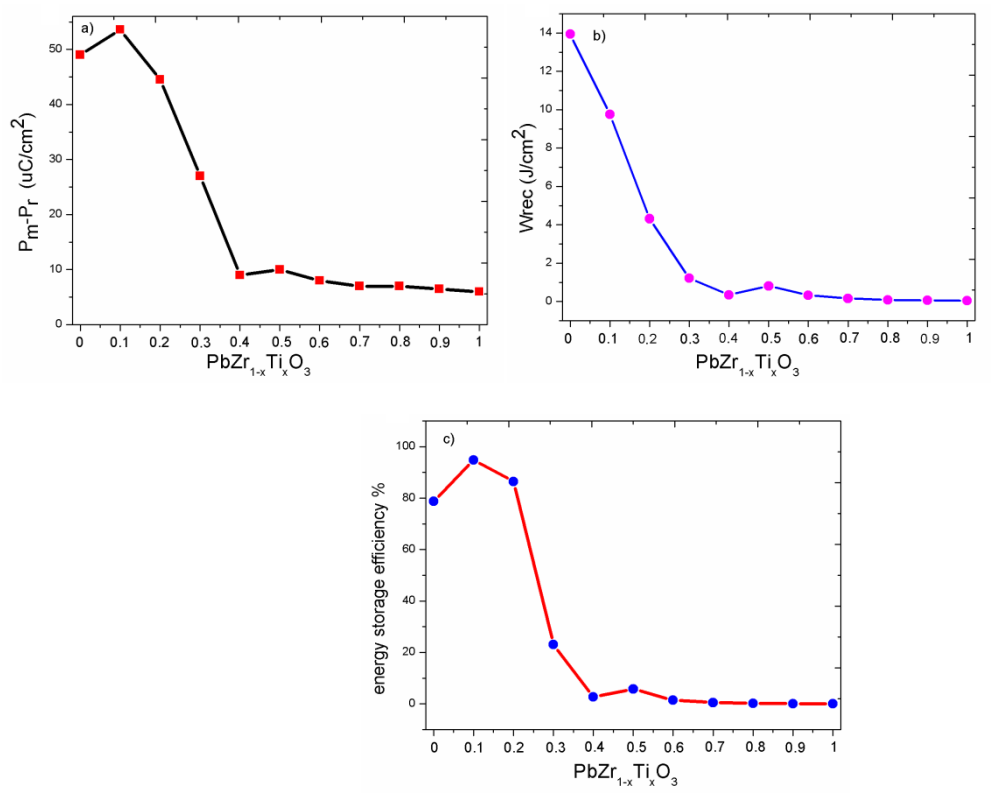

Figure.4.8 :(a) *$\Delta P=P_m-P_r$,* ***(b)*** *recoverable energy density,* ***(c)*** *energy storage efficiency as a function of x value in PZT thin films at 300K.*

4.4 Conclusion:

In summary, we have investigated the ferroelectric and energy storage properties of PZT by Monte Carlo simulation. The calculated exchange coupling constants corresponding to the experimental curie temperatures were found equal to J_{1tt} = 6.915 meV, J_{2tt} =3.457 meV, J_{1zz} = 4.542 meV, J_{2zz} =2.271 meV, J_{1tz} = 5.947 meV and J_{2tz} =2.973 meV. Also, we have examined the influence of the temperature on hysteresis loops, P_r ,P_s, and coercive field (E_c) of $PbZr_{1-x}Ti_xO_3$ thin films. We note that the saturation polarization (P_s), remanent polarization (P_r), coercive field (E_c), and critical temperature (Tc) increased with increasing x values in $PbZr_{1-x}Ti_xO_3$ system. For $PbZr_{0.5}Ti_{0.5}O_3$ phase, we found that the remanent polarization (P_r) and coercive field (Ec) decreased with increasing the temperature and vanish at the critical temperature (Tc). Moreover, the obtained values of Curie temperature and coercive field (Ec) for $PbZr_{0.5}Ti_{0.5}O_3$ thin films are Ec=95 kV/cm and Tc=533K respectively, closer to the experimental results. Furthermore, at 300K, the recoverable energy densities of 13.93 J/cm^3 and 9.74 J/cm^3 were obtained in PZT for x=0 and 0.1, with an energy density efficiency of 78.73% and 94%, respectively, promising for high-energy storage capacitors applications.

Chapter 5

Monte Carlo simulation investigation of magnetoelectric coupling in MFe_2O_4/PZT/MFe_2O_4 (M=Ni,Co) at low dimensionality

5.1 Introduction:

Magnetoelectric (ME)materials that simultaneously possess both ferroelectricity and (anti-)ferromagnetism have received a great research interest due to their good magnetoelectric properties and their technological potential [40]. The magnetoelectric effect permits the possibility of controlling the electrical polarization by an applied magnetic field, or an induced magnetization under an electric field [42], [200]. Single-phase magnetoelectric materials present usually a weak magnetoelectric coupling or this coupling occurs at low temperatures [228]. Composing the ferroelectric and (anti-)ferromagnetic materials is another pathway to create and enhance the magnetoelectric effect through a stress/strain-mediated magnetoelectric coupling at the interface [1]. The direct magnetoelectric effect, which is the occurrence of an electrical polarization (P) when a magnetic field (H) is applied, it can be expressed by the equation: $\Delta P = \alpha \Delta H$, where, H is the external magnetic field and α is the magnetoelectric coefficient. In contrast, the converse magnetoelectric effect, i.e, the induced magnetization (M) by applying an external electric field (E), can be written as $\Delta M = \alpha \Delta E$ [229].

Moreover, magnetoelectric properties in multilayered thin-film heterostructures, which is one of the most promising magnetoelectric mechanisms, have attracted great research interests due to their strong magnetoelectric effect at room temperature and above[230].Also for their wide range of applications in spintronics, multistate memory devices, microelectronics, spin transport and optoelectronics[131]. Experimentally, several ME materials have been utilized to obtain a magnetoelectric effect through the thin film. G. Srinivasan et al [19] achieved a magnetoelectric voltage coefficient of 460 mV/(cm.Oe) in bilayers and 1500 mV/(cm.Oe) for multilayers based on nickel ferrite and lead zirconate titanate (NFO/PZT). In addition, ME voltage coefficient of 50 mV/(cm.Oe) for x=0 and 280 mV/(cm.Oe) for x=0.4 were achieved in $Co_{1-x}Zn_xFe_2O_4$/PZT thin films [81]. Z. Tang et al.[231] investigated the ME effect in lead-free $Bi_4Ti_3O_{12}$/CFO composite films. Further, K. Bi et al [183] studied the ME coupling in Ni–PZT–Ni trilayers and a ME voltage coefficient of 2.3V/(cm.Oe) was obtained. A large magnetoelectric voltage coefficient of 4680 mV/(cm.Oe) was yielded in PZT/Terfenol-D discs at room temperature by J. Ryu et al [80]. A ME inductor was presented by Liu et al. in Metglas/[011]$Pb(Mg_{1/3}Nb_{2/3})O_3$-$PbTiO_3$ multiferroic composites [232]. On the other hand, modeling effort was undertaken to investigate the ME properties, using the first-principles density functional calculations, J. Lee et al. [233] investigated the magnetoelectric coupling in Fe/$PbTiO_3$/Fe. Furthermore, X. Zhong et al.[234]observed a good magnetoelectric performance in Co/$BiFeO_3$ heterostructure.

Moreover, M/BaTiO3 (M = Ni, Fe) superlattices [178], $Co/BaTiO_3/Co$ [179], Co2MnSi/PbTiO3 (001) ultrathin bilayer [235], $La_{0.66}Sr_{0.33}MnO_3/\ PbZr_{0.2}Ti_{0.8}O_3$ heterostructures [180], $M/BiFeO_3$ (M = Co,Fe) superlattice [181] and Co/PZT (001) interface [182] were investigated by first-principles theory. By using the Monte Carlo simulation, I.F. Sharafullin et al.[236] have analyzed phase transitions and magnetoelectric behavior in ferromagnetic/ferroelectric superlattice. Z. Wang et al.[237] focused on the dielectric properties of the antiferroelectric/ferroelectric BiFeO3/YMnO3 bilayer. However, H.H. Ortiz-Álvarez et al. [238] reported the simulations of ME effect in a bilayer ferroelectric/ferromagnetic in multiferroic.

In this chapter, we focus on the direct magnetoelectric effect where the electric polarization (P) in the ferroelectric thin film PZT is modified by a magnetic field (H). Magnetoelectric voltage coefficient of NFO/PZT, CFO/PZT, NFO/PZT/CFO, and NFO/PZT/NFO heterostructures was carried out using Monte Carlo simulations. The emphasis was placed on the effect of the temperature on the magnetization, electric polarization and their susceptibilities. The influence of $\mathbf{J_{me}}$ on P-H hysteresis loops and the magnetoelectric voltage coefficient was also discussed.

5.2 Model and simulations:

Ferrimagnetic $NiFe_2O_4$ crystallizes in the inverse cubic spinel structure (space group Fd3m) at room temperature with a lattice parameter a = 8.337 Å [188] as shown in **Figure.5.1a**. The tetrahedron A sites are occupied by Fe^{3+} Fe(T) cations and the octahedron B sites are occupied by an equal number of randomly distributed Co^{3+}/Ni^{2+} and Fe^{3+} Fe(O) cations. the lattice parameters of the tetragonal structure of PZT are a = 4.030 Å and c = 4.145 Å [6] (**Figure.5.1b**), The unit cells of PZT were assigned to the electrical dipoles in interaction. Ti and Zr cations are randomly distributed in B-sites. **Figure.5.1(a-b)** shows the crystal structure of MFO and PZT. The heterostructures (NFO/PZT, CFO/PZT, NFO/PZT/CFO and NFO/PZT/NFO) are modeled by superposition of PZT on top of MFO (001) (M=Co/Ni) as shown in Figure.1(c-e). The mismatch between $NiFe_2O_4$ and PZT equals to 3.32 % which reasonably low. In our simulations the spins are implemented in Heisenberg model, which have been used previously to investigate the magnetoelectric properties of ferromagnetic/ferroelectric superlattice [236].

In this work, Monte Carlo simulation in framework of Heisenberg model with Metropolis Algorithm are used to investigate the ferroelectric, magnetic and magnetoelectric properties of NFO/PZT, CFO/PZT, NFO/PZT/CFO and NFO/PZT/NFO heterostructures. Spin and dipole flips are accepted or rejected according to the Metropolis algorithm [160]. Our calculations were performed with the periodic boundary conditions in the x- and y-axis and the free boundary conditions are applied in the z-axis. 10^6 steps are required to reach the equilibrium of the system. According to the model described in [236]. The Hamiltonian of this system is described by:

$$H = H_{Fm} + H_{Fe} + H_{me} \tag{5.1}$$

Where H_{Fe} is the energy of the ferroelectric subsystem, H_{Fm} refers to the energy of the magnetic subsystem and H_{me} corresponds to the interactions between the two subsystems. The Hamiltonian of the magnetic subsystem (MFO, M = Ni and Co) is described by:

$$H_{Fm} = -J_1 \sum_{<i,j>} S_i^{Fe(T)} S_j^{Fe(T)} - J_2 \sum_{<i,j>} S_i^{Fe(T)} S_j^{Fe(O)} - J_3 \sum_{<i,j>} S_i^{Fe(T)} S_j^{M} - J_4 \sum_{<i,j>} S_i^{Fe(O)} S_j^{Fe(O)} - J_5 \sum_{<i,j>} S_i^{Fe(O)} S_j^{M} - J_6 \sum_{<i,j>} S_i^{M} S_j^{M} - H \sum_i \left(S_i^{Fe(T)} + S_i^{Fe(O)} + S_i^{M} \right) \quad (5.2)$$

Where <i,j> denotes nearest-neighbor i and j sites. $S^{Fe(O)} = 5/2$, $S^{Fe(T)} = 5/2$, $S^{Co} = 3/2$ and $S^{Ni} = 1$ are the spins of Fe(T), Fe(O), Ni and Co, respectively. J_β ($\beta = 1,2,3,4,5$ and 6) are the exchange couplings between the nearest-neighbor pairs of spins $S_i^{Fe(T)}S_j^{Fe(T)}$, $S_i^{Fe(T)}S_j^{Fe(O)}$, $S_i^{Fe(T)}S_j^{M}$, $S_i^{Fe(O)}S_j^{Fe(O)}$, $S_i^{Fe(O)}S_j^{M}$, and $S_i^{M}S_j^{M}$, sites, respectively. Exchange coupling interactions in MFO (M=Ni and Co) are calculated using the method reported in [239](**table.5.1**). H is the external magnetic field. All spins in the magnetic subsystem are described in Heisenberg model, where $\overrightarrow{S_i} = \vec{S}_i^x + \vec{S}_i^y + \vec{S}_i^z$.

Based on our previous work [240] in which we have studied the ferroelectric and energy storage properties of PZT using Monte Carlo simulation in framework of Ising model, the Ferroelectric properties of PZT can be modeled by the following Hamiltonian:

$$H_{Fe} = -\sum_{<ij>} J_{1tt} p_i p_j - \sum_{<ij>} J_{2tt} p_i p_j - \sum_{<ij>} J_{1zz} \sigma_i \sigma_j - \sum_{<ij>} J_{2zz} \sigma_i \sigma_j - \sum_{<ij>} J_{1tz} p_i \sigma_j - \sum_{<ij>} J_{2tz} p_i \sigma_j - 2\mu E \sum_i (\sigma_i + p_i) \quad (5.3)$$

where, $p = \pm 2, \pm 1, 0$ and $\sigma = \pm 1, 0$ denote dipole moments of $PbTiO_3$ and $PbZrO_3$, respectively. J_{1tt} and J_{1zz} are the exchange coupling constants between nearest-neighbors dipoles p_i-p_j and σ_i–σ_j of $PbTiO_3$ and $PbZrO_3$, respectively. J_{2tt} and J_{2zz} are the exchange coupling constants between next-nearest-neighbors dipoles p_i-p_j and σ_i–σ_j for $PbTiO_3$ and $PbZrO_3$, respectively. J_{1tz} and J_{2tz} are the exchange coupling constants between nearest-neighbors and next-nearest-neighbors dipoles p_i-σ_j of $PbTiO_3$ and $PbZrO_3$, respectively**.** Exchange coupling interactions in PZT are listed in **table.5.2**. The μ is the effective dipole moment and E is an external electric field.

The magnetoelectric interaction between the ferroelectric and magnetic sublattices at the interface can be expressed by[236]:

$$H_{me} = -J_{me} \sum_k p_k \left[S_i S_j \right] \quad (5.4)$$

where, J_{me} is the magnetoelectric coupling interaction between two adjacent magnetic and ferroelectric layers at the interface, this interaction is represented in the **Figure.5.1(e).**

The partial magnetizations in the magnetic subsystem, $m_{\mathrm{Fe\,Tet}}$, $m_{\mathrm{Fe\,Oct}}$, m_{Ni} and m_{Co}, are defined as [241]:

$$m_\alpha = \frac{1}{N_\alpha} < \sum_i S^\alpha > \quad \text{with (α=Fe(T), Fe(O), Ni and Co)} \quad (5.5)$$

The total magnetization and magnetic susceptibility of the magnetic subsystem are defined as:

$$m_{Total} = (m_{\mathrm{Fe(O)}} + m_{\mathrm{Fe(T)}} + m_{\mathrm{M}})/3 \quad \text{(M=Ni and Co)} \quad (5.6)$$

$$\chi_{Total} = \frac{N}{K_B T} \left(< m_{Total}^2 > - < m_{Total} >^2 \right) \quad (5.7)$$

The electrical polarizations (P) and susceptibility (χ) of ferroelectric subsystem are computed from Monte Carlo simulation [212] are given by:

$$P = \frac{1}{N}\sum_i^N p_i \tag{5.8}$$

$$\chi = \frac{N}{K_B T}(\langle p^2\rangle - \langle p\rangle^2) \tag{5.9}$$

where N is the total number of dipole moments (p_i) in ferroelectric subsystem, and K_B is the Boltzmann constant chosen to be equals 1.

Table.5.1*: Exchange couplings (meV) in MFO (M=Ni and Co).*

	J_1	J_2	J_3		J_4	J_5		J_6	
S_i-S_j	Fe(T)- Fe(T)	Fe(T)- Fe(O)	Fe(T)-Ni	Fe(T)-Co	Fe(O)- Fe(O)	Fe(T)-Ni	Fe(T)-Co	Ni-Ni	Co-Co
Exchange couplings	2.758	3.275	2.593	2.249	4.143	2.752	2.417	1.983	2.760

Table.5.2*: values of exchange coupling constant of PZT reported in* [240].

	J_{1tt}	J_{1zz}	J_{2tt}	J_{2zz}	J_{1tz}	J_{2tz}
values of exchange coupling (meV)	6.915	4.542	3.457	2.271	5.947	2.973

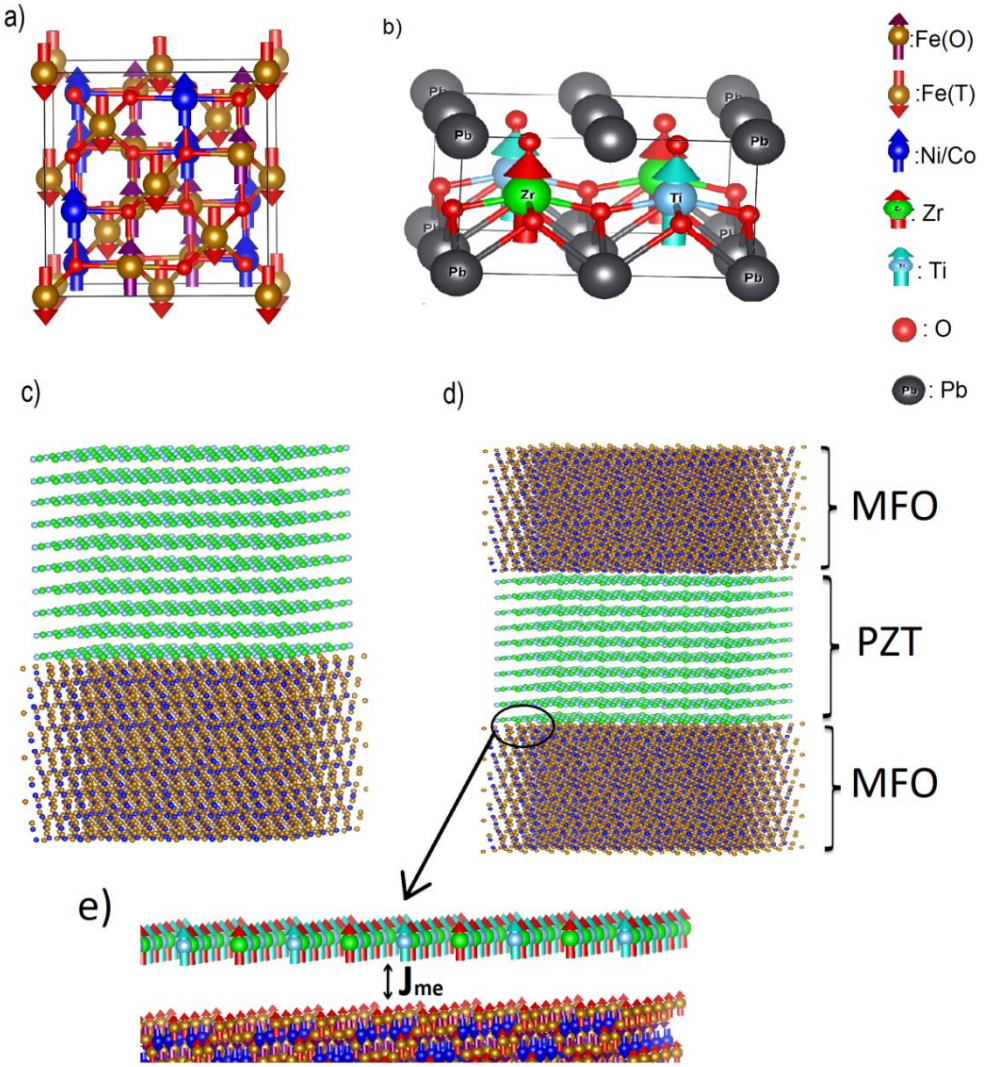

Figure.5.1: Structure representation of: **(a)** spinel MFO, **(b)** tetragonal PZT, **(c)** MFO/PZT heterostructures, **(d)** MFO/PZT/MFO heterostructures, **(e)**MFO/PZT interface (M= Ni and Co).

5.3 Results and discussion:

5.3.1 Magnetic and ferroelectric properties:

Figure.5.2a displays the total magnetization and magnetic susceptibility (χ_m) versus temperature in NFO. While, **Figure.5.2b** illustrates the partial magnetization per spin for Fe(T), Fe(O) and Ni in NFO as a function of temperature. As shown in **Figure.5.2a**, the total magnetization starts from a maximum and decreases and then vanishes when the temperature is above the critical temperature (T_C). The transition from ferrimagnetic phase to paramagnetic phase indicated by the peaks of the magnetic susceptibility, which corresponds to the critical temperature (Tc=843K). In addition, the temperature dependence of total magnetization and magnetic susceptibility (χ_m) for CFO were illustrated in **Figure.5.3a**. The magnetic susceptibility peak is located at T=790 K indicating a phase transition from ferromagnetic to paramagnetic phase. On the other hand, we plot in **Figure.5.3b** the magnetization per spin for Fe(O), Fe(T) and Co in CFO versus the temperature. We note that for both NFO and CFO, a second-order phase transition was observed at the critical temperature T_C. The calculated values of Curie temperature for both NFO and CFO are in

good agreement with the experimental results reported in [242]–[244]. Furthermore, **Figure.5.4** shows the calculated electric polarization (**P**) and electric susceptibility (χ_e) in PZT as a function of temperature. At low temperature, all the electric dipoles are aligned in (001) direction. The electric polarization takes a maximum and decreases continuously as we increase the temperature, and then vanishes at the critical temperature. The observed behavior indicates that the system undergoes a second-order phase transition at T_C=665 K. The phase transition from ferroelectric to paraelectric phases is indicated by the peak of electric susceptibility [245]. This may be taken as a first validation of the extracted exchange interactions.

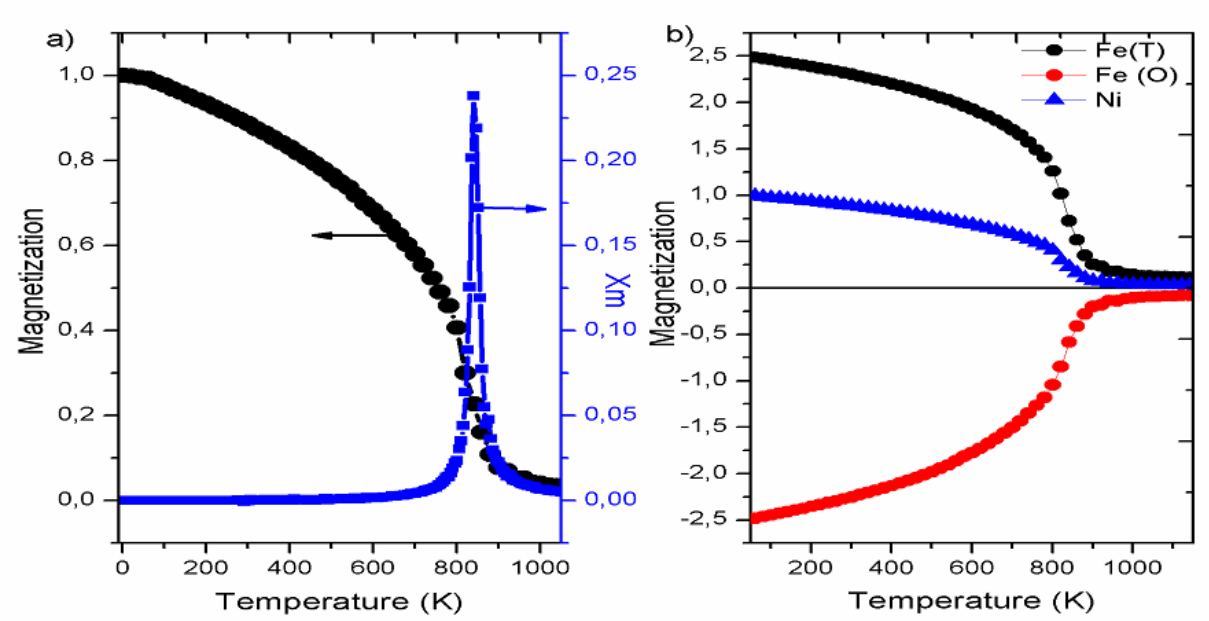

Figure.5.2: (a) total magnetization and magnetic susceptibility (χ_m), **(b)** partial magnetization in $NiFe_2O_4$as a function of temperature

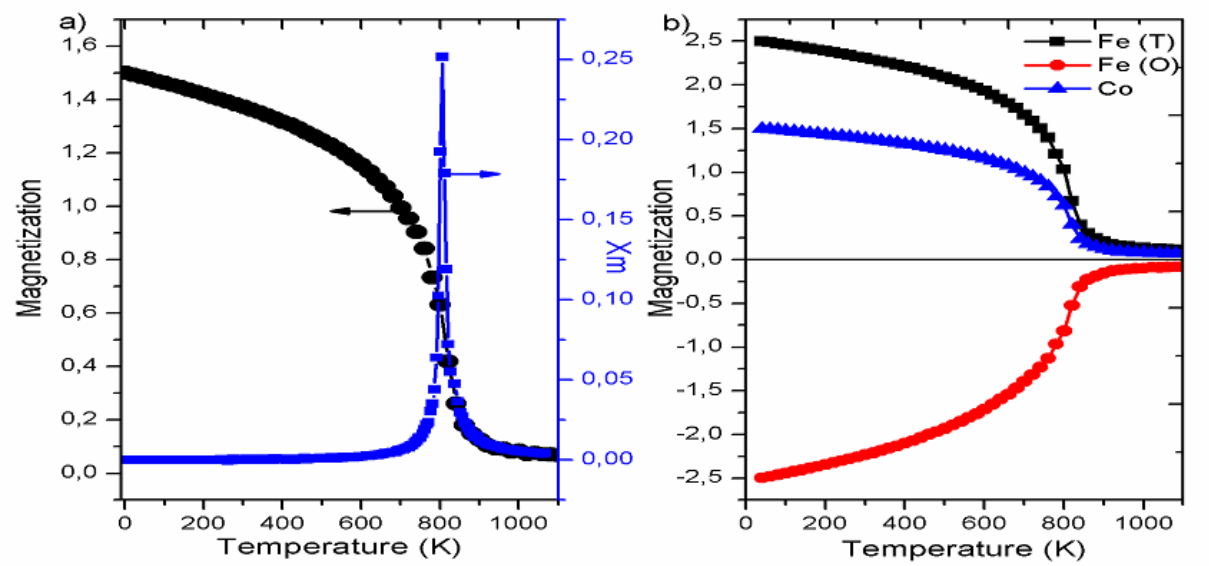

Figure.5.3: (a) total magnetization and magnetic susceptibility (χ_m), **(b)** partial magnetization in $CoFe_2O_4$ as a function of temperature.

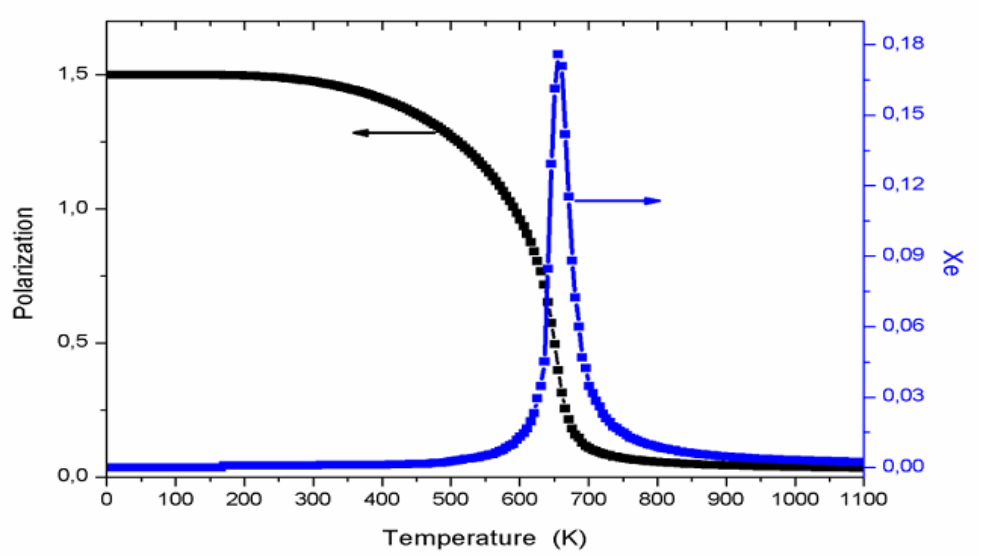

Figure.5.4: electric polarization (P) and electric susceptibility (χ_e) in PZT as a function of temperature.

5.3.2 Magnetoelectric effects:

Here in we focused on magnetoelectric effects in NFO/PZT, CFO/PZT, NFO/PZT/CFO and NFO/PZT/NFO heterostructures. The heterostructure are built by sticking NFO or CFO layer on top of PZT layer, which interact within magnetoelectric coupling interactions $\mathbf{J_{me}}$. The magnetoelectric voltage coefficient α is calculated using the following expression [81], [229]:

$$\alpha = \frac{\Delta P}{\Delta H} \tag{5.10}$$

where, ΔP is the induced electrical polarization for an applied magnetic field ΔH.

Figure.5.5 shows the magnetoelectric voltage coefficient (MEVC) as a function of $\mathbf{J_{me}}$ in NFO/PZT and CFO/PZT. The magnetoelectric voltage coefficient rises with increasing the $\mathbf{J_{me}}$, indicating the presence of a strong correlation between the magnetoelectric voltage coefficient and $\mathbf{J_{me}}$. We mention here that magnetoelectric coupling interactions $\mathbf{J_{me}}$ corresponding to the experimental magnetoelectric voltage coefficient for NFO/PZT and CFO/PZT are **4.120** and **0.625** meV, respectively [19], [81]. Experimentally, NFO/PZT heterostructures with lower magnetostriction have a strong magnetoelectric voltage coefficient, whereas CFO/PZT heterostructures with a strong magnetostrictive present a weaker magnetoelectric voltage coefficient. This can be explained by the strong interfacial magnetoelectric coupling interaction $\mathbf{J_{me}}$=4.120 meV at NFO/PZT interface, while the predicted $\mathbf{J_{me}}$ for CFO/PZT interface is 0.625 meV.

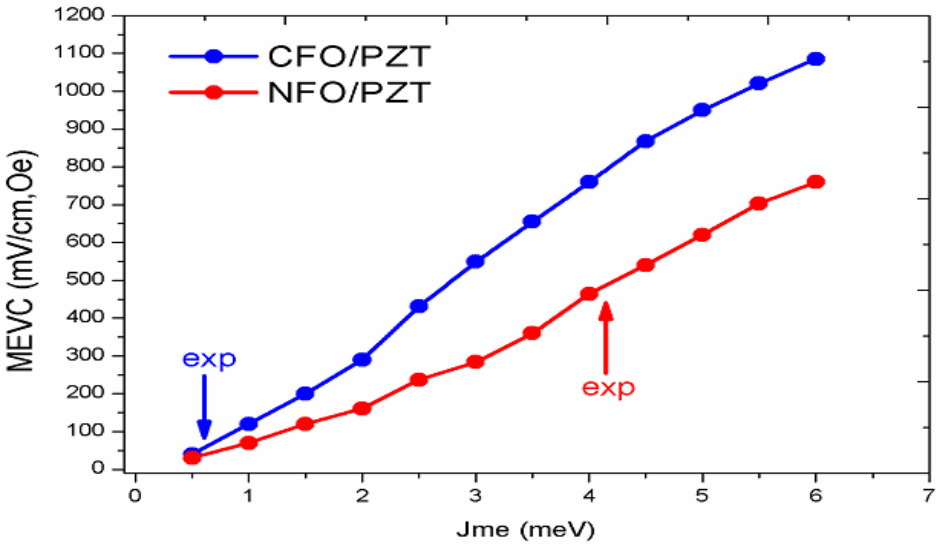

Figure.5.5: Magnetoelectric voltage coefficient as a function of $\mathbf{J_{me}}$ in NFO/PZT and CFO/PZT interfaces.

Hysteresis loops, **M-H** and **P-H,** for NFO/PZT and CFO/PZT interfaces given at 300K for different values of $\mathbf{J_{me}}$ are shown in **Figure.5.6(a-b).** For $\mathbf{J_{me}}$=0, a typical M-H hysteresis loops was obtained for both of NFO/PZT and CFO/PZT interfaces. In this case, the electric polarization kept constant and is not influenced by the magnetic field H (not presented here). It should be noted that changes in $\mathbf{J_{me}}$ influenced on electric polarization. This behavior is because the spin moments and electric dipoles at the interface are interacted via the interfacial magnetoelectric coupling interaction $\mathbf{J_{me}}$. In this section, we choose the calculated values of $\mathbf{J_{me}}$ corresponding to the experimental magnetoelectric voltage coefficient ($\mathbf{J_{me}}$=4.120 meV for NFO/PZT interface and $\mathbf{J_{me}}$=0.625 meV for CFO/PZT interface). A large area of P-H hysteresis loops was observed in NFO/PZT in comparison with CFO/PZT, due to high $\mathbf{J_{me}}$ at the NFO/PZT interface. **Figure.5.6(c-d)** shows M-H and P-H Hysteresis loops at 300K for NFO/PZT/NFO and NFO/PZT/CFO heterostructures. For NFO/PZT/CFO heterostructure (see **Figure.5.6d**), the PZT is under two different interfacial magnetoelectric coupling interactions on both sides ($\mathbf{J_{me}}$=4.120 meV at NFO/PZT interface and $\mathbf{J_{me}}$=0.625 meV at CFO/PZT interface). Therefore, the area of P-H hysteresis loops becomes large in comparison with NFO/PZT. Concerning NFO/PZT/NFO (**Figure.5.6c)**, the PZT undergoes a large interfacial magnetoelectric coupling interaction $\mathbf{J_{me}}$=4.120 meV in both sides. As a result, the applied magnetic fields can change the direction of the electric dipoles and forcing them to be oriented in the same direction of magnetic spins. A large remanent polarization Pr and coercive magnetic field $\mathbf{H_c}$ **(**250 Oe) were attainted. Interestingly, the presented results show that the interfacial magnetoelectric coupling interaction $\mathbf{J_{me}}$ is an important mechanism for the control of electrical polarization.

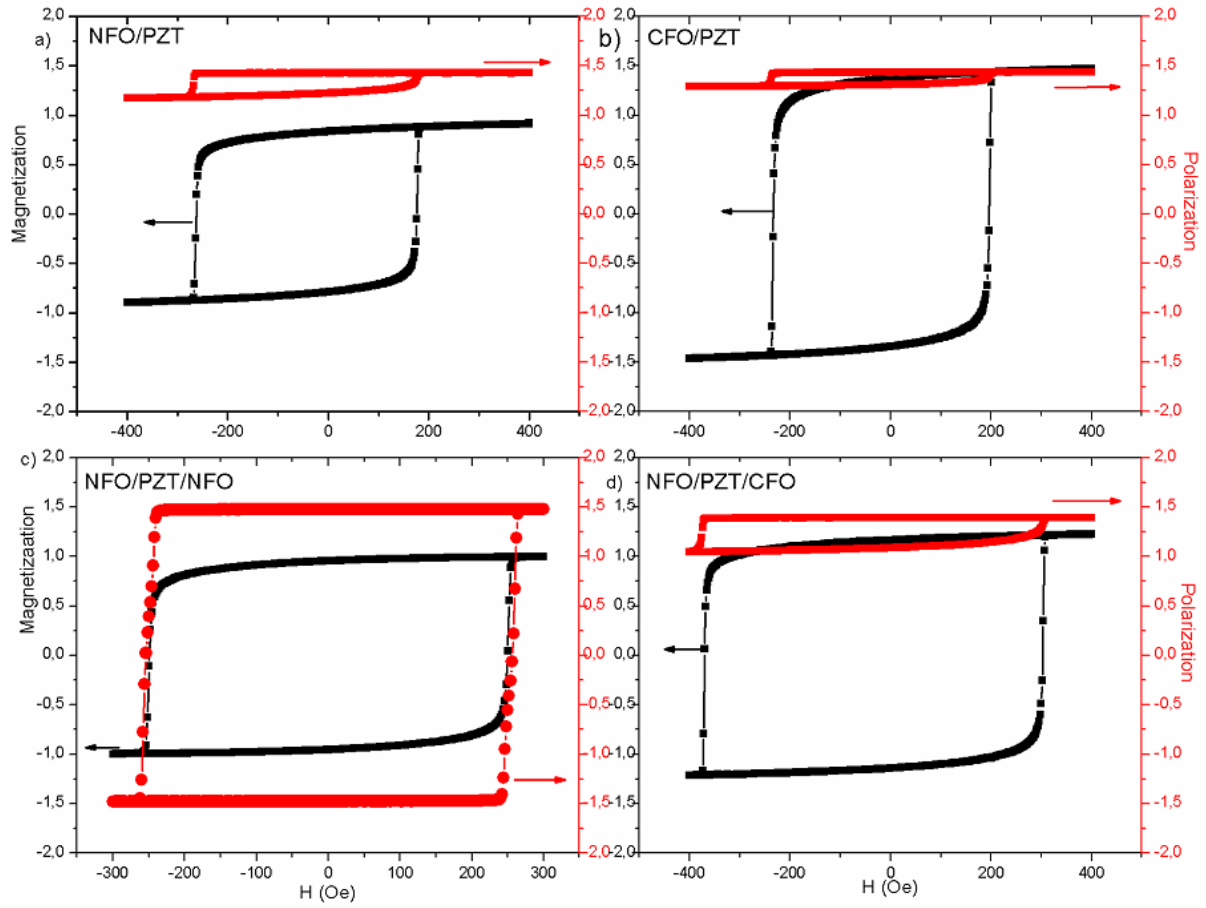

Figure.5.6: Hysteresis loop M-H and P-H for :**(a)**NFO/PZT, **(b)** CFO/PZT, **(c)** NFO/PZT/NFO and **(d)** NFO/PZT/CFO at 300K.

Figure.5.7(a-d) presents the magnetoelectric voltage coefficient as a function of applied magnetic field (**H**) for NFO/PZT, CFO/PZT, NFO/PZT/NFO and NFO/PZT/CFO at 300K. At the applied magnetic field $\mathbf{H=H_c}$, the magnetoelectric voltage coefficient increases sharply and shows a peak with the highest value of ME voltage. The maximum magnetoelectric voltage coefficients that are predicted are 460, 50, 1405 and 650 mV/(cm.Oe) for NFO/PZT, CFO/PZT, NFO/PZT/CFO and NFO/PZT/NFO, respectively. The calculated value of the magnetoelectric voltage coefficient in the proposed NFO/PZT/NFO and NFO/PZT/CFO heterostructures are comparable to the experimental results (1225 mV/(cm.Oe)) reported by L. Jian et al.[80] in PZT/NFO/PZT films. A remarkable enhancement of the magnetoelectric voltage coefficient can be achieved in NFO/PZT/CFO and NFO/PZT/NFO heterostructures. Such behavior is due to the electric polarization driven by the magnetic force through an interfacial magnetoelectric coupling interaction $\mathbf{J_{me}}$, resulting a strong magnetoelectric voltage coefficient (see **Figure.5.6(c-d)**). In **the table.3,** we report some experimental reports of the magnetoelectric voltage coefficient in nanocomposites thin films.

Table.5.3: *Some magnetoelectric thin-film composites and their magnetoelectric voltage coefficients.*

magnetoelectric composite	**magnetoelectric voltage coefficient** mV/(cm.Oe)	**Ref**
Terfenol-D/PMN-PT/Terfenol-D	12880	[110]
Terfenol-D/PZT/Terfenol-D	7380	[80]

PZT/Terfenol-D discs	4680	[80]
PZT/$LaNiO_3$/HfO_2/Ni	3200	[87]
NFO/PZT/NFO	**1405**	**This work**
NFO/PZT multilayer	1500	[19]
PZT/NFO/PZT	1225	[246]
NFO/PZT/CFO	**650**	**This work**
NFO/PZT bilayer	460	[19]
$Co_{0.6}Zn_{0.4}Fe_2O_4$/PZT PZT/CFO	280 50	[81]
PZT/$La_{0.7}Sr_{0.3}MnO_3$	160	[18]
PZT/$La_{0.7}Ca_{0.3}MnO_3$	60	[18]

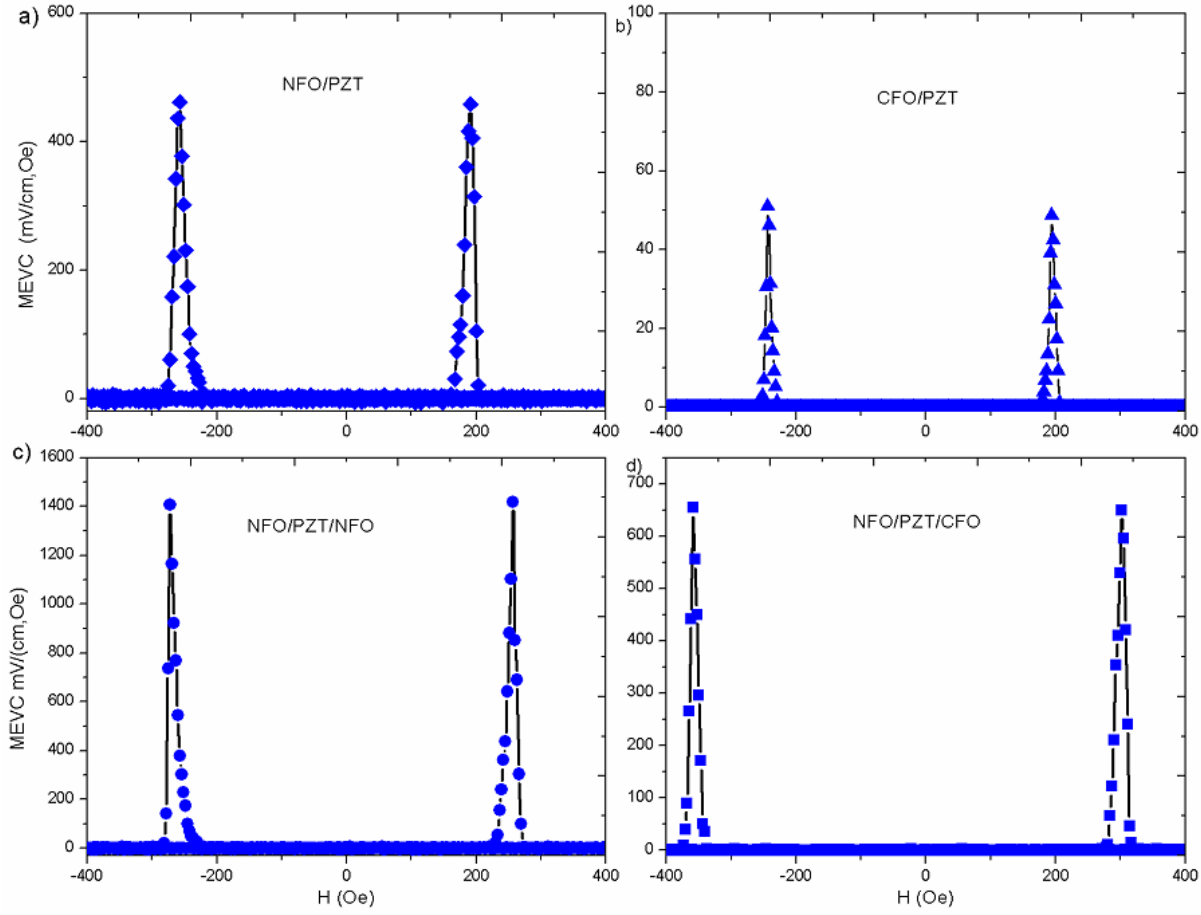

Figure.5.7: Magnetoelectric voltage coefficient as a function of applied field H for :**(a)** NFO/PZT, **(b)** CFO/PZT, **(c)** NFO/PZT/NFO and **(d)** NFO/PZT/CFO at 300K.

5.4 Conclusion:

The magnetoelectric effect in MFe_2O_4/PZT and MFe_2O_4/PZT/MFe_2O_4 (M=Ni and Co) heterostructures was investigated by Monte Carlo simulation. In the present chapter, we highlighted the effects of the temperature on the magnetization, electric polarization and their susceptibilities. Further, the behavior of **M-H** and **P-H** hysteresis loops and magnetoelectric voltage coefficient as a function of interfacial magnetoelectric coupling interaction $\mathbf{J_{me}}$was also analyzed. The obtained results show that the interfacial magnetoelectric coupling interaction ($\mathbf{J_{me}}$) plays an important role in controlling the electric polarization. We note here in that the $\mathbf{J_{me}}$ values corresponding to the experimental magnetoelectric voltage coefficient are $\mathbf{J_{me}}$=4.120 meV for NFO/PZT interface and $\mathbf{J_{me}}$=0.625 meV for CFO/PZT interface. Moreover, the large magnetoelectric voltage coefficients of 650 and 1405 mV/(cm.Oe) were predicted in NFO/PZT/CFO and NFO/PZT/NFO, respectively. The calculated results show good agreement with the experimental results reported in the examined literature.

Chapter 6

Prediction of Magnetoelectric properties of defect $BiFeO_3$ thin films using Monte Carlo simulations.

6.1 Introduction:

Multiferroic materials having both ferroelectric and magnetic order constitute an interesting and promising class of materials. In fact, these materials were found endorsing attractive physical properties, both in experimental and theoretical investigations [247]. They bear potentials for extended functionalities in terms of innovative devices, especially, for technological applications such as sensors, data storage devices, microelectronics, actuators, transducers, sensors, and spintronic devices [13], [248]. However, most of these applications involve a strong coupling between the spontaneous polarization and spontaneous magnetization, known as magnetoelectric (ME) coupling, in which the magnetization can be tuned by an applied electric field and vice versa [1]. Among these multiferroic materials, BiFeO3 (BFO) is one of the most studied materials recently due to the simultaneous existence of room temperature ferroelectricity and antiferromagnetism with very high Curie temperature T_C = 1103 K and a G-type antiferromagnetic ordering with a Néel temperature T_N = 643 K [249]. Experimentally, several attempts have been made by the researchers to enhance magneto-electric coupling in the multiferroic BFO. Recently, F. Pedro-García et al.[250] studied the effects of the Sr and Ni co-doping of BiFeO3 on the crystal structure and multiferroic properties. Further, S. Atiq et al. examined the magnetoelectric properties of Ni and Cr co-doped BiFeO3 [251]. In comparison to single doped $BiFeO_3$, A.S. Priya et al. observed a strong magnetoelectric coupling for Dy and Cu co-doped BFO[252]. On the other hand, multiferroic heterostructures with alternate ferroelectric/ferromagnetic layers show a high magnetoelectric voltage coefficient, R. K. Kotnala et al. have achieved a magnetoelectric voltage coefficient of 515 mV/(cm.Oe) in trilayer thin films of BaTiO3/BiFeO3/BaTiO3 [253]. Interestingly, M. Lorenz et al. have achieved the highest value of the magnetoelectric voltage coefficient of 24 V/(cm.Oe) [254] and 49 V/(cm.Oe) [89] at 300 K in BaTiO3-BiFeO3 superlattices. A clear correlation of magnetoelectric coefficients with increasing oxygen partial pressure during growth was observed. Moreover, many experimental works have been done on BFO doped by rare-earth (RE) (RE=La, Ho, Dy, Eu, Er, Gd and Tb) to improve its multiferoic properties [10], [255], [256]. Furthermore, it has been observed that RE doped BFO undergoes a structural phase transition from rhombohedral to orthorhombic phase [257].

It is worth mentioning that the Monte Carlo simulation been used to describe the magnetoelectric properties. A. Albaalbaky et al.[258] studied the magnetoelectric properties of $CuCrO_2$ using first principles and Monte Carlo simulations, H. H. Ortiz-Álvarez et al.[238]

investigated the magnetoelectricity in a bilayer ferroelectric/ferromagnetic multiferroic system. A. S. ErchidiElyacoubi et al.[259] reported the magnetoelectric coupling in RMn_2O_5 multiferroic material. I. F. Sharafullin et al.[236] investigated the magnetoelectric coupling and surface effects on a multiferroic superlattice formed by magnetic and ferroelectric sublayers. Recently, using Monte Carlo simulation and Mean-field theory, I.F. Sharafullin et al.[260] studied the magnetoelectric interactions at the interface of magnetic/ferroelectric superlattice. In this chapter, ferroelectric, magnetic and magnetoelectric properties of multiferroic BFO thin films were studied using Monte Carlo simulation. Thermodynamic quantities such as internal energy, specific heat, magnetization, electric polarization, and their susceptibilities as a function of temperature in BFO thin films have been given. Electric dipole defects were proposed as a mechanism to enhance the magnetoelectric coupling in BFO.

6.2 Model and simulations:

Multiferroic $BiFeO_3$ (BFO) crystalizes in a rhombohedral structure with R3c space group at room temperature, which is usually described by the hexagonal lattice [249] (see **Figure.1a**). BFO has a ferroelectric transition at T_C=1103 K and an antiferromagnetic phase transition at T_N =650 K [249], [261]. We consider that the BFO systems are composed of two sublattices, the first sublattice involves an anti-ferromagnetic order of Fe-spins and the second one involves the electric dipoles at Bi sites (at the center of the unit cell) as shown in **Figure.1(b,c,e).** Monte Carlo Simulation within the Metropolis algorithm [262] is used to simulate the BFO thin films described by the Hamiltonian (1). The periodic boundary conditions were applied in the x and y-axis, while a free boundary condition was applied in the z-axis. The system contains the total number of *N* Fe-spins and *N* electric dipoles, which were be accepted or rejected according to the Metropolis algorithm. The data was collected after discarding the first 10^5 Monte Carlo steps, which needed to reach the equilibrium of the system. In the calculations, the defects are randomly distributed in B_i-sites, and the defect-sites is replaced by P=0 in the sublattice of electric dipoles.

Based on the model described in [260], the Hamiltonian governed the BFO system is defined as follows:

$$\mathbf{H} = \mathbf{H_m} + \mathbf{H_e} + \mathbf{H_{me}} \tag{6.1}$$

Where H_e and H_m are the energy of ferroelectric and magnetic sublattices, respectively. H_{me} corresponds to the interaction between the two sublattices. The Hamiltonian of magnetic sublattice is described by:

$$\boldsymbol{H_m} = -\boldsymbol{J_{m1}}\sum_{<i,j>}(\boldsymbol{S_i^x S_j^x} + \boldsymbol{S_i^y S_j^y} + \boldsymbol{S_i^z S_j^z}) - \boldsymbol{J_{m2}}\sum_{<i,j>}(\boldsymbol{S_i^x S_j^x} + \boldsymbol{S_i^y S_j^y} + \boldsymbol{S_i^z S_j^z}) - \boldsymbol{D_{ij}}\sum_{<i,j>}(\boldsymbol{S_i} \times \boldsymbol{S_j}) - \boldsymbol{H}\sum_{\boldsymbol{i}}(\boldsymbol{S_i^z}) \tag{6.2}$$

Where <i,j> denoted nearest-neighbor i and j sites. $\vec{S_i} = \vec{S_i^x} + \vec{S_i^y} + \vec{S_i^z}$ is the classical Heisenberg spins of the Fe atoms with $S = 5/2$, . J_{m1} and J_{m2} are the exchange coupling interactions between two first nearest neighbors spin S_iS_j and two second nearest neighbors spin S_iS_j , respectively (see **Figure.6.1b**). Exchange coupling interactions in BFO are calculated using the method reported in [239](see **table.6.1**). $\boldsymbol{D_{ij}}$ is the Dzyaloshinskii–Moriya interactions ($\mathbf{D_{ij}}$=**D**=0.107 meV [263]) H is the external magnetic field. For ferroelectric sublattices, the following Hamiltonian was assumed to be:

$$\boldsymbol{H_e = -J_{e1} \sum_{<ij>} p_i p_j - J_{e2} \sum_{<ij>} p_i p_j - 2\mu E \sum_i p_i} \quad (6.3)$$

Where $p = \pm 1$ denotes the dipole moments of BFO. Je_1 and Je_2 are the exchange coupling constants between two first nearest neighbors dipoles p_i-p_j and two second nearest neighbors dipoles p_i-p_j (see **Figure.6.1c**), respectively, which are listed in **Table.6.1**. μ is the effective dipole moment and E is an external electric field.
Magnetoelectric interactions between ferroelectric and magnetic sublattices can be chosen as [260] :

$$\boldsymbol{H_{me} = -J_{me} \sum_k p_k \cdot \left[S_i^x S_j^x + S_i^y S_j^y + S_i^z S_j^z \right]} \quad (6.4)$$

where, $\mathbf{J_{me}}$ is the magnetoelectric coupling interaction between electric dipoles (p) and spin moments (S) at the interface, which is represented in **Figure.6.1.d.**
The partial magnetizations (m) in magnetic sublattice is defined as [217], [241]:

$$m = \frac{2}{N} < \sum_i S_i > \quad (6.5)$$

The total magnetization (M_{Total}) and magnetic susceptibility (χ_m) of magnetic sublattice are defined as:

$$M_{Total} = \frac{(m_{\text{up}} + m_{\text{down}})}{2} \quad (6.6)$$

$$\chi_M = \frac{N}{K_B T} \left(< M_{Total}^2 > - < M_{Total} >^2 \right) \quad (6.7)$$

Where m_{up} and m_{down} are the partial magnetization of spin up and spin down in magnetic sublattice. The parameters; electrical polarization (P) and susceptibility (χ_e) of ferroelectric sublattice are computed from Monte Carlo simulation [212] are given by:

$$P = \frac{1}{N} \sum_i^N p_i \quad (6.8)$$

$$\chi_e = \frac{N}{K_B T} (\langle p^2 \rangle - \langle p \rangle^2) \quad (6.9)$$

where N is the total number of dipole moments (p_i) in ferroelectric sublattice, and K_B is the Boltzmann constant chosen to be equal 1.

***Table.6.1**: Exchange coupling interactions (meV) in BFO.*

	Exchange coupling interactions (meV)				
	J_{m1}	J_{m2}	J_{e1}	J_{e2}	J_{me}
Value	1.568	-0.784	8.530	5.118	4.202

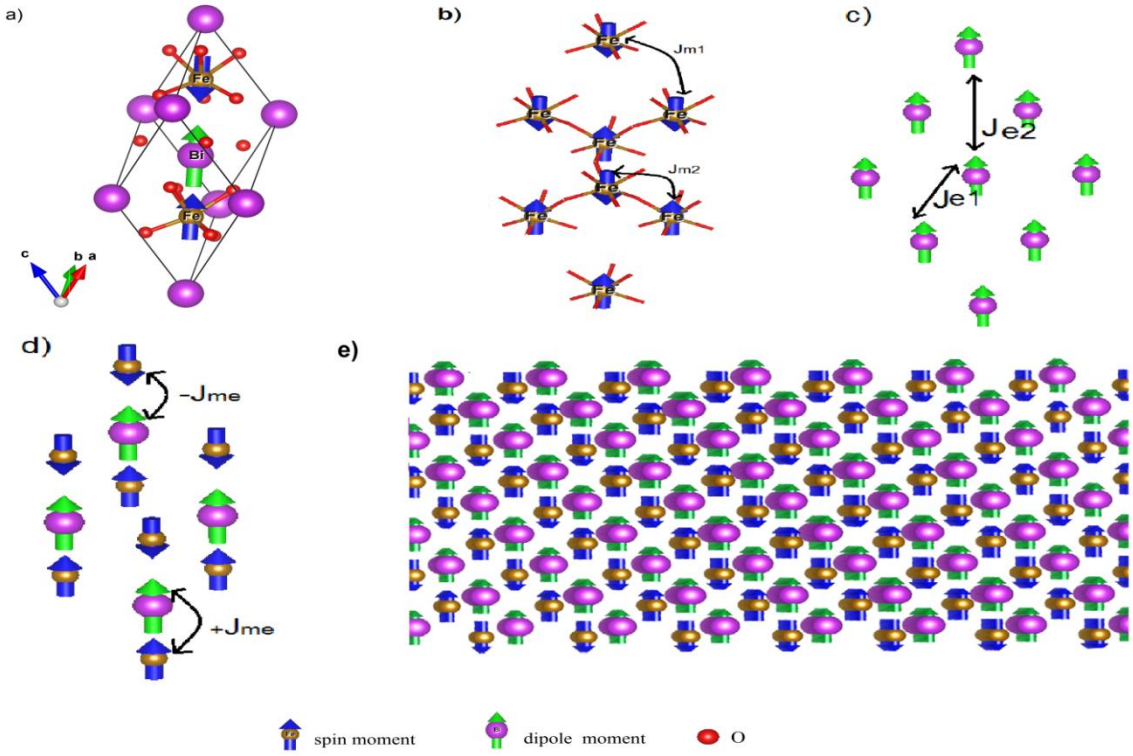

Figure.6.1: (a) Rhombohedral unit cell of BiFeO3 including 2 formula units, schematic representation of the magnetic interactions (b), electric dipole-dipole interactions (c) and magnetoelectric interaction (d). Structure of $BiFeO_3$ thin films (e).

6.3 Results and discussion:

6.3.1 Ferroelectric and magnetic properties:

Figure.6.2(a,b) shows the sublattice magnetizations (M), electric polarization (P) and their susceptibilities of BFO thin films as a function of temperature. **Figure.6.2a** presents the sublattice magnetizations and the corresponding susceptibilities χ_m . One can observe that the sublattice magnetization decreases continuously from the saturation values 5/2 as the temperature increases indicating that the magnetic systems undergoes a second-order phase transition from the antiferromagnetic phase to the paramagnetic phase which occurs at Tc = 650K. When the temperature approaches Tc, a rapid increase of the magnetic susceptibility χ_m is observed before to reach its maximum value. Elseways, electric polarization (P) starts from its maximum +1, and decreases as the temperature increases, then vanishes at the critical temperature, as seen in **Figure.6.2b**. Moreover, near of critical temperature, the electrical susceptibility χ_e increases very rapidly and exhibits a peak at T=Tc = 1100 K. It was observed that the ferroelectric systems undergo a second-order phase transition from the ferroelectric phase to paraelectric phase at 1100K.

Figure.6.3a displays the internal energy as a function of temperature. At low temperature, the internal energy is minimal, then rises as the temperature increases before to reach its maximum at higher temperatures. It should be mentioned that the total internal energy presents a weak bump at T=650K,which is attributed to the magnetic transition from the antiferromagnetic phase to the paramagnetic phase. The calculated specific heat Cv of BFO is presented in **Figure.6.3b,** Two clear peaks were observed in the Cv curve at T_N=650

K and T_C=1100K, respectively, which corresponds to the magnetic transition (T_N) from the antiferromagnetic to the paramagnetic phase and ferroelectric transition (T_c) from the ferroelectric to paraelectric phase, respectively. The specific heat C_v of the system exhibits a second-order phase transition at both the transition temperature T_N=650K and T_C=1100K, respectively. The calculated values of T_C and T_N are in good agreement with the experimental results reported in [261].

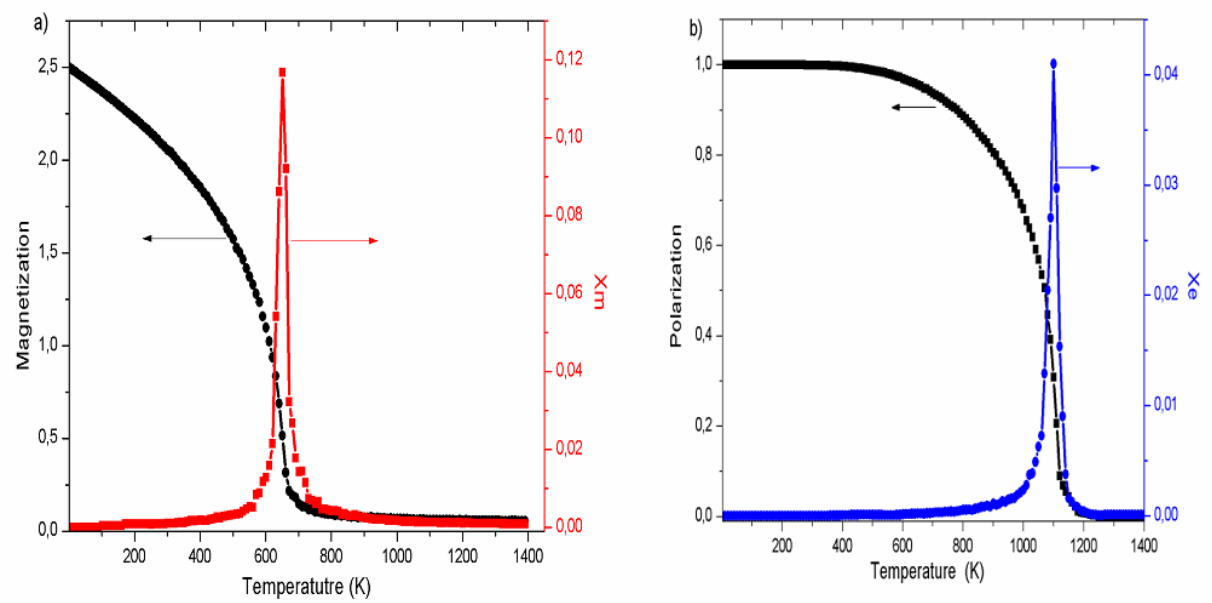

Figure.6.2 :(a) sublattice magnetizations and magnetic susceptibility (χ_m), **(b)** electric polarization (P) and their susceptibility (χ_e) in BFO thin films as a function of temperature.

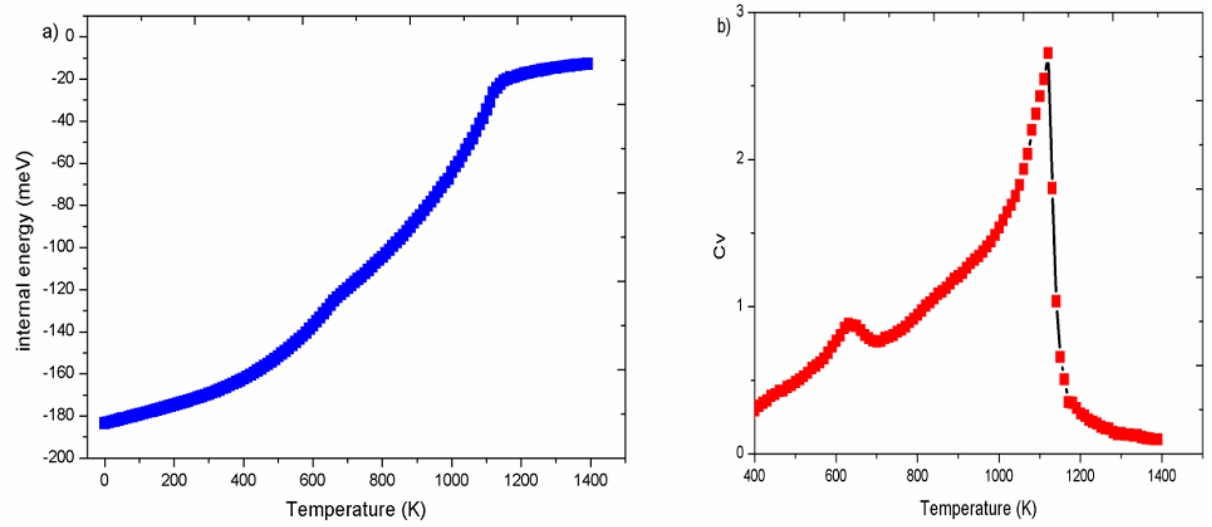

Figure.6.3 : (a) Internal energy and (b) specific heat as a function of temperature in BFO thin films.

6.3.2 Magnetoelectric effects :

Figure.6.4 shows the M-H and P-H hysteresis loop for different values of magnetoelectric coupling interaction $\mathbf{J_{me}}$ in BFO thin films at 300K. The presence of a one hysteresis loop with weak remanent magnetization in the **M-H** loop suggesting that the **BFO** presents the weak ferromagnetism due to the Moriya interaction (DMI) [263]. It is found that for $\mathbf{J_{me}}$=0

meV the polarization is not switchable (**figure.6.4.a)** and the increasing of magnetoelectric coupling interaction $\mathbf{J_{me}}$ leads to more and more obvious P-H hysteresis loop, indicating that the electric dipoles are switchable by an applied magnetic field. Furthermore, when the magnetoelectric coupling interaction $\mathbf{J_{me}}$ is large enough, a complete switching of the electric dipole by magnetic field has been observed. Moreover, The P-H loop exhibits a typical ferroelectric hysteresis loop, indicating that the BFO is in a ferroelectric state (see **figure.6.4.b**).

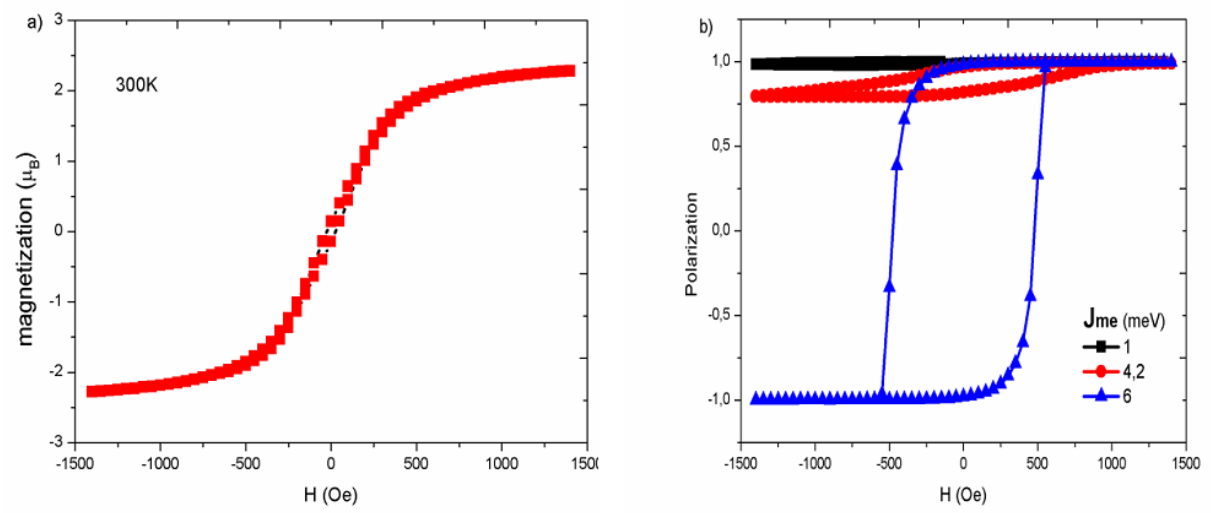

Figure.6.4: Hysteresis loop M-H and P-H for different $\mathbf{J_{me}}$ values in BFO thin films at 300K.

Magnetoelectric voltage coefficient (MEVC) as a function of magnetoelectric coupling interaction $\mathbf{J_{me}}$ at room temperature is plotted in **figure.6.5a,** with increasing $\mathbf{J_{me}}$. The value of the magnetoelectric voltage coefficient shows a small variation up to a $\mathbf{J_{me}}$ of 4.560 meV, following by a sharp increase from 15 to 200 mV/(cm.Oe). Then, the magnetoelectric voltage coefficient increases non-linearly with increasing $\mathbf{J_{me}}$. Noting that the magnetoelectric coupling interactions $\mathbf{J_{me}}$ corresponding to the experimental magnetoelectric voltage coefficient (~10 mV/(cm.Oe)) [98], [264] is found equal to 4.202 meV. The observed behavior can be explained by the competition between the magnetoelectric coupling interaction $\mathbf{J_{me}}$ and ferroelectric coupling interaction $\mathbf{J_{e1}}$ and $\mathbf{J_{e2}}$. So, a high $\mathbf{J_{me}}$ is needed to switch electric dipoles to the direction of the applied magnetic field, which leads to a large magnetoelectric voltage coefficient. **Figure.6.5b** shows the magnetoelectric voltage coefficient as a function of the applied magnetic field (H) for $\mathbf{J_{me}}$= 4.202 meV at 300K. At H= ±560 Oe, the magnetoelectric voltage coefficient rises rapidly and presented a peak with the highest value of ME voltage. As we can observed, the shape of the magnetoelectric peak is similar to the reported experimental data [98], [264]. The maximum of magnetoelectric voltage coefficient is around of 10 mV/(cm.Oe), which is closer to the experimental results reported in the literature [98], [264].

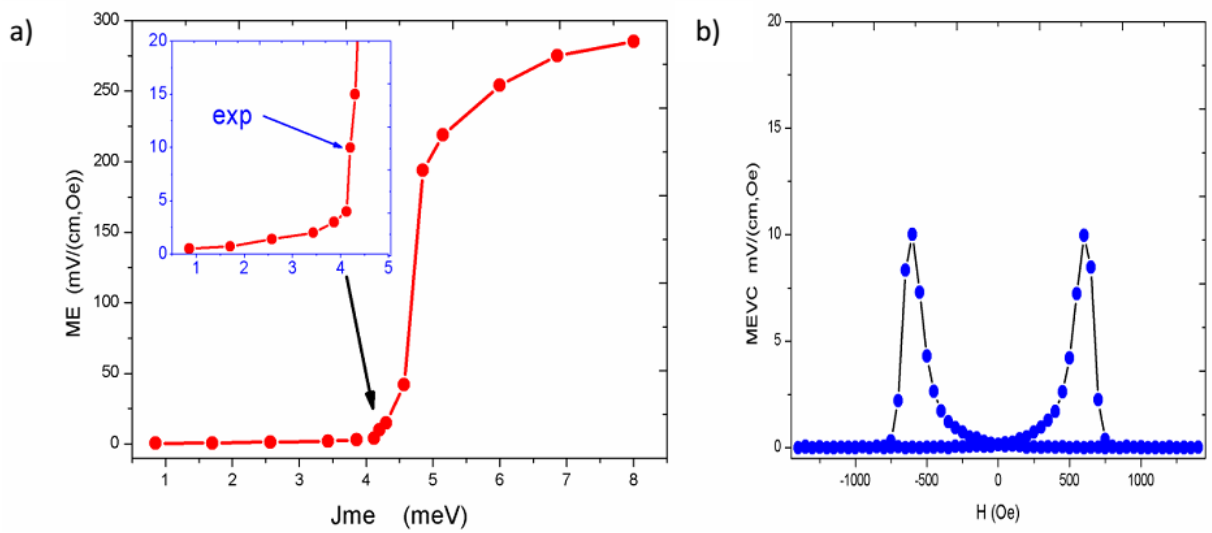

Figure.6.5 :(a) magnetoelectric voltage coefficient as a function of $\mathbf{J_{me}}$ values and **(b)** magnetoelectric voltage coefficient as a function of applied field H for $\mathbf{J_{me}}$=4.202meVmeVin BFO thin films at 300K.

6.3.3 defect effects:

Figure.6.6a shows the magnetoelectric voltage coefficient as a function of the applied magnetic field (H) for different defect concentration % in BFO thin films. As the defect increases, the peak of the magnetoelectric voltage coefficient (MEVC) rises and reached its maximum values at **25%** and then decreaces and shifted from high values of magnetic field (**H**) to zero **Oe**. The effect of electric dipole defect on magnetoelectric voltage coefficient (MEVC) at T= 300K and $\mathbf{J_{me}}$=4.202 meV in BFO thin films is shown in **Figure.6.6b,** it is found that for defect concentration up to 25%, the magnetoelectric voltage coefficient increases rapidly and reaches its maximum at 25%, and then decreases slowly with increasing the defect concentration. Interestingly, a high magnetoelectric voltage coefficient of 104 mV/(cm.Oe) was obtained at 25% defects in BFO thin films. This large value of magnetoelectric can be attributed to the reduction of exchange coupling interactions ($\mathbf{J_{e1}}$ and $\mathbf{J_{e2}}$) between the electric dipoles due to the electric dipole defects. As a result, a completed switch of electric dipoles induced by an applied magnetic field. The calculated results are in good agreement with the experimental magnetoelectric voltage coefficient achieved in **(1-x)$\mathbf{BiFeO_3$–x$BaTiO_3}$** films (**124 mV/cm.Oe** at **300K)** [254].

Figure.6.7 presents the P-H hysteresis loop for different defect concentration % in BFO thin films at 300K and $\mathbf{J_{me}}$=4.202 meV. As the defect concentration increases, a reduction in the area of P-H hysteresis loop and remanent polarization was observed. Further, our simulation demonstrated that the electric polarization can be switched completely with defect concentration over **20%**, where all electric dipoles turn to the direction of the applied magnetic, due to the reduction of exchange coupling interactions (Je1 and Je2) between the electric dipoles. So, the defect mechanism can be used to control the polarization switching by the magnetic field in BFO system. The aforementioned polarization switching by applied magnetic field (**H**) produced a large magnetoelectric voltage coefficient (**MEVC**), it is worth mentioning that **25%** of defects in **BFO** thin films exhibits a large magnetoelectric voltage coefficient, which makes it more suitable for magnetoelectric devices.

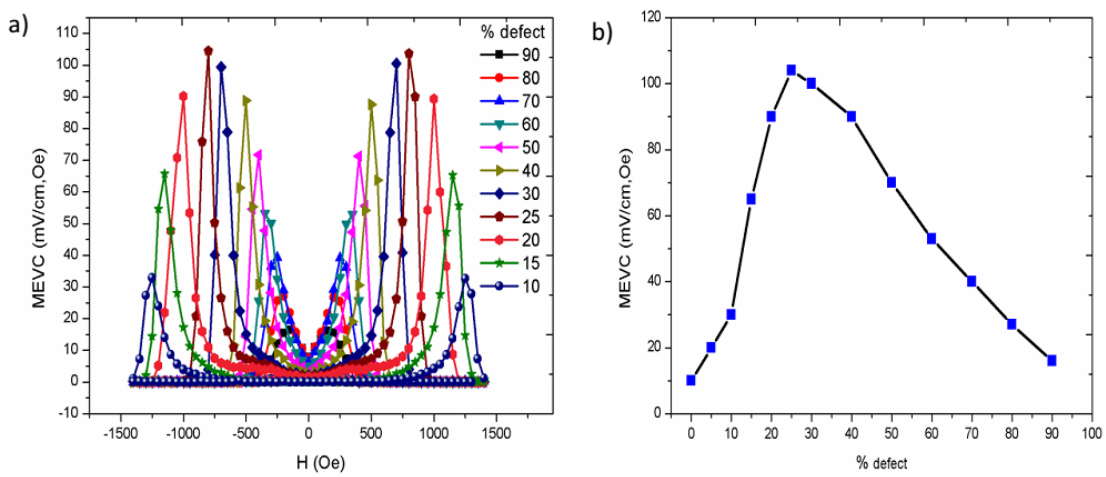

Figure.6.6 : (a) magnetoelectric voltage coefficient (MEVC) as a function of applied magnetic field H for different defect concentration % in BFO thin films and **(b)** defect effects on magnetoelectric voltage coefficient (MEVC) at 300K and J_{me}=4.202 meV.

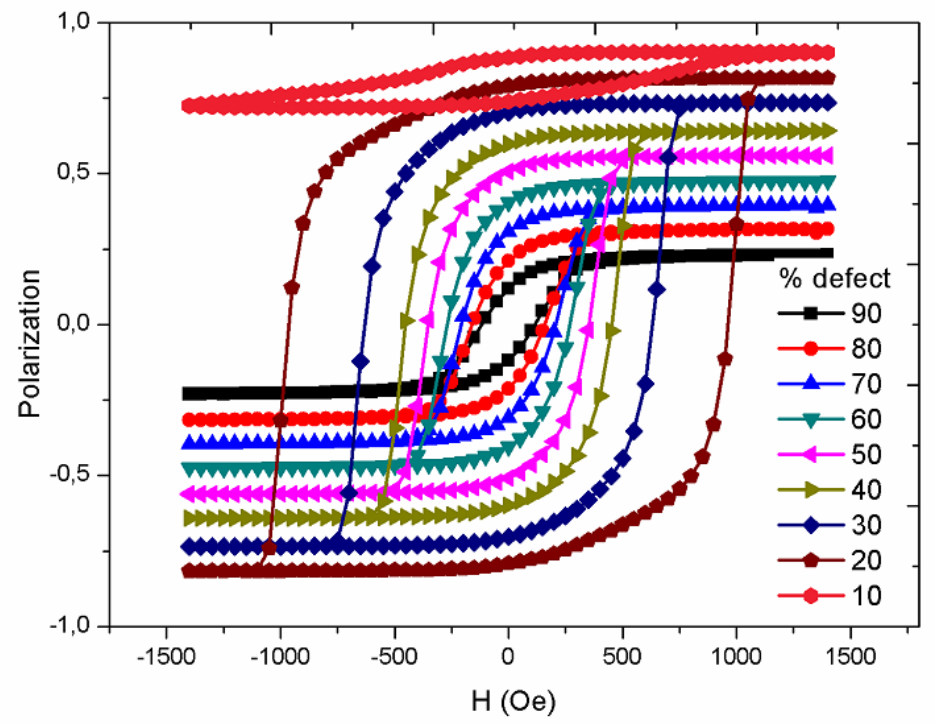

Figure.6.7: electric polarization as a function of applied field H for different defect concentration % in BFO thin films at 300K and $\mathbf{J_{me}}$=4.202meV.

6.4 Conclusion:

In summary, ferroelectric, magnetic, and magnetoelectric properties of BFO thin films were investigated using Monte Carlo simulation. The calculated exchange coupling interactions of magnetic and ferroelectric sublattices (in meV) are found $\mathbf{J_{m1}}$=1.568, $\mathbf{J_{m2}}$=-0.784, $\mathbf{J_{e1}}$=8.530, $\mathbf{J_{e2}}$= 5.118, respectively. The thermal variation of internal energy, specific heat, magnetization, electric polarization and their susceptibilities in BFO thin films have been obtained. The BFO thin film undergoes two-phase transitions, the magnetic transition at $\mathbf{T_N}$=650K and the ferroelectric transition at $\mathbf{T_C}$=1100K. The calculated magnetoelectric coupling interactions, corresponding to experimental data in BFO system, was found at $\mathbf{J_{me}}$=4.202 meV. Moreover, the effect of magnetoelectric coupling interactions $\mathbf{J_{me}}$ on M-H, P-H hysteresis loops and magnetoelectric voltage coefficient were studied. A strong correlation between magnetoelectric voltage coefficients and defect on electric dipoles was observed. Interestingly, a large magnetoelectric voltage coefficient of **104 mV/(cm.Oe)** was carried out in BFO thin films with **25%** defects using Monte Carlo simulation, which makes it more suitable for magnetoelectric devices. The computed results are very close to the reported experimental data.

Chapter 7

First principles study on $BiFeO_3$-$REMnO_3$ (RE = Er, Eu, Gd, Ho, La, Tb)

7.1. Introduction:

Perovskite $BiFeO_3$ is one of the most studied multiferroic system which possesses both ferroelectricity and antiferromagnetic orders, has potential applications in information storage, sensors , electric random access memories (FeRAMs), potential magnetoelectrics, spintronics [97], [265], [266] due to the room temperature multiferroic properties [267], [268]. At 300K, BiFeO3 adopts a rhombohedral perovskite structure with a space group of *R3c* [269], with a large remnant polarization of ~90 μC cm^{-2} [270]. Further, this compound exhibits ferroelectricity with a Curie temperature T_C = 1103 K [271] and antiferromagnetic order at room temperature, with weak ferromagnetism with a Neel temperature T_N = 643 K [272].

Recently, intense experimental and theoretical research investigations have been focused on the effects of simultaneous substitution of Bi and Mn in $BiFeO_3$ in order to improve its multiferroic properties for multifunctional applications. M.A. Basith et al.[273], [274] reported that the dielectric and magnetic properties of $BiFeO_3$ improved by co–substitution of Bi- and Fe- sites of $BiFeO_3$ by Gd and Ti. Further, Tang et al[231] showed that the ferroelectric properties were enhanced in $Bi_{0.9}Gd_{0.1}Fe_{0.9}Mn_{0.1}O_3$ in comparison with $BiFeO_3$. In addition, Zhou et al. surmised that saturation magnetization and optical band gap increased in Sm and Mn co–doped $BiFeO_3$ [275]. In the other hand, a structural transformation from rhombohedral (R3c) to orthorhombic (Pn21a) symmetry with significantly enhanced magnetization was obtained in $BiFeO_3$ co-substituted with Gd and Mn [276]. Similar improvement of multiferroic properties was observed by Lahmar et al.[255], [277] for rare earth element (RE) and Mn co-substitution of $BiFeO_3$, where a structural transition from monoclinic ($BiFeO_3$) to orthorhombic ($BiFeO_3$-REMnO3) was highlighted up to 10 mol% substitution concentration.

In the present chapter, spontaneous polarization, magnetic, and electronic properties of RE- and Mn- co- substituted $BiFeO_3$ were investigated by first principles. Furthermore, a pseudo Jahn−Teller distortion was predicted for BiFeO3-GdMnO3 system. To the best of our knowledge, first-principles study of RE- and Mn- co-substituted $BiFeO_3$ has not been reported yet. Thus, these results are likely to offer useful information to the research communities' deal with BFO based multiferroic materials.

7.2. Computational methods:

Density functional theory (DFT) [23] calculations were performed within the local spin density approximation (LSDA+U) as implemented in the ABINIT package [152]. We include an effective Hubbard parameter U_{eff}=U-J equal to 4.5 eV, which is sufficient to describe related bulk properties and is a better description of localized Fe(3d) and Mn(3d) electron [278]. While for rare earth 4f-orbitals, the U_{eff} is fixed in about 8 eV [279]. We use optimized pseudo-potentials generated with OPIUM [280]. These calculations are performed with a kinetic energy cutoff of 50 Hartree, and 10 x 8 x 10 Monkhorst-Pack k-point mesh as well a sa Gaussian smearing of 0.04 eV. Spin-polarized calculations with a G-type antiferromagnetic order were performed for $BiFeO_3$-$REMnO_3$. Notice that in our calculation, the spin-orbit interaction is not included.

M. Hasan et al.[276] reported that the $BiFeO_3$-$GdMnO_3$ crystalized under orthorhombic (Pn21a) with lattice parameters: a=5.587 Å, b=7.7987 Å and c=5.451 Å. Likewise, Lahmar et al.[255] observed that the structure of $BiFeO_3$ was adapted to the structure of rare-earth manganites REMnO3 by adding 10 mol%. Herein, the co-substitution of $BiFeO_3$ with 12.5 % of RE and Mn were created by changing Bi and Fe atoms by RE and Mn atoms in $BiFeO_3$, respectively. Then, we optimized both the lattice parameters and the atomic positions of the $BiFeO_3$-$REMnO_3$ structure to obtain their ground state properties by minimization of the total energy, (see **Figure.7.1**).

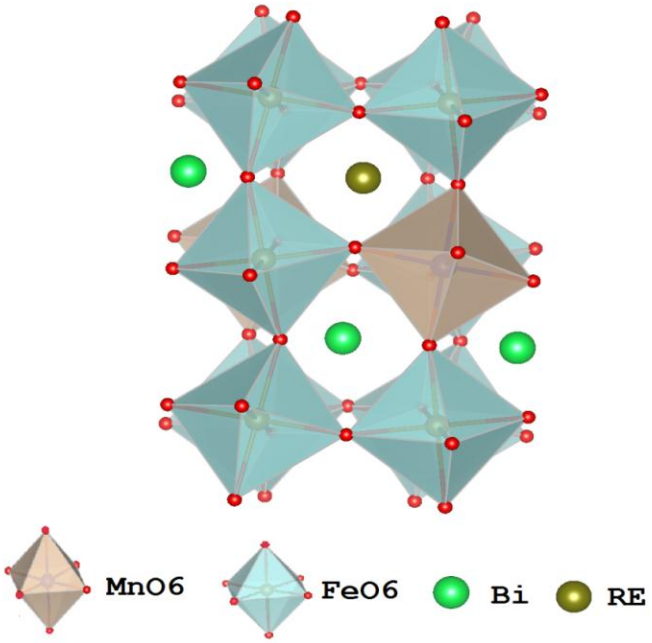

Figure.7.1: structure of $BiFeO_3$-$REMnO_3$ (RE=Er, Eu, Gd, Ho, La, Tb)

7.3. Results and discussion

7.3.1. Structural analysis

Table.7.1 summarizes the optimized lattice parameters of $BiFeO_3$-$REMnO_3$ for different rare earth elements (RE = Er, Eu, Gd, Ho, La, Tb). The lattice parameters calculated are compared to the available experimental results. We note that the calculated lattice parameters for RE = Gd are close to the experimental results obtained by M. Hasan et al.[276], with the observation of a structural transformation from rhombohedral (R3c) to orthorhombic (Pn21a) symmetry in co-substitution with Gd and Mn in $BiFeO_3$.

***Table.7.1**: The calculated lattice parameters of $BiFeO_3$-$REMnO_3$. The experimental values are taken from Ref* [276].

	a (Å)	**b (Å)**	**c(Å)**
$BiFeO_3$-$ErMnO_3$	10.476	14.435	10.211
$BiFeO_3$-$EuMnO_3$	10.394	14.516	10.191
$BiFeO_3$-$GdMnO_3$	10.355	14.410	10.113
Exp : Ref [276]	10.56	14.72	10.30
$BiFeO_3$-$HoMnO_3$	10.385	14.475	10.170
$BiFeO_3$-$LaMnO_3$	10.388	14.608	10.253
$BiFeO_3$-$TbMnO_3$	10.391	14.449	10.176

7.3.2. Electronic and magnetic properties

Figure.7.2a illustrates the total density of states of $BiFeO_3$-$REMnO_3$ (RE = Er, Eu, Gd, Ho, La, Tb). The vertical dashed lines denote Fermi energy level, which is indicated at 0 eV. Noting that the total density of state of $BiFeO_3$-$LaMnO_3$ is symmetrical. As a result, a minimum of magnetic moment per cell of 1.5 μ_B (see **Figure.7.2b**) and metallic behavior were observed for $BiFeO_3$-$LaMnO_3$. While, asymmetrical total density of states with metal characteristic are observed for $BiFeO_3$-$REMnO_3$ with RE = Er, Eu, Ho and Tb. Whereas, a half-metallic property has been observed in $BiFeO_3$-$GdMnO_3$ and the total magnetic moment increases by 4.3μ_B in comparison with $BiFeO_3$-$LaMnO_3$. **Figure.7.2b** shows the total and partial magnetic moments in $BiFeO_3$-$REMnO_3$. We note that the total magnetic moment is decisively governed by the magnetic moments of rare-earth elements. Our calculations achieved a total magnetic moments of 3.58, 4.69, 5.8, 4.27, 1.5 and 6.31 μ_B in BiFeO3-REMnO3 for RE= Er, Eu, Gd, Ho, La and Tb, respectively. It is worth noting that these results are similar to the observations reported on RE doped $BiM_{0.8}Fe_{0.9}Co_{0.1}O_3$ (RE=La and Er) studied by first-principles [281]. Experimentally, W. Ye et al.[282] reported that (Ho, Mn) co-doped $BiFeO_3$ thin films enhanced the basic magnetization. Moreover, this observation is in agreement with the results reported in refs.[255], [277], where the improvement of the mutiferroic properties was attributed to the RE- and Mn- co-substituted $BiFeO_3$.

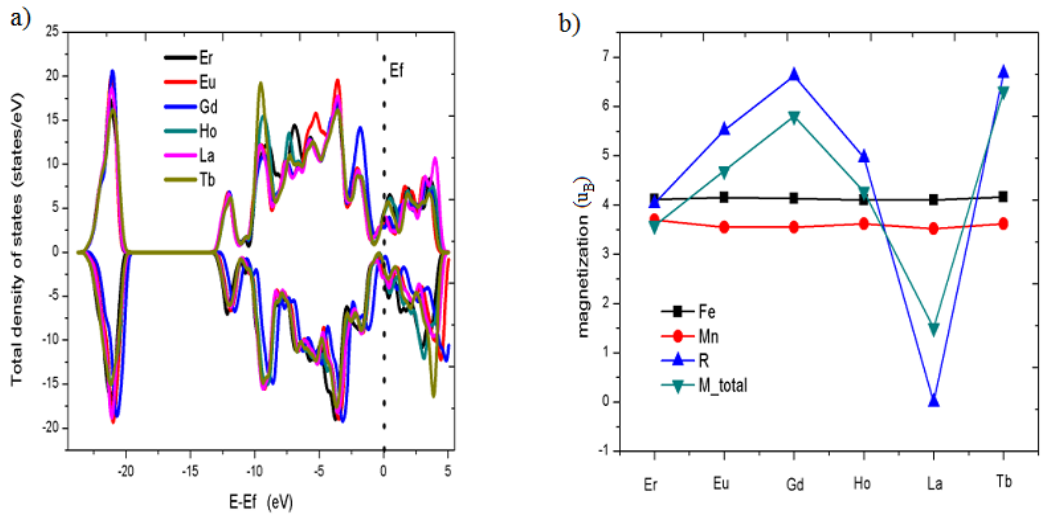

Figure.7.2: (a) Total density of states and (b) magnetic moments of $BiFeO_3$-$REMnO_3$ (RE = Er, Eu, Gd, Ho, La, Tb), the Fermi energy is set to be 0 eV.

The spin up of the Er-4f state is presented from -9 to -2.5 eV which is hybridized with the Mn-3d, Bi-6p, Fe-3d and O-2p states as shown in **Figure.7.3a**. In addition, the conduction band minimum is principally among the contribution of the strong hybridizations of Er-4f, Er-5p and Bi-6p states. Experimentally, the magnetization improved in $Bi_{0.8}Er_{0.2}Fe_{0.9}Mn_{0.1}O_3$ compounds [283], due to the super-exchange interaction between Er-4f and Fe-3d electrons [283]. The density of states of $BiFeO_3$-$EuMnO_3$ is illustrated in **Figure.7.3b**. The valence band between -6 to 2.5 eV, is formed by states of Eu-4f, Mn-3d, Bi-6p, and O-2p atoms. The top of the conduction band is mainly formed by Eu-4f, Eu-4d, Fe-4d and Bi-6p. For $BiFeO_3$-$GdMnO_3$, the spin up of Gd-4f localized in top of the valence band between 2.5 and 0 eV, which is hybridized with the O-2p state with a small contribution of Mn-d and Bi-s (see **Figure.7.3c**. In addition, the spin up Mn-3d state at Fermi level converts the systems to half-metallic character.

A similar behavior has been observed for $BiFeO_3$-$HoMnO_3$, where the Ho-4f states hybridized in valence band with the Mn-3d, Bi-6p, Fe-3d and O-2p states as shown in F**igure.7.3d**. Further, the Fermi level are occupied by the Ho-4d Mn-3d and O-2p states, suggesting that the incorporation of Ho and Mn changed the $BiFeO_3$ from a semiconductor to a conductor material. The maximum of valence band is composed of Bi-6p, O-2p, Mn-3d and La-4d states with a strong overlapping between -7.5 eV and 0 eV as shows in **Figure.7.3e**. However, Spin up of the Fe-3d state and spin down of Fe1-3d are localized at -9 eV, which is hybridized with the O-2p state. In addition, the lowest conduction band is composed of Bi-6p, Fe-3d, La-4d and La-5p states with small admixture of O-2p states. Moreover, The partial density of states of $BiFeO_3$-$TbMnO_3$ is presented in **Figure.7.3f.** The valence band maximum is dominated by the Mn-3d, Bi-4d and O-2p states. The main Tb-4f valence band is found at around -9 eV, which hybridized with the Fe-3d and small contribution of Mn-3d and O-2p states. In addition, it is found that the unoccupied Tb-4f state are around 4 eV above the Fermi level. It can also be observed that in all $BiFeO_3$-

$REMnO_3$ there is a sharp peak that appears at the Fermi level and it is half occupied with the spin up of Mn-3d. Densities of states of in BiFeO3-REMnO3 indicates that the strong hybridization of RE-4f, Mn-3d, Bi-6p, Fe-3d and O-2p states could be the electronic origin of magnetoelectric coupling in this system.

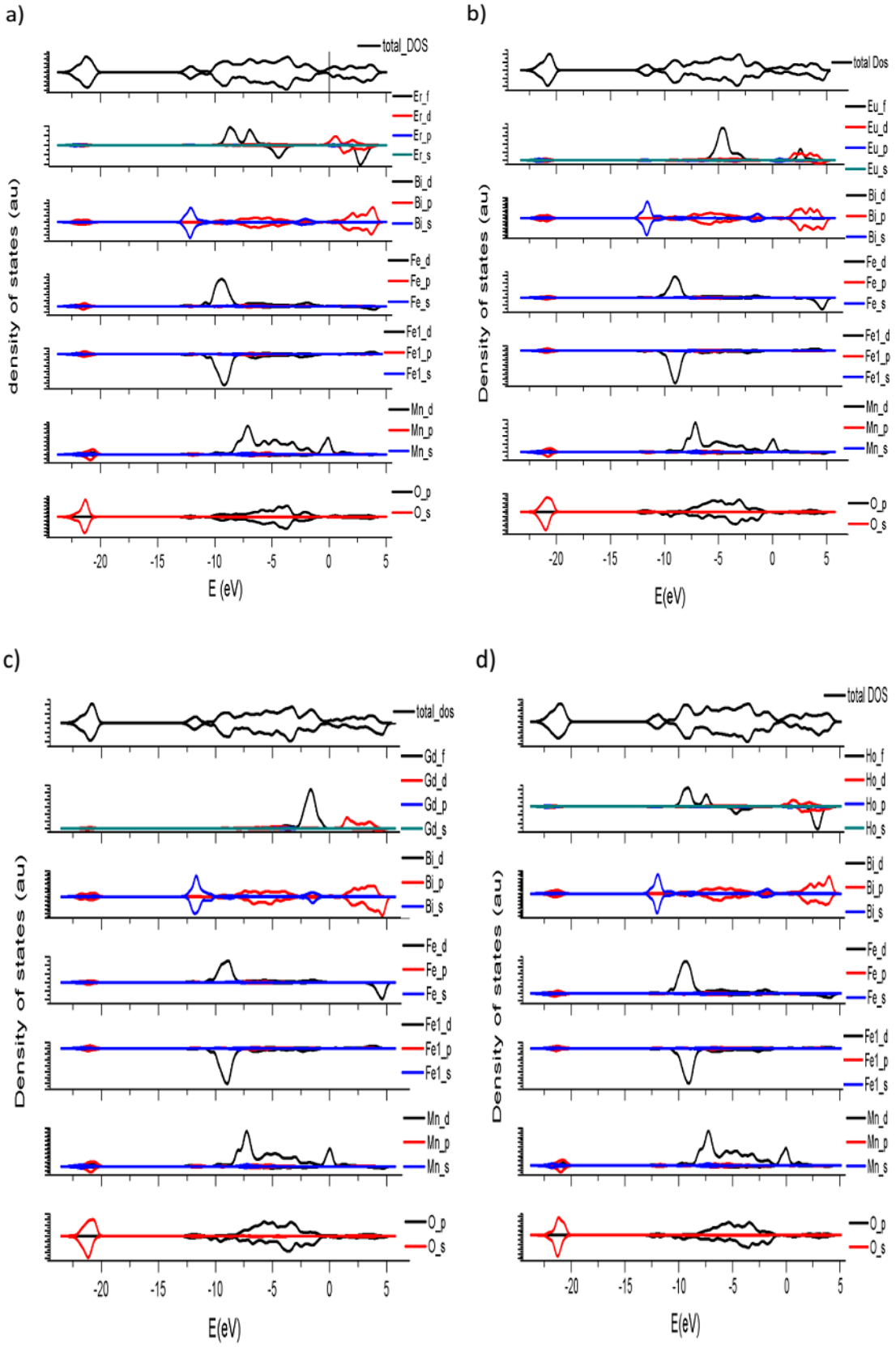

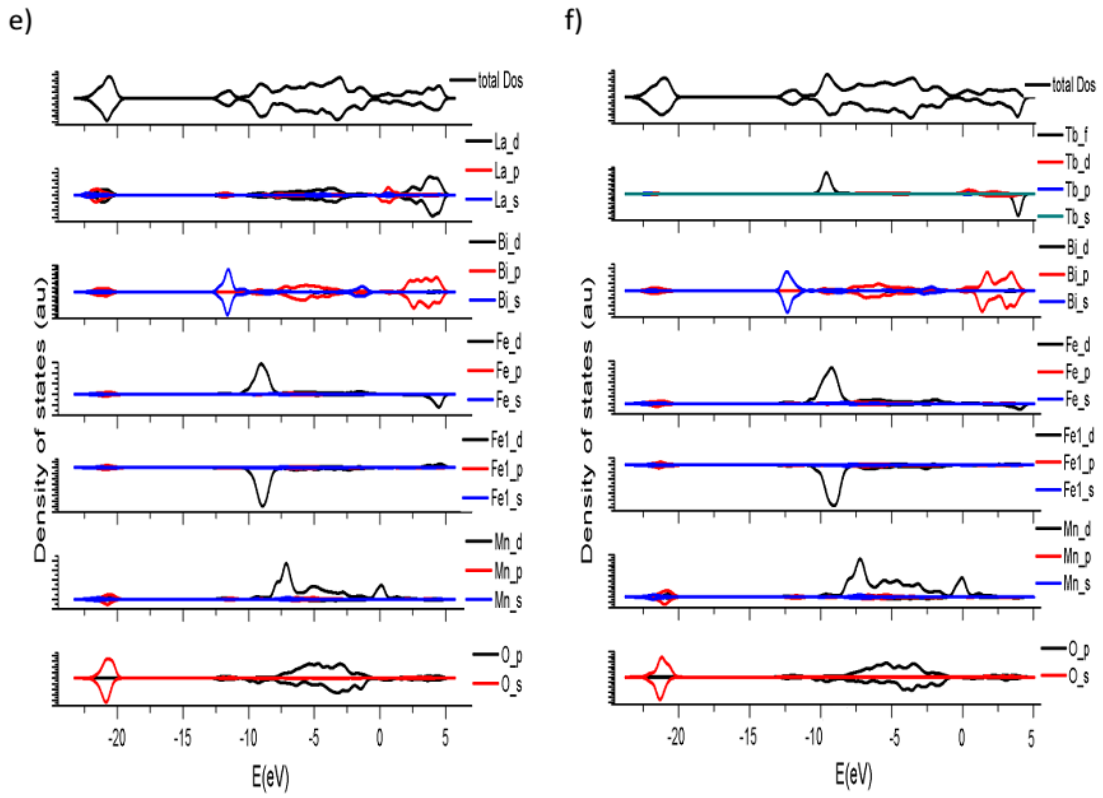

Figure.7.3: Total and partial densities of states of (a) $BiFeO_3$-$ErMnO_3$, (b) $BiFeO_3$-$EuMnO_3$, (c) $BiFeO_3$-$GdMnO_3$, (d) $BiFeO_3$-$HoMnO_3$, (e) $BiFeO_3$-$LaMnO_3$ and (f) $BiFeO_3$-$TbMnO_3$ compounds, the Fermi energy is set to be 0 eV.

The Fe-3d electrons in $BiFeO_3$ stay at high-spin configuration t_{2g}^3 e_g^2, (the valence of Fe ions is close to +3 (Fe^{3+})), and both of spin up and spin down states of Fe-3d are split by the octahedral crystal ligand field into t_{2g} and e_g orbitals [284]. **Figure.7.4b** presents the spin up and spin down of Gd-d, Fe-3d and O-2p states, which are characterized by a strong overlapping of Gd-d, Fe-3d (e_g) and O-2p states between -7.5 eV and 0 eV, indicating the covalent feature for the Gd–O bonding and the hybridization between the Fe-3d and O-2p states decreases. As a result, Gd doping decreases the valence fluctuation of Fe ions, the remanent magnetization decreases and increases the local magnetic moment due to high magnetic moment of Gd, which is in good agreement with experimental study reported by Lahmar et al. [10], where the magnetization decreases with increasing the concentration of $GdMnO_3$ (see **Figure.7.4a**). Also, a similar behavior was observed by M. Hasan et al.[276]in Mn doping in $Bi_{0.85}Gd_{0.15}Fe_{1-x}Mn_xO_3$ system, in which the saturation magnetization rises gradually up to 10% Mn doping in $Bi_{0.85}Gd_{0.15}Fe_{1-x}Mn_xO_3$ system. However, a further increasing of the Mn doping concentration, saturation magnetization decreased.

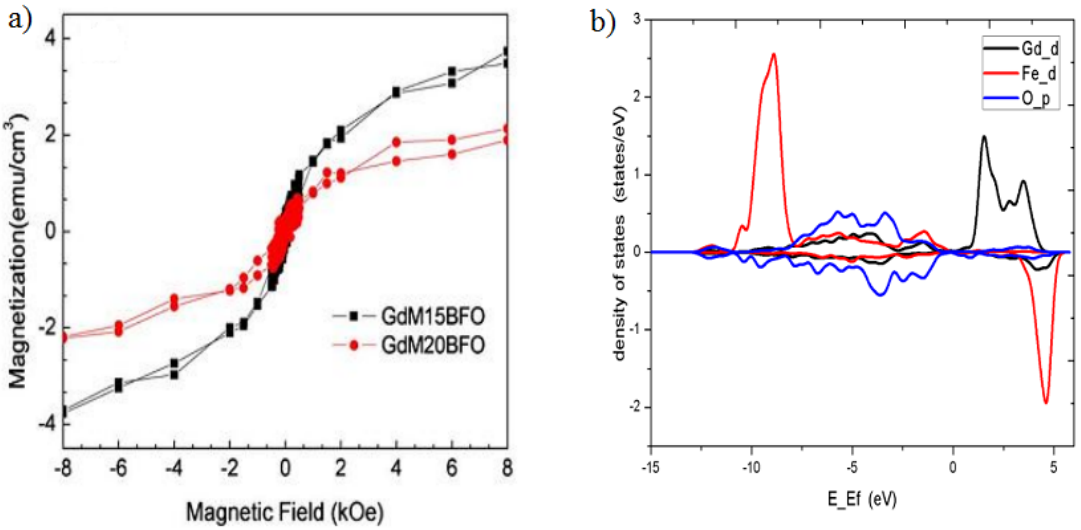

Figure.7.4. (a) Magnetization vs magnetic field of $Bi_{0.85}Gd_{0.15}Fe_{0.85}Mn_{0.15}O_3$ (GdM15BFO) and $Bi_{0.8}Gd_{0.2}Fe_{0.8}Mn_{0.2}O_3$ (GdM20BFO) thin films at RT reported in [10].**(b)** Partial densities of states of BiFeO3-$GdMnO_3$ (Gd-d, Fe-3d and O-2p states), the Fermi energy is set to be 0 eV.

7.3.3 Jahn-Teller distortion:

Jahn-Teller distortion or Jahn-Teller effect was proposed in 1937, which removes the degeneracy of the e_g and t_g orbitals and undergoes distortion to form a system of lower symmetry and minimum of energy [285]. The electronic configuration of Mn in $BiFeO_3$-$GdMnO_3$ is $3d^4$, with the oxidation state of Mn^{3+}, giving a high-spin configuration for Mn^{3+}, which leads to the activation of the Jahn-Teller distortion [286]. There are two different electronic configurations for Mn^{3+} ion: $(t_{2g})^3(dz^2)$ which induces two bonds along the z-axis direction and $(t_{2g})^3$ $d(x^2-y^2)$ which induces four bonds in the xy-plane. The **Figure.7.5a** shows the calculated Mn–O and Fe–O bond lengths in $BiFeO_3$-$GdMnO_3$. The bond lengths of the Mn–O bonds in MnO_6 octahedron are 3.735 Å, 3.715 Å, 3.676 Å, 3.709 Å, 3.653 Å and 3.634 Å. While, the Fe-O bonds in FeO_6 octahedron are 3.749 Å, 3.782 Å, 3.706 Å, 3.733 Å, 3.727 Å and 3.688 Å. Comparing with FeO_6 octahedron, the O atoms move towards the Mn atom, indicating that a local distortion takes place around of Mn^{3+} ions in $BiFeO_3$-$GdMnO_3$. The partial density of states of Mn-3d states, Mn-$3dz^2$ and Mn-$3d(x^2- y^2)$ orbital of Mn atoms is shown in **Figure.7.5b.** Our calculations show that the distortion is not a strict Jahn-Teller distortion but is instead a preferential elongation of two of the Mn–O bonds (**i.e.,** the pseudo Jahn-Teller distortion) due to the hybridization of the unoccupied 3d dxz and dx^2-y^2 orbitals **(**see **Figure.7.5b).** L. F. J. Piper et al. [287] reported similar distortion of the Mn local environment in Li_xMnPO_4 studied by soft and hard synchrotron-based spectroscopy with first-principles density functional theory within the GGA+U.

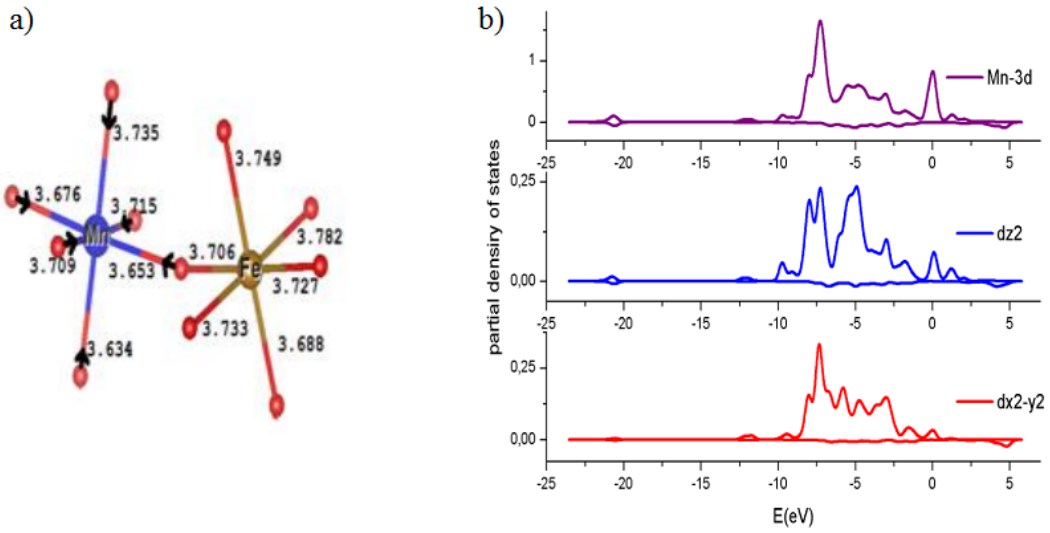

Figure.7.5: (a) pseudo Jahn–Teller distortion of the MnO_6 octahedron around of Mn in $BiFeO_3$-$GdMnO_3$, **(b)** the partial density of states of Mn-3d states, Mn-3dz^2 andMn-3d(x^2- y^2) orbital of Mn atoms in$BiFeO_3$-$GdMnO_3$. The Fermi energy is set to be 0 eV.

Another important parameter describes the octahedral tilting angle (θ) between two adjacent octahedra, which are manifested by angles between different Fe-O-Fe and Fe-O-Mn bonds in these octahedra. The Fe-O-Fe and Mn-O-Fe bond angles between two adjacent octahedra in $BiFeO_3$-$GdMnO_3$ are shown in **Figure.7.6a**.We note that both Fe-O-Fe and Mn-O-Fe bond angles are lower than 180° and the tilting angle θ for Fe-O-Fe is lower than the Mn–O–Fe (from ~ 152° to ~ 154° in b-axis and from ~ 150.92° to ~ 154.72° in a-axis)in $BiFeO_3$-$GdMnO_3$. The achieved values for Fe-O-Fe bond angle are very comparable to the experimental results of $Bi_{0.85}Gd_{0.15}Fe_{0.9}Mn_{0.1}O_3$[276]. In addition, the O-Mn-O and O-Fe-O bond angles are 178.15° and 179.15°, respectively, which are lower than 180° (see **Figure.7.6b)**. Also, the individual octahedron MnO6/ FeO6 shows that the individual O-Mn and Mn-O / O-Fe and Fe-O bond angles are not identical with 90° (**see Figure.7.6b)**, indicating that the individual octahedron also contains distortions arising both from asymmetry in Mn-O bond lengths and bond angles. The changes in the tilting angle θ for Fe-O-Fe and Mn–O–Fe indicated a rotation of oxygen octahedra which can be explain the origin of the peak at 300 cm−1 observed in Raman measurements [277]. It is worth mentioning that the phase transition temperature of rhombohedral (R3c)- to-orthorhombic (Pn21a) was found to depend on Mn concentration in $Bi_{0.85}Gd_{0.15}Fe_{1-x}Mn_xO_3$.The stabilization of a pure orthorhombic phase at room temperature is reached for x=0.15 [255], [276], [277]. Furthermore, the increasing of Gd/Mn doping in $Bi_{1-y}Gd_yFe_{1-x}Mn_xO_3$ produced the changes in Mn-O bond lengths and bond angles, leading to a local stresses in the system responsible for the stabilization of the orthorhombic phase.

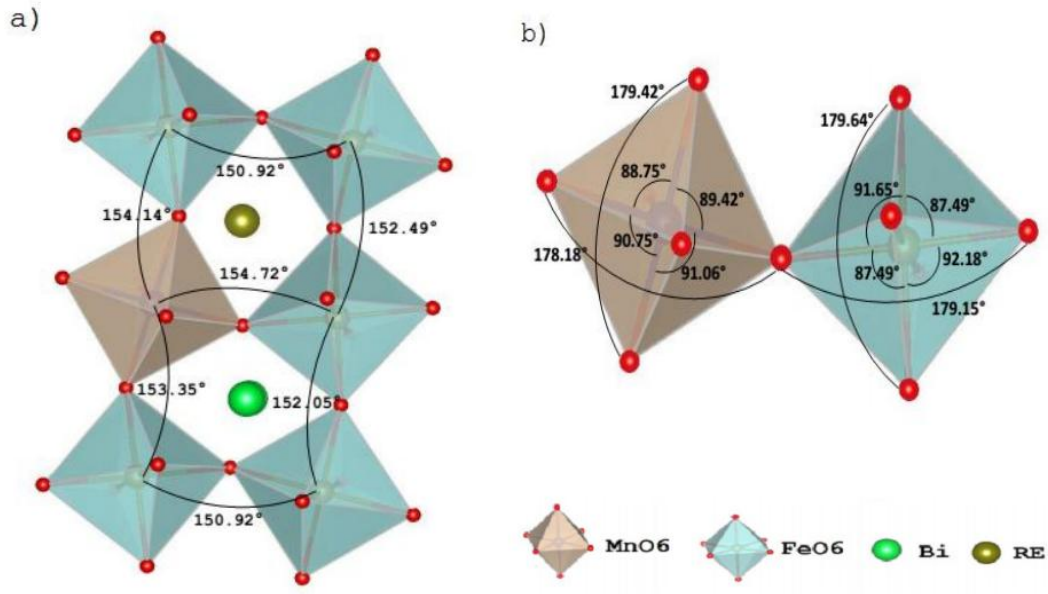

Figure.7.6: (a) Fe–O–Fe and Fe–O–Mn bond angles between two adjacent octahedra and **(b)** Mn–O and Fe–O bond angles in the individual octahedron in in $BiFeO_3$-$GdMnO_3$

7.3.4 Spontaneous polarizations:

Spontaneous polarization was computed using first principle calculations based on the Berry phase method [288]. The total polarization can be expressed as the sum of ionic polarization (P_{ion}) and electronic polarization (P_{el}) [289]. The Berry phase calculation yields a spontaneous polarization of 56.06, 60.84, 47.80, 62.02, 49.73 and34.97μC/cm^{2}in $BiFeO_3$-$REMnO_3$ for RE= Er, Eu, Gd, Ho, La and Tb, respectively, as shown in **Figure.7.7a**. Excellent agreement between the calculated spontaneous polarization and the experimental results reported by Lahmar et al.[255], [277]. In addition, Y. Han et al. [283] observed a similar improvement of ferroelectric property in $Bi_{0.8}Er_{0.2}Fe_{0.9}Mn_{0.1}O_3$. Moreover, a giant 2Pr value of 231.4 μC/cm2 is observed in $Bi_{0.92}Ho_{0.08}Fe_{0.97}Mn_{0.03}O_3$ thin films by W. Ye et al [282]. The direction of spontaneous polarizations in $BiFeO_3$-$REMnO_3$ depends on the rare earth elements as shown in **Figure.7.7b,** where the direction of spontaneous polarization in $BiFeO_3$-$REMnO_3$ is [111] for RE= Er, Eu, Gd, Ho and Tb, while the direction of spontaneous polarization in $BiFeO_3$-$LaMnO_3$ is [101] and [001] for $BiFeO_3$-$TbMnO_3$.

Several works were demonstrated that $REMnO_3$ doped $BiFeO_3$ (or RE doped $BiFeO_3$) systems exhibit an enhancement of ferroelectric, ferromagnetic and electrochemical properties at concentration of 10%. M. S. Bozgeyik et al.[290] showed an improvement of saturation magnetization in $Bi_{0.9}La_{0.1}Fe_{0.9}Gd_{0.1}O_3$ (about four times) in comparison of $Bi_{0.9}La_{0.1}FeO_3$. A saturation magnetization of 2.20 emu/g was measured in Bi0.85Gd0.15Fe0.9Mn0.1O3 with coexistence of the both rhombohedral (R3c) and orthorhombic (Pn21a) phases [276]. Furthermore, the maximum of piezoelectric coefficient, remanent polarization, and strain were obtained for x = 0.10–0.12 in $Bi_{1-x}Sm_xFe_{0.99}Ti_{0.01}O_3$ thin films [291]. The obtained results were related to the coexistence of R3c and Pna21 phases (Morphotropic phase

boundary (MPB)) which leads to the sharp increase of these properties [292]. Regarding the presented work, the density functional theory clarifies the properties of the bridging phase $Pna2_1$ that is the origin of high multiferoic properties in $BiFeO_3$-$REMnO_3$.

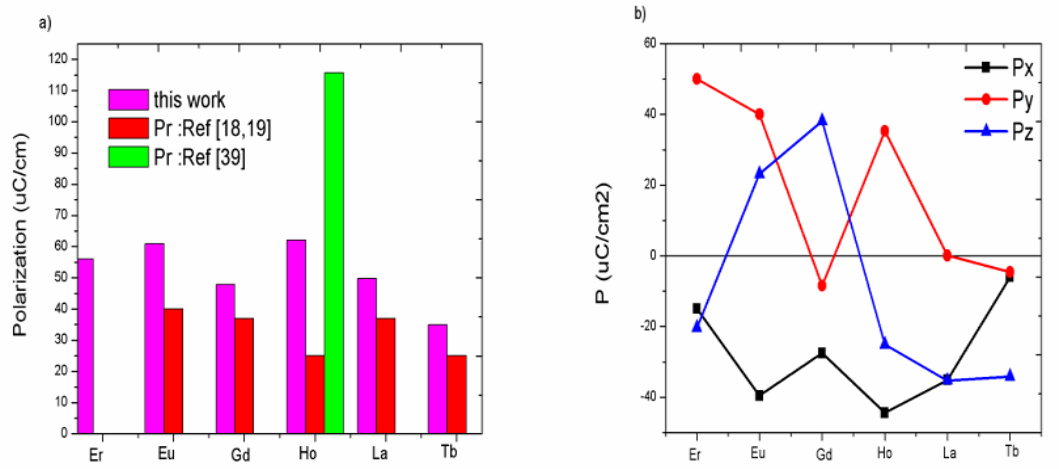

Figure.7.7 : (a) Total spontaneous polarization with the experimental results reported in [18,19,39] and **(b)** its projection on (x, y, z) axis for $BiFeO_3$-$REMnO_3$ (RE = Er, Eu, Gd, Ho, La, Tb).

7.4 Conclusion:

First-principles in the framework of the density functional theory has been used to study the multiferroic properties of $BiFeO_3$-$REMnO_3$(RE = Er, Eu, Gd, Ho, La, Tb). Our calculations achieved a total magnetic moment of 3.58, 4.69, 5.8, 4.27, 1.5 and 6.31 μ_B in $BiFeO_3$-$REMnO_3$ for RE= Er, Eu, Gd, Ho, La and Tb, respectively. In comparison with FeO_6 octahedron, the O atoms move towards the Mn atom, indicating that a local distortion takes place around of Mn^{3+} ions in $BiFeO_3$-$GdMnO_3$. Our calculations showed that the distortion is not a strict Jahn-Teller distortion but it is a preferential elongation of two of the Mn-O bonds (i.e., the pseudo Jahn -Teller distortion) due to the hybridization of the unoccupied 3d dxz and dx^2-y^2 orbitals. Measurements of the tilting angle θ for Fe-O-Fe in $BiFeO_3$-$GdMnO_3$ are found lower than the Mn-O-Fe (from ~ 152° to ~ 154° in b-axis, and from ~ 150.92° to ~ 154.72° in a-axis), which are lower than 180°. The Berry phase calculation yields a spontaneous polarization of 56.06, 60.84, 47.80, 62.02, 49.73 and 34.97 $\mu C/cm^2$ in $BiFeO_3$-$REMnO_3$ for RE= Er, Eu, Gd, Ho, La and Tb, respectively, which are close to the experimental results.

General Conclusions

Numerical modelling of functional materials is developing rapidly to satisfy the need to improve existing devices and to set up innovative systems. Several approaches (equivalent circuit method, DFT, simulation, etc.) are possible. In all cases, it is essential to have pertinent laws of such behavior which necessary for these numerical tools. The aims of this thesis is the theoretical investigations and magnetoelectric prediction in some functional thin films. By using density functional theory (DFT) and Monte Carlo simulation we have analyzed the magneto-electric, magnetic, electronic and ferroelectric properties of (2-2)-type nanocomposites (CoFe2O4/PbZr0.5Ti0.5O3 and NiFe2O4/PbZr0.5Ti0.5O3), single-phase BiFeO3 and MnGdO3-doped BiFeO3.

DFT results indicate that the NFO/ZTO is more favorable energetically than the NFO/PbO at the NiFe2O4/PZT interface. As well as the electronic origin of the strong magnetoelectric coupling at the NFO/ZTO interface is due to the hybridization of the orbitals of the Ni, Fe, T, Zr, O interface atoms. The calculated magnetoelectric couplings at the NiFe2O4/PZT interface for NFO/ZTO and NFO/PbO are respectively: $\boldsymbol{\alpha_s = 3.15 \times 10^{-10}}$ et $\mathbf{0.52 \times 10^{-10}}$ G.cm/V, which are of the same order of magnitude as the calculated magnetoelectric coefficient given in the literature. These values are of the same order in magnitude with the calculated magnetoelectric coefficient ($\mathbf{6.7 \times 10^{-10}}$ G.cm/V) in Ni/$PbTiO_3$ heterointerface [202], and with $\mathbf{2.3 \times 10^{-10}}$ G.cm/V in Ni/$BaTiO_3$ system [178]. In addition, the stronger bonding in the NFO/ZTO interfacial layers will inevitably increase the cohesive energy between the NFO and PZT layers, which is already evident from the results of work of separation. Obviously, the magnetoelectric coupling for the NFO/ZTO and NFO/PbO interfaces demonstrate that the magnetoelectric coupling depends strongly on the bonding mechanisms at the interface.

A Monte Carlo model has been developed to study the ferroelectric properties of PbZr1-xTixO3 (PZT). The proposed model aims to calculate the exchange couplings in PbZr1-xTixO3. The effect of temperature on the ferroelectric properties of PZT, such as hysteresis cycles, polarization and coercivity field have been studied. It's observed that the polarization curves are symmetric for both positive and negative external electrical field values. Also, the area of hysteresis loops becomes narrower as the content of Zr in PZT increases. For x=0 , $PbZrO_3$ thin films was in the antiferroelectric state, evidenced by the presence of a double hysteresis loop with zero remanent polarization. While increasing x values, a weak ferroelectricity is observed for $PbZr_{0.9}Ti_{0.1}O_3$ and $PbZr_{0.8}Ti_{0.2}O_3$. However, beyond x=0.3, a typical ferroelectric hysteresis loops are observed. In addition, the phase diagram as a function of the x-values of Ti in PbZr1-xTixO3 was determined. The obtained values are in good agreement with experimental results reported by Isaku Kanno et al [8] in (001) $PbZr_{1-x}Ti_xO_3$ epitaxial films grown on $SrTiO_3$ substrates using radio-frequency sputtering technique. Furthermore, at 300K, the recoverable

energy densities of **13.93** J/cm^3 and **9.74** J/cm^3 were obtained in PZT for x=0 and 0.1, with an energy density efficiency of **78.73**% and **94**%, respectively, which is closer to the experimental results (**14.5**J/cm^3) reported in [227].

On the other hand, the ferroelectric, magnetic and magnetoelectric properties of the heterostructures NiFe2O4/PZT (NFO/PZT), CoFe2O4/PZT (CFO/PZT), NiFe2O4/PZT/CoFe2O4 (NFO/PZT/CFO) and NiFe2O4/PZT/NiFe2O4 (NFO/PZT/NFO) were obtained using Monte Carlo simulation with Heisenberg model. The effect of temperature on magnetic polarization, electrical polarization and their susceptibilities were examined. We note that magnetoelectric coupling interactions $\mathbf{J_{me}}$ corresponding to the experimental magnetoelectric voltage coefficient for NFO/PZT and CFO/PZT are **4.120** and **0.625** meV, respectively. Experimentally, NFO/PZT heterostructures with lower magnetostriction have a strong magnetoelectric voltage coefficient, whereas CFO/PZT heterostructures with a strong magnetostrictive present a weaker magnetoelectric voltage coefficient. This can be explained by the strong interfacial magnetoelectric coupling interaction $\mathbf{J_{me}}$=**4.120** meV at NFO/PZT interface, while the predicted $\mathbf{J_{me}}$ for CFO/PZT interface is **0.625** meV. The maximum magnetoelectric voltage coefficients that are predicted are **500, 55, 1405** and **650** mV/(cm.Oe) for NFO/PZT, CFO/PZT, NFO/PZT/NFO and NFO/PZT/CFO, respectively. The calculated value of the magnetoelectric voltage coefficient in the proposed NFO/PZT/CFO and NFO/PZT/NFO heterostructures are comparable to the experimental results (**1225** mV/(cm.Oe)) reported by L. Jian [246] in PZT/NFO/PZT films. The presented theoretical results can provide suitable guidance for developing magnetoelectric devices.

The simulation of the ferroelectric, magnetic and magnetoelectric properties of thin films of the multiferroic BiFeO3 are obtained in this work using Monte Carlo simulation. The exchange coupling interactions in the magnetic and ferroelectric subalattices corresponding to the experimental critical temperature have been estimated. Thermodynamic quantities such as internal energy, specific heat, magnetization, electric polarization and their susceptibilities as a function of temperature in **BFO** thin films were studied. The presence of a one hysteresis loop with weak remanent magnetization in the **M-H** loop suggesting that the **BFO** presents the weak ferromagnetism due to the Moriya interaction (DMI). It is found that for $\mathbf{J_{me}}$ up to 1 meV the polarization is not switchable and the increasing of magnetoelectric coupling interaction $\mathbf{J_{me}}$ leads to more and more obvious **P-H** hysteresis loop, indicating that the electric dipoles are switchable by an applied magnetic field. Also, when the magnetoelectric coupling interaction $\mathbf{J_{me}}$ is large enough, a complete switching of the electric dipole by magnetic field has been observed. The electric dipole defects were proposed as a mechanism to enhance the magnetoelectric coupling in **BFO**. Indeed, our simulation demonstrated that the electric polarization can be switched completely with defect concentration **%** at **Bi**-sites in **BFO** thin films at **300K** and $\mathbf{J_{me}}$=**4.202** meV, where all electric dipoles turn to the direction of the applied magnetic, due to the reduction of exchange coupling interactions (Je1 and

Je2) between the electric dipoles. A large magnetoelectric voltage coefficient of **104** mV/(cm.Oe) was predicted in BFO thin films with 25% defects, which makes it more suitable for magnetoelectric devices.

The structural and multiferroic properties of the solid solution BiFeO3-REMnO3 (RE = Er, Eu, Gd, Ho, La, Tb) were studied using the functional density theory. Simultaneous substitution of RE and Mn in the 12.5% BiFeO3 was performed. We found that the total magnetic moment in BiFeO3-REMnO3 is governed by the magnetic moments of the rare earth elements. Our calculations yielded total magnetic moments of 3.58, 4.69, 5.8, 4.27, 1.5 and 6.31μB in BiFeO3-REMnO3 for RE= Er, Eu, Gd, Ho, La and Tb, respectively. The spontaneous polarization in BiFeO3-REMnO3 is respectively: 56.06, 60.84, 47.80, 62.02, 49.73 and 34.97μC/cm2, for RE= Er, Eu, Gd, Ho, La and Tb. The results obtained are similar to the experimental results.

References

[1] N. A. Spaldin et M. Fiebig, « The Renaissance of Magnetoelectric Multiferroics », *Science*, vol. 309, n° 5733, p. 391‑392, juill. 2005, doi: 10.1126/science.1113357.

[2] M. Gajek *et al.*, « Tunnel junctions with multiferroic barriers », *Nat. Mater.*, vol. 6, n° 4, p. 296‑302, avr. 2007, doi: 10.1038/nmat1860.

[3] M. Ye. Zhuravlev, S. S. Jaswal, E. Y. Tsymbal, et R. F. Sabirianov, « Ferroelectric switch for spin injection », *Appl. Phys. Lett.*, vol. 87, n° 22, p. 222114, nov. 2005, doi: 10.1063/1.2138365.

[4] G. Zhong *et al.*, « Deterministic, Reversible, and Nonvolatile Low-Voltage Writing of Magnetic Domains in Epitaxial BaTiO3/Fe3O4 Heterostructure », *ACS Nano*, vol. 12, n° 9, p. 9558‑9567, sept. 2018, doi: 10.1021/acsnano.8b05284.

[5] H. Zhang, J.-Q. Dai, et Y.-M. Song, « Influences of interfacial terminations on electronic structure and magnetoelectric coupling in Fe/KNbO3 superlattices », *Chem. Phys. Lett.*, vol. 619, p. 163‑168, janv. 2015, doi: 10.1016/j.cplett.2014.11.064.

[6] B. Noheda, D. E. Cox, G. Shirane, R. Guo, B. Jones, et L. E. Cross, « Stability of the monoclinic phase in the ferroelectric perovskite ${\mathrm{PbZr}}_{1\ensuremath{-}x}{\mathrm{Ti}}_{x}{\mathrm{O}}_{3}$ », *Phys. Rev. B*, vol. 63, n° 1, p. 014103, déc. 2000, doi: 10.1103/PhysRevB.63.014103.

[7] S. Dong, J.-F. Li, et D. Viehland, « Circumferentially magnetized and circumferentially polarized magnetostrictive/piezoelectric laminated rings », *J. Appl. Phys.*, vol. 96, n° 6, p. 3382‑3387, sept. 2004, doi: 10.1063/1.1781764.

[8] I. Kanno, H. Kotera, K. Wasa, et T. Matsunaga, « T. kamada, and R. Takayama,“ », *Crystallogr. Charact. Epitaxial Pb Zr Ti O3 Film Differ. Zrti Ratio Grown Radio-Freq.-Magnetron Sputtering” J Appl Phys*, vol. 93, n° 7, p. 4091–4096, 2003.

[9] T. MORITA et A. CHO, « A Hydrothermally Deposited Epitaxial PbTiO3 Thin Film on SrRuO3 Bottom Electrode for the Ferroelectric Ultra-High Density Storage Medium », *Integr. Ferroelectr.*, vol. 64, n° 1, p. 247‑257, janv. 2004, doi: 10.1080/10584580490894645.

[10] A. Lahmar, S. Habouti, C.-H. Solterbeck, M. Dietze, et M. Es-Souni, « Multiferroic properties of Bi0.9Gd0.1Fe0.9Mn0.1O3 thin film », *J. Appl. Phys.*, vol. 107, n° 2, p. 024104, janv. 2010, doi: 10.1063/1.3283919.

[11] R. Ramesh et N. A. Spaldin, « Multiferroics: progress and prospects in thin films », *Nat. Mater.*, vol. 6, n° 1, p. 21‑29, janv. 2007, doi: 10.1038/nmat1805.

[12] S. Shankar, M. Kumar, P. Brijmohan, S. Kumar, O. P. Thakur, et A. K. Ghosh, « Signature of multiferroicity and impedance analysis of Co1−xZnxFe2−xLaxO4 nanoparticles », *J. Mater. Sci. Mater. Electron.*, vol. 27, n° 12, p. 13259‑13265, déc. 2016, doi: 10.1007/s10854-016-5473-6.

[13] B. D. Lakshmi, O. F. Caltun, I. Dumitru, K. Pratap, B. P. Rao, et P. S. V. S. Rao, « Bi0.95Mn0.05FeO3 - Ni0.5Zn0.5Fe2O4 Nanocomposites with Multiferroic Properties », *Mater. Today Proc.*, vol. 2, n° 6, p. 3806‑3812, janv. 2015, doi: 10.1016/j.matpr.2015.08.010.

[14] L. Zeng, M. Zhou, K. Bi, et M. Lei, « Giant magnetoelectric effect in negative magnetostrictive/piezoelectric/positive magnetostrictive semiring structure », *J. Appl. Phys.*, vol. 119, n° 3, p. 034102, janv. 2016, doi: 10.1063/1.4940382.

[15] M. D. Nguyen, M. Dekkers, E. P. Houwman, H. T. Vu, H. N. Vu, et G. Rijnders, « Lead-free (K0.5Na0.5)NbO3 thin films by pulsed laser deposition driving MEMS-based piezoelectric cantilevers », *Mater. Lett.*, vol. 164, p. 413‑416, févr. 2016, doi: 10.1016/j.matlet.2015.11.044.

[16] Y. Pei *et al.*, « Effect of CoFe2O4 Content on the Dielectric and Magnetoelectric Properties in CoFe2O4/ Pb(Mg1/3Nb2/3)0.35Ti0.65O3 Composites », *Ferroelectrics*, vol. 410, n° 1, p. 82‑87, nov. 2010, doi: 10.1080/00150193.2010.492726.
[17] N. Ortega, A. Kumar, et J. F. Scott, « DB chrisey, M. Tomazawa, S. Kumari, DGB Diestra, and RS Katiyar », *J Phys Condens Matter*, vol. 24, p. 445901, 2012.
[18] G. Srinivasan, E. T. Rasmussen, B. J. Levin, et R. Hayes, « Magnetoelectric effects in bilayers and multilayers of magnetostrictive and piezoelectric perovskite oxides », *Phys. Rev. B*, vol. 65, n° 13, p. 134402, mars 2002, doi: 10.1103/PhysRevB.65.134402.
[19] G. Srinivasan, E. T. Rasmussen, J. Gallegos, R. Srinivasan, Yu. I. Bokhan, et V. M. Laletin, « Magnetoelectric bilayer and multilayer structures of magnetostrictive and piezoelectric oxides », *Phys. Rev. B*, vol. 64, n° 21, p. 214408, nov. 2001, doi: 10.1103/PhysRevB.64.214408.
[20] A. M. Kadomtseva, A. K. Zvezdin, Yu. F. Popov, A. P. Pyatakov, et G. P. Vorob'ev, « Space-time parity violation and magnetoelectric interactions in antiferromagnets », *J. Exp. Theor. Phys. Lett.*, vol. 79, n° 11, p. 571‑581, juin 2004, doi: 10.1134/1.1787107.
[21] Z. V. Gabbasova *et al.*, « Bi(1-x)R(x)FeO(3)(R=rare earth): a family of novel magnetoelectrics », *Phys. Lett. A*, vol. 158, n° 9, p. 491‑498, sept. 1991, doi: 10.1016/0375-9601(91)90467-M.
[22] P. Hohenberg et W. Kohn, « Inhomogeneous Electron Gas », *Phys. Rev.*, vol. 136, n° 3B, p. B864‑B871, nov. 1964, doi: 10.1103/PhysRev.136.B864.
[23] W. Kohn et L. J. Sham, « Self-Consistent Equations Including Exchange and Correlation Effects », *Phys. Rev.*, vol. 140, n° 4A, p. A1133‑A1138, nov. 1965, doi: 10.1103/PhysRev.140.A1133.
[24] E. Defaÿ, *Integration of Ferroelectric and Piezoelectric Thin Films: Concepts and Applications for Microsystems*. John Wiley & Sons, 2013.
[25] D. Damjanovic, « Ferroelectric, dielectric and piezoelectric properties of ferroelectric thin films and ceramics », *Rep. Prog. Phys.*, vol. 61, n° 9, p. 1267–1324, sept. 1998, doi: 10.1088/0034-4885/61/9/002.
[26] L. E. Cross, « Ferroelectric materials for electromechanical transducer applications », *Mater. Chem. Phys.*, vol. 43, n° 2, p. 108‑115, févr. 1996, doi: 10.1016/0254-0584(95)01617-4.
[27] A. F. Devonshire, « XCVI. Theory of barium titanate », *Lond. Edinb. Dublin Philos. Mag. J. Sci.*, vol. 40, n° 309, p. 1040‑1063, oct. 1949, doi: 10.1080/14786444908561372.
[28] P. Chandra et P. B. Littlewood, « A Landau Primer for Ferroelectrics », in *Physics of Ferroelectrics: A Modern Perspective*, Berlin, Heidelberg: Springer, 2007, p. 69‑116.
[29] E. Bousquet, « First-Principles study of ferroelectric oxide nanostructures », mars 31, 2009. http://bictel.ulg.ac.be/ETD-db/collection/available/ULgetd-03232009-095839/ (consulté le févr. 11, 2020).
[30] D. Lebeugle *et al.*, « Room-temperature coexistence of large electric polarization and magnetic order in $\mathrm{Bi}\mathrm{Fe}{\mathrm{O}}_{3}$ single crystals », *Phys. Rev. B*, vol. 76, n° 2, p. 024116, juill. 2007, doi: 10.1103/PhysRevB.76.024116.
[31] L. D. Landau et E. M. Lifshitz, « Electrodynamics of Continuous Media, Eddison-Wesley », *Read. MA*, 1960.
[32] J. B. Goodenough, « Theory of the Role of Covalence in the Perovskite-Type Manganites $[\mathrm{La}, M(\mathrm{II})]\mathrm{Mn}{\mathrm{O}}_{3}$ », *Phys. Rev.*, vol. 100, n° 2, p. 564‑573, oct. 1955, doi: 10.1103/PhysRev.100.564.
[33] P. W. Anderson, « New Approach to the Theory of Superexchange Interactions », *Phys. Rev.*, vol. 115, n° 1, p. 2‑13, juill. 1959, doi: 10.1103/PhysRev.115.2.
[34] P. Curie, « Sur la symétrie dans les phénomènes physiques, symétrie d'un champ électrique et d'un champ magnétique », *J. Phys. Théorique Appliquée*, vol. 3, n° 1, p. 393‑415, 1894, doi: 10.1051/jphystap:018940030039300.

[35] I. E. DZYALOSHINSKII, « On the magneto-electrical effects in antiferromagnets », *Sov. Phys. JETP*, vol. 10, p. 628‑629, 1960.
[36] D. N. Astrov, « The magnetoelectric effect in antiferromagnetics », *Sov Phys JETP*, vol. 11, n° 3, p. 708–709, 1960.
[37] G. T. Rado et V. J. Folen, « Observation of the Magnetically Induced Magnetoelectric Effect and Evidence for Antiferromagnetic Domains », *Phys. Rev. Lett.*, vol. 7, n° 8, p. 310‑311, oct. 1961, doi: 10.1103/PhysRevLett.7.310.
[38] J. Van Suchtelen, « Product properties: a new application of composite materials », *Philips Res Rep*, vol. 27, n° 1, p. 28–37, 1972.
[39] B. D. Tellegen, « The gyrator, a new electric network element », *Philips Res Rep*, vol. 3, n° 2, p. 81–101, 1948.
[40] M. Fiebig, « Revival of the magnetoelectric effect », *J. Phys. Appl. Phys.*, vol. 38, n° 8, p. R123–R152, avr. 2005, doi: 10.1088/0022-3727/38/8/R01.
[41] C.-W. Nan, M. I. Bichurin, S. Dong, D. Viehland, et G. Srinivasan, « Multiferroic magnetoelectric composites: Historical perspective, status, and future directions », *J. Appl. Phys.*, vol. 103, n° 3, p. 031101, févr. 2008, doi: 10.1063/1.2836410.
[42] C.-W. Nan, « Magnetoelectric effect in composites of piezoelectric and piezomagnetic phases », *Phys. Rev. B*, vol. 50, n° 9, p. 6082‑6088, sept. 1994, doi: 10.1103/PhysRevB.50.6082.
[43] R. E. Newnham, D. P. Skinner, et L. E. Cross, « Connectivity and piezoelectric-pyroelectric composites », *Mater. Res. Bull.*, vol. 13, n° 5, p. 525‑536, mai 1978, doi: 10.1016/0025-5408(78)90161-7.
[44] V. Morin, « Elaboration de composites multiférroïque et caractérisation de l'effet magnétoélectrique », thesis, Université Paris-Saclay (ComUE), 2015.
[45] J. G. Wan *et al.*, « Magnetoelectric CoFe2O4–Pb(Zr,Ti)O3 composite thin films derived by a sol-gel process », *Appl. Phys. Lett.*, vol. 86, n° 12, p. 122501, mars 2005, doi: 10.1063/1.1889237.
[46] A. McDannald, M. Staruch, G. Sreenivasulu, C. Cantoni, G. Srinivasan, et M. Jain, « Magnetoelectric coupling in solution derived 3-0 type PbZr0.52Ti0.48O3:xCoFe2O4 nanocomposite films », *Appl. Phys. Lett.*, vol. 102, n° 12, p. 122905, mars 2013, doi: 10.1063/1.4799174.
[47] A. McDannald *et al.*, « Switchable 3-0 magnetoelectric nanocomposite thin film with high coupling », *Nanoscale*, vol. 9, n° 9, p. 3246‑3251, 2017, doi: 10.1039/C6NR08674H.
[48] R. A. Islam, J. Jiang, F. Bai, D. Viehland, et S. Priya, « Correlation between structural deformation and magnetoelectric response in (1−x) Pb(Zr0.52Ti0.48)O3–xNiFe1.9Mn0.1O4 particulate composites », *Appl. Phys. Lett.*, vol. 91, n° 16, p. 162905, oct. 2007, doi: 10.1063/1.2799261.
[49] C.-S. Park, J. Ryu, J.-J. Choi, D.-S. Park, C.-W. Ahn, et S. Priya, « Giant Magnetoelectric Coefficient in 3–2 Nanocomposite Thick Films », *Jpn. J. Appl. Phys.*, vol. 48, n° 8R, p. 080204, août 2009, doi: 10.1143/JJAP.48.080204.
[50] J. Van Den Boomgaard, D. R. Terrell, R. A. J. Born, et H. F. J. I. Giller, « An in situ grown eutectic magnetoelectric composite material », *J. Mater. Sci.*, vol. 9, n° 10, p. 1705‑1709, oct. 1974, doi: 10.1007/BF00540770.
[51] S. Q. Ren, L. Q. Weng, S.-H. Song, F. Li, J. G. Wan, et M. Zeng, « BaTiO3/CoFe2O4 particulate composites with large high frequency magnetoelectric response », *J. Mater. Sci.*, vol. 40, n° 16, p. 4375‑4378, août 2005, doi: 10.1007/s10853-005-1057-1.
[52] J. Y. Zhai, N. Cai, L. Liu, Y. H. Lin, et C. W. Nan, « Dielectric behavior and magnetoelectric properties of lead zirconate titanate/Co-ferrite particulate composites », *Mater. Sci. Eng. B*, vol. 99, n° 1, p. 329‑331, mai 2003, doi: 10.1016/S0921-5107(02)00565-2.

[53] Y. Liu *et al.*, « Magnetoelectric ceramic composites prepared by spark plasma sintering with notably enhanced magnetoelectric effect », *J. Mater. Sci. Mater. Electron.*, vol. 28, n° 4, p. 3746‑3751, févr. 2017, doi: 10.1007/s10854-016-5983-2.
[54] G. Sreenivasulu, V. H. Babu, G. Markandeyulu, et B. S. Murty, « Magnetoelectric effect of (100−x)BaTiO3–(x)NiFe1.98O4 (x=20–80 wt %) particulate nanocomposites », *Appl. Phys. Lett.*, vol. 94, n° 11, p. 112902, mars 2009, doi: 10.1063/1.3095600.
[55] R. A. Islam, V. Bedekar, N. Poudyal, J. P. Liu, et S. Priya, « Magnetoelectric properties of core-shell particulate nanocomposites », *J. Appl. Phys.*, vol. 104, n° 10, p. 104111, nov. 2008, doi: 10.1063/1.3013437.
[56] G. Srinivasan, C. P. DeVreugd, C. S. Flattery, V. M. Laletsin, et N. Paddubnaya, « Magnetoelectric interactions in hot-pressed nickel zinc ferrite and lead zirconante titanate composites », *Appl. Phys. Lett.*, vol. 85, n° 13, p. 2550‑2552, sept. 2004, doi: 10.1063/1.1795365.
[57] V. R. Mudinepalli, S. H. Song, et B. S. Murty, « Enhanced magnetoelectric properties in lead-free Ni0.83Co0.15Cu0.02Fe1.9O4-δ–Na0.5Bi0.5TiO3 composites by spark plasma sintering », *Scr. Mater.*, vol. 82, p. 9‑12, juill. 2014, doi: 10.1016/j.scriptamat.2014.03.004.
[58] X.-M. Liu, S.-Y. Fu, et C.-J. Huang, « Synthesis and magnetic characterization of novel CoFe2O4–BiFeO3 nanocomposites », *Mater. Sci. Eng. B*, vol. 121, n° 3, p. 255‑260, août 2005, doi: 10.1016/j.mseb.2005.04.009.
[59] K. Mori et M. Wuttig, « Magnetoelectric coupling in Terfenol-D/polyvinylidenedifluoride composites », *Appl. Phys. Lett.*, vol. 81, n° 1, p. 100‑101, juin 2002, doi: 10.1063/1.1491006.
[60] R. Mahajan, K. Patankar, M. Kothale, S. Chaudhari, V. Mathe, et S. Patil, « Magnetoelectric effect in cobalt ferrite-barium titanate composites and their electrical properties », *Pramana*, vol. 58, n° 5, p. 1115‑1124, mai 2002, doi: 10.1007/s12043-002-0227-9.
[61] R. P. Mahajan, K. K. Patankar, M. B. Kothale, et S. A. Patil, « Conductivity, dielectric behaviour and magnetoelectric effect in copper ferrite-barium titanate composites », *Bull. Mater. Sci.*, vol. 23, n° 4, p. 273‑279, août 2000, doi: 10.1007/BF02720082.
[62] Y. R. Dai, P. Bao, J. S. Zhu, J. G. Wan, H. M. Shen, et J. M. Liu, « Internal friction study on CuFe2O4/PbZr0.53Ti0.47O3 composites », *J. Appl. Phys.*, vol. 96, n° 10, p. 5687‑5690, nov. 2004, doi: 10.1063/1.1805187.
[63] M. I. Bichurin, V. M. Petrov, et G. Srinivasan, « Theory of low-frequency magnetoelectric coupling in magnetostrictive-piezoelectric bilayers », *Phys. Rev. B*, vol. 68, n° 5, p. 054402, août 2003, doi: 10.1103/PhysRevB.68.054402.
[64] H. Wu, G. Chai, T. Zhou, Z. Zhang, T. Kitamura, et H. Zhou, « Adjustable magnetoelectric effect of self-assembled vertical multiferroic nanocomposite films by the in-plane misfit strain and ferromagnetic volume fraction », *J. Appl. Phys.*, vol. 115, n° 11, p. 114105, mars 2014, doi: 10.1063/1.4868896.
[65] H. Zheng *et al.*, « Multiferroic BaTiO3-CoFe2O4 Nanostructures », *Science*, vol. 303, n° 5658, p. 661‑663, janv. 2004, doi: 10.1126/science.1094207.
[66] F. Zavaliche *et al.*, « Electric Field-Induced Magnetization Switching in Epitaxial Columnar Nanostructures », *Nano Lett.*, vol. 5, n° 9, p. 1793‑1796, sept. 2005, doi: 10.1021/nl051406i.
[67] I. Levin, J. Li, J. Slutsker, et A. L. Roytburd, « Design of Self-Assembled Multiferroic Nanostructures in Epitaxial Films », *Adv. Mater.*, vol. 18, n° 15, p. 2044‑2047, 2006, doi: 10.1002/adma.200600288.
[68] A. Imai *et al.*, « Epitaxial Bi5Ti3FeO15–CoFe2O4 Pillar–Matrix Multiferroic Nanostructures », *ACS Nano*, vol. 7, n° 12, p. 11079‑11086, déc. 2013, doi: 10.1021/nn404779x.

[69] Z. Wang *et al.*, « Magnetoelectric Assisted 180° Magnetization Switching for Electric Field Addressable Writing in Magnetoresistive Random-Access Memory », *ACS Nano*, vol. 8, n° 8, p. 7793‑7800, août 2014, doi: 10.1021/nn503369y.
[70] N. Benatmane, S. P. Crane, F. Zavaliche, R. Ramesh, et T. W. Clinton, « Voltage-dependent ferromagnetic resonance in epitaxial multiferroic nanocomposites », *Appl. Phys. Lett.*, vol. 96, n° 8, p. 082503, févr. 2010, doi: 10.1063/1.3319507.
[71] S. Ojha, W. C. Nunes, N. M. Aimon, et C. A. Ross, « Magnetostatic Interactions in Self-Assembled CoxNi1–xFe2O4/BiFeO3 Multiferroic Nanocomposites », *ACS Nano*, vol. 10, n° 8, p. 7657‑7664, août 2016, doi: 10.1021/acsnano.6b02985.
[72] T. Amrillah *et al.*, « Flexible Multiferroic Bulk Heterojunction with Giant Magnetoelectric Coupling via van der Waals Epitaxy », *ACS Nano*, vol. 11, n° 6, p. 6122‑6130, juin 2017, doi: 10.1021/acsnano.7b02102.
[73] J. Wan, Y. Weng, Y. Wu, Z. Li, J. Liu, et G. Wang, « Controllable phase connectivity and magnetoelectric coupling behavior in CoFe2O4–Pb(Zr,Ti)O3 nanostructured films », *Nanotechnology*, vol. 18, n° 46, p. 465708, oct. 2007, doi: 10.1088/0957-4484/18/46/465708.
[74] Y. S. Oh, S. Crane, H. Zheng, Y. H. Chu, R. Ramesh, et K. H. Kim, « Quantitative determination of anisotropic magnetoelectric coupling in BiFeO3–CoFe2O4 nanostructures », *Appl. Phys. Lett.*, vol. 97, n° 5, p. 052902, août 2010, doi: 10.1063/1.3475420.
[75] J. Ma, Z. Shi, et C.-W. Nan, « Magnetoelectric Properties of Composites of Single Pb(Zr,Ti)O3 Rods and Terfenol-D/Epoxy with a Single-Period of 1-3-Type Structure », *Adv. Mater.*, vol. 19, n° 18, p. 2571‑2573, 2007, doi: 10.1002/adma.200700330.
[76] L. Yan, Y. Yang, Z. Wang, Z. Xing, J. Li, et D. Viehland, « Review of magnetoelectric perovskite–spinel self-assembled nano-composite thin films », *J. Mater. Sci.*, vol. 44, n° 19, p. 5080‑5094, oct. 2009, doi: 10.1007/s10853-009-3679-1.
[77] L. Yan, Z. Wang, Z. Xing, J. Li, et D. Viehland, « Magnetoelectric and multiferroic properties of variously oriented epitaxial BiFeO3–CoFe2O4 nanostructured thin films », *J. Appl. Phys.*, vol. 107, n° 6, p. 064106, mars 2010, doi: 10.1063/1.3359650.
[78] V. Loyau, V. Morin, G. Chaplier, M. LoBue, et F. Mazaleyrat, « Magnetoelectric effect in layered ferrite/PZT composites. Study of the demagnetizing effect on the magnetoelectric behavior », *J. Appl. Phys.*, vol. 117, n° 18, p. 184102, mai 2015, doi: 10.1063/1.4919722.
[79] J. More-Chevalier *et al.*, « Magnetoelectric coupling in Pb(Zr,Ti)O3—Galfenol thin film heterostructures », *Appl. Phys. Lett.*, vol. 107, n° 25, p. 252903, déc. 2015, doi: 10.1063/1.4938218.
[80] J. Ryu, A. V. Carazo, K. Uchino, et H.-E. Kim, « Magnetoelectric Properties in Piezoelectric and Magnetostrictive Laminate Composites », *Jpn. J. Appl. Phys.*, vol. 40, n° 8R, p. 4948, août 2001, doi: 10.1143/JJAP.40.4948.
[81] G. Srinivasan, E. T. Rasmussen, et R. Hayes, « Magnetoelectric effects in ferrite-lead zirconate titanate layered composites: The influence of zinc substitution in ferrites », *Phys. Rev. B*, vol. 67, n° 1, p. 014418, janv. 2003, doi: 10.1103/PhysRevB.67.014418.
[82] Z. Chu *et al.*, « Enhanced Resonance Magnetoelectric Coupling in (1-1) Connectivity Composites », *Adv. Mater.*, vol. 29, n° 19, p. 1606022, 2017, doi: 10.1002/adma.201606022.
[83] E. Lage *et al.*, « Magnetic domain control and voltage response of exchange biased magnetoelectric composites », *Appl. Phys. Lett.*, vol. 104, n° 13, p. 132405, mars 2014, doi: 10.1063/1.4870511.
[84] H. Greve, E. Woltermann, H.-J. Quenzer, B. Wagner, et E. Quandt, « Giant magnetoelectric coefficients in (Fe90Co10)78Si12B10-AlN thin film composites », *Appl. Phys. Lett.*, vol. 96, n° 18, p. 182501, mai 2010, doi: 10.1063/1.3377908.

[85] C.-G. Duan, S. S. Jaswal, et E. Y. Tsymbal, « Predicted Magnetoelectric Effect in $\mathrm{Fe}/{\mathrm{BaTiO}}_{3}$ Multilayers: Ferroelectric Control of Magnetism », *Phys. Rev. Lett.*, vol. 97, n° 4, p. 047201, juill. 2006, doi: 10.1103/PhysRevLett.97.047201.
[86] H. J. A. Molegraaf *et al.*, « Magnetoelectric Effects in Complex Oxides with Competing Ground States », *Adv. Mater.*, vol. 21, n° 34, p. 3470‑3474, 2009, doi: 10.1002/adma.200900278.
[87] H. Palneedi *et al.*, « A flexible, high-performance magnetoelectric heterostructure of (001) oriented Pb(Zr0.52Ti0.48)O3 film grown on Ni foil », *APL Mater.*, vol. 5, n° 9, p. 096111, sept. 2017, doi: 10.1063/1.4993239.
[88] Y. Wang *et al.*, « An Extremely Low Equivalent Magnetic Noise Magnetoelectric Sensor », *Adv. Mater.*, vol. 23, n° 35, p. 4111‑4114, 2011, doi: 10.1002/adma.201100773.
[89] M. Lorenz *et al.*, « Correlation of Interface Impurities and Chemical Gradients with High Magnetoelectric Coupling Strength in Multiferroic BiFeO3–BaTiO3 Superlattices », *ACS Appl. Mater. Interfaces*, vol. 9, n° 22, p. 18956‑18965, juin 2017, doi: 10.1021/acsami.7b04084.
[90] H. Palneedi *et al.*, « Unleashing the Full Potential of Magnetoelectric Coupling in Film Heterostructures », *Adv. Mater.*, vol. 29, n° 10, p. 1605688, 2017, doi: 10.1002/adma.201605688.
[91] M. Feng *et al.*, « Optimizing direct magnetoelectric coupling in Pb(Zr,Ti)O3/Ni multiferroic film heterostructures », *Appl. Phys. Lett.*, vol. 106, n° 7, p. 072901, févr. 2015, doi: 10.1063/1.4913471.
[92] J. Zhou, H. He, Z. Shi, G. Liu, et C.-W. Nan, « Dielectric, magnetic, and magnetoelectric properties of laminated PbZr0.52Ti0.48O3/CoFe2O4 composite ceramics », *J. Appl. Phys.*, vol. 100, n° 9, p. 094106, nov. 2006, doi: 10.1063/1.2358191.
[93] Z. Fang, S. G. Lu, F. Li, S. Datta, Q. M. Zhang, et M. El Tahchi, « Enhancing the magnetoelectric response of Metglas/polyvinylidene fluoride laminates by exploiting the flux concentration effect », *Appl. Phys. Lett.*, vol. 95, n° 11, p. 112903, sept. 2009, doi: 10.1063/1.3231614.
[94] P. Royen et K. Swars, « Das System Wismutoxyd-Eisenoxyd im Bereich von 0 bis 55 Mol% Eisenoxyd », *Angew. Chem.*, vol. 69, n° 24, p. 779‑779, 1957, doi: 10.1002/ange.19570692407.
[95] S. V. KISELEV, « Detection of magnetic order in ferroelectric BiFeO_3 by neutron diffraction », *Sov Phys*, vol. 7, p. 742, 1963.
[96] Y. E. Roginskaya, Y. Y. Tomashpolskii, Y. N. Venevtsev, V. M. Petrov, et G. S. Zhdanov, « The nature of the dielectric and magnetic properties of BiFeO3 », *Sov Phys JETP*, vol. 23, p. 47–51, 1966.
[97] J. Wang *et al.*, « Epitaxial BiFeO3 Multiferroic Thin Film Heterostructures », *Science*, vol. 299, n° 5613, p. 1719‑1722, mars 2003, doi: 10.1126/science.1080615.
[98] J. M. Caicedo, J. A. Zapata, M. E. Gómez, et P. Prieto, « Magnetoelectric coefficient in BiFeO3 compounds », *J. Appl. Phys.*, vol. 103, n° 7, p. 07E306, févr. 2008, doi: 10.1063/1.2839276.
[99] Y. Zhang, C. Deng, J. Ma, Y. Lin, et C.-W. Nan, « Enhancement in magnetoelectric response in CoFe2O4–BaTiO3 heterostructure », *Appl. Phys. Lett.*, vol. 92, n° 6, p. 062911, févr. 2008, doi: 10.1063/1.2841048.
[100] W. Liang *et al.*, « Role of the interface on the magnetoelectric properties of BaTiO3 thin films deposited on polycrystalline Ni foils », *J. Mater. Chem. C*, vol. 2, n° 4, p. 708‑714, déc. 2013, doi: 10.1039/C3TC31571A.

[101] A. Stognij *et al.*, « Ion-beam sputtering deposition and magnetoelectric properties of layered heterostructures (FM/PZT/FM)n, where FM – Co or Ni78Fe22 », *Eur. Phys. J. - Appl. Phys.*, vol. 63, n° 2, août 2013, doi: 10.1051/epjap/2013120541.
[102] H. Landolt, *Magnetic and other properties of oxides and related compounds*, vol. 4. Springer, 1970.
[103] B. Jaffe, W. R. Cook, et H. Jaffe, « Piezoelectric ceramics. Academic Press, London », in *JCPDS 71-2171*, 1971.
[104] N. Setter, « Piezoelectric Materials and Devices. Ceramics Laboratory », *EPFL Swiss Fed. Inst. Technol. Lausanne*, 2005.
[105] A. J. Moulson et J. M. Herbert, *Electroceramics: Materials, Properties, Applications*. John Wiley & Sons, 2003.
[106] D. I. Woodward, J. Knudsen, et I. M. Reaney, « Review of crystal and domain structures in the ${\mathrm{PbZr}}_{x}{\mathrm{Ti}}_{1\ensuremath{-}x}{\mathrm{O}}_{3}$ solid solution », *Phys. Rev. B*, vol. 72, n° 10, p. 104110, sept. 2005, doi: 10.1103/PhysRevB.72.104110.
[107] R. Martínez, A. Kumar, R. Palai, G. Srinivasan, et R. S. Katiyar, « Observation of strong magnetoelectric effects in Ba0.7Sr0.3TiO3/La0.7Sr0.3MnO3 thin film heterostructures », *J. Appl. Phys.*, vol. 111, n° 10, p. 104104, mai 2012, doi: 10.1063/1.4717727.
[108] U. Bottger, S. Tiedke, et R. Waser, *Polar Oxides: Properties, Characterization, and Imaging*. Wiley-VCH, 2005.
[109] E. Nakamura *et al.*, *Ferroelectrics and Related Substances*. Springer-Verlag, 1990.
[110] J. Ryu, S. Priya, K. Uchino, et H.-E. Kim, « Magnetoelectric Effect in Composites of Magnetostrictive and Piezoelectric Materials », *J. Electroceramics*, vol. 8, n° 2, p. 107‑119, août 2002, doi: 10.1023/A:1020599728432.
[111] S. Dong, J.-F. Li, et D. Viehland, « Ultrahigh magnetic field sensitivity in laminates of TERFENOL-D and Pb(Mg1/3Nb2/3)O3–PbTiO3 crystals », *Appl. Phys. Lett.*, vol. 83, n° 11, p. 2265‑2267, sept. 2003, doi: 10.1063/1.1611276.
[112] J. Zhai, Z. Xing, S. Dong, J. Li, et D. Viehland, « Detection of pico-Tesla magnetic fields using magneto-electric sensors at room temperature », *Appl. Phys. Lett.*, vol. 88, n° 6, p. 062510, févr. 2006, doi: 10.1063/1.2172706.
[113] S. Dong, J. Zhai, J. Li, et D. Viehland, « Small dc magnetic field response of magnetoelectric laminate composites », *Appl. Phys. Lett.*, vol. 88, n° 8, p. 082907, févr. 2006, doi: 10.1063/1.2178582.
[114] C. Fang *et al.*, « Significant reduction of equivalent magnetic noise by in-plane series connection in magnetoelectric Metglas/Mn-doped Pb(Mg1/3Nb2/3)O3-PbTiO3laminate composites », *J. Phys. Appl. Phys.*, vol. 48, n° 46, p. 465002, oct. 2015, doi: 10.1088/0022-3727/48/46/465002.
[115] D. Burdin, D. Chashin, N. Ekonomov, L. Fetisov, Y. Fetisov, et M. Shamonin, « DC magnetic field sensing based on the nonlinear magnetoelectric effect in magnetic heterostructures », *J. Phys. Appl. Phys.*, vol. 49, n° 37, p. 375002, août 2016, doi: 10.1088/0022-3727/49/37/375002.
[116] S. Reis *et al.*, « Characterization of Metglas/poly(vinylidene fluoride)/Metglas magnetoelectric laminates for AC/DC magnetic sensor applications », *Mater. Des.*, vol. 92, p. 906‑910, févr. 2016, doi: 10.1016/j.matdes.2015.12.086.
[117] Z. Chu *et al.*, « A magnetoelectric flux gate: new approach for weak DC magnetic field detection », *Sci. Rep.*, vol. 7, n° 1, p. 1‑8, août 2017, doi: 10.1038/s41598-017-09420-w.
[118] S. Dong, J. Zhai, F. Bai, J.-F. Li, et D. Viehland, « Push-pull mode magnetostrictive/piezoelectric laminate composite with an enhanced magnetoelectric voltage coefficient », *Appl. Phys. Lett.*, vol. 87, n° 6, p. 062502, août 2005, doi: 10.1063/1.2007868.

[119] J. Zhang *et al.*, « High-resolution current sensor utilizing nanocrystalline alloy and magnetoelectric laminate composite », *Rev. Sci. Instrum.*, vol. 83, n° 11, p. 115001, nov. 2012, doi: 10.1063/1.4763570.
[120] X. Yu, G. Lou, H. Chen, C. Wen, et S. Lu, « A Slice-Type Magnetoelectric Laminated Current Sensor », *IEEE Sens. J.*, vol. 15, n° 10, p. 5839‑5850, oct. 2015, doi: 10.1109/JSEN.2015.2451551.
[121] M. Bichurin, R. Petrov, V. Leontiev, G. Semenov, et O. Sokolov, « Magnetoelectric Current Sensors », *Sensors*, vol. 17, n° 6, p. 1271, juin 2017, doi: 10.3390/s17061271.
[122] Z. Wu, L. Bian, S. Wang, et X. Zhang, « An angle sensor based on magnetoelectric effect », *Sens. Actuators Phys.*, vol. 262, p. 108‑113, août 2017, doi: 10.1016/j.sna.2017.04.049.
[123] T. Lafont *et al.*, « Magnetostrictive–piezoelectric composite structures for energy harvesting », *J. Micromechanics Microengineering*, vol. 22, n° 9, p. 094009, août 2012, doi: 10.1088/0960-1317/22/9/094009.
[124] L. Bian, Y. Wen, P. Li, Q. Gao, et M. Zheng, « Magnetoelectric transducer with high quality factor for wireless power receiving », *Sens. Actuators Phys.*, vol. 150, n° 2, p. 207‑211, mars 2009, doi: 10.1016/j.sna.2009.01.003.
[125] Y. Zhou, Y. Yan, et S. Priya, « Co-fired magnetoelectric transformer », *Appl. Phys. Lett.*, vol. 104, n° 23, p. 232906, juin 2014, doi: 10.1063/1.4883492.
[126] C. M. Leung *et al.*, « Highly efficient solid state magnetoelectric gyrators », *Appl. Phys. Lett.*, vol. 111, n° 12, p. 122904, sept. 2017, doi: 10.1063/1.4996242.
[127] J. Lou, D. Reed, M. Liu, et N. X. Sun, « Electrostatically tunable magnetoelectric inductors with large inductance tunability », *Appl. Phys. Lett.*, vol. 94, n° 11, p. 112508, mars 2009, doi: 10.1063/1.3103273.
[128] Y. Yan *et al.*, « Correlation between tunability and anisotropy in magnetoelectric voltage tunable inductor (VTI) », *Sci. Rep.*, vol. 7, n° 1, p. 1‑10, nov. 2017, doi: 10.1038/s41598-017-14455-0.
[129] A. El-Ghazaly *et al.*, « Electrically Tunable Integrated Thin-Film Magnetoelectric Resonators », *Adv. Mater. Technol.*, vol. 2, n° 8, p. 1700062, 2017, doi: 10.1002/admt.201700062.
[130] C. E. Ciomaga *et al.*, « Engineering magnetoelectric composites towards application as tunable microwave filters », *J. Phys. Appl. Phys.*, vol. 49, n° 12, p. 125002, févr. 2016, doi: 10.1088/0022-3727/49/12/125002.
[131] A. K. Zvezdin, *Nanomagnetism and spintronics*. Lille, 2005.
[132] S. Shtrikman et D. Treves, « Observation of the Magnetoelectric Effect in ${\mathrm{Cr}}_{2}$${\mathrm{O}}_{3}$ Powders », *Phys. Rev.*, vol. 130, n° 3, p. 986‑988, mai 1963, doi: 10.1103/PhysRev.130.986.
[133] D. R. Hartree, « the waves mechanics of an atom with non-coulombic central field: parts I, II, III », in *Proc. Cambridge Phil. Soc*, 1928, vol. 24, p. 111.
[134] P. A. M. Dirac et R. H. Fowler, « Quantum mechanics of many-electron systems », *Proc. R. Soc. Lond. Ser. Contain. Pap. Math. Phys. Character*, vol. 123, n° 792, p. 714‑733, avr. 1929, doi: 10.1098/rspa.1929.0094.
[135] M. Born et R. Oppenheimer, « Zur Quantentheorie der Molekeln », *Ann. Phys.*, vol. 389, n° 20, p. 457‑484, 1927, doi: 10.1002/andp.19273892002.
[136] P. Kiréev, *La physique des semiconducteurs. 2e édition, édition Mir*. Moscou, 1975.
[137] I. Koutiri, « Etude ab initio du trioxyde de tungstène WO3 en volume et en surface », phdthesis, Université de Bourgogne, 2012.
[138] L. H. Thomas, « The calculation of atomic fields », *Math. Proc. Camb. Philos. Soc.*, vol. 23, n° 5, p. 542‑548, janv. 1927, doi: 10.1017/S0305004100011683.

[139] E. Fermi, « Eine statistische Methode zur Bestimmung einiger Eigenschaften des Atoms und ihre Anwendung auf die Theorie des periodischen Systems der Elemente », *Z. Für Phys.*, vol. 48, n° 1, p. 73‑79, janv. 1928, doi: 10.1007/BF01351576.
[140] H. Eschrig, *The fundamentals of density functional theory*, vol. 32. Springer, 1996.
[141] P. Rg et W. Yang, *Density-functional theory of atoms and molecules*. Oxford University Press, New York, 1989.
[142] D. M. Ceperley et B. J. Alder, « Ground State of the Electron Gas by a Stochastic Method », *Phys. Rev. Lett.*, vol. 45, n° 7, p. 566‑569, août 1980, doi: 10.1103/PhysRevLett.45.566.
[143] P. a. M. Dirac, « Note on Exchange Phenomena in the Thomas Atom », *Math. Proc. Camb. Philos. Soc.*, vol. 26, n° 3, p. 376‑385, juill. 1930, doi: 10.1017/S0305004100016108.
[144] J. P. Perdew, « Generalized gradient approximations for exchange and correlation: A look backward and forward », *Phys. B Condens. Matter*, vol. 172, n° 1, p. 1‑6, juin 1991, doi: 10.1016/0921-4526(91)90409-8.
[145] « Lee J G, Computational Materials Science, ISBN: 978-1-439... - Google Scholar ». https://scholar.google.com/scholar?hl=fr&as_sdt=0%2C5&q=Lee+J+G%2C+Computational+Materials+Science%2C+ISBN%3A+978-1-4398-3616-3+2012+&btnG= (consulté le févr. 13, 2020).
[146] O. Gunnarsson, M. Jonson, et B. I. Lundqvist, « Descriptions of exchange and correlation effects in inhomogeneous electron systems », *Phys. Rev. B*, vol. 20, n° 8, p. 3136‑3164, oct. 1979, doi: 10.1103/PhysRevB.20.3136.
[147] Z. Perdew, « Local density approximation Phys », *Rev B*, vol. 23, p. 5075, 1981.
[148] « Perdew + Phys. Rev. B 45 (1992) 13244-13249. - Google Scholar ». https://scholar.google.com/scholar?q=Perdew+%2B+Phys.+Rev.+B+45+%281992%29+13244-13249.&hl=fr&as_sdt=0%2C5&as_ylo=1992&as_yhi=1992 (consulté le févr. 13, 2020).
[149] M. T. Yin et M. L. Cohen, « Theory of static structural properties, crystal stability, and phase transformations: Application to Si and Ge », *Phys. Rev. B*, vol. 26, n° 10, p. 5668‑5687, nov. 1982, doi: 10.1103/PhysRevB.26.5668.
[150] D. R. Hamann, « Semiconductor Charge Densities with Hard-Core and Soft-Core Pseudopotentials », *Phys. Rev. Lett.*, vol. 42, n° 10, p. 662‑665, mars 1979, doi: 10.1103/PhysRevLett.42.662.
[151] J. Heyd, J. E. Peralta, G. E. Scuseria, et R. L. Martin, « Energy band gaps and lattice parameters evaluated with the Heyd-Scuseria-Ernzerhof screened hybrid functional », *J. Chem. Phys.*, vol. 123, n° 17, p. 174101, oct. 2005, doi: 10.1063/1.2085170.
[152] X. Gonze *et al.*, « First-principles computation of material properties: the ABINIT software project », *Comput. Mater. Sci.*, vol. 25, n° 3, p. 478‑492, nov. 2002, doi: 10.1016/S0927-0256(02)00325-7.
[153] X. Gonze *et al.*, « P. h. Ghosez, M. Veithen, J », *Raty V Olevano F Bruneval Reining R Godby G Onida DR Hamann DC Allan Z Krist.*, vol. 220, p. 558, 2005.
[154] H. J. Monkhorst et J. D. Pack, « Special points for Brillouin-zone integrations », *Phys. Rev. B*, vol. 13, n° 12, p. 5188‑5192, juin 1976, doi: 10.1103/PhysRevB.13.5188.
[155] P. Giannozzi *et al.*, « QUANTUM ESPRESSO: a modular and open-source software project for quantum simulations of materials », *J. Phys. Condens. Matter*, vol. 21, n° 39, p. 395502, sept. 2009, doi: 10.1088/0953-8984/21/39/395502.
[156] J. P. Perdew, K. Burke, et M. Ernzerhof, « Generalized Gradient Approximation Made Simple », *Phys. Rev. Lett.*, vol. 77, n° 18, p. 3865‑3868, oct. 1996, doi: 10.1103/PhysRevLett.77.3865.

[157] J. P. Perdew, M. Ernzerhof, et K. Burke, « Rationale for mixing exact exchange with density functional approximations », *J. Chem. Phys.*, vol. 105, n° 22, p. 9982‑9985, déc. 1996, doi: 10.1063/1.472933.
[158] D. Vanderbilt, « Soft self-consistent pseudopotentials in a generalized eigenvalue formalism », *Phys. Rev. B*, vol. 41, n° 11, p. 7892‑7895, avr. 1990, doi: 10.1103/PhysRevB.41.7892.
[159] N. Marzari, D. Vanderbilt, A. De Vita, et M. C. Payne, « Thermal Contraction and Disordering of the Al(110) Surface », *Phys. Rev. Lett.*, vol. 82, n° 16, p. 3296‑3299, avr. 1999, doi: 10.1103/PhysRevLett.82.3296.
[160] N. Metropolis et S. Ulam, « The Monte Carlo Method », *J. Am. Stat. Assoc.*, vol. 44, n° 247, p. 335‑341, sept. 1949, doi: 10.1080/01621459.1949.10483310.
[161] M. H. Kalos et P. A. Whitlock, *Monte Carlo Method, ISBN: 978-3-527-40760-6*. John Wiley & Sons, 2008.
[162] H. Niederreiter, *Random number generation and quasi-Monte Carlo methods*, vol. 63. Siam, 1992.
[163] K. Hukushima et K. Nemoto, « Exchange Monte Carlo Method and Application to Spin Glass Simulations », *J. Phys. Soc. Jpn.*, vol. 65, n° 6, p. 1604‑1608, juin 1996, doi: 10.1143/JPSJ.65.1604.
[164] P. J. Green, « Reversible jump Markov chain Monte Carlo computation and Bayesian model determination », *Biometrika*, vol. 82, n° 4, p. 711‑732, déc. 1995, doi: 10.1093/biomet/82.4.711.
[165] B. Larget et D. L. Simon, « Markov chain Monte Carlo algorithms for the Bayesian analysis of phylogenetic trees », *Mol. Biol. Evol.*, vol. 16, n° 6, p. 750–759, 1999.
[166] R. J. Glauber, « Time-Dependent Statistics of the Ising Model », *J. Math. Phys.*, vol. 4, n° 2, p. 294, déc. 2004, doi: 10.1063/1.1703954.
[167] T.-D. Lee et C.-N. Yang, « Statistical theory of equations of state and phase transitions. II. Lattice gas and Ising model », *Phys. Rev.*, vol. 87, n° 3, p. 410, 1952.
[168] S. Kobe, « Ernst Ising—Physicist and Teacher », *J. Stat. Phys.*, vol. 88, n° 3, p. 991‑995, août 1997, doi: 10.1023/B:JOSS.0000015184.19421.03.
[169] P. Diaconis et L. Saloff-Coste, « What do we know about the Metropolis algorithm? STOC'95: Proceedings of the Twenty-Seventh Annual ACM Symposium on Theory of Computing », *ACM*, p. 112–129, 1995.
[170] J. G. Amar, F. E. Sullivan, et R. D. Mountain, « Monte Carlo study of growth in the two-dimensional spin-exchange kinetic Ising model », *Phys. Rev. B*, vol. 37, n° 1, p. 196‑208, janv. 1988, doi: 10.1103/PhysRevB.37.196.
[171] S.-W. Cheong et M. Mostovoy, « Multiferroics: a magnetic twist for ferroelectricity », *Nat. Mater.*, vol. 6, n° 1, p. 13‑20, janv. 2007, doi: 10.1038/nmat1804.
[172] N. A. Hill, « Why Are There so Few Magnetic Ferroelectrics? », *J. Phys. Chem. B*, vol. 104, n° 29, p. 6694‑6709, juill. 2000, doi: 10.1021/jp000114x.
[173] F. Matsukura, Y. Tokura, et H. Ohno, « Control of magnetism by electric fields », *Nat. Nanotechnol.*, vol. 10, n° 3, p. 209‑220, mars 2015, doi: 10.1038/nnano.2015.22.
[174] G. Zhong, D. Zou, S. Xie, et J. Li, « First-principles study of interfacial magnetoelectric coupling in Fe3Ga/BaTiO3/Fe3Ga heterostructure », *J. Appl. Phys.*, vol. 125, n° 18, p. 184102, mai 2019, doi: 10.1063/1.5086349.
[175] M. K. Niranjan, J. P. Velev, C.-G. Duan, S. S. Jaswal, et E. Y. Tsymbal, « Magnetoelectric effect at the ${\text{Fe}}_{3}{\text{O}}_{4}/{\text{BaTiO}}_{3}$ (001) interface: A first-principles study », *Phys. Rev. B*, vol. 78, n° 10, p. 104405, sept. 2008, doi: 10.1103/PhysRevB.78.104405.
[176] M. K. Niranjan, J. D. Burton, J. P. Velev, S. S. Jaswal, et E. Y. Tsymbal, « Magnetoelectric effect at the SrRuO3/BaTiO3 (001) interface: An ab initio study », *Appl. Phys. Lett.*, vol. 95, n° 5, p. 052501, août 2009, doi: 10.1063/1.3193679.

[177] J. Lee, « Magnetoelectricity in Fe/PbTiO3/Fe superlattices », *Curr. Appl. Phys.*, vol. 17, n° 5, p. 675‑678, mai 2017, doi: 10.1016/j.cap.2017.02.018.
[178] J.-Q. Dai, H. Zhang, et Y.-M. Song, « Interfacial electronic structure and magnetoelectric effect in M/BaTiO3 (M=Ni, Fe) superlattices », *J. Magn. Magn. Mater.*, vol. 324, n° 22, p. 3937‑3943, nov. 2012, doi: 10.1016/j.jmmm.2012.06.046.
[179] D. Cao, M.-Q. Cai, W. Y. Hu, et C.-M. Xu, « Magnetoelectric effect and critical thickness for ferroelectricity in Co/BaTiO3/Co multiferroic tunnel junctions », *J. Appl. Phys.*, vol. 109, n° 11, p. 114107, juin 2011, doi: 10.1063/1.3587172.
[180] M. Hammouri, E. Fohtung, et I. Vasiliev, « Ab initiostudy of magnetoelectric coupling in La0.66Sr0.33MnO3\hspace0.167em/\hspace0.167emPbZr0.2Ti0.8O3multiferroic heterostructures », *J. Phys. Condens. Matter*, vol. 28, n° 39, p. 396004, août 2016, doi: 10.1088/0953-8984/28/39/396004.
[181] K. Wang, N. Si, Y.-L. Zhang, F. Zhang, A.-B. Guo, et W. Jiang, « First-principles study on magnetoelectric coupling effect of M/BiFeO3 (M = Co, Fe) multiferroic superlattice », *Vacuum*, vol. 165, p. 105‑112, juill. 2019, doi: 10.1016/j.vacuum.2019.04.009.
[182] V. S. Borisov, S. Ostanin, I. V. Maznichenko, A. Ernst, et I. Mertig, « Magnetoelectric properties of the $\text{Co}/{\text{PbZr}}_{x}$${\text{Ti}}_{1\ensuremath{-}x}$${\text{O}}_{3}$ (001) interface studied from first principles », *Phys. Rev. B*, vol. 89, n° 5, p. 054436, févr. 2014, doi: 10.1103/PhysRevB.89.054436.
[183] K. Bi et Y. G. Wang, « Magnetoelectric Ni–Pb(Zr,Ti)O3–Ni trilayers prepared by electroless deposition », *Solid State Commun.*, vol. 150, n° 5, p. 248‑250, févr. 2010, doi: 10.1016/j.ssc.2009.11.017.
[184] K. Tahmasebi, A. Barzegar, J. Ding, T. S. Herng, A. Huang, et S. Shannigrahi, « Magnetoelectric effect in Pb(Zr0.95Ti0.05)O3 and CoFe2O4 heteroepitaxial thin film composite », *Mater. Des.*, vol. 32, n° 4, p. 2370‑2373, avr. 2011, doi: 10.1016/j.matdes.2010.11.045.
[185] R. O. Cherifi *et al.*, « Electric-field control of magnetic order above room temperature », *Nat. Mater.*, vol. 13, n° 4, p. 345‑351, avr. 2014, doi: 10.1038/nmat3870.
[186] V. I. Anisimov, F. Aryasetiawan, et A. I. Lichtenstein, « J. Phys.: Condens. Matter », 1997.
[187] V. I. Anisimov, J. Zaanen, et O. K. Andersen, « Band theory and Mott insulators: Hubbard U instead of Stoner I », *Phys. Rev. B*, vol. 44, n° 3, p. 943‑954, juill. 1991, doi: 10.1103/PhysRevB.44.943.
[188] Q.-C. Sun *et al.*, « Optical band gap hierarchy in a magnetic oxide: Electronic structure of NiFe${}_{2}$O${}_{4}$ », *Phys. Rev. B*, vol. 86, n° 20, p. 205106, nov. 2012, doi: 10.1103/PhysRevB.86.205106.
[189] T. Qi, I. Grinberg, et A. M. Rappe, « Band-gap engineering via local environment in complex oxides », *Phys. Rev. B*, vol. 83, n° 22, p. 224108, juin 2011, doi: 10.1103/PhysRevB.83.224108.
[190] Q.-L. Fang, J.-M. Zhang, et K.-W. Xu, « Vacancy and doping driven ferromagnetism in BaTiO3 perovskite », *Phys. B Condens. Matter*, vol. 424, p. 79‑83, sept. 2013, doi: 10.1016/j.physb.2013.04.058.
[191] H. Perron *et al.*, « Structural investigation and electronic properties of the nickel ferrite NiFe2O4: a periodic density functional theory approach », *J. Phys. Condens. Matter*, vol. 19, n° 34, p. 346219, juill. 2007, doi: 10.1088/0953-8984/19/34/346219.
[192] K. Fujita et Y. Gohda, « First-Principles Study of Magnetoelectric Coupling at $\mathrm{Fe}/\mathrm{Bi}\mathrm{Fe}{\mathrm{O}}_{3}(001)$ Interfaces », *Phys. Rev. Appl.*, vol. 11, n° 2, p. 024006, févr. 2019, doi: 10.1103/PhysRevApplied.11.024006.

[193] S. I. Youssef, M. G. Natera, R. J. Begum, B. S. Srinivasan, et N. S. S. Murthy, « Polarised neutron diffraction study of nickel ferrite », *J. Phys. Chem. Solids*, vol. 30, n° 8, p. 1941‑1948, août 1969, doi: 10.1016/0022-3697(69)90170-X.
[194] V. N. Antonov, B. N. Harmon, et A. N. Yaresko, « Electronic structure and x-ray magnetic circular dichroism in ${\mathrm{Fe}}_{3}{\mathrm{O}}_{4}$ and Mn-, $\mathrm{Co}\ensuremath{-},$ or Ni-substituted ${\mathrm{Fe}}_{3}{\mathrm{O}}_{4}$ », *Phys. Rev. B*, vol. 67, n° 2, p. 024417, janv. 2003, doi: 10.1103/PhysRevB.67.024417.
[195] Zs. Rák, C. J. O'Brien, et D. W. Brenner, « First-principles investigation of boron defects in nickel ferrite spinel », *J. Nucl. Mater.*, vol. 452, n° 1, p. 446‑452, sept. 2014, doi: 10.1016/j.jnucmat.2014.05.031.
[196] S. C. Ray *et al.*, « Local atomic and electronic structures and ferroelectric properties of PbZr0.52Ti0.48O3: An x-ray absorption study », *Appl. Phys. Lett.*, vol. 99, n° 4, p. 042909, juill. 2011, doi: 10.1063/1.3607475.
[197] Q. X. Zhao *et al.*, « First-Principles Study of the Electronic Structure and Spontaneous Polarization of PbZr0.4Ti0.6O3 », *Advanced Materials Research*, 2009. https://www.scientific.net/AMR.79-82.1249 (consulté le févr. 13, 2020).
[198] M. P. Moret, M. a. C. Devillers, K. Wörhoff, et P. K. Larsen, « Optical properties of PbTiO3, PbZrxTi1−xO3, and PbZrO3 films deposited by metalorganic chemical vapor on SrTiO3 », *J. Appl. Phys.*, vol. 92, n° 1, p. 468‑474, juin 2002, doi: 10.1063/1.1486048.
[199] I. I. Oleinik, E. Y. Tsymbal, et D. G. Pettifor, « Atomic and electronic structure of $\mathrm{Co}/{\mathrm{SrTiO}}_{3}/\mathrm{Co}$ magnetic tunnel junctions », *Phys. Rev. B*, vol. 65, n° 2, p. 020401, déc. 2001, doi: 10.1103/PhysRevB.65.020401.
[200] W. Eerenstein, N. D. Mathur, et J. F. Scott, « Multiferroic and magnetoelectric materials », *Nature*, vol. 442, n° 7104, p. 759‑765, août 2006, doi: 10.1038/nature05023.
[201] J.-R. Cheng, W. Zhu, N. Li, et L. E. Cross, « Electrical properties of sol-gel-derived Pb(Zr0.52Ti0.48)O3 thin films on a PbTiO3-coated stainless steel substrate », *Appl. Phys. Lett.*, vol. 81, n° 25, p. 4805‑4807, déc. 2002, doi: 10.1063/1.1528288.
[202] J.-Q. Dai, Y.-M. Song, et H. Zhang, « Magnetoelectric coupling at the epitaxial Ni/PbTiO3 heterointerface from first principles », *Phys. B Condens. Matter*, vol. 456, p. 383‑387, janv. 2015, doi: 10.1016/j.physb.2014.08.048.
[203] X. Hao, J. Zhai, L. B. Kong, et Z. Xu, « A comprehensive review on the progress of lead zirconate-based antiferroelectric materials », *Prog. Mater. Sci.*, vol. 63, p. 1‑57, juin 2014, doi: 10.1016/j.pmatsci.2014.01.002.
[204] J. Baedi, S. M. Hosseini, et A. Kompany, « The effect of excess titanium and crystal symmetry on electronic properties of Pb(Zr1−xTix)O3 compounds », *Comput. Mater. Sci.*, vol. 43, n° 4, p. 909‑916, oct. 2008, doi: 10.1016/j.commatsci.2008.02.008.
[205] Y. Lei, Y. Chen, et J. D. Lee, « Atomistic study of lattice structure of BiScO3 », *Comput. Mater. Sci.*, vol. 41, n° 2, p. 242‑246, déc. 2007, doi: 10.1016/j.commatsci.2007.04.003.
[206] J. M. Liu, X. Wang, H. L. W. Chan, et C. L. Choy, « Monte-Carlo simulation on the dipole alignment in ferroelectric square lattice », *Mater. Sci. Eng. B*, vol. 113, n° 1, p. 67‑72, oct. 2004, doi: 10.1016/j.mseb.2004.06.019.
[207] M. G. Shaikh, S. Phanish, et S. M. Sivakumar, « Domain switching criteria for ferroelectrics », *Comput. Mater. Sci.*, vol. 37, n° 1, p. 178‑186, août 2006, doi: 10.1016/j.commatsci.2005.12.040.
[208] M. Sepliarsky, R. L. Migoni, et M. G. Stachiotti, « Ab initio supported model simulations of ferroelectric perovskites », *Comput. Mater. Sci.*, vol. 10, n° 1, p. 51‑56, févr. 1998, doi: 10.1016/S0927-0256(97)00175-4.

[209] T. Janssen et J. A. Tjon, « One-dimensional model for a crystal with displacive modulation », *Phys. Rev. B*, vol. 24, n° 4, p. 2245‑2248, août 1981, doi: 10.1103/PhysRevB.24.2245.
[210] J.-M. Liu *et al.*, « Scaling of dynamic hysteresis in ferroelectric spin systems », *J. Phys. Condens. Matter*, vol. 13, n° 6, p. L153–L161, janv. 2001, doi: 10.1088/0953-8984/13/6/104.
[211] Y. Laosiritaworn, S. Ananta, J. Poulter, et R. Yimnirun, « Monte Carlo investigation of hysteresis properties in ferroelectric thin-films under the effect of uniaxial stresses », *Ceram. Int.*, vol. 35, n° 1, p. 181‑184, janv. 2009, doi: 10.1016/j.ceramint.2007.10.034.
[212] Y. Benhouria, I. Essaoudi, A. Ainane, R. Ahuja, et F. Dujardin, « Monte Carlo simulation of dielectric properties of a mixed spin-3/2 and spin-5/2 Ising ferrielectric nanowires », *Ferroelectrics*, vol. 507, n° 1, p. 58‑68, janv. 2017, doi: 10.1080/00150193.2017.1283170.
[213] S. Bin-Omran, I. A. Kornev, et L. Bellaiche, « Wang-Landau Monte Carlo formalism applied to ferroelectrics », *Phys. Rev. B*, vol. 93, n° 1, p. 014104, janv. 2016, doi: 10.1103/PhysRevB.93.014104.
[214] O. Gindele, A. Kimmel, M. G. Cain, et D. Duffy, « Shell Model force field for Lead Zirconate Titanate Pb(Zr1–xTix)O3 », *J. Phys. Chem. C*, vol. 119, n° 31, p. 17784‑17789, août 2015, doi: 10.1021/acs.jpcc.5b03207.
[215] X. S. Wang, C. L. Wang, et W. L. Zhong, « First-order phase transition in ferroelectric superlattice described by the transverse Ising model », *Solid State Commun.*, vol. 122, n° 6, p. 311‑315, mai 2002, doi: 10.1016/S0038-1098(02)00150-3.
[216] O. El Rhazouani, Z. Zarhri, A. Benyoussef, et A. El Kenz, « Magnetic properties of the fully spin-polarized Sr2CrOsO6 double perovskite: A Monte Carlo simulation », *Phys. Lett. A*, vol. 380, n° 13, p. 1241‑1246, mars 2016, doi: 10.1016/j.physleta.2016.02.003.
[217] O. El Rhazouani, A. Benyoussef, Z. Zarhri, et A. El Kenz, « Antisite disorder study by Monte Carlo simulation of the double perovskite Sr2CrReO6 », *J. Magn. Magn. Mater.*, vol. 401, p. 897‑901, mars 2016, doi: 10.1016/j.jmmm.2015.11.014.
[218] I. Ponomareva, I. I. Naumov, I. Kornev, H. Fu, et L. Bellaiche, « Atomistic treatment of depolarizing energy and field in ferroelectric nanostructures », *Phys. Rev. B*, vol. 72, n° 14, p. 140102, oct. 2005, doi: 10.1103/PhysRevB.72.140102.
[219] Y. Cai, S. Luo, Z. Wang, J. Xiong, et H. Gu, « J Materiomics », 2016.
[220] N. N. WATHORE, C. M. LONKAR, et D. K. KHARAT, « Effect of temperature on polarization reversal of strontium-doped lead zirconate titanate (PSZT) ceramics », *Bull. Mater. Sci.*, vol. 34, n° 1, p. 129‑132, févr. 2011, doi: 10.1007/s12034-011-0038-z.
[221] K. Iijima, Y. Tomita, R. Takayama, et I. Ueda, « Preparation of c-axis oriented PbTiO3 thin films and their crystallographic, dielectric, and pyroelectric properties », *J. Appl. Phys.*, vol. 60, n° 1, p. 361‑367, juill. 1986, doi: 10.1063/1.337654.
[222] S. Prosandeev *et al.*, « Anomalous properties of antiferroelectric ${\text{PbZrO}}_{3}$ under hydrostatic pressure », *Phys. Rev. B*, vol. 89, n° 21, p. 214111, juin 2014, doi: 10.1103/PhysRevB.89.214111.
[223] Z. Ž. Lazarević, N. Ž. Romčević, M. Todorović, et B. D. Stojanović, « Structural and ferroelectrical properties of bismuth titanate ceramic powders prepared by mechanically assisted synthesis », *Sci. Sinter.*, vol. 39, n° 2, p. 177‑184, 2007.
[224] S. Xu, « Trolier-McKinstry, W. Ren, B. Xu, Z.-L. Xie, and KJ Hemker », *J Appl Phys*, vol. 89, n° 2, p. 1336, 2001.
[225] F. Xu, S. Trolier-McKinstry, W. Ren, B. Xu, Z.-L. Xie, et K. J. Hemker, « Domain wall motion and its contribution to the dielectric and piezoelectric properties of lead zirconate titanate films », *J. Appl. Phys.*, vol. 89, n° 2, p. 1336, déc. 2000, doi: 10.1063/1.1325005.

[226] M. Benyoussef *et al.*, « Dielectric, ferroelectric, and energy storage properties in dysprosium doped sodium bismuth titanate ceramics », *Ceram. Int.*, vol. 44, n° 16, p. 19451‑19460, nov. 2018, doi: 10.1016/j.ceramint.2018.07.182.
[227] M. Ye, Q. Sun, X. Chen, Z. Jiang, et F. Wang, « Effect of Eu Doping on the Electrical Properties and Energy Storage Performance of PbZrO3 Antiferroelectric Thin Films », *J. Am. Ceram. Soc.*, vol. 94, n° 10, p. 3234‑3236, 2011, doi: 10.1111/j.1551-2916.2011.04814.x.
[228] C. A. F. Vaz, J. Hoffman, C. H. Ahn, et R. Ramesh, « Magnetoelectric Coupling Effects in Multiferroic Complex Oxide Composite Structures », *Adv. Mater.*, vol. 22, n° 26‑27, p. 2900‑2918, 2010, doi: 10.1002/adma.200904326.
[229] J. Ma, J. Hu, Z. Li, et C.-W. Nan, « Recent Progress in Multiferroic Magnetoelectric Composites: from Bulk to Thin Films (Adv. Mater. 9/2011) », *Adv. Mater.*, vol. 23, n° 9, p. 1061‑1061, 2011, doi: 10.1002/adma.201190024.
[230] G. Dong *et al.*, « Thermal Driven Giant Spin Dynamics at Three-Dimensional Heteroepitaxial Interface in Ni0.5Zn0.5Fe2O4/BaTiO3-Pillar Nanocomposites », *ACS Nano*, vol. 12, n° 4, p. 3751‑3758, avr. 2018, doi: 10.1021/acsnano.8b00962.
[231] Z. Tang, J. Chen, Y. Bai, et S. Zhao, « Magnetoelectric coupling effect in lead-free Bi4Ti3O12/CoFe2O4composite films derived from chemistry solution deposition », *Smart Mater. Struct.*, vol. 25, n° 8, p. 085020, juill. 2016, doi: 10.1088/0964-1726/25/8/085020.
[232] B. Peng, C. Zhang, Y. Yan, et M. Liu, « Voltage-Impulse-Induced Nonvolatile Control of Inductance in Tunable Magnetoelectric Inductors », *Phys. Rev. Appl.*, vol. 7, n° 4, p. 044015, avr. 2017, doi: 10.1103/PhysRevApplied.7.044015.
[233] J. Lee, N. Sai, T. Cai, Q. Niu, et A. A. Demkov, « Interfacial magnetoelectric coupling in tricomponent superlattices », *Phys. Rev. B*, vol. 81, n° 14, p. 144425, avr. 2010, doi: 10.1103/PhysRevB.81.144425.
[234] X. Zhong *et al.*, « Magnetoelectric couplings in high-density array of nanoscale Co/BiFeO3 multiferroic heterostructures », *Appl. Phys. Lett.*, vol. 114, n° 1, p. 012901, janv. 2019, doi: 10.1063/1.5066997.
[235] L. Y. Chen, C. L. Chen, K. X. Jin, X. J. Du, et A. Ali, « Favorable magnetoelectric phenomenon in Co2MnSi/PbTiO3 (001) ultrathin bilayer: A density functional theory study », *J. Appl. Phys.*, vol. 114, n° 14, p. 144101, oct. 2013, doi: 10.1063/1.4824369.
[236] I. F. Sharafullin, A. G. Nugumanov, A. R. Yuldasheva, A. R. Zharmukhametov, et H. T. Diep, « Modeling of magnetoelectric and surface properties in superlattices and nanofilms of multiferroics », *J. Magn. Magn. Mater.*, vol. 475, p. 453‑457, avr. 2019, doi: 10.1016/j.jmmm.2018.11.116.
[237] Z. Wang, W. Wang, Q. Li, M. Tian, Z. Gao, et Y. Liu, « Monte Carlo simulation of dieletric properties of the antiferroelectric/ferroelectric BiFeO3/YMnO3 bilayer in the external electric field », *Phys. E Low-Dimens. Syst. Nanostructures*, vol. 110, p. 127‑133, juin 2019, doi: 10.1016/j.physe.2019.02.022.
[238] H. H. Ortiz-Álvarez, C. M. Bedoya-Hincapié, et E. Restrepo-Parra, « Monte Carlo simulation of charge mediated magnetoelectricity in multiferroic bilayers », *Phys. B Condens. Matter*, vol. 454, p. 235‑239, déc. 2014, doi: 10.1016/j.physb.2014.08.002.
[239] O. El rhazouani, Y. Ziat, et A. Benyoussef, « Monte Carlo simulation for calculating the exchange couplings in Ca2CrNO6 (N = Mo, Re) double perovskites », *Mod. Electron. Mater.*, vol. 3, n° 3, p. 99‑103, sept. 2017, doi: 10.1016/j.moem.2017.09.004.
[240] M. A. Tamerd *et al.*, « Modelling of the ferroelectric and energy storage properties of PbZr1-xTixO3 thin films using Monte Carlo simulation », *Mater. Res. Express*, vol. 6, n° 12, p. 126429, janv. 2020, doi: 10.1088/2053-1591/ab625f.
[241] O. El Rhazouani, A. Benyoussef, S. Naji, et A. El Kenz, « Magnetic properties of double perovskite Sr2CrReO6: Mean field approximation and Monte Carlo simulation »,

Phys. Stat. Mech. Its Appl., vol. 397, p. 31‑39, mars 2014, doi: 10.1016/j.physa.2013.11.006.
[242] R. C. Rai, S. Wilser, M. Guminiak, B. Cai, et M. L. Nakarmi, « Optical and electronic properties of NiFe2O4 and CoFe2O4 thin films », *Appl. Phys. A*, vol. 106, n° 1, p. 207‑211, janv. 2012, doi: 10.1007/s00339-011-6549-z.
[243] K. Dileep, B. Loukya, N. Pachauri, A. Gupta, et R. Datta, « Probing optical band gaps at the nanoscale in NiFe2O4 and CoFe2O4 epitaxial films by high resolution electron energy loss spectroscopy », *J. Appl. Phys.*, vol. 116, n° 10, p. 103505, sept. 2014, doi: 10.1063/1.4895059.
[244] A. J. Rondinone, A. C. S. Samia, et Z. J. Zhang, « Superparamagnetic Relaxation and Magnetic Anisotropy Energy Distribution in CoFe2O4 Spinel Ferrite Nanocrystallites », *J. Phys. Chem. B*, vol. 103, n° 33, p. 6876‑6880, août 1999, doi: 10.1021/jp9912307.
[245] S. Bin-Omran, « Phase-transition character in (Ba0.50,Sr0.50)TiO3 nanodots from first principles », *J. Alloys Compd.*, vol. 674, p. 82‑88, juill. 2016, doi: 10.1016/j.jallcom.2016.03.038.
[246] L. Jian *et al.*, « Strong sub-resonance magnetoelectric coupling in PZT-NiFe2O4-PZT thin film composite », *Nano-Struct. Nano-Objects*, vol. 18, p. 100272, avr. 2019, doi: 10.1016/j.nanoso.2019.100272.
[247] Y. Shimakawa, M. Azuma, et N. Ichikawa, « Multiferroic Compounds with Double-Perovskite Structures », *Materials*, vol. 4, n° 1, p. 153‑168, janv. 2011, doi: 10.3390/ma4010153.
[248] I. Kaur et N. K. Verma, « Magnetic and electric properties of BFO–NFO nanocomposites », *Mater. Sci. Semicond. Process.*, vol. 33, p. 32‑35, mai 2015, doi: 10.1016/j.mssp.2015.01.032.
[249] G. Catalan et J. F. Scott, « Physics and Applications of Bismuth Ferrite », *Adv. Mater.*, vol. 21, n° 24, p. 2463‑2485, 2009, doi: 10.1002/adma.200802849.
[250] F. Pedro-García, L. G. Betancourt-Cantera, A. M. Bolarín-Miró, C. A. Cortés-Escobedo, A. Barba-Pingarrón, et F. Sánchez-De Jesús, « Magnetoelectric coupling in multiferroic BiFeO3 by co-doping with strontium and nickel », *Ceram. Int.*, vol. 45, n° 8, p. 10114‑10119, juin 2019, doi: 10.1016/j.ceramint.2019.02.058.
[251] S. Atiq *et al.*, « Multifunctionality of magnetoelectrically coupled Ni/Cr co-doped BiFeO3 multiferroics », *J. Alloys Compd.*, vol. 789, p. 400‑408, juin 2019, doi: 10.1016/j.jallcom.2019.03.058.
[252] A. S. Priya, I. B. S. Banu, et S. Anwar, « Influence of Dy and Cu doping on the room temperature multiferroic properties of BiFeO3 », *J. Magn. Magn. Mater.*, vol. 401, p. 333‑338, mars 2016, doi: 10.1016/j.jmmm.2015.10.059.
[253] R. K. Kotnala, R. Gupta, et S. Chaudhary, « Giant magnetoelectric coupling interaction in BaTiO3/BiFeO3/BaTiO3 trilayer multiferroic heterostructures », *Appl. Phys. Lett.*, vol. 107, n° 8, p. 082908, août 2015, doi: 10.1063/1.4929729.
[254] M. Lorenz *et al.*, « Correlation of magnetoelectric coupling in multiferroic BaTiO3-BiFeO3 superlattices with oxygen vacancies and antiphase octahedral rotations », *Appl. Phys. Lett.*, vol. 106, n° 1, p. 012905, janv. 2015, doi: 10.1063/1.4905343.
[255] A. Lahmar, S. Habouti, M. Dietze, C.-H. Solterbeck, et M. Es-Souni, « Effects of rare earth manganites on structural, ferroelectric, and magnetic properties of BiFeO3 thin films », *Appl. Phys. Lett.*, vol. 94, n° 1, p. 012903, janv. 2009, doi: 10.1063/1.3064954.
[256] M. Muneeswaran, J.-W. Jang, J. H. Jeong, A. Akbari-Fakhrabadi, et N. V. Giridharan, « Effect of dopant-induced defects on structural, electrical, and enhanced ferromagnetism and magnetoelectric properties of Dy and Sr co-doped BiFeO3 », *J. Mater. Sci. Mater. Electron.*, vol. 30, n° 8, p. 7359‑7366, avr. 2019, doi: 10.1007/s10854-019-01048-y.

[257] S. Kazhugasalamoorthy *et al.*, « Investigations on the properties of pure and rare earth modified bismuth ferrite ceramics », *J. Alloys Compd.*, vol. 493, n° 1, p. 569‑572, mars 2010, doi: 10.1016/j.jallcom.2009.12.157.
[258] A. Albaalbaky, Y. Kvashnin, D. Ledue, R. Patte, et R. Frésard, « Magnetoelectric properties of multiferroic ${\mathrm{CuCrO}}_{2}$ studied by means of ab initio calculations and Monte Carlo simulations », *Phys. Rev. B*, vol. 96, n° 6, p. 064431, août 2017, doi: 10.1103/PhysRevB.96.064431.
[259] A. S. E. Elyacoubi, R. Masrour, et A. Jabar, « Magnetoelectric coupling in RMn2O5 multiferroic: a Monte Carlo simulation », *Phase Transit.*, vol. 92, n° 6, p. 556‑562, juin 2019, doi: 10.1080/01411594.2019.1602271.
[260] I. F. Sharafullin, M. Kh. Kharrasov, et H. T. Diep, « Magneto-ferroelectric interaction in superlattices: Monte Carlo study of phase transitions », *J. Magn. Magn. Mater.*, vol. 476, p. 258‑267, avr. 2019, doi: 10.1016/j.jmmm.2018.12.088.
[261] J.-G. Park, M. D. Le, J. Jeong, et S. Lee, « Structure and spin dynamics of multiferroic BiFeO3 », *J. Phys. Condens. Matter*, vol. 26, n° 43, p. 433202, oct. 2014, doi: 10.1088/0953-8984/26/43/433202.
[262] M. El Yadari, L. Bahmad, A. El Kenz, et A. Benyoussef, « Monte Carlo study of the double perovskite nano Sr2VMoO6 », *J. Alloys Compd.*, vol. 579, p. 86‑91, déc. 2013, doi: 10.1016/j.jallcom.2013.01.158.
[263] H. Wang *et al.*, « Overcoming the Limits of the Interfacial Dzyaloshinskii–Moriya Interaction by Antiferromagnetic Order in Multiferroic Heterostructures », *Adv. Mater.*, vol. 32, n° 14, p. 1904415, 2020, doi: 10.1002/adma.201904415.
[264] G. S. Lotey et N. K. Verma, « Magnetoelectric coupling in multiferroic BiFeO3 nanowires », *Chem. Phys. Lett.*, vol. 579, p. 78‑84, juill. 2013, doi: 10.1016/j.cplett.2013.06.016.
[265] H. Naganuma et S. Okamura, « Structural, magnetic, and ferroelectric properties of multiferroic BiFeO3 film fabricated by chemical solution deposition », *J. Appl. Phys.*, vol. 101, n° 9, p. 09M103, mai 2007, doi: 10.1063/1.2711279.
[266] D. S. Rana, I. Kawayama, K. Mavani, K. Takahashi, H. Murakami, et M. Tonouchi, « Understanding the Nature of Ultrafast Polarization Dynamics of Ferroelectric Memory in the Multiferroic BiFeO3 », *Adv. Mater.*, vol. 21, n° 28, p. 2881‑2885, 2009, doi: 10.1002/adma.200802094.
[267] L. W. Martin *et al.*, « Multiferroics and magnetoelectrics: thin films and nanostructures », *J. Phys. Condens. Matter*, vol. 20, n° 43, p. 434220, oct. 2008, doi: 10.1088/0953-8984/20/43/434220.
[268] T. Zhao *et al.*, « Electrical control of antiferromagnetic domains in multiferroic BiFeO 3 films at room temperature », *Nat. Mater.*, vol. 5, n° 10, p. 823‑829, oct. 2006, doi: 10.1038/nmat1731.
[269] F. Kubel et H. Schmid, « Acta Crystallogr., Sect. B: Struct. Sci. », 1990.
[270] J. B. Neaton, C. Ederer, U. V. Waghmare, N. A. Spaldin, et K. M. Rabe, « First-principles study of spontaneous polarization in multiferroic $\mathrm{Bi}\mathrm{Fe}{\mathrm{O}}_{3}$ », *Phys. Rev. B*, vol. 71, n° 1, p. 014113, janv. 2005, doi: 10.1103/PhysRevB.71.014113.
[271] G. A. Smolenskii, « VA isupov, AI Agranovskaya, and NN Krainik », *Sov Phys Solid State*, vol. 2, p. 2651, 1961.
[272] P. Fischer, M. Polomska, I. Sosnowska, et M. Szymanski, « Temperature dependence of the crystal and magnetic structures of BiFeO3 », *J. Phys. C Solid State Phys.*, vol. 13, n° 10, p. 1931–1940, avr. 1980, doi: 10.1088/0022-3719/13/10/012.
[273] M. A. Basith *et al.*, « Simple top-down preparation of magnetic Bi0.9Gd0.1Fe1−xTixO3 nanoparticles by ultrasonication of multiferroic bulk material », *Nanoscale*, vol. 6, n° 23, p. 14336‑14342, nov. 2014, doi: 10.1039/C4NR03150D.

[274] M. A. Basith, O. Kurni, M. S. Alam, B. L. Sinha, et B. Ahmmad, « Room temperature dielectric and magnetic properties of Gd and Ti co-doped BiFeO3 ceramics », *J. Appl. Phys.*, vol. 115, n° 2, p. 024102, janv. 2014, doi: 10.1063/1.4861151.
[275] W. Zhou *et al.*, « Effects of Sm and Mn co-doping on structural, optical and magnetic properties of BiFeO3 films prepared by a sol–gel technique », *Mater. Lett.*, vol. 144, p. 93‑96, avr. 2015, doi: 10.1016/j.matlet.2015.01.038.
[276] M. Hasan *et al.*, « Saturation magnetization and band gap tuning in BiFeO3 nanoparticles via co-substitution of Gd and Mn », *J. Alloys Compd.*, vol. 687, p. 701‑706, déc. 2016, doi: 10.1016/j.jallcom.2016.06.171.
[277] A. Lahmar et M. Es-Souni, « Sequence of structural transitions in BiFeO3–RMnO3 thin films (R=Rare earth) », *Ceram. Int.*, vol. 41, n° 4, p. 5721‑5726, mai 2015, doi: 10.1016/j.ceramint.2014.12.157.
[278] L. Yin, W. Mi, et X. Wang, « Prediction of a metal–insulator transition and a two-dimensional electron gas in orthoferrite LaTiO3/tetragonal BiFeO3 heterostructures », *J. Mater. Chem. C*, vol. 3, n° 42, p. 11066‑11075, oct. 2015, doi: 10.1039/C5TC02672E.
[279] D. Mekam, S. Kacimi, M. Djermouni, M. Azzouz, et A. Zaoui, « Ab initio calculations on RE–TM–O3 perovskites: A comparative study of cation effect », *Results Phys.*, vol. 2, p. 156‑163, janv. 2012, doi: 10.1016/j.rinp.2012.09.008.
[280] A. M. Rappe, K. M. Rabe, E. Kaxiras, et J. D. Joannopoulos, « Optimized pseudopotentials », *Phys. Rev. B*, vol. 41, n° 2, p. 1227‑1230, janv. 1990, doi: 10.1103/PhysRevB.41.1227.
[281] N. Gao *et al.*, « First principles investigation on the electronic, magnetic and optical properties of Bi0.8M0.2Fe0.9Co0.1O3 (M=La, Gd, Er, Lu) », *Comput. Theor. Chem.*, vol. 1084, p. 36‑42, mai 2016, doi: 10.1016/j.comptc.2016.03.001.
[282] W. Ye, G. Tan, G. Dong, H. Ren, et A. Xia, « Improved multiferroic properties in (Ho, Mn) co-doped BiFeO3 thin films prepared by chemical solution deposition », *Ceram. Int.*, vol. 41, n° 3, Part B, p. 4668‑4674, avr. 2015, doi: 10.1016/j.ceramint.2014.12.013.
[283] Y. Han *et al.*, « Enhancement of magnetic and ferroelectric properties of BiFeO3 by Er and transition element (Mn, Co) co-doping », *Mater. Sci. Eng. B*, vol. 188, p. 26‑30, oct. 2014, doi: 10.1016/j.mseb.2014.05.012.
[284] M. Abbate *et al.*, « Controlled-valence properties of ${\mathrm{La}}_{1\mathrm{\ensuremath{-}}\mathit{x}}$${\mathrm{Sr}}_{\mathit{x}}$${\mathrm{FeO}}_{3}$ and ${\mathrm{La}}_{1\mathrm{\ensuremath{-}}\mathit{x}}$${\mathrm{Sr}}_{\mathit{x}}$${\mathrm{MnO}}_{3}$ studied by soft-x-ray absorption spectroscopy », *Phys. Rev. B*, vol. 46, n° 8, p. 4511‑4519, août 1992, doi: 10.1103/PhysRevB.46.4511.
[285] H. A. Jahn, E. Teller, et F. G. Donnan, « Stability of polyatomic molecules in degenerate electronic states - I—Orbital degeneracy », *Proc. R. Soc. Lond. Ser. - Math. Phys. Sci.*, vol. 161, n° 905, p. 220‑235, juill. 1937, doi: 10.1098/rspa.1937.0142.
[286] J. D. Dunitz et L. E. Orgel, « Electronic properties of transition-metal oxides—I: Distortions from cubic symmetry », *J. Phys. Chem. Solids*, vol. 3, n° 1, p. 20‑29, janv. 1957, doi: 10.1016/0022-3697(57)90043-4.
[287] L. F. J. Piper *et al.*, « Elucidating the Nature of Pseudo Jahn–Teller Distortions in LixMnPO4: Combining Density Functional Theory with Soft and Hard X-ray Spectroscopy », *J. Phys. Chem. C*, vol. 117, n° 20, p. 10383‑10396, mai 2013, doi: 10.1021/jp3122374.
[288] R. D. King-Smith et D. Vanderbilt, « Theory of polarization of crystalline solids », *Phys. Rev. B*, vol. 47, n° 3, p. 1651‑1654, janv. 1993, doi: 10.1103/PhysRevB.47.1651.
[289] Q. Zhang, Q. Jing, H. Duan, et H. Cao, « The relationship between covalent bonds and the optical response in a nonpolar family ATeMoO6 (A=Mg, Zn, Cd): A Berry-phase

investigation », *J. Solid State Chem.*, vol. 264, p. 22‑28, août 2018, doi: 10.1016/j.jssc.2018.04.031.

[290] M. S. Bozgeyik, N. Kirkgecit, R. K. Katiyar, et R. S. Katiyar, « Monitoring structural variation on Gd ratio of La modified bismuth ferrite ceramics with enhanced magnetization », *J. Alloys Compd.*, vol. 819, p. 153050, avr. 2020, doi: 10.1016/j.jallcom.2019.153050.

[291] X. X. Shi, X. Q. Liu, et X. M. Chen, « Structure evolution and piezoelectric properties across the morphotropic phase boundary of Sm-substituted BiFeO3 ceramics », *J. Appl. Phys.*, vol. 119, n° 6, p. 064104, févr. 2016, doi: 10.1063/1.4941820.

[292] P. Mandal *et al.*, « Morphotropic Phase Boundary in the Pb-Free (1 − x)BiTi3/8Fe2/8Mg3/8O3–xCaTiO3 System: Tetragonal Polarization and Enhanced Electromechanical Properties », *Adv. Mater.*, vol. 27, n° 18, p. 2883‑2889, 2015, doi: 10.1002/adma.201405452.

List of publications :

1. **M. A. Tamerd et al.,** « Magnetoelectric coupling at the NiFe2O4/PZT (001) interface: A density functional theory investigation », Superlattices Microstruct., vol. 139, p. 106401, mars 2020, doi: 10.1016/j.spmi.2020.106401.

2. **M. A. Tamerd et al.**, « Modelling of the ferroelectric and energy storage properties of PbZr1-xTixO3 thin films using Monte Carlo simulation », Mater. Res. Express, vol. 6, no 12, p. 126429, janv. 2020, doi: 10.1088/2053-1591/ab625f.

3. **M. Ait Tamerd et al.,** « Phase diagrams and magnetic properties of double perovskite Ba2CrMoO6 », Int. J. Mod. Phys. B, vol. 29, no 27, p. 1550174, oct. 2015, doi: 10.1142/S021797921550174X.

4. **M. A. Tamerd et al**., « First-principles study of electronic, electrical and optical properties of HoMn 2 O 5 », J. Phys. Conf. Ser., vol. 758, p. 012009, oct. 2016, doi: 10.1088/1742-6596/758/1/012009.

5. B. Abraime, K. El Maalam, L. Fkhar, A. Mahmoud, F. Boschini, **M. Ait Tamerd**, A. Benyoussef, et al.« Influence of synthesis methods with low annealing temperature on the structural and magnetic properties of CoFe2O4 nanopowders for permanent magnet application », J. Magn. Magn. Mater., vol. 500, p. 166416, avr. 2020, doi: 10.1016/j.jmmm.2020.166416.

6. B. Abraime, A. Mahmoud, F. Boschini, **M. Ait Tamerd**, A. Benyoussef, M. Hamedoun, Y. Xiao, A. El Kenz, et O. Mounkachi. « Tunable maximum energy product in CoFe2O4 nanopowder for permanent magnet application », J. Magn. Magn. Mater., vol. 467, p. 129‑134, déc. 2018, doi: 10.1016/j.jmmm.2018.07.063.

7. B. Abraime, **M. Ait Tamerd**, A. Mahmoud, F. Boschini, A. Benyoussef, M. Hamedoun, Y. Xiao, A. El Kenz, et O. Mounkachi., « Experimental and theoretical investigation of SrFe12O19 nanopowder for permanent magnet application », Ceram. Int., vol. 43, no 17, p. 15999‑16006, déc. 2017, doi: 10.1016/j.ceramint.2017.08.187.

8. A. Nid-bahami, S. S. Ahmed, **M. Ait Tamerd**, H. Zaari, A. El Kenz, et A. Benyoussef, « Electronic and magnetic properties of double perovskite Sr2CoUO6: Heisenberg model », Phys. Stat. Mech. Its Appl., vol. 490, p. 1259 ‑ 1266, janv. 2018, doi: 10.1016/j.physa.2017.08.027.

9. **Mohamed Ait Tamerd**, Brahim Abraime, Omar El Rhazouani, Abdelilah Lahmar, Mimoun El Marssi, Mohammed Hamedoun, Abdelilah Benyoussef, Abdallah El Kenz. Theoretical investigation of magnetoelectric coupling in MFe2O4/PZT/MFe2O4 (M=Ni,Co) at low dimensionality.**(submitted)**

10. **M. Ait Tamerd** , B. Abraime , A. Kadiri, A. Lahmar , M. El Marssi, M. Hamedoun, A. Benyoussef, A. El Kenz . Prediction of Magnetoelectric properties of defect BiFeO3 thin films using Monte Carlo simulations. **(submitted)**

11. First principles study on BiFeO3-REMnO3 (RE = Er, Eu, Gd, Ho, La, Tb). **M. Ait Tamerd**, B. Abraime, A. Lahmar, M. El Marssi, A. Benyoussef, A. El Kenz. **(submitted)**

12 . KADIRI, **M. AIT TAMERD**, G.Dimitri Ngantso R.KUMAR,Y.EL AMRAOUI , H. Ez-Zahraouy, A.Benyoussef. Effects of size for an assembly of Core-Shell nanoparticles with the cubic structure: Monte Carlo simulations. **(submitted)**

UNIVERSITÉ MOHAMMED V-RABAT
FACULTÉ DES SCIENCES
RABAT

Title : Theoretical investigations and magnetoelectric prediction in some functional thin films.

Abstract: In this thesis, we studied the mechanisms governing extrinsic and intrinsic magnetoelectric coupling using density functional theory (DFT) and Monte Carlo simulation in multiferroic compounds. The electronic origin of the strong magnetoelectric coupling of the NiFe2O4/PZT heterostructure was analyzed by the density functional theory. In addition, the ferroelectric, magnetic and magnetoelectric properties of NiFe2O4/PZT , CoFe2O4/PZT, NiFe2O4/PZT/CoFe2O4 and NiFe2O4/PZT/NiFe2O4 heterostructures were obtained by Monte Carlo simulation and the maximum magnetoelectric voltage coefficient is 1405 mV/(cm.Oe) was predicted in NiFe2O4/PZT/NiFe2O4. The second part of this manuscript is dedicated to the simulation of the intrinsic magnetoelectric coupling in BiFeO3. A large magnetoelectric voltage coefficient of 104mV/(cm.Oe) has been predicted in BiFeO3 thin films with 25% of the defects. In addition, the multiferroic properties of BiFeO3 doped with rare earth and Mn were analyzed by the DFT.

Keywords: magnetoelectric, DFT, Monte Carlo simulation, multiferroics, NiFe2O4/PZT , BiFeO3.

Titre : Étude théorique et la prédiction magnétoélectrique dans certaines couches minces fonctionnelles.

Résumé : Dans le cadre de cette thèse, nous avons étudié les mécanismes régissant le couplage magnétoélectrique extrinsèque et intrinsèque en utilisant la théorie de la fonctionnelle de la densité (DFT) et la simulation de Monte Carlo dans les composés multiferroïques. L'origine électronique du fort couplage magnétoélectrique de l'hétérostructure NiFe2O4/PZT a été analysé par la théorie de la fonctionnelle de la densité. De plus, les propriétés ferroélectriques, magnétiques et magnétoélectriques des hétérostructures NiFe2O4/PZT , CoFe2O4/PZT, NiFe2O4/PZT/CoFe2O4 et NiFe2O4/PZT/NiFe2O4 ont été obtenu par la simulation Monte Carlo et le coefficient maximum de voltage magnétoélectrique est de 1405 mV/(cm.Oe) a été prédit dans NiFe2O4/PZT/NiFe2O4. La deuxième partie de ce manuscrit est consacrée à la modélisation et la simulation du couplage magnétoélectrique intrinsèque dans le $BiFeO_3$. Un coefficient important de voltage magnétoélectrique de 104 mV/(cm.Oe) a été prédit dans les couches minces de $BiFeO_3$ avec 25% des défauts. En addition, les propriétés multiferroïques de $BiFeO_3$ dopé par terre rare et Mn sont été analysé par la DFT.

Mots-clés : magnétoélectrique, DFT, simulation Monte Carlo,multiferroïques, hétérostructure NiFe2O4/PZT, $BiFeO_3$.

Faculté des Sciences, 4 Avenue Ibn Battouta B.P. 1014 RP, Rabat-Maroc Tel +212 (0) 37 77 18 34/35/38, Fax : +212 (0) 37 77 42 61, http://www.fsr.ac.ma